CHAPTER ONE

INTRODUCTION

1.1 Background of the Study

The atmosphere or air is a mixture of different gases which include 78 % of nitrogen, 21 % of oxygen, 0.93 % argon, 0.04 % carbon dioxide, an average of 1 % water vapour at sea level and 0.4 % water vapour over the entire atmosphere and small amount of other gases. Water vapor is an important constituent in the Earth's atmosphere and its distribution in space and time must be known to understand and predict weather and climate (Ward *et al*., 2019). The amount of water vapour in the air depends on the time of the day, latitude, seasonal changes and air temperature. The quantity of water vapour in air can be expressed in terms of mass, volume or amount of substance.

Water vapour like other gases in air contributes to the total pressure of the air/atmosphere of about 760 mmHg or 101325 Pa or 1.01325 bars. Dalton's law states that "The total pressure of a gas is equal to the sum of the different gases' partial pressures". Mathematically,

$$P = P_1 + P_2 + P_3 + P_4 + \ldots + P_n, \qquad 1.1$$

where P_1, P_2, P_3, P_4 and P_n are the partial pressures of the constituent gases. The partial pressure of gas in a mixture is the pressure the gas would exert if it occupied the container alone (Zakariyah, 2013). The partial pressure of water vapour is the pressure due to proportion of water vapour in the air. This is called the vapour pressure (P_v). At any given temperature, the air has a limit to the quantity of water vapour it can contain. When the concentration of water vapour present in air at a given temperature reaches its possible maximum value, it is said to be

saturated. At this point, the vapour pressure will have its maximum value which is referred to as the saturated vapour pressure (SVP). Saturated vapour pressure is defined as "The pressure exerted by the vapour of a substance's pure liquid (or solid) phase when at a given temperature, it is in equilibrium with a plane surface of that substance" (Sherwood, 2010). The water vapour pressure becomes saturated when dynamical equilibrium between the escaping and returning molecules in a closed container for instance is established. Saturated water vapour pressure depends on temperature only and independent on the presence of other gases or ambient pressure. It increases with an increasing temperature though in an exponential manner.

The water vapour in the air brings about clouds, rain, snow, thunder, or lightning. Water vapour being a greenhouse gas plays a very important role in life on earth by absorbing ultraviolet solar radiation, warming the surface through heat retention (greenhouse effect) and reducing temperature extremes between day and night. Thus, the presence of water vapour in the atmosphere makes the earth habitable. However, its variations affect different aspects of the environment –animals, human beings, agriculture, weather, industry, electronics and medicine among others. It also influences various physical, chemical and biological processes and hence can bring about global warming and climate change.

Humidity generally is the amount of water vapour present in the air. It is a physical parameter which describes the degree of dryness of the atmosphere (Tripathy *et al*., 2016). Air humidity is not a constant value and can significantly change in a short time (Korotcenkov, 2018). There are three types of humidity – absolute humidity or vapour density (dv), relative humidity (RH) and specific humidity.

The amount of water vapor in a volume unit of air is referred to as the absolute humidity of the air, usually expressed as grams in a cubic meter of air (Voutilainen, 2005). The maximum value of absolute humidity is the saturated humidity at the prevailing temperature, i.e. the maximum amount of water vapor that the air can hold (Lars & Elmarsson, 1994, Voutilainen, 2005). The vapor concentration or absolute humidity of a mixture of water vapor and dry air is defined as the ratio of the mass of water vapor M_w to the volume V occupied by the mixture:

$$D_v = \frac{M_w}{V} \qquad 1.2$$

$M_w = n_w \times m_w$, n_w is a number of moles of water vapor present in the volume V and m_w is the molecular mass of water (Korotcenkov, 2018). Absolute humidity is expressed in gm^{-3}.

Specific humidity is a measure of the actual mass of water dissolved into an air sample (Krepcik, 2010). It is the ratio of the mass of water vapour to the mass of moist air:

$$Q = \frac{M_w}{M_w + M_a} \qquad 1.3$$

where Q is the specific humidity, M_w is the mass of water vapour and M_a is the mass of the dry air (Korotcenkov, 2018). Specific humidity is expressed in % or g/kg.

Absolute humidity and specific humidity are not functions of temperature since it is simply the amount of water vapour present per unit volume of the air. Specific or absolute humidity is used to calculate total precipitable water in an air column and to quantify water vapour transport in the atmosphere (Wood *et al*., 2019).

Relative humidity (expressed in percentage) is a measure of how much moisture is present compared to how much moisture the air can hold at a particular temperature (Shelton, 2008). Relative humidity reports the amount of water vapour in air relative to the saturation vapour content at a given temperature, T, usually expressed as a percentage (Wood *et al*., 2019). Relative humidity can also be defined in terms vapour pressure and saturation vapour pressure of moist air as the ratio of the vapour pressure (P_v) of the moist air to its saturation vapor pressure (P_s) at its temperature, which is expressed in % (Chia-Yen and Gwo-Bin, 2005).

$$RH = \frac{P_v}{P_s} X\ 100\% \qquad 1.4$$

Based on equation 1.2, relative humidity is defined as the ratio of actual vapour density to the saturated vapour density:

$$\text{Relative humidity} = \frac{\text{actual vapour density}}{\text{saturation vapour density}} \text{ x } 100\% \qquad 1.5$$

Relative humidity is a function of temperature. It decreases with increasing temperature. At dew point temperature, the relative humidity of cooling air or condensing air becomes 100%.

Humidity is one of the fundamental abiotic factors that defines any habitat and is a determinant of which animals and plants can thrive in a given environment. The human body dissipates heat through perspiration and evaporation. The environment becomes hotter with increasing humidity. Thus, the rate of evaporation of sweat becomes slower than the rate at which the body is sweating making the body hot and sticky. Commonly reported mold or moisture or humidity related health effects are for example: irritative and general symptoms such as rhinitis, sore throat, hoarseness, cough, phlegm, shortness of breath, eye irritation, eczema, tiredness,

headache, nausea, difficulties in concentration, and fever; infections such as common cold, otitis, maxillary sinusitis, and bronchitis; and allergic diseases such as allergy, asthma, and alveolitis (Voutilainen, 2005).

Many manufacturing processes, such as semiconductor manufacturing and chemical gas purification, rely on precisely controlled humidity levels (Hong *et al*, 2019**)**. Extremely humid and extremely dry climates can cause problems in electronics. Electronics and water do not mix. Some of the environmental conditions affecting electronic equipment and systems include moisture, dust, vibration, air cooling and heating (Nishinaka *et al*., 2002 & Rosa and Brad, 2009). High humidity can decrease the insulation resistance in electrolytic capacitors, increased leakage current and reduced gain in transistors, formation of condensation on internal components of electronic equipment, coating of circuit boards in moisture, corrosion and breakage of electronic components, short circuits in electronic devices and device failure. Low humidity environments can lead to static electricity discharge which can results in irreversible damage to components.

Weather plays a major role in determining the success of agricultural pursuits. Most field crops are dependent solely upon weather to provide life-sustaining water and energy and livestock are also dependent upon weather for their comfort and food supplies (Vining, 1990). Humidity can also affect plant turgor pressure, which is an indicator of the amount of water in plant cells. When humidity is low, moisture evaporates from plants very quickly and plants can wilt rapidly if too much water is pulled out of plant cells through transpiration. Plants require a higher humidity when the temperature is high and a lower humidity when it is low to help moderate the transpiration rate of the plants so that when it is hot the plant will tend to transpire

heavily, making the RH high will tend to reduce transpiration and delay the point at which the plant starts to wilt and when temperatures are low then RH should be reduced (Shamshiri, 2007). Relative humidity (RH) directly influences the water relations of plant and indirectly affects leaf growth, photosynthesis, pollination, occurrence of diseases and finally economic yield (Sandhu and Dhaliwal, 2016). Humidity is also an important consideration for post-harvest storage of crops. Cold temperature and low humidity are important for the long-term storage of grains (corn, wheat etc). The appearance, texture, flavor and levels of these important bioactive compounds in fruits and vegetables are greatly influenced by postharvest conditions such as precooling method, storage temperature, humidity and atmosphere composition (Lester, 2006 and Nunes, 2008).

A sensor is a device that receives and responds to a signal or stimulus (Fraden, 2004). This definition considers all manner of sensors ranging from body sensors such as ear, eye, tongue, nose and skin to electronic sensors. A more precise definition of a sensor is a device that receives a stimulus (the quantity, property, or condition that is sensed) and responds with an electrical signal (Fraden, 2004). It detects a change in a physical stimulus and turns it into a signal which can be measured or recorded (Sureshkumar and Rajesh, 2018). It acquires information from the 'real world'. The basic principle of a sensor can therefore, be illustrated as in Figure 1.1.

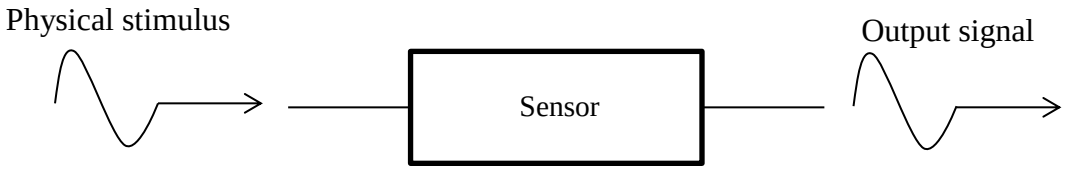

Figure 1.1 Illustration of the principle of a sensor

A sensor acquires a physical quantity and converts it into a signal which could be optical, electrical, or mechanical signal. Sinha (2017) listed some of the physical quantities that their changes can be detected as motion, position, displacement, velocity, acceleration, force, strain, pressure, flow, sound, moisture, light, radiation, temperature and chemical presence.

There are various classes of sensors but electronic sensors are of greatest importance to this research. A sensing system is a complete system that gathers information about events or qualities of the physical world and transforms it into the electronic signals that are used in conventional signal processing systems (Zook, 2008). Figure 1.2 illustrates a typical electronic sensor system.

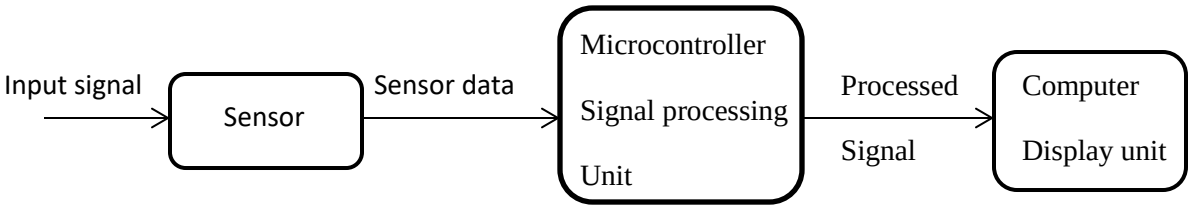

Figure 1.2 A Typical electronic sensor system

The electronic sensor detects and measures a physical quantity such as humidity, temperature, pressure or loudness and converts it into an electronic signal which could be analog or digital. The microcontroller such as Arduino nano or Arduino uno processes the data from the sensor and sends to the computer system for display of the result.

Humidity sensors detect and measure the water vapour levels in an environment. Humidity/moisture sensing, control, monitoring and measurement are very crucial in the homes,

agriculture, industries among others. Humidity measurements at the Earth's surface are required for meteorological analysis and forecasting, climate studies and many special applications in hydrology, agriculture, aeronautical services and environmental studies in general (Balasubramanian, 2015). In manufacturing of semiconductors and electronics, the generation of products changes more and more rapidly. As a result, the control of humidity and dew point in the manufacturing process has become stricter. Humidity control is also important at liquid crystal display plants, paint plants and during wafer processing. In medical applications, humidity control is required for respiratory equipment, sterilizers, incubators, pharmaceutical processing and biological products. Humidity control is also necessary in chemical gas purification, dryers, ovens, film desiccation, paper and textile production, and food processing. In agriculture, measurement of humidity is important for plantation protection (dew prevention), soil moisture monitoring, farm produce storage among others. For domestic applications, humidity control is required for living environment in buildings, cooking control for microwave ovens among others.

Humidity sensing instruments typically rely on measurements of temperature, pressure, mass, mechanical or electrical change in a substance when moisture is absorbed from which the humidity can then be derived (Gammel, 2013). Some of these classical hygrometers include metal-paper coil hygrometer, hair tension hygrometers, psychrometer (Wet-and-dry-bulb thermometer), sling psychrometer and chilled mirror dew point hygrometer.

Modern and most commonly used humidity sensors include capacitive relative humidity sensor, resistive relative humidity sensor, thermal conductivity humidity sensor and gravimetric

humidity sensor. Resistive and capacitive are electronic humidity sensors (Fenner & Zdankiewicz, 2001, Hong *et al*., 2019). The capacitive-type sensor is superior in linearity of sensor output and in stability at high humidity to the resistive-type sensor (Griesel *et al*., 2012). Capacitive humidity sensors have better linearity, accuracy, and higher thermal stability than resistive humidity sensors (Lee *et al*., 2011).

The prefix nano is equal to 10^{-9}, which is billionth (Cracknell and Bolton, 2009). The prefix nano in the word nanotechnology means a billionth, 1 x 10^{-9} (Poole and Owens 2003). They further stated that nanotechnology deals with various structures of matter having dimensions of the order of a billionth of a metre. Nanomaterials describe, in principle, materials of which a single unit is sized (in at least one dimension) between 1 to 1000 nanometres (10^{-9} metre) but 1 to 100 nm is the usual definition of nanoscale (Regtien, 2012 and Prem *et al*., 2019). A nanoparticle is the most fundamental component in the fabrication of a nanostructure because of its large surface area. A nanoparticle is far smaller than the world of everyday objects that are described by Newton's laws of motion but bigger than an atom or a simple molecule that are governed by quantum mechanics (Horikoshi and Serpone, 2013). Nanoparticles can be viewed or defined based on the specific application. Nanoparticles and nanomaterials are defined by various organizations: International Organization for Standardization (ISO), American Society of Testing and Materials (ASTM), National Institute of Occupational Safety and Health (NIOSH), Scientific Committee on Consumer Products (SCCP), British Standards Institution (BSI), and Bundesanstalt für Arbeitsschutz und Arbeitsmedizin (BAuA) in Table 1.1 (Horikoshi and Serpone, 2013).

Table 1.1 Summarized definitions of nanoparticles and nanomaterials (Horikoshi and Serpone, 2013).

Organization	Nanoparticle	Nanomaterial
ISO	A particle spanning 1 – 100nm (diameter)	-
ASTM	An ultrafine particle whose length in 2 or 3 places is 1 – 100nm	-
NIOSH	A particle with diameter between 1 and 100nm or a fiber spanning the range 1 – 100nm	-
SCCP	At least one side is in the nanoscale range	Materials for which at least one side or internal structure is in the nanoscale
BSI	All the fields or diameters are in the nanoscale range.	Materials for which at least one side or internal structure is in the nanoscale
BAuA	All the fields or diameters are in the nanoscale range.	Materials consisting of a nanostructure or a nanosubstance

Zinc oxide is an inorganic compound with the formula ZnO. It usually appears as a white powder and nearly insoluble in water (More *et al*., 2018). It is widely used as an additive in numerous materials and products including rubbers, plastics, ceramics, glass, cement, lubricants, paints, ointments, adhesives, sealants, pigments, foods, batteries, ferrites, fire retardants and first-aid tapes. ZnO occurs naturally as the mineral zincite (Luptáková *et al*., 2015). Most ZnO used commercially is produced synthetically (Kumar and Sharada, 2015). Zinc oxide is soluble in acids and alkalies and insoluble in alcohol (Lewis, 2007). When heated to decomposition it emits toxic fumes of zinc oxide (Lewis, 2004). Zinc oxide is stable under recommended storage conditions (Sigma-Aldrich, 2013). The vapour pressure of zinc oxide is approximately 0 mmHg (NIOSH, 2005). This is a great advantage for reliable relative humidity values. In the ambient conditions, ZnO crystallizes in the wurtzite phase which is a tetrahedrally coordinated structure with hexagonal lattice (Bekkari *et al*., 2019). Zinc oxide (ZnO) is one of the more attractive semiconducting metal oxides owing to its interesting properties including a wide and direct

bandgap (3.37 eV) and large exciton binding energy (60 meV) as well as high transparency (Bekkari *et al*., 2017). Table 1.2 summarizes some important properties of ZnO.

Table 1.2 Properties of zinc oxide (ZnO) (Raut and Thorat, 2015)

Property	Value/quality
Molar mass	81.408 g/mol
Odor	odorless
Density	5.606 g/cm^3
Melting point	1975 °C (decomposes)
Boiling point	2360 °C
Solubility in water	0.16 mg/100 mL (30 °C)
Band gap	3.3 eV (direct)
Refractive index (n_D)	2.0041

Recent studies have attempted to develop more sophisticated humidity sensors by manipulating several sensor characteristics such as refractive index, frequency range, capacitance, impedance and sensing mechanisms (Chen *et al*., 2005; Tripathy *et al*., 2016). These characteristics are strictly determined by the sensing medium material, porosity, surface area and pore size distribution (Tripathy *et al*., 2016). Zinc oxide (ZnO) is one of the most widely applied humidity sensing materials and it has many merits such as its low-cost preparation, plentiful and controllable surface morphology, perfect chemical and thermal stability and high electrical sensitivity to humidity (Chang *et al*., 2010 and Yang *et al*., 2017).

Semiconductor nanomaterials have received great attentions in the fabrication of humidity sensors. Among the various semiconductor oxide nanomaterials, zinc oxide is a versatile material because of its physic-chemical properties such as mechanical, electrical, optical, magnetic and chemical sensing properties and a wide band gap of 3.3 eV (Kolekar *et al*., 2013). ZnO particle size in nano-range shows tremendous increase in specific surface area with low dimensions

which results in a wider range and efficient application in a variety of fields (Jadhav *et al*, 2014). ZnO is therefore, a key technological material for relative humidity sensors.

Solvothermal synthesis is a chemical reaction in a closed system in the presence of a solvent (aqueous and non-aqueous solution) at a temperature higher than that of the boiling point of such a solvent (Demazeau, 2008). A solvothermal process involves high pressures. When aqueous solution is used as solvent, the process is referred to as hydrothermal synthesis. The method involves a reaction between a heated alkaline solution and another containing the precursor at room temperature (Gusatti *et al*., 2011).

Solvothermal synthesis is one of the techniques that could be used for the synthesis of ZnO nanomaterials. The technique has proved to facilitate greatly the fabrication of ZnO nanoparticles at ambient temperature with good controllability in the synthesis of ZnO nanocrystals by solvothermal process. The effect of reaction temperature, concentration of (precursor and time of growth plays vital role on the properties of ZnO (Singh *et al*., 2012). The process involves the use of a solvent under moderate to high pressure (typically between 1 atm and 10,000 atm) and temperature (typically between 100 °C and 1000 °C) that facilitates the interaction of precursors during synthesis (Gersten, 2018).

Zinc oxide nanoparticles can be synthesized using different salt precursors such as Zinc Chloride ($ZnCl_2$), Zinc Acetate ($ZnC_4H_6O_4$), Zinc Nitrate ($ZnNO_3$) and Zinc Sulphate Heptahydrate ($ZnSO_4 \cdot 7H_2O$). In chemical synthesis, capping agents and stabilizers are extensively used in order to control the size and to avoid agglomeration (Tanner *et al*., 2015). Triethyl amine, Oleic acid, Thioglycerol, EDTA, Tetraethyl Ammonium Bromide, Tetraethyl Orthosilicate,

Poly(ethylene glycol), Poly(ethylene phthalate), Ethylene Glycol, Gelatin, Poly(vinyl alcohol) (PVA) and Poly(vinyl pyrrolidine) are the frequently employed capping agents and stabilizers (Haq *et al*.**,** 2017). Advantages of solvothermal synthesis of ZnO powder include: production of nanometer size ZnO powder, carrying out the reaction under moderate conditions, production of powders with different morphologies by adjusting the reaction condition and the prepared powders have different properties from that of bulk (Singh *et al*., 2012).

1.2 Statement of the Problem

Nigeria is found in the tropics where the climate is seasonally damp and very humid. In the extremely high humidity, higher condensation of water on the metal surfaces occurs. The concentration of molecules of water vapor rises with increasing Relative Humidity (RH). The molecular thickness of the layers of water may eventually lead to ionic conduction that accelerates the rate of corrosion. In applications such as military, industrial, commercial or consumer electronics, certain equipment contain devices highly sensitive to environmental conditions. This contributes to high corrosion and damaging of equipment in the country. This damaged equipment are littered all over in the country polluting the environment. High and low humidity poses a lot of discomfort and health hazard to human beings. The humidity of the environment also affects production and storage of crops in agriculture. Nigeria needs serious humidity monitoring and control.

The climate of South Eastern part of Nigeria is classified under the tropical savanna climates. South Eastern Nigeria has the following summarized weather averages: monthly temperature range of 25.3 ^{0}C to 28.3 ^{0}C with annual average of 26.4 ^{0}C; monthly relative humidity range of

65.3 % to 84.3 % with annual average relative humidity of 77.5 % and monthly precipitation range of 10.1 mm to 312.0 mm with annual average relative humidity of 161.1 mm (Weatherbase, 2017).

In a data centre or computer room for instance, relative humidity has to be maintained between 45 % and 55 %, for optimal performance and reliability (Ciprian and Lehman, 2009). The range is far below what is obtainable in South Eastern Nigeria. The humidity sensor that will be needed in the South Eastern Nigeria will be resistant to condensation (moisture) because of the high range of relative humidity and relatively high temperature range. This study tends to fabricate a capacitive relative humidity sensor that will have high resistance to condensation. The relative humidity range for the capacitance will be from 5 % RH to 100 % RH with operating temperature of 5 ^{0}C to 100 ^{0}C and target accuracy of ± 1 %RH. The sensor will be suitable for the climatic conditions of the South Eastern Nigeria.

1.3 Aim and Objectives

The aim of this study is to fabricate a capacitive relative humidity (RH) sensor using nanostructured zinc oxide (ZnO) produced by solvothermal synthesis technique as a dielectric.

The objectives of the study include to

1. Synthesize ZnO nanoparticles by solvothermal synthesis technique using sodium lauryl sulphate (SLS) and linear alkylbenzene sulphonate (LAS or LABS) as capping agents.
2. Characterize the synthesized ZnO nanoparticles using Raman Spectroscopy, Thermogravimetric Analysis (TGA), Brunauer–Emmett–Teller (BET) surface area analysis and particle-size distribution (PSD) analysis and compare the results from SLS and LABS.

3. Fabricate nanostructured ZnO capacitive RH sensor on interdigitated electrodes (IDEs).
4. Calibrate the nanostructured ZnO capacitive RH sensor using linear regression and five saturated salt solutions.
5. Determinate the effect of annealing temperature on the nanostructured ZnO capacitive RH sensor.

1.4 Scope of the Study

This study is on the fabrication of a capacitive relative humidity sensor by solvothermal synthesis technique using nanostructure zinc oxide (ZnO) as a dielectric. It is limited to the synthesis, characterization and comparison of ZnO nanoparticles by solvothermal synthesis technique using sodium lauryl sulphate (SLS) and linear alkylbenzene sulphonate (LAS or LABS) as capping agents and fabrication, calibration and characteristics of the of nanostructured ZnO capacitive relative humidity sensor.

1.5 Significance of the Study

The study will be beneficial in the homes, agriculture, aviation, industries, medicine, weather forecasting, schools and government, especially in South Eastern Nigeria where relative humidity is very high.

1. In the homes, people need comfort and some are with illnesses affected by humidity. The study will help to create more awareness on the effect of humidity on the body and the possible ways of monitoring using the relative humidity sensor and taking preventive measures in homes. Some of the preventive measures include use of home heating, ventilating and air conditioning systems (HVAC systems) that have relative humidity

sensor incorporated in them. This will enhance human comfort and healthy living, especially in a high humid environment as Eastern part of Nigeria.

2. Humidity sensing and monitoring is very essential at meteorology stations for reporting and predicting weather. This study will go a long way in helping the meteorological stations in the area under study for efficient weather forecasting.
3. Controlling or monitoring of humidity is of paramount importance in many industrial applications. In textile industries, the change in humidity has a direct impact on the properties of fabric, cotton, linen, wool and silk and they require different humidity levels. Considering the RH range of the humidity sensor in this study, the favorable humidity levels for each of the materials will be determined.
4. In semiconductor the study will be applied in proper humidity monitoring and control during wafer production and storage of electronic equipment.
5. In agriculture, measurement of humidity is important for plantation protection (dew prevention), soil moisture monitoring, food processing, and storage of farm produce.
6. The study will help the management of schools, colleges, polytechnics and universities in humidity monitoring and control in the institution's information and communication technology (ICT) centres, computer rooms and data centres in institutions. This will ensure the durability of the computers and other equipment at the centres and computer rooms.
7. The results of this research will assist manufacturers of RH sensors in the choice of capping agents for the synthesis of ZnO nanoparticles, selection of microcontrollers for application in RH sensor system, application of linear regression in calibration of sensors

and understanding of the effect of annealing temperature on the nanostructured ZnO capacitive RH sensor performance.

8. The methods, results and discussions presented in this work will add to the existing literature on the synthesis and characterization of ZnO nanoparticles and fabrication of capacitive relative humidity sensors and serve as a reference material on the fabrication of capacitive relative humidity sensor for students and future researchers.

1.6 Limitations of the Study

The problem the researcher encountered during this research is unavailability of appropriate research institute and laboratories for the synthesis and characterization of ZnO nanoparticles and fabrication of the nanostructured ZnO capacitive humidity sensor in the locality of the researcher and the entire Eastern Nigeria. This made the research very expensive and time consuming as a result of too many researchers scrambling for the few facilities available.

CHAPTER TWO

LITERATURE REVIEW

2.1 Review of Related works

Researches have shown that zinc oxide nanoparticles can be synthesized using different techniques such as solgel synthesis, hydrothermal synthesis, solvothermal synthesis, microemulsion method, precipitation method, physical vapor deposition, vapor- liquid- solid process, soft chemical method, and electrophoretic deposition. The solvothermal approach has proved to facilitate greatly the fabrication of ZnO nanoparticles at ambient temperature with good controllability (Singh *et al*., 2012). Studies have also shown the effective use of ZnO nanoparticles in fabrication of capacitive relative humidity and other humidity sensors.

Yiamsawas *et al*. (2009) researched on the preparation of ZnO nanostructures by solvothermal method. The synthesis of ZnO nanostructures was carried out by solvothermal process at 80°C using a mixture of poly vinyl pyrrolidone (PVP), NaOH and Zinc Acetate Dehydrate in ethanol. White powder of ZnO nanoparticles was produced. The powder was analyzed in terms of the structural, morphology and optical properties. The grown ZnO nanostructures were characterized by X-ray Diffraction (XRD), Field-emission Scanning Electron Microscopy (FESEM) and Ultraviolet-visible (UV-vis) spectroscopy. The mixed solvent of ethylene glycol and absolute ethanol without polymer template was also investigated. The synthesized ZnO nanoparticles prepared in ethylene glycol have the diameters of 68.1±7 nm. The ZnO nanorod was obtained by using absolute ethanol as solvent, giving the diameter and length of 8.2±2 nm and 54.3±11 nm, respectively. The absence of PVP with the use of mixed solvent gave the ZnO semi-sphere shape with its diameter and length of 68.1±9 nm and 108.4±9 nm, respectively. ZnO nanocrystals were successfully obtained by using solvothermal process at 80°C.

Singh *et al*. (2012) studied the preparation of ZnO nanoparticles by solvothermal process. The ZnO nanoparticles were synthesized at 50 ^{0}C for 6 hours under autogenous pressure using a mixture of the solutions of $Zn(CH_3COO)_2.2H_2O$ and NaOH in methanol. The white milky solution obtained was centrifuged and dried. A white powder of ZnO nanocrystal was obtained. The size and structure of nanocrystal were confirmed with the XRD technique. The synthesized ZnO particle size was 11 nm. The band gap from UV absorption spectrum analysis was 3.39 eV which showed its quantum confinement effect. The characteristic peak of ZnO at 473 cm^{-1} in IR absorption spectra was also noticed. The analysis confirmed the production of ZnO nanoparticles.

Bhat *et al*. (2013) worked on the synthesis of ZnO nanostructures by solvothermal method. ZnO nanostructure was synthesized 160 ^{0}C for 8 hours using a solution of $Zn(CH_3COO)_2.2H_2O$ in methanol mixed with a solution of NaOH in methanol which helped to adjusted pH of the solution to the required value. The resulting white powder was washed with methanol, filtered and then dried in air in an oven at 100 ^{0}C. The structures, morphology, and optical properties of the grown ZnO nanostructures were characterized by X-ray Diffraction (XRD), Field-emission Scanning Electron Microscopy (FESEM), Energy dispersive spectroscopy (EDS) in the FESEM, Ultraviolet-visible (UV-vis) spectroscopy, respectively. The results showed wurtzite structure of the ZnO nanostructures with good crystalline quality. There was also evidence of the growth of ZnO nanoparticles along with hexagonal shaped nanorods. The results also indicated that the solvents as well as the pH values of the $Zn(CH_3COO)_2.2H_2O$ solutions may be playing an important role in the morphology of the of ZnO nanostructures in solvothermal synthesis.

Saric *et al*. (2015) worked on the solvothermal synthesis of zinc oxide microspheres. The experiments were divided into four groups using the solution of Zinc acetylacetonate monohydrate ($Zn(CH_3COCHCOCH_3)_2.H_2O$) in ethanol, $Zn(CH_3COCHCOCH_3)_2.H_2O$ in octanol, $Zn(CH_3COCHCOCH_3)_2.H_2O$ and triethanolamine (TEA) in ethanol and TEA and $Zn(CH_3COCHCOCH_3)_2.H_2O$ in octanol. In each case, the synthesis was done at 170 ^{0}C for 4 hours. The precipitates obtained were centrifuged and washed several times with ethanol and dried. The structures, morphology, and optical properties of the grown ZnO nanostructures were characterized by X-ray Diffraction (XRD), Field-emission Scanning Electron Microscopy (FESEM), Energy dispersive spectroscopy (EDS) in the FESEM, Ultraviolet-visible (UV-vis) spectroscopy, respectively. TEA played a crucial role in the control of the morphology and particle size of primary ZnO acting both as a suppressor of primary ZnO nanoparticle growth which then aggregate into sphere and also as a grown particle modifier of thus assembled nano/micron ZnO spheres. It was established that the way of ZnO nanoparticles growth and their aggregation depend on the molar ratio (TEA)/($Zn(CH_3COCHCOCH_3)_2.H_2O$) and the type of alcohol used as a solvent. The increase in the mole ratio of TEA to $Zn(CH_3COCHCOCH_3)_2.H_2O$ favoured the formation of bigger densely packed ZnO spheres. Doubling the molar ratio of TEA to $Zn(acac)_2$ in the presence of ethanol favoured the formation of huge spherical aggregates (> 3 μm) assembled from fine and uniform ZnO nanoparticles (~20 nm). The morphology and final particle size of obtained ZnO were dependent on the polarity of the solvent used. The presence of small polar molecules of ethanol in addition to TEA favoured the aggregation of big and densely packed ZnO spheres of regular shape. The change of solvent from ethanol to octanol caused a reduction in the ZnO crystallite size. TEA and octanol can provide a steric barrier between ZnO particles which allowed a stable dispersibility of the suspension without precipitation.

Widiyastuti *et al*. (2017) investigated on the morphology and optical properties of Zinc oxide nanoparticles synthesized by solvothermal method. A solution of Zinc acetate dehydrate $Zn(CH_3COO)_2.2H_2O$) in ethanol was mixed with lithium hydroxide (LiOH) solution. The synthesis was carried out at temperatures of 120 ^{0}C, 140 ^{0}C, 160 ^{0}C and 180 °C for 12 hours. The generated particles were centrifugation, washed and dried at temperature 60 °C for 6 hours. The powder produced was characterized by its morphology, crystallinity, chemical bonding and photoluminescence spectra using scanning electron microscopy (FE-SEM, Hitachi), x-ray diffraction (XRD, Phillips), and photoluminescence spectrometer (Simadzu) respectively. The results showed that spherical particles were produced and the sizes increased with temperatures. In addition, for temperature of 180 °C, the particle sphericity decreased. The average sizes were 32 nm, 38 nm, 42 nm and 60 nm for synthesis temperatures of 120 ^{0}C, 140 ^{0}C, 160 ^{0}C and 180 ^{0}C respectively. The particles morphology was deformed from spherical to nanorod when LiOH was added to the precursor. The diameter and length of nanorod increased with increasing the temperatures from 120 ^{0}C to 140 ^{0}C. The size decreased steeply with the increase of temperature from 140 ^{0}C to 180 ^{0}C. The results showed that the size and sphericity of the ZnO nanoparticles depend on the synthesizing temperature.

Garza *et al*. (2013) researched on microwave-assisted solvothermal synthesis of porous Zinc Oxide (ZnO) nanostructures. Porous ZnO nanostructures were synthesized by reaction of $Zn(CH_3COO)_2 \cdot 2H_2O$ with water, in 2-propanol as solvent, via a facile microwave-assisted solvothermal method. The obtained products were characterized by means of X-ray powder diffraction (XRD), UV-Vis spectrophotometry, Fourier transform infrared spectroscopy (FT-IR) and field emission scanning electron microscopy (FE-SEM). The results showed that ZnO

nanoparticles were of hexagonal crystalline structure. The nanoparticles had minimum average diameter of 37 nm which were agglomerated into irregular and spheroidal nanostructures with dimensions larger than 1 μm and high porosity. Mesopores and macropores with hexagonal geometry were found. It was determined that the size of the ZnO nanostructures is not a function of microwave irradiation time and water concentration.

Ghoshal *et al*. (2009) studied synthesis of ZnO nanoparticles by solvothermal method and their ammonia sensing properties. The synthesis was carried out at 200 ^{0}C, 150 ^{0}C and 135 ^{0}C using zinc acetate dehydrate ($Zn(CH_3COO)_2,2H_2O$] dissolved in a mixed solution of different volume ratio ethylene glycol (EG) and ethanol (E). The precipitate was collected, washed with water and ethanol and dried in air at ambient temperature. The synthesis was also performed with pure ethylene glycol and ethanol as the solvent. The shape and size of ZnO nanoparticles were adjusted by changing the volume composition of the solvents and the synthesis temperature. Phase purity was confirmed by X-ray diffraction (XRD) and crystal size was determined by transmission electron microscopy (TEM). The shape of the particles was gradually changed from ellipsoidal to spherical with the increase of the amount of EG, that is with the decrease in the pH value of the solvent. Few hollow spheres were observed for the samples synthesized with higher amount of EG at low temperature due to capping ability of EG and lower thermal energy. The smallest diameter nanoparticles exhibited five times greater sensitivity to ammonia at a relatively lower temperature than that of larger particles.

Gusatti *et al*. (2011) worked on effect of different precursors in the chemical synthesis of ZnO nanocrystals. Solochemical synthesis was performed using precursor solutions of zinc chloride ($ZnCl_2$) and zinc nitrate hexahydrate ($Zn(NO_3)_2.6H_2O$). The resulting samples were characterized

regarding phase composition, particle size and morphology by means of XRD and TEM. Single crystalline ZnO nanoparticles with hexagonal wurtzite structure were produced and had high quality. The average crystallite sizes obtained were 20 nm and 29 nm. The particles had nanometric prism-like and rod-like morphologies. The use of $ZnCl_2$ as precursor alters the composition of the final product, forming ZnO nanocrystals mixed with $Zn5(OH)_8Cl_2.H_2O$ crystals. The obtained ZnO nanostructures exhibited rod-like morphology and average diameter of approximately 23 nm. Hence, the results indicated the lower efficiency of the proposed solochemical method in the synthesis of ZnO nanocrystals using high concentration of $ZnCl_2$ precursor solution.

Khalil *et al*. (2013) studied synthesis and characterization of ZnO nanoparticles by thermal decomposition of a curcumin zinc complex. ZnO nanoparticles were generated by thermal decomposition of a binuclear zinc (II) curcumin complex as single source precursor. Synthesized nanoparticles were characterized by X-ray diffraction, Fourier transform infrared spectroscopy, transmission electron microscopy and selected area electron diffraction microscopy. Thermal behavior of the precursor showed a considerable weight loss at about 374 ^{0}C by an exothermic reaction with a maximum weight loss rate of 14 %/min. Complete decomposition of precursor was observed within 49 min with a heating rate of 10 ^{0}C/min. Results revealed monodispersed hexagonal zincite structure with an average size of 117 ± 4 nm. The precursor has potential for synthesizing metal oxide nanoparticles.

Jayaraj *et al*. (2017) studied Synthesis of ZnO nanoparticles by hydrothermal method. Zinc oxide (ZnO) nanoparticles were synthesized using solutions of $Zn(CH_3COO)_2.2H_2O$ in methanol which

was mixed with NaOH solution prepared in methanol. The hydrothermal synthesis was done by varying the growth temperature and concentration of the precursors. The formation of ZnO nanoparticles were confirmed by x-ray diffraction (XRD), transmission electron microscopy (TEM) and selected area electron diffraction (SAED) studies. The nanoparticles had the hexagonal wurtzite structure. The average size of the ZnO nanoparticles produced was about 7-24 nm which increased with growth temperature and decreased with concentration of the precursors. Due to quantum confinement effects, the band gap of the ZnO nanoparticles was blue shifted compared with the bulk material.

Tripathy *et al*. (2016) worked on the Design and Development for Capacitive Humidity Sensor Applications of Lead-Free Ca,Mg,Fe,Ti-Oxides-Based Electro-Ceramics with Improved Sensing Properties via Physisorption. The capacitive humidity sensor was developed using lead-free Ca,Mg,Fe,Ti-Oxide (CMFTO)-based electro-ceramics with perovskite structures synthesized by solid-state step-sintering. The relative humidity sensor was measured by creating ambiences with different humidity levels by silting a series of standard saturated salt solutions ($MgCl_2$, $Mg(NO_3)_2$, NaCl, KCl and KNO_3) in conical flasks with stoppers to produce environments with relative humidity (RH) values of 33 %, 55 %, 75 %, 85 % and 95 % at 25 ^{0}C respectively. The CMFTO-based humidity sensor showed a high sensitivity of up to 3000% compared to other materials, even at lower signal frequency. It showed a rapid response time (14.5 s) and recovery time (34.27 s) and very low hysteresis (3.2 %) in a 33 %–95 % relative humidity range which are much lower values than those of existing conventional sensors. CMFTO nano-electro-ceramics appears to be very promising materials for fabricating high-performance capacitive humidity sensors.

Yang *et al.* (2017) worked on Stable and Fast-Response Capacitive Humidity Sensors Based on a ZnO Nanopowder/PVP-RGO Multilayer. The capacitive-type humidity sensors were prepared by sequentially drop-coating the aqueous suspensions of zinc oxide (ZnO) nanopowders and polyvinyl pyrrolidone–reduced graphene oxide (PVP-RGO) nanocomposites onto interdigitated electrodes. Different RH environments of saturated salt solutions of LiCl, CH_3COOK, $MgCl_2$, K_2CO_3, NaBr, NaCl, KCl, and K_2SO_4 were used for the calibration of the sensor. A commercial hygrometer (Rotronic HP22-A, $\pm$0.8 % RH) was also calibrated. The humidity sensing properties of the sensors were investigated by recording their capacitance responses to humidity at room temperature (~22 ^{0}C) using an LCR Meter. Significant improvements in both sensitivity and linearity were achieved for the ZnO/PVP-RGO sensors. Additionally, the ZnO/PVP-RGO sensor exhibited small hysteresis (~3.9 % RH), fast response and recovery times over a full humidity range measurement (90 %RH of 12.0 s and a 10 %RH of 3.0 s during adsorption and desorption processes, respectively) and long-term stability. The study indicated that ZnO/PVP-RGO may be a promising candidate material for the fabrication of high-performance humidity sensors.

Wang (2013) researched on the fabrication of relative humidity sensors based on polyimide nanoparticles. Interdigitated electrodes (IDEs) were fabricated for the humidity sensor using micro fabrication technology. Aluminum was used as the material for IDEs. Silver conductive epoxy was used to bond wire on Al pads. Polyimide (PI-2555) was used as the sensing material. A layer of the Polyimide (PI) nanoparticles was deposited on IDEs using the traditional spinning and electrospraying to form the capacitive relative humidity sensor. A capacitive sensing circuit (C-V circuit) was used for the humidity measurement. This sensor has a good repeatability

between increasing RH and decreasing RH from 15 % RH to 70 % RH. The RH could not be kept stable for 6 hours. It started to change after about 2 hours. From 12 % RH to 21% RH, the response time of the RH sensor was around 5 minutes with low hysteresis with increasing and decreasing humidity. The results also showed that higher film density results in higher linearity and sensitivity.

Singh *et al*. (2018) worked on the enhanced moisture sensing properties of a nanostructured ZnO coated capacitive sensor. The average crystallite size of the ZnO nanoparticles was ∼16 nm with a surface roughness of ∼3 nm. A thin film of zinc oxide (ZnO) nanoparticles was deposited on the electrodes in fabricating the sensor. The effect of the ZnO nanoparticles on the sensitivity of the moisture sensor cell was studied using wheat grains with moisture content from 7 %RH to 25 %RH. An enhancement in sensitivity of 36.4 %RH at 1 MHz and 97.4 %RH at 500 Hz was observed. The results established ZnO as a sensing material for improving the utility of moisture sensors.

Sin *et al*. (2014) investigated the enhancement of nanocomposite for humidity sensor application. The nanocomposited ZnO/SnO_2 was synthesized on ZnO coated glass using thermal chemical vapor deposition (CVD). ZnO/SnO_2 composite nanorods were successfully synthesized. The SnO_2 nanorods, ZnO agglomerate nanoparticle and ZnO/SnO_2 nanoflower were successfully grown on ZnO template layer. The structural properties of ZnO agglomerate nanoparticle, SnO_2 nanorod, and ZnO/SnO_2 composite nanorods were characterized using field emission scanning electron microscopy (FESEM). The sensor properties were characterized using current-voltage (I–V) measurement. The humidity chamber was set at the same room temperature (25 ^{0}C) with

percent relative humidity (RH%) varied in the range of 40–90 %RH. The SnO_2 nanorods and ZnO agglomerate nanoparticles produce sensitivity with 16 and 11 ratios of times. The ZnO/SnO_2 composite nanorods gave the highest sensitivity with ratio of 265 times. The response and recovery time for these ZnO/SnO_2 composite nanorods were the fastest among ZnO nanoparticles and SnO_2 nanorods with 227 s and 34 s respectively. Thus, ZnO/SnO_2 composite nanorods proved the best enhancement for humidity sensor application.

Sin *et al*. (2011) researched on the electrical characteristics of aluminum doped zinc oxide (ZnO) thin film for humidity sensor applications. The particles of zinc oxide were grown successfully on the glass substrate by sol gel method. The effects of Al doping concentration at $0 \sim 0.6$ at % on the Al doped ZnO thin film properties were investigated using current-voltage measurement. Photoluminescence (PL) showed an emissions band with two peaks centered at about 380nm (ultra-violet (UV)) and 600nm (green) in a room temperature. The length of the nanorods increases as the doping concentration increases. XRD results showed the intensity of the (002) peak decreased with the increasing of doping concentration. Parameter 0.6 at % Aluminum doped showed high sensitivity and suitable for humidity sensor.

Santhaveesuk *et al*. (2016) studied high performance humidity sensor based on ZnO nanoparticles synthesized by co-precipitation method. ZnO nanoparticles were synthesized by co-precipitation method using zinc nitrate ($ZnNO_3$) and sodium hydroxide (NaOH) as the raw materials. It was observed that the synthesized temperatures had great effect on the size of ZnO nanoparticles. The lower synthesized temperatures resulted in the smaller nanoparticles. By adjusting the mole ratio of sodium hydroxide, the size of ZnO nanoparticles was also changed.

The smallest ZnO particles were 47 nm obtained with 0.7 mole of sodium hydroxide. The smallest ZnO nanoparticles from each synthesized temperatures were fabricated as humidity sensor, showing an impressive performance under different relative humidity (17-94 % RH). The ZnO nanoparticles humidity sensor synthesized at 75 °C exhibited high response for 2 times higher than that of synthesized at 95 °C. This was attributed to the higher surface area of ZnO nanoparticles for absorbed water molecule.

Ghanem *et al*. (2015) worked on humidity sensor characteristics based on ZnO nanostructure grown by sol-gel method. The work dealt with ZnO thin films, electrical and structural properties characterization and relative humidity sensing test. Films were deposited on glass substrate by sol-gel method. The solutions were prepared using zinc acetate mixed with 2-methoxyethanol and monoethanolamine (MEA) as solvent and stabiliser, respectively. X-ray diffraction (XRD) analysis of ZnO thin films showed wurzite structure. The scanning electron microscope (SEM) images revealed that the synthesised ZnO films were composed of irregular fibre-like stripes and wrinkle network. It was observed that the sensor resistance decreases from 22 MΩ to 0.40 MΩ with increasing relative humidity from 15 %RH to 95 %RH at 25 °C. At relative humidity of 95 %RH, a response time of 7 s at 100 °C was recorded which indicated that temperature had strong influence on the response and recovery times. The results suggested that the prepared ZnO film has interesting potential in humidity sensing.

Misra *et al.* (2018) worked on doped and undoped zinc oxide as humidity sensor. They gave a comparative performance of pure ZnO and Fe_2O_3-doped ZnO nanomaterials as humidity sensor. Fe_2O_3 doping was done for improvement of sensitivity. Characterizations of materials were done

using SEM and XRD. The samples were annealed at 500 °C for 3 hours. Maximum sensitivity was found to be 22.18 MΩ/ %RH for Fe_2O_3-doped ZnO sensing elements. The Fe_2O_3-doped ZnO samples showed better sensitivity as compared to undoped ZnO nonmaterials for humidity sensing studies. The sensors developed from Fe_2O_3-doped ZnO nonmaterials annealed at 500 °C showed the best sensing behaviours for humidity sensing studies with sensitivity 22.18 MΩ/ %RH. The sensing elements developed from Fe_2O_3-doped ZnO nonmaterials annealed at 500 °C had properties like low effect of ageing, low hysteresis and high reproducibility. Therefore, Fe_2O_3-doped ZnO sensors, annealed at 500 °C proved to be promising practical humidity sensors.

Pandey *et al*. (2012) worked on ZnO/TiO_2 nanocomposite characterization and moisture sensing studies. The work investigated on the morphological and relative humidity sensing behaviour of ZnO/TiO_2 nanocomposite powder pellets obtained through solid-state reaction route. Resistance of the pellets was observed to decrease with increase in relative humidity in the 10 – 90 %RH range. Sensing element with 15 weight % of TiO_2 in ZnO showed best results with a sensitivity of 9·08 MΩ/ %RH in 10-90 % relative humidity range. The sensing element manifested crystallite size of 71 nm as measured from XRD and average grain size of 207 nm calculated from SEM micrograph. The sensing element manifested low hysteresis, less effect of ageing and good reproducibility. The response and recovery times were measured to be 84 s and 396 s respectively. ZnO/TiO_2 nanocomposite therefore proved a good quality sensing material for humidity sensors.

Shukla *et al*. (2015) investigated the sensitivity of polyaniline-zinc oxide composite to humidity. Polyaniline was synthesized by oxidative polymerization of aniline under acidic condition and was mixed with different proportions of ZnO. The mixtures were pressed into pellets of organic-inorganic composite and then subjected to varying humidity. The ZnO dopant influenced the physical and chemical properties of conducting polyaniline. The resistance of polyaniline decreased with increase in ZnO dopant concentration and lied between kΩ and few MΩ as relative humidity increased from 20 to 90 %RH. For critical concentration of 10 weight % of ZnO in polyaniline the sensitivity to humidity was highest and also had the best response and recovery times of 36 and 48 seconds respectively. It was concluded that polyaniline-zinc oxide composite pellets may lead to efficient humidity sensors.

2.2 Humidity Sensors

Humidity sensing technology has a very long history. Hence, authors and researchers have varied views or opinions in relative humidity sensors classifications. Humidity sensors are categorized into the following five generations of humidity sensors (Kolpakov *et al.,* 2014):

i. The first generation humidity sensors were mechanical humidity sensors, which were based mainly on change in the mechanical properties of some materials such as horse or human hairs. These first mechanical sensors, which were slow and imprecise, were used throughout human history until the second half of twentieth century.

ii. The second generation humidity sensors were electronic humidity sensors that were the dominant technology today.

iii. The third generation sensors of fiber technologies were mainly based on interferometric techniques.

iv. The fourth generation is nano-technology based humidity sensors, complementary metal oxide semiconductor micro-electro-mechanical system (CMOS-MEMS) humidity sensors.

v. The fifth generation of humidity sensing technology based on optical fibres.

The general classification of humidity sensors are the optical humidity sensors, acoustic humidity sensors and electronic humidity sensors (Kolpakov *et al.,* 2014).

In 1937 an electrolytic humidity sensor based on lithium chloride (LiCl) developed by Dunmore became the first and only electrical moisture sensor available until around the middle of the 1970s (Farahani *et al*., 2014). They identified the following classifications of humidity sensors:

i. Yamamoto and Shimizu (1982) classification of RH sensors based on three main groups of the sensing element types of electrolytes, porous ceramics and organic polymers.

ii. Traversa (1995) classification of RH sensors based on three main groups of porous ceramics and organic polymer films.

iii. Chen and Lu (2005) classification into organic, semiconductor and organic polymer types of RH sensors.

RH sensors can further be categorized into ceramic type (semiconductor), organic polymer-based sensors, and organic/inorganic hybrid sensors (polymer/ceramic), 80% of the sensor types are based on the electrolytic properties of the sensing matter, by virtue of the inner water electrolytes (Farahani *et al*., 2014). Flexible, chipless and wireless humidity sensors are built based on the difference in dielectric constant (capacitive), proton/ionic conduction (resistive), refractive index (optical), frequency (impedance) or mass of the active material against humidity level (Mogera *et al*., 2014; Hassan *et al*., 2016)

Among the different ways of sensing humidity like contraction of materials, optical methods, etc., exploiting electrical properties of materials is more compatible with recent compact humidity sensors because the size of sensors can be minimized in this way (Yeo *et al.*, 2008). Hence, relative humidity sensors can also be classified based on the electrical properties of the materials of the sensors. These sensors are sometimes referred to as electronic sensors. Humidity sensors which use the changes of electrical properties of materials with humidity can be divided into two groups including the resistive type and the capacitive type (Yasrebi *et al.*, 2015).

In this review, humidity sensors will be broadly classified into two groups – the classical humidity sensors and modern humidity sensors. Classical humidity sensors include psychrometer, hair hygrometer, lithium chloride dew point sensor and chilled mirror hygrometer. Modern humidity sensors include resistive humidity sensor, capacitive humidity sensor, thermal conductivity humidity sensor, and gravimetric humidity sensor.

2.2.1 Psychrometer

The psychrometer is a hygrometric instrument based on the principle that dry air enhances evaporation, opposed to wet air, which hinders it (Gallicchio and Teague, 2017). It is designed to indicate the relative humidity, that is, the ratio of the partial pressure of water vapour in the air phase to the equilibrium partial pressure of vapour in vapour-saturated air at the same temperature (Hillel, 1998). A psychrometer measures the relative humidity in the atmosphere through the use of two thermometers (Kestrel, 2012):

1. a dry bulb thermometer, which is used to measure the temperature by being exposed to the air

2. A wet bulb thermometer, which measures temperature by having the bulb dipped in a liquid.

Through the comparison of both temperatures, individuals determine the relative humidity of the surrounding area by calculating the difference between the temperatures. Some of the factors influencing the performance and accuracy of the psychrometric method are: (a) the sensitivity, accuracy, and agreement in reading of the thermometers, (b) the speed of air past the wet-bulb thermometer, (c) the incident radiation on the thermometers, (d) the size, shape, material , and wetting of the wick, (e) the relative positions of wet- and dry-bulb thermometers, and (f) the temperature and purity of the water used to wet the wick (Wexler and Emil, 1963). Psychrometers can be in stationary, mobile versions or digital forms. Different types of psychrometers include

(a) Wall mounted or stationary psychrometers,

(b) Sling psychrometers

(c) Assmann or aspiration psychrometers.

(a) Wall Mounted Type Psychrometer

Figure 2.1 shows the structure of a wall mounted type psychrometer**.** The psychrometer consists of dry-bulb and wet-bulb thermometers. The dry bulb thermometer (T_d) is left uncovered for maximum exposure to air. The wet-bulb thermometer (T_w) is kept wet by covering it with some wet cloth or a muslin wrap or gauze socked or dipped inside a water tank until it is required for use. When in use, water evaporates from the surface of T_w. Latent heat of evaporation is absorbed from T_w making its temperature lower than the air temperature (T_d). At a lower humidity, water evaporates more rapidly and the temperature of T_w reduces faster due to the

cooling effect of evaporation. The temperature readings of T_d and T_w are taken. The temperature of the wet-bulb is always lower than the temperature of the dry-bulb due to the cooling effect of evaporation taking place at the wet bulb temperature.

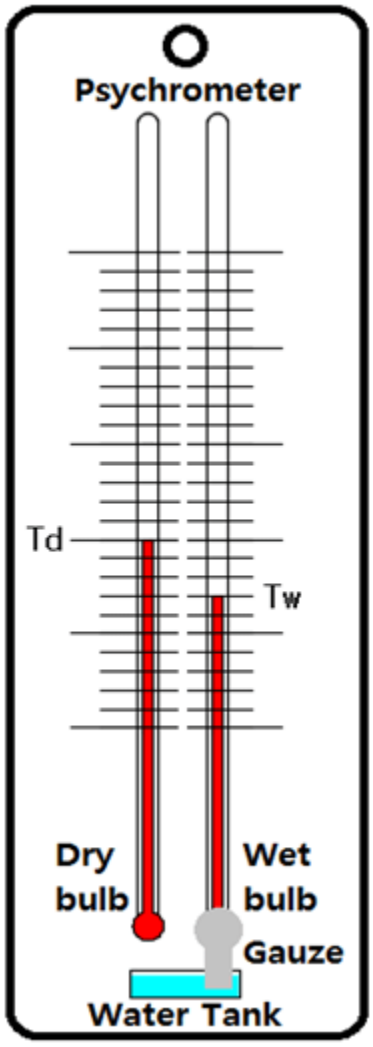

Figure 2.1 psychrometer (Heat – tech, 2018)

(b) Sling Psychrometer or Whirling Hygrometer

Sling Psychrometer is used to measure both the dry bulb and wet bulb temperatures, which are a measure of humidity content in air at a particular period. Figure 2.2 shows a Sling Psychrometer. The main parts of Sling Psychrometer are described in Figure 2.3.

Figure 2.2 Sling Psychrometer (Nasco, 2018).

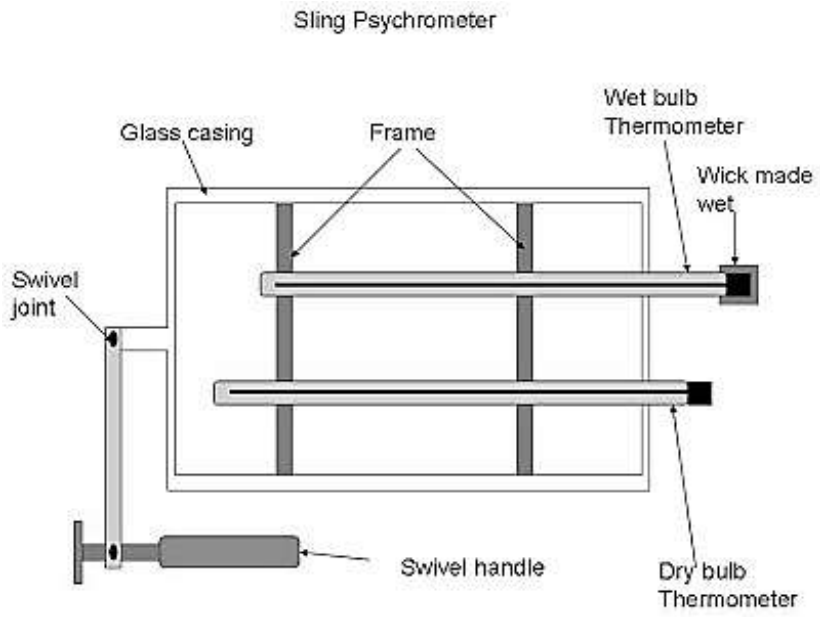

Figure 2.3 Sling psychrometer (Writeup, 2014)

The frame holds two thermometers. The two thermometers are mercury in glass thermometers. The dry-bulb thermometer is directly in contact with the air and measures the temperature of the air. The temperature indicated by the dry-bulb thermometer is the dry-bulb temperature. The wet bulb thermometer has a sensing bulb covered with cotton or muslin wick dipped in pure water. The temperature indicated by the wet-bulb thermometer is the wet-bulb temperature. The glass casing covers the frame carrying the two thermometers. A rotating handle is attached to the frame-glass casing – thermometer arrangement. The arrangement is to ensure that the air at the wet bulb is always in immediate contact with the wet wick.

1. Operation of the Sling Psychrometer

In order to measure the dry bulb and wet bulb temperature, the psychrometer frame – glass covering – thermometer arrangement is rotated at 5 m/s to 10 m/s to get the necessary air motion (Writeup, 2014). Correct/accurate measurement of wet bulb temperature is obtained only if air

moves with velocity around the wet wick. In order to get this air velocity, the psychrometer is being rotated. The dry bulb thermometer indicates the temperature of the air. At the same time, when the air in contact with the wet-bulb thermometer and passes on the wet wick present on the bulb of the thermometer, the moisture present in the wick starts evaporating and a cooling effect is produced at bulb. The wet bulb thermometer indicates the wet-bulb temperature. The wet-bulb temperature will be less when compared with the dry bulb temperature. If the surrounding air is dry, more moisture evaporates from the wick, cooling the wet-bulb thermometer more so there is a greater difference between the temperatures of the two thermometers and if the surrounding air is holding as much moisture as possible - if the relative humidity is 100 %RH - there is no difference between the two temperatures. In order words, the relative humidity is inversely proportional to the amount of moisture in the surrounding air. Partial relative humidity charts designed by meteorologists are used for finding the relative humidity for each degree difference in the dry bulb and wet bulb temperatures.

The accuracy of the psychrometer depends on the period of its rotation. If the rotation is for a short period, then the wet bulb temperature recorded will not be proper, and if it is rotated for a longer period, the wick will get dried soon and the wet bulb temperature will not be at its minimum value (Writeup, 2014).

The main limitation of psychrometer is that the wet wicking freezes at wet-bulb temperature below 0 ^{0}C and the water reservoir freezes when the ambient temperature drops below 0 ^{0}C (Dario and Vito, 2010). Regular maintenance is needed to ensure that water reservoirs are kept topped up (Bramer *et al*., 2018). If the wick is covered with dirt, the wick will become stiff and its water absorbing capacity will reduce, however, a stiff/dirty wick will resume normalcy when

boiled in hot water (Writeup, 2014). Psychrometer is limited by low measurement accuracy compared to electronic sensors (Wei *et al*., 2016).

(c) Assmann Psychrometer

Assmann's psychrometer shown in figure 2.4, like other psychrometers, consists of dry-bulb thermometer which measures the temperature (t_1) of surrounding environment and the wet-bulb thermometer with the bulb covered with a wet fabric. Evaporation from the wet-bulb thermometer lowers the temperature (t_2) of surrounding air as a result of the latent heat of liquid-to-vapor phase transition extracted from the wet bulb. The psychrometric difference between the two temperatures (t_1 - t_2) depends on the air humidity. For precise measurement, Assman's psychrometer includes a fan that prevents water vapor from the formation of saturated vapor environment (Academic, 2017).

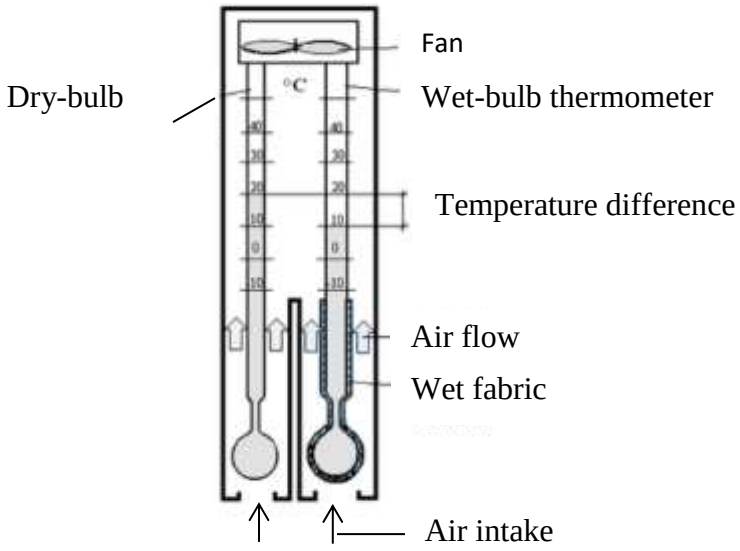

Figure 2.4 Assmann psychrometer (Academic, 2017)

When careful handling is provided, the psychrometric measuring method presents several advantages such as: reproducibility of measurements, no drifting, no hysteresis effects, self-cleaning of the wick with every wetting (World Meteorological Organization (Sonntag, 1987). The disadvantage of the instrument is its decreasing accuracy at temperatures below 0 °C (Sonntag, 1987).

2.3 Determination of Relative Humidity Using Psychrometric Formula and Psychrometric Table

Relative humidity is calculated from dry-bulb temperature or wet-bulb temperature, the difference in temperature between a dry bulb and a wet bulb, and atmospheric pressure using the formula

$$e = e_{sw} - Ap(T_d - T_w) \quad 2.1$$

where e is the partial pressure of water vapour in the air; e_{sw} is the saturated water vapor pressure at the wet-bulb temperature; A = 0.000662 K^{-1} is psychrometer coefficient; p is the atmospheric pressure; T_d is the dry-bulb temperature and T_w is the wet-bulb temperature (Heat-tech, 2018). If the wet bulb thermometer is dipped into ice, the formula becomes

$$e = e_{si} - Ap(T_d - T_i) \quad 2.2$$

where e is the partial pressure of water vapour in the air; e_{si} is the saturated water vapor pressure at the wet-bulb temperature with repect to ice; A = 0.00044 K^{-1} is psychrometer coefficient; p is the atmospheric pressure; T_d is the dry-bulb temperature and T_i is the wet-bulb temperature with respect to ice.

Relative humidity (H) is the ratio of the vapor pressure (e) of the moist air to its saturation vapor pressure (e_s) at its temperature, which is expressed in %. The relative humidity (H, H_w or H_i) can be calculated by respectively substituting in the equations given below:

$$H = (e/e_s) \times 100\ \% \quad (2.3)$$

$$H_w = (e/e_{sw}) \times 100\ \% \quad (2.4)$$

$$H_i = (e/e_{si}) \times 100\ \% \quad (2.5)$$

where H_w when the wet bulb is dipped in water and e_{sw} are the saturation vapor pressure with respect to water, and H_i when the wet bulb is dipped in ice and e_{si} are the saturation vapor pressure with respect to ice.

The easiest way to calculate the RH using the psychrometer is by using psychometric tables and charts. A solution schematic drawn on a psychrometric chart helps a designer visualize and calculate the work done on an airstream without the need for advanced mathematics (Krepcik, 2010).

2.3.1 Application of Psychrometer

Psychrometers measure the humidity of air in a general environment or specific area such as a chamber or structure. A better understanding of the relationship between air temperature and relative humidity and other air properties using a psychrometric chart can be used in selection and management of a livestock building ventilation system, a grain drying system or a home humidifier (Shelton, 2008). The study of psychrometric variables gives the idea about the changes in properties of air during the course of drying and in turn the efficiency of dryer which helps to improve the post-harvest drying, cooling and cooling conditions of perishable agricultural products (Maheshwari, 2014). Establishment of irrigation guidelines for agricultural

crops, management of leaf water potential, water potential in stems, fruits, roots and seeds are some applications of thermocouple psychrometer (Cancela *et al*., 2011). Psychrometers are also used for the measurement of comfort conditions in air conditioned environments, hospital operating rooms, storage areas and laboratories; tests in industrial atmospheres where high humidity or low humidity may be critical in manufacturing processes, school athletics – to determine safe conditions for practice (Dumey, 2014).

2.4 Hair Hydrometer

Certain hygroscopic materials such as human hair, animal membranes, wood, paper, etc., undergo changes in linear dimensions when they absorb moisture from the surrounding air (Writeup, 2018). Hence, they can be employed in the construction of relative humidity sensors such as hair hygrometer which uses mechanical humidity sensing technique.

The hair hygrometer according to the description of Ahrens, 2012 is constructed on the principle that the length of human hair increases by 2.5 percent as the relative humidity increases from 0 to 100 %. The instrument uses human (or horse) hair to measure relative humidity. A number of strands of hair (with oil removed) are attached to a system of levers. A small change in hair length is magnified by a linkage system and transmitted to the dial/scale as shown in Figure 2.5.

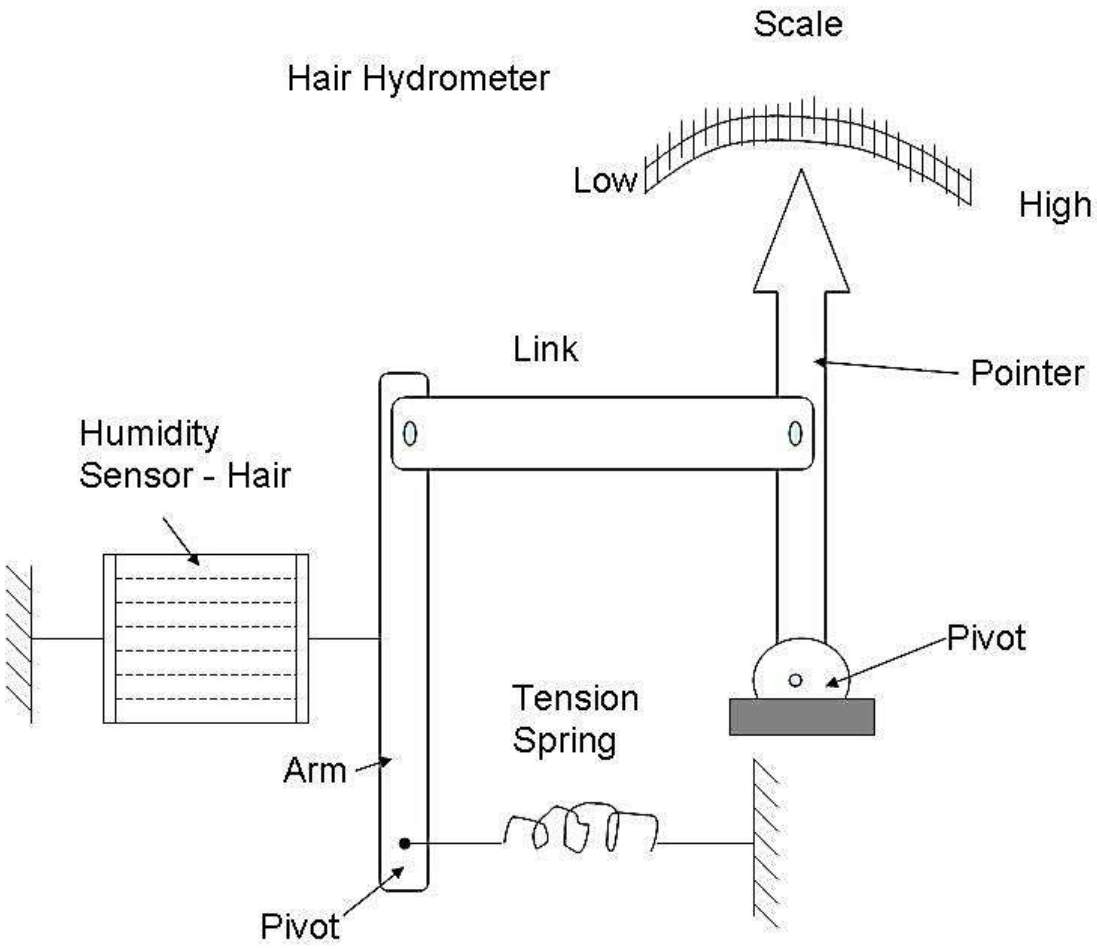

Figure 2.5 The main parts of hair hygrometer (Writeup, 2018)

The dial is calibrated to show relative humidity, which is read directly or recorded on a chart. Often the chart is attached to a clock driven rotating drum that gives a continuous record of relative humidity.

The hair hygrometer is not as accurate as the psychrometer (especially at very high and very low relative humidity and very low temperatures) and requires frequent calibration, principally in areas that experience large daily variations in relative humidity. The hair hygrometer, therefore, suffers the limitation of slow response and change in its calibration.

Hair hydrometers are used in the temperature range of 0 ^{0}C to 75 ^{0}C and in the RH (Relative Humidity) range of 30 %RH to 95 %RH (Writeup, 2018).

2.5 Lithium Chloride Dew Point humidity Sensor

The saturated salt lithium chloride sensor has been one of the most widely used dew point sensors and its popularity stems from its simplicity, low cost, durability, and the fact that it provides a fundamental measurement (Rittersma, 2002). The sensor consists of a metal cylinder covered with an absorbent fabric and a bifilar winding of inert electrodes (Figure 2.6). The metal cylinder is coated with a dilute solution of lithium chloride. An alternating current is passed through the winding and the salt solution causing resistive heating. As the metal cylinder heats up, water evaporates from the salt at a rate which is controlled by the vapour pressure of water in the surrounding air. The resistance of the salt solution increases as the metal cylinder begins to dry out, causing less current to flow through the winding. This allows the metal cylinder to cool.

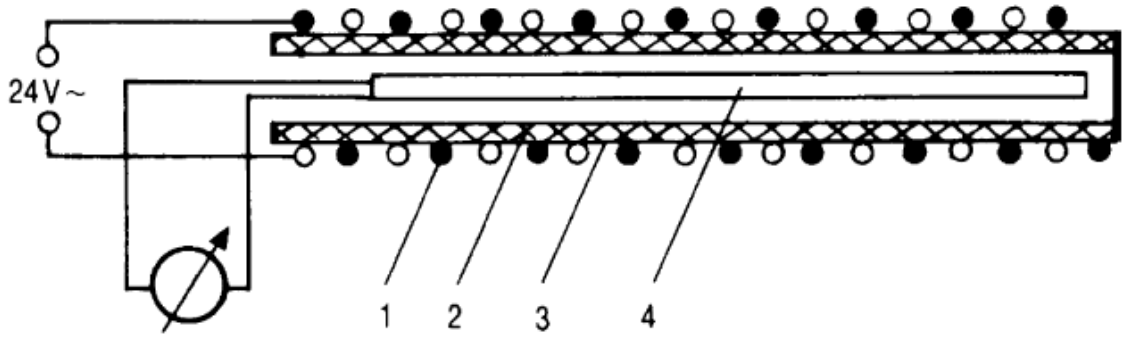

Figure 2.6 LiCl dew point sensor schematic: (1) heating electrode; (2) wick soaked with LiCl; (3) metal housing/cylinder and (4) measurement electrode (Rittersma, 2002)

The heating and cooling of the metal cylinder reaches an equilibrium point where it neither takes on nor gives off water. This equilibrium temperature is directly proportional to the water vapour pressure or dew point of the surrounding air. This value is measured using a platinum resistance

thermometer (PRT) and output directly as a dew point temperature. If a saturated salt sensor becomes contaminated, it can easily be cleaned and recharged with lithium chloride.

The limitations of LiCl dew point humidity sensor are its relatively slow response time; a lower limit of the measurement range which is imposed by the nature of the lithium chloride; and inability to measure dew points when the vapour pressure of water is below the saturation vapour pressure of lithium chloride, which occurs at about 11 % RH (Rittersma, 2002). The sensor has unsatisfactory accuracy, particularly with very high or very low humidity and excessive lag at low temperatures; and its accuracy is completely destroyed if it is washed by rain (Campbell, 1969). The lithium chloride dew-point hygrometer only reads and controls the dew-point temperature of air instead of the relative humidity, which is more important in industry, agriculture, food storage, and hygiene (Zhang *et al*., 1986).

Lithium chloride dew-point hygrometer can be used in refrigeration controls, dryers, dehumidifiers, airline monitoring and pill coaters.

2.6 Chilled Mirror Hygrometers (CMHs)

CMHs make a direct measurement of the dew point temperature of a gas by allowing a sample of gas of unknown water vapor content to condense on an inert, chilled, mirror-polished metal surface (Beaubien, 2005). The surface is chilled to the temperature at which water on the chilled mirror surface is in equilibrium with the water vapor pressure in the gas sample above the surface. Yankee Environmental Systems (YES), 2005) explained in figure 2.7 that a mirror is constructed from a material with good thermal conductivity such as silver or copper, and properly plated with an inert metal such as iridium, rubidium, nickel, or gold to prevent

tarnishing and oxidation. The mirror is chilled using a thermoelectric cooler until dew just begins to form of light.

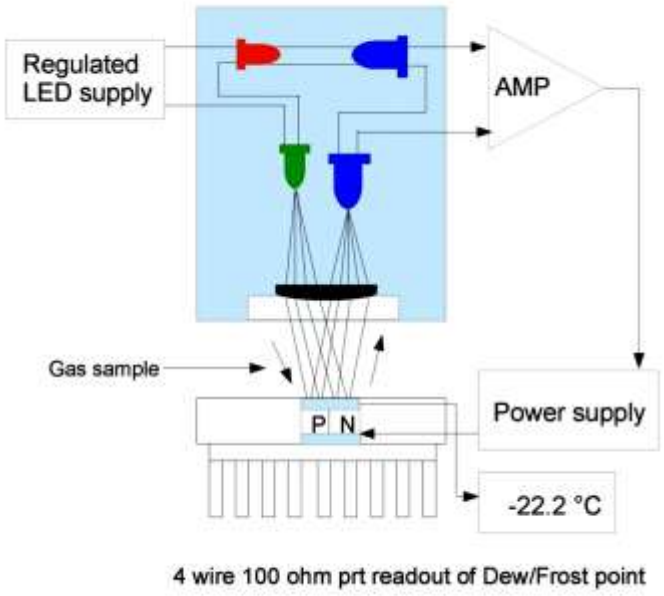

Figure 2.7 block diagram of chilled mirror hygrometer (Yankee Environmental Systems, 2005)

The light typically from a solid-state broadband light emitting diode is aimed at the mirror surface and a photodetector monitors. As the gas sample flows over the chilled mirror, dew droplets form on the mirror surface, and the reflected light is scattered. As the amount of reflected light decreases, the photodetector output also decreases. This in turn controls the thermoelectric heat pump via an analog or digital control system that maintains the mirror temperature at the dew point. A precision miniature platinum resistance thermometer (PRT) properly embedded in the mirror monitors the mirror temperature at the established dew point. At an equilibrium condition above the ice point, i.e., 0 °C, the sensor measures the dew point. Below 0 °C the sensor measures the frost point. However, if the mirror is kept extremely clean, it is possible for dew to exist below 0 °C.

Chilled-mirror hygrometers suffer from intrinsic errors, which are mainly attributable to 1) the temperature gradient from the mirror surface to the embedded thermometer, 2) the thermal conductance of the thermometer leads, and 3) the self-heating of the thermometer and readout calibration which practically limits the resulting measurement accuracy (Jifang *et al*., 2016). Chilled mirror hygrometers are heavy, complex, sensitive to flow rates, and need regular maintenance (Tennermann, 2011).

2.6.1 Applications of CMHs

Some of these applications of CMHs in metrology and standards laboratories include: continuous industrial process control, meteorological monitoring, automated QC of manufacturing processes, e.g. pharmaceuticals, steel production and photography film, critical environment monitoring, e.g. clean rooms, museums, storage vaults, measurement of water vapor in extreme operating environments, e.g. curing ovens, heat treating, automotive exhaust testing, plant air, or gas analysis, environmental test chambers and research and development (R&D) (Yankee Environmental Systems, 2005). When CMH systems are embedded in precision humidity generators, they constitute a calibration system in which secondary humidity measuring devices such as polymer and inorganic oxide transmitters can be calibrated (Schultz, 2015).

2.7 Resistive Humidity Sensor

The working principle of resistive sensors for relative humidity estimation is based on the electrical impedance change with humidity (Massaroni, 2019). Resistance-based humidity sensors operate through the detection of environmental fluctuations of water vapour counts, which directly affect electrical impedance of the active sensing layer (Najeeb *et al*., 2018). The change of resistance to humidity follows an inverse exponential association, and almost varies

from 1 KΩ to 100 MΩ (Farahani *et al*., 2014). The active materials for resistive humidity sensors include ceramics, metals, metal, poly-electrolytes, polymers, low molecular weight organic materials, porous organic/inorganic materials, nano-materials and their composites (Harun *et al*., 2012).

The basic structure of resistive humidity sensor from TDK, 2018 is shown in figure 2.8. In fabricating the sensor, a noble metal thick film conductor such as gold or ruthenium oxide is printed in a comb shape on an alumina substrate to form electrodes. A polymer material is applied on these electrodes to form a humidity sensing film. The "humidity sensing" mechanism of the polymer film can be explained by the existence of movable ions that are enabled to move freely through the absorption of water molecules. When the sensor absorbs the water vapour and ionic functional groups are dissociated, it increases its electrical conductivity.

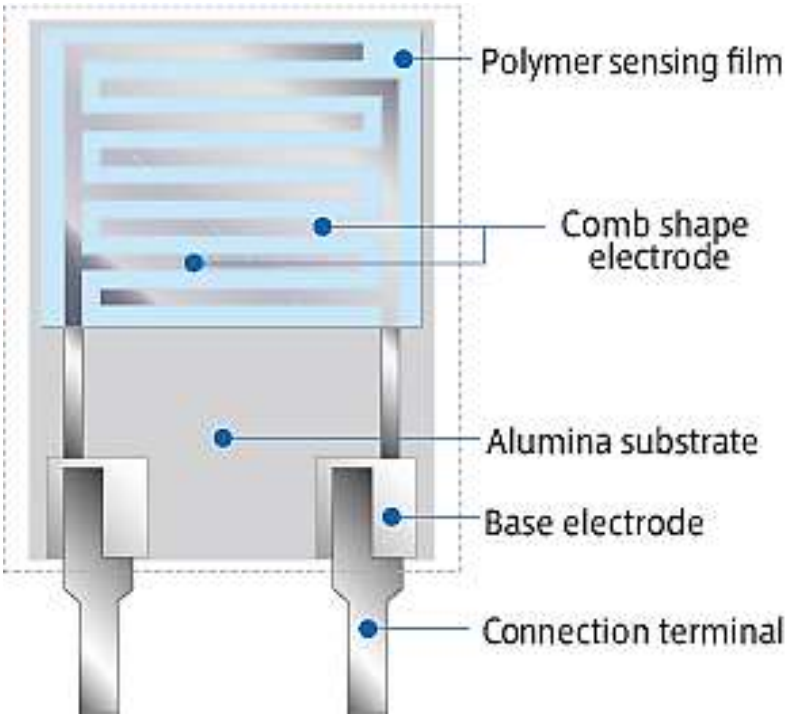

Figure 2.8 Resistive humidity sensor (TDK, 2018)

Resistance relative humidity sensor element has disadvantages such as difficulty in performing measurement in the low humidity range (5 % RH or lower), difficulty in securing a dynamic range in circuits because the impedance variation range exhibits an exponential characteristic reaching four to five digits, and large property fluctuations due to temperature (TDK, 2018). A distinct advantage of resistive RH sensors is their interchangeability, usually within ±2 % RH, which allows the electronic signal conditioning circuitry to be calibrated by a resistor at a fixed RH point, eliminates the need for humidity calibration standards, so resistive humidity sensors are generally field replaceable (Gupta, 2015).

2.8 Capacitive Relative Humidity Sensors

Capacitive relative humidity sensors have two basic structures: parallel plate (PP) capacitor and interdigital/interdigitated electrodes (IDEs) capacitor (Hong *et al*., 2019). A parallel plate capacitive RH sensor has the sensing material sandwiched in between the two layers of parallel plate electrodes. Capacitive RH sensor is made of a hydrophilic material that reaches equilibrium with the ambient relative humidity; the equilibrium moisture content affects the capacitance dielectric constant as a consequence of the absorbed water vapour (Dario *et al*., 2010). Various sensing materials such as polymers, metal oxides, porous materials and nano-materials have been investigated for advanced humidity sensors (Han *et al*., 2017). Materials such as porous ceramics, porous silicon, porous silicon carbide and hygroscopic polymers, porous Al_2O_3 thin films, plasma-etched polyimide and thin polyimide films have been used as sensitive layers for humidity sensors (Chia-Yen *et al*., 2005).

Capacitive humidity sensors offer several advantages, including very low power consumption and high output signals (Chia-Yen *et al*., 2005). Capacitive humidity sensors exhibit linear

responses, fast response and recovery times and low hysteresis (Farahani *et al* 2014). Capacitive humidity sensors have a sensitivity range of 0.005 pF/ % RH to 0.077 pF/ % RH, with response times between 4 s and 47 s (Lee *et al*., 2011). Capacitive relative humidity sensor has wide temperature range, excellent stability, fast response, full recovery from condensation, highly resistant to chemicals, small size, low cost and very little maintenance requirement as advantages of capacitive relative humidity sensors (Rotronic, 2014).

The formation of clusters of absorbed water molecules leads to hysteresis; this is a serious disadvantage in capacitive humidity sensors (Chen *et al*., 2005; Hernández-Rivera et al., 2017).

2.8.1 Operation of capacitive relative humidity sensor

Figure 2.9 shows the absorption of water vapour by interdigital/interdigitated electrodes (IDEs) capacitive relative humidity sensor. When no moisture is present in the sensor, the dielectric constant and the sensor geometry determine the value of the capacitance. When water vapour blows over the surface, it is adsorbed on the surface. The adsorbed molecules diffuse in the polymer inducing a variation of its permittivity. The variation in permittivity causes variation in capacitance. At normal room temperature, the dielectric constant of water vapor has a value of about 80, which is much larger than the dielectric constant of the sensor dielectric material of about 2 to 15. Therefore, absorption of moisture by the sensor results in an increase in sensor capacitance. At equilibrium conditions, the amount of moisture present in a hygroscopic material depends on both ambient temperature and ambient water vapor pressure. This is true also for the hygroscopic dielectric material used in the sensor.

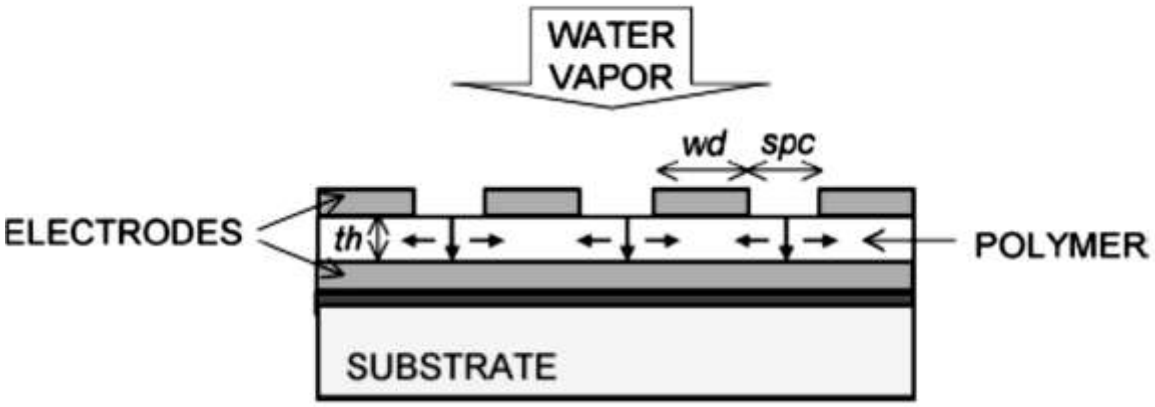

Figure 2.9 The absorption of water vapour by capacitive humidity sensor (Karthick et al, 2011)

2.9 Thermal Conductivity Humidity Sensor

Thermal Conductivity Humidity Sensor measures the absolute humidity by calculating the difference between the thermal conductivity of dry air and humid air (Naik, 2018). In figure 2.10, two tiny thermistors with negative temperature coefficient are used to for a bridge circuit. One thermistor is hermetically sealed in a chamber filled with dry Nitrogen while the other is exposed to open environment through small venting holes. When the circuit is powered on, the resistances of the two thermistors are calculated and the difference between those two values is directly proportional to absolute Humidity (Electronic Hub, 2014). The resistive heating increases their temperature to greater than 200 °C. The heat dissipated from the sealed thermistor is greater than the exposed thermistor due to the difference in the thermal conductively of the water vapor as compared to dry nitrogen (Roveti, 2001).

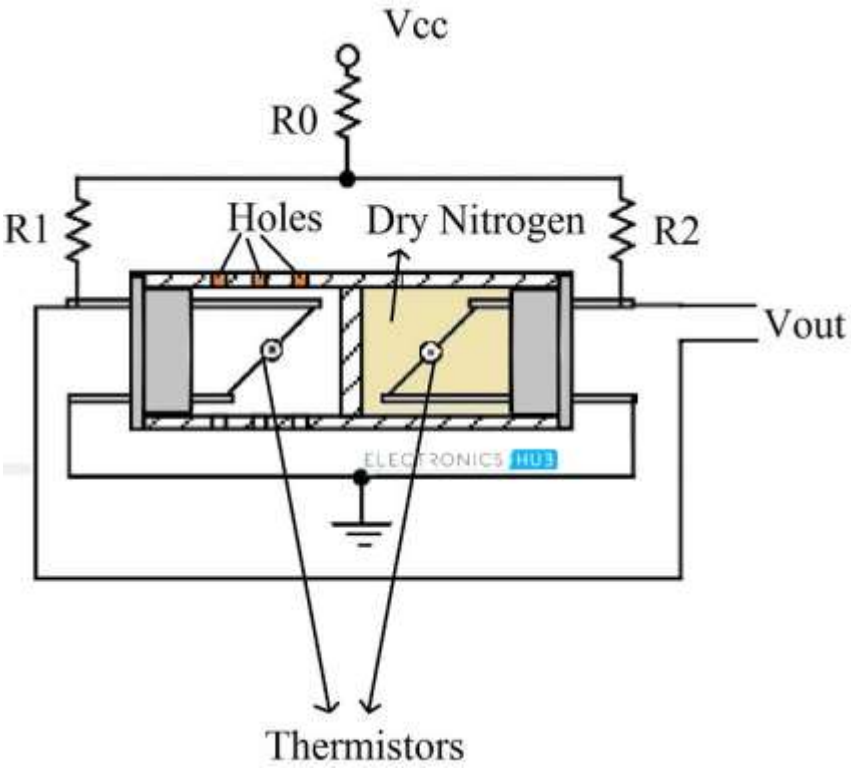

Figure 2.10 Thermal Conductivity Humidity Sensor (Electronic Hub, 2014)

Roveti (2001) noted that absolute humidity sensors are very durable; operate at temperatures up to 575 °F (300 °C) and resistant to chemical vapors by virtue of the inert materials used for their construction, i.e., glass, semiconductor material for the thermistors, high-temperature plastics, or aluminum. The disadvantage of the thermal conductivity sensor is that output signal is affected by the operating temperature

Some applications of thermal humidity sensors in appliances such as clothes dryers and both microwave and steam-injected ovens. For industrial applications they are used in kilns for drying wood; machinery for drying textiles, paper, and chemical solids; pharmaceutical production; cooking; and food dehydration.

2.10 Gravimetric Humidity Sensor

A Gravimetric hygrometer measures the mass of an air sample compared to an equal volume of dry air. This is considered the most accurate primary method to determine the moisture content of the air (Wexler, 1964). Figure 2.11 shows NIST gravimetric hygrometer described below.

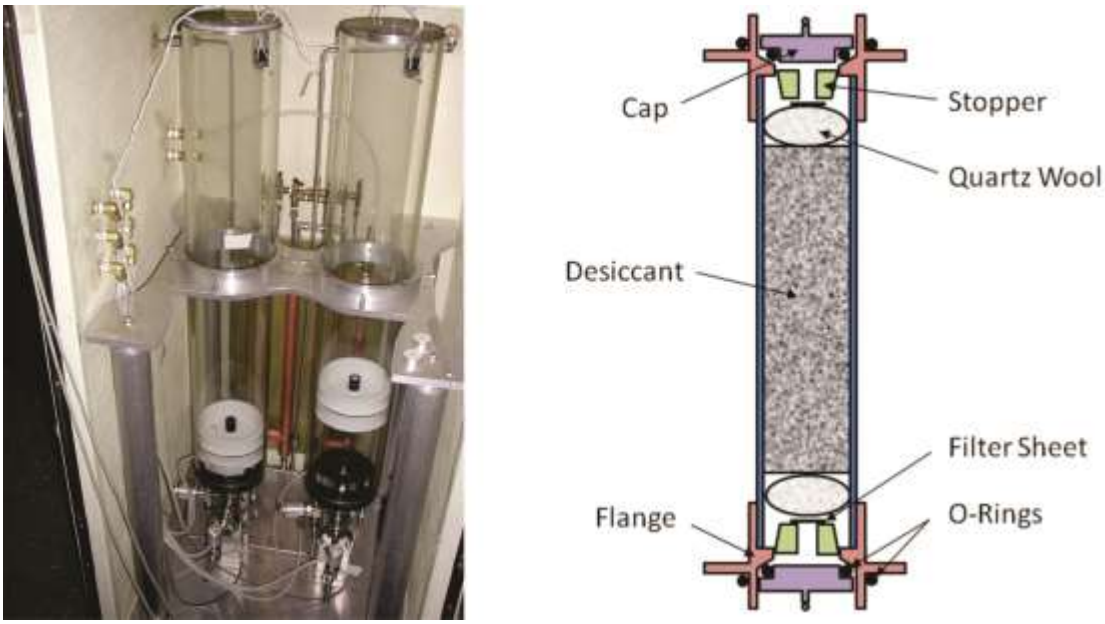

Figure 2.11 Gravimetric hygrometers (Corey, 2016)

The gravimetric hygrometer measures the water mole fraction in a gas exiting the generator. It separates the water from the gas using desiccants and subsequently determines the masses of the water and the gas separately. These masses are then used to calculate the water mole fraction in the gas, one of the principal humidity quantities. The NIST gravimetric hygrometer is the only working gravimetric hygrometer in a National Measurement Institute today (NIST, 2016). It is capable of determining water mole fractions with an expanded uncertainty ($k = 2$) of 0.1%.

Ggravimetric hygrometer is a large and cumbersome instrument that is very time consuming to use, expensive to build and can be expensive to operate because of the long sample times

required for accurate results at low humidity levels and is not a practical option for most laboratories or field measurements (Brenner, 2010).

2.11 Humidity Sensor Parameters or Performance Characteristics

Some important humidity sensor parameters also known as performance characteristics include accuracy, range, span, linearity, reliability, repeatability, hysteresis, response time and sensitivity.

1. **Accuracy**

Accuracy is the closeness of agreement between a quantity value obtained by measurement and the true value of the quantity measured (Marina & Bertil, 2007). It is the extent to which the measured value might be wrong and normally expressed in percentage. It is the amount of uncertainty in a measurement with respect to an absolute standard. The accuracy of a sensing system represents the correctness of its output in comparison to the actual value of the measured, and to assess the accuracy, either the system is benchmarked against a standard value of the quantity measured or the output is compared with a measurement system with a superior accuracy (Kalantar-Zadeh, 2013). Accuracy specifications usually contain the effect of errors due to gain and offset parameters.

Accuracy can be related to absolute or relative error. Absolute accuracy is the difference between the result of the measurement and the true value of the quantity being measured. It can be calculated as

Absolute error = Output value – true value (Kalantar-Zadeh, 2013). 2.6

$$\text{Relative error} = \frac{\text{output value} - \text{true value}}{\text{true value}} \quad \text{(Kalantar-Zadeh, 2013).} \qquad 2.7$$

The absolute error has the same unit as the measured quantity while the relative error is unitless. The percentage error can be obtained as follows:

$$e = \frac{\Delta X}{(X_{max} - X_{min})} \text{ x } 100\% \qquad 2.8$$

where ΔX is the change in sensor values, X_{max} and X_{min} are the maximum and minimum values the sensor is designed to operate at (Kalantar-Zadeh, 2013).

Absolute error has the same unit as the measure quantity while the relative error is unitless. Errors are produced by fluctuations in the output signal and can be systematic (e.g., drift or interferences from other systems) or random such as random noise (Kalantar-Zadeh, 2013).

2. Range

The range or span of an instrument defines the minimum and maximum values of a quantity that the instrument is designed to measure (Morris, 2001). It the absolute difference between the lowest (Y_{min}) and highest (Y_{max}) values of the stimulus or the physical quantity being measured.

3. Linearity

A sensor said to be linear if its response (y) to a physical quantity (x) is idealized to have the form: $y(x) = Ax$, $0 \leq x \leq x_{max}$, $A>0$. Hence, the closeness of the calibration curve to a specified straight line shows the linearity of a sensor and its degree of resemblance to a straight line describes how linear a system is (Kalantar-Zadeh, 2013). Figure 2.12 illustrates the concept of linearity and linear approximation to a sensor's output response.

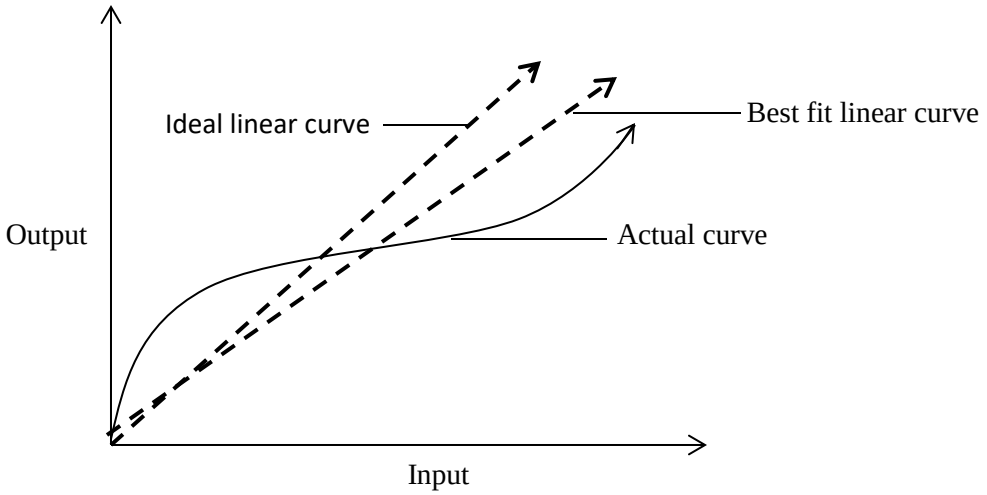

Figure 2.12: linearity and linear approximation to a sensor's output response.

4. Repeatability

Repeatability is the closeness of the agreement between the results of successive measurements of the same measurand carried out under the same conditions of measurement (Antikainen *et al*., 2002). When all operating and environmental conditions remain constant, repeatability is the sensing system's ability to produce the same response for successive measurements (Kalantar-Zadeh, 2013). Repeatability of a sensor can be long-term or short-term. It can be calculated by finding the percentage of input full scale of the maximum difference between two readings taken at different times under identical input conditions. This is expressed mathematically as

$$\text{Repeatability} = \frac{\text{high value} - \text{low value}}{\text{full range}} \times 100\ \% \qquad 2.9$$

5. Response Time and recovery time

Response time is generally expressed as the time at which the output reaches a certain percentage (for instance, 95 %) of its final value, in response to a step change of the input (Kalantar-Zadeh,

2013). On the other hand, recovery time is defined as the time required for a sensor to return to 90 % of the original baseline signal upon removal the target gas (Arafat *et al*., 2012).

Both response and recovery times significantly affect the performance of humidity sensors. Response and recovery times of sensors affect the RH-increasing and RH-decreasing processes. Figure 2.13 illustrates the response and recovery times of a capacitive relative humidity sensor for humidity levels between 23 % RH and 86 % RH. The sensor response time (humidification from 23 % RH to 86 % RH) is approximately 10.5 s, and the recovery time (desiccation from 86 % RH to 23 % RH) is approximately 41 s.

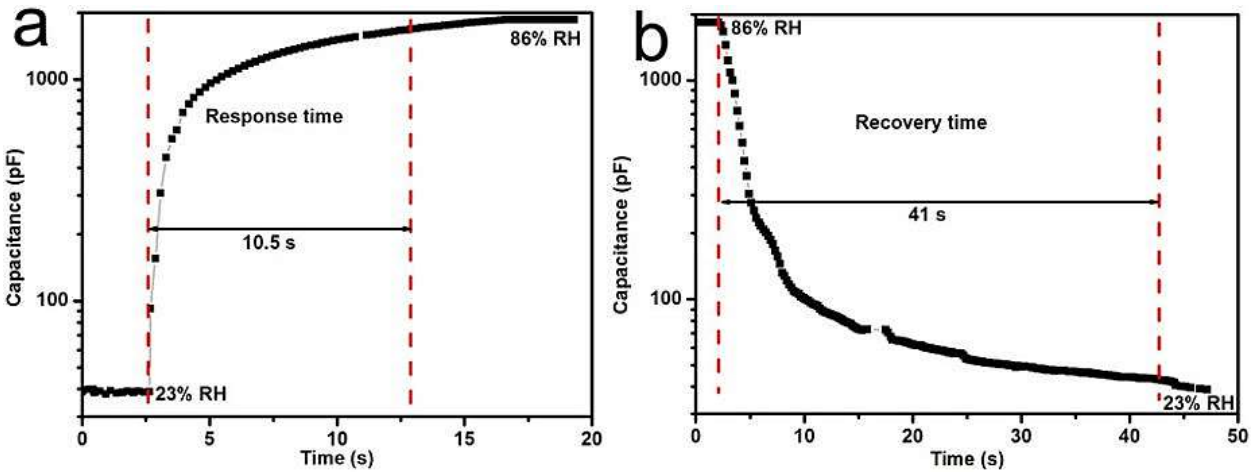

Figure 2.13 Response time (a) and recovery time (b) of a capacitive relative humidity sensor for humidity levels between 23 % RH and 86 % RH (Hengchang *et a*l., 2013).

6. Sensitivity

The sensitivity of measurement is a measure of the change in instrument output that occurs when the quantity being measured changes by a given amount (Morris, 2001). The sensitivity **(S)** of a capacitive relative humidity sensor can be expressed as Equation

$$S = \frac{\Delta C}{C_0} \Big/ \Delta \%RH \qquad 2.10$$

where $\Delta C = C_1 - C_0$, C_0 is the capacitance measured at the minimum RH humidity value, C_1 is the capacitance measured at maximum humidity value and Δ(% RH) is the difference between the relative humidity values when measuring C_1 and C_0 (Hong et al, 2019)

7. Hysteresis

Hysteresis in humidity sensors is the difference between output readings for the same measurand, depending on the trajectory followed by the sensor (Kalantar-Zadeh**,** 2013). It is the deviation of the sensor's output at any given point when approached from two different directions. Figure 2.14 illustrates the concept of hysteresis in humidity sensor responses. In the graph, the decreasing curve represents desorption of water vapour from the sensor while the increasing curve represents the absorption of water vapour by the sensor. The magnitude of the error depicts the hysteresis value of the sensor. The higher the error or gap between the two curves, the higher the hysteresis.

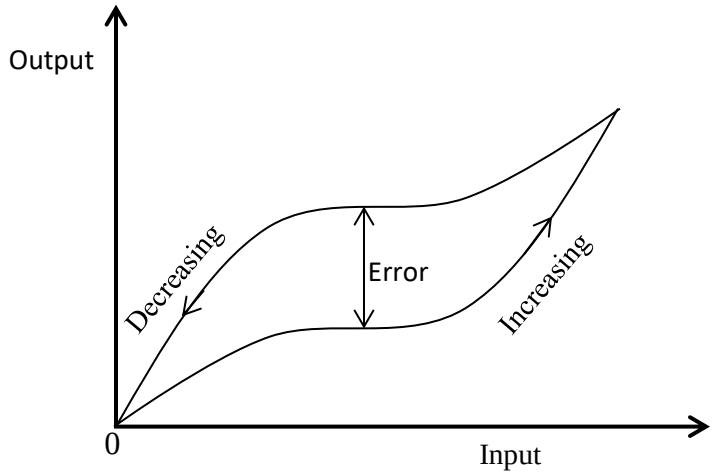

Figure 2.14 Illustration of the concept of hysteresis in sensor

Hysteresis is a critical drawback of capacitive humidity sensors. It may cause deformation of the sensing material (such as polymer) owing to water clusters and consequently influence the sensor performance (Liu *et al*., 2017). The capacitance variation with the humidity is measured to investigate the hysteresis behavior of the humidity sensor. In figure 2.15 the humidity is increased from 10 % RH to 90 % RH and then decreased to 10 % RH in steps of 10 % RH. The hysteresis increases at the beginning, reaches its maximum value at 60 % RH, and then decreases with a further increase in the RH. The humidity sensor exhibits maximum hysteresis *H* of 0.95 % RH at 60 % RH, which is calculated by

$$H = \frac{C_{D60} - C_{A60}}{S} \ (\%RH) \qquad 2.12$$

where S is the sensitivity of the sensor, C_{D60} and C_{A60} are the capacitance values measured at 60 % RH in the desorption and absorption process, respectively (Liu *et al*., 2017).

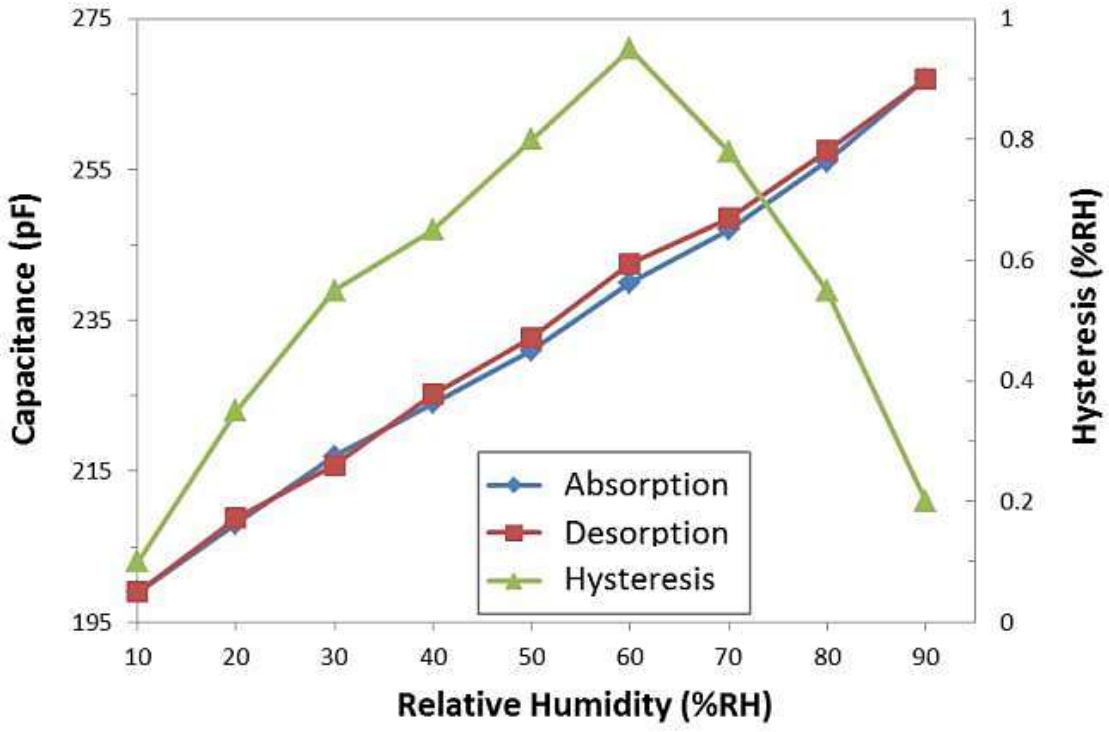

Figure 2.15 Hysteresis characteristics of the humidity sensors in relative humidity variation from 10 % RH to 90 % RH (Liu *et al*, 2017).

2.12 Material Characterization Techniques

There are four major groups of characterization techniques (Jillavenkatesa *et al*., 2001):

1. Techniques which use radiation as a probe for the characterization. These techniques provide structural, chemical and optical information of the sample. They are Raman, Nuclear Magnetic Resonance (NMR), Fourier transform infrared spectroscopy (FTIR), InfraRed (IR), Atomic force microscophy (AFM), X-rays, lasers, etc.,
2. Techniques which use heat as a probe for the characterization. These techniques provide thermodynamic information about the sample referring to thermal stability, decomposition pathways, viscoelastic properties of a material, phase changes, etc, Calorimetry and thermal methods commonly used are: Thermogravimetric Analysis (TGA), Differential Scanning calorimetry (DSC) and Differential Mechanical Thermal calorimetry (DMTC),
3. Techniques which use molecule as a probe for the characterization. These techniques provide thermodynamic, chemical and structural information about the sample. They involve exposing the material to different probe molecules (vapors and/or gases) under different experimental conditions. Physical and chemical changes are recorded and further analysed as well as Sorption mechanisms (absorption, adsorption and desorption). Most common techniques are Dynamic Vapor Sorption (DVS), Inverse gas chromatography (IGC), BET surface area analysis, and
4. The particle-size distribution (PSD) of a powder, or granular material, or particles dispersed in fluid, is a list of values or a mathematical function that defines the relative amount, typically by mass, of particles present according to size.

2.13 Material Deposition Techniques

Interdigitated electrodes (IDEs) are widely used for various sensor applications, such as gas sensor, humidity sensor, biosensor, and so forth (Chou *et al*., 2014). The electrical signals generated by the sensing material are detected through IDEs. Sensors can be fabricated using IDEs and different methods of deposition of the sensing material such as screen printing, photolithography, inkjet printing, spin coating, Blade technique and chemical vapour deposition.

2.13.1 Screen Printing

Screen printing started in China before being adopted and refined by Japan and other Asian countries and introduced to Europe in the late 1700 s, and was officially patent by an English man named Samuel Simon in 1907 (Fong and Youwen, 2016). Simon's method was largely used to print high quality custom wallpaper, as well as on silk or linen material products that were exclusive only to the affluent at the time. Techniques for screen printing continued to be refined as time progressed and so too did its application. These days, common products from the screen printing industry include posters, labels, decals, signage, and all types of textiles and electronic circuit boards.

Screen printing consists of three elements: the screen (which is the image carrier), the squeegee, and ink (Fong and Youwen, 2016). The screen printing process uses a porous mesh stretched tightly over a frame made of wood or metal, with proper tension being critical in producing accurate colour registration. A stencil is produced on the screen either manually or photo

chemically, and defines the image that will be printed. It can be used to print on a wide variety of materials: paper, plastics, glass, metals, and fabrics.

In electronics, screen printing is a technique which uses a mesh to transfer ink onto a substrate, except in areas made impermeable to the ink due a blocking stencil. It is used to create electrical devices by defining patterns such as IDEs on substrates. The substrates can be printed circuit board, glass, metal or plastics. Screen printing process involves the use of a screening material, such as a photographic paper, coated with a film (the stencil). The screen printing process sequence of producing a humidity sensor using screen printing technique is shown in figure 2.16. It uses a stencil and printed electronic ink to create the circuit on the board. The design is applied or printed to the stencil. The board is aligned underneath63 the stencil and the ink is squeegeed across the stencil. The ink is then cured by applying heat or UV cured.

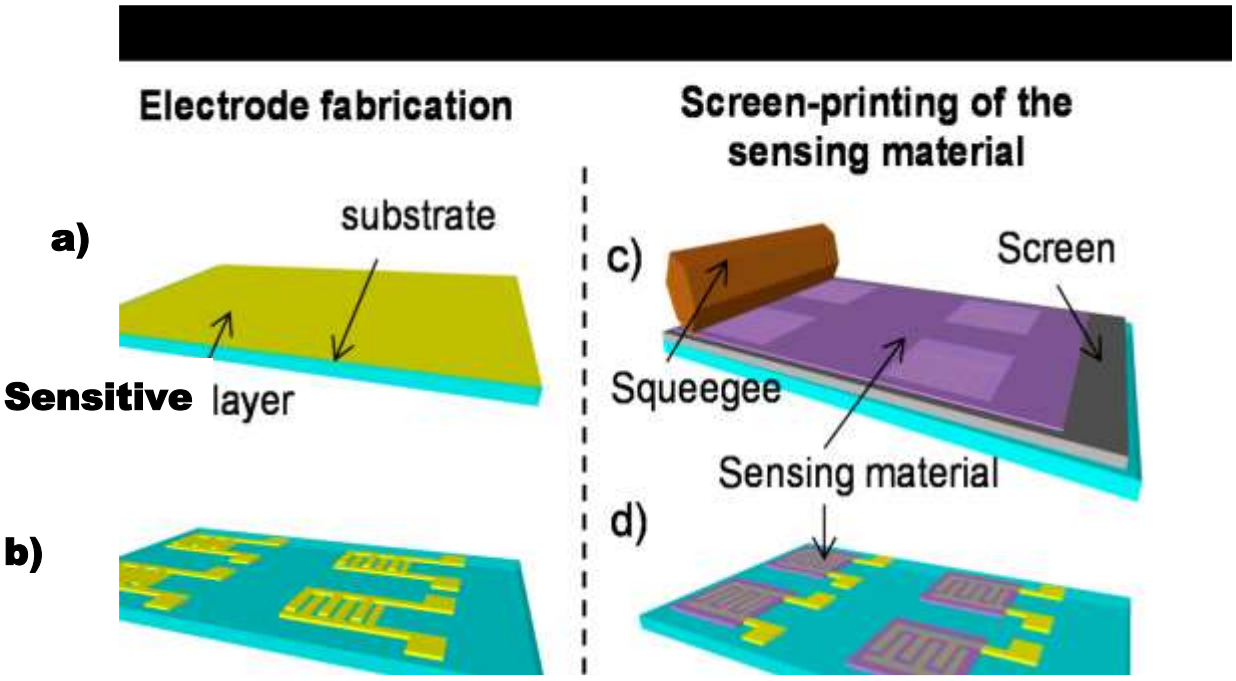

Figure 2.16 Process sequence of humidity sensor; a) the substrate coated with a sensitive (conducting) layer, b) interdigitated electrodes (sensors), c) screen printing of the sensing material, d) sensors after screen printing (Dubourg *et al*, 2017)

The ink must be cured correctly in order to properly bond with the substrate and create the component. Improperly cured ink has poor conductivity. The ink is cured through a laser sintering process so that the ink can be cured at a high temperature without damaging the substrate. The printing must be at the correct thickness to prevent cracking during sintering process. Hence, one of the biggest advantages of screen-printing is the thickness of the printed ink film and the process is widely used in the manufacture of printed circuit boards (Aijazi, 2014).

2.13.2 Spin Coating

Spin coating is a simple process for rapidly depositing thin coatings onto relatively flat substrates (Birnie, 2004). It is a method used to apply a uniform film onto a solid surface by using centrifugal force and requires a liquid–vapor interface (Smith *et al*., 2013).

Spin coating was first used to apply coatings and pitch for several decades ago. Emslie *et al.* (1958) developed the first spin coating model, which has been used as a basis for future more specific or complicated models (Lawrence and Zhou, 1991). The technique can be used to coat small substrates (from a few mm square) or flat panel TVs which might be a metre or more in diameter. It is used for coating substrates with everything from photoresists, insulators, organic

semiconductors, synthetic metals, nanomaterials, metal and metal oxide precursors, transparent conductive oxides, and many more materials (Spooner, 2019).

The whole process is divided into four stages, which are deposition, spin-up, spin-off and evaporation of solvents (Sahu *et al*., 2009). Spin coating generally involves the application of a thin film (a few nm to a few um) evenly across the surface of a substrate by coating (casting) a solution of the desired material in a solvent (an "ink") while it is rotating (Spooner, 2019). Figure 2.17 shows the stages involved in spin coating a small molecule in solution using a static dispense.

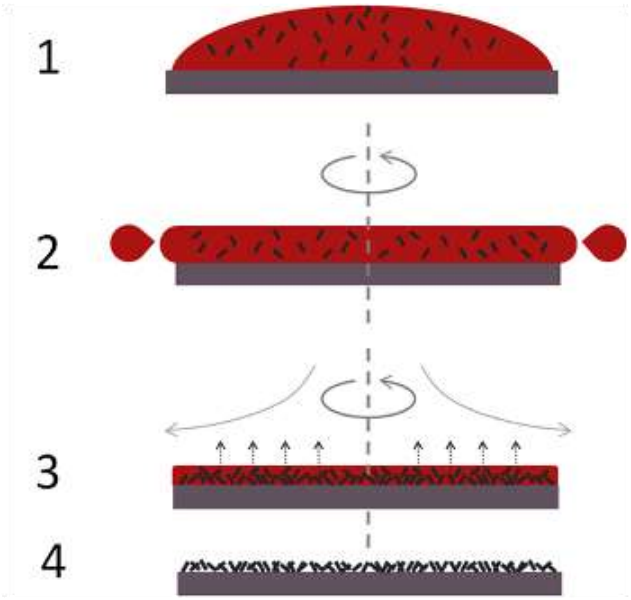

Figure 2.17 Example of spin coating a small molecule in solution using a static dispense (Spooner, 2019).

1. First the substrate is coated in the ink containing the molecules dissolved in a solvent (1).
2. Then the substrate is rotated at high speed and the majority of the ink is flung off the side (2).

3. Airflow then dries the majority of the solvent, leaving a plasticized film (3)
4. Before the film fully dries to just leave the molecules on the surface (4).

The rotation of the substrate at high speed (usually >10 rotations per second = 600 rotations per minute) means that the centripetal force combined with the surface tension of the solution pulls the liquid coating into an even covering. During this time the solvent then evaporates to leave the desired material on the substrate in an even covering. In general, the thickness of a spin coated film is proportional to the inverse of the square root of spin speed as in the equation below, where *t* is the thickness and *w* is the angular velocity (Spooner, 2019):

$$t \propto \frac{1}{\sqrt{\omega}} \qquad 2.13$$

The final film thickness and other properties will depend on the nature of the resin (viscosity, drying rate, percent solids, surface tension, etc.) and the parameters chosen for the spin process (Tyona, 2013). Factors such as final rotational speed, acceleration, and fume exhaust contribute to how the properties of coated films are defined (Mitzi *et al*., 2004; Hellstrom, 2007; Tyona, 2013).

1. Advantages and Disadvantages of Spin Coating

The simplicity and relative ease with which the spin coating process can be set up, the thin and uniform coating that can be achieved, and the fast drying times which in turn results in high consistency at both macroscopic and nano length scales are some of the advantages of spin coating (Spooner, 2019). In spin coating, the film thickness is easily changed by changing spin speed or switching to a different viscosity photoresist without multiple coupled parameters; the film has the ability to get progressively more uniform as it thins and the operating system is cheap and fast (Sahu et al., 2009).

Despite the numerous advantages spin coating is limited by inability to spin large substrates at a sufficiently high rate in order to allow the film to thin, an inherent slow batch (single substrate) process, lower performance for some particular nano-technologies (small molecule OFETs for example) as a result of fast drying times and typically very low material usage (at around 10 % or less) with the rest of the material being flung off the side and wasted (Luurtsema, 1997).

2.14 Calibration of a Relative Humidity (RH) Sensor

The accuracy of a relative humidity sensor can be checked by obtaining humidity values from the sensor and comparing it to a reference standard. The humidity calibration method is based on the fact that a sealed off air volume in equilibrium with a supersaturated saline solution reaches a well-determined relative humidity (RH); its value depends strongly on the selected salt and on the equilibrium temperature (T) of the system (Mayer *et al*., 2005). The "saturated salt" method can be used to produce the standards for measuring relative humidity. These salts are used to create micro-environments of known relative humidity (RH) percentages (i.e., reference standards), and the relative humidity of sensors are read inside the micro-environment. Table 2.1 shows the equilibrium relative humilities generated over saturated solutions of a selection of salts. The gaps shown in the table indicates that no reliable data are available. The values listed in the table are taken from papers by Greenspan, 1976; O'Brien, 1948; Wexler and Hasegawa, 1954; Young, 1967.

Table 2.1 The equilibrium relative humidity generated over saturated solutions of a selection of salts.

Saturated salt solution	Temperature ^{0}C										
	0	5	10	15	20	25	30	35	40	50	60
	Relative humidity (%)										

Potassium sulphate	99	98	98	98	98	97	97	97	96	96	-
Potassium nitrate	96	96	96	95	95	94	92	91	89	85	-
Potassium chloride	89	88	87	86	85	84	84	83	82	81	80
Ammonium sulphate	82	82	82	82	81	81	81	80	80	79	-
Sodium chloride	76	76	76	76	75	75	75	75	75	74	75
Sodium nitrate	-	-	-	-	65	64	63	62	61	-	-
Ammonium nitrate	-	-	75	70	67	64	60	53	-	-	-
Sodium dichromate	61	59	57	57	55	54	53	51	50	49	47
Magnesium nitrate	60	59	57	56	54	53	51	50	48	45	-
Potassium carbonate	43	43	43	43	43	43	43	-	-	-	-
Magnesium chloride	34	34	33	33	33	33	32	32	32	31	29
Potassium acetate	-	-	23	23	23	23	22	-	-	-	-
Lithium chloride	11	11	11	11	11	11	11	11	11	11	11
Potassium hydroxide	-	14	12	11	9	8	7	7	6	6	6

2.14.1 Preparation of salt solutions for the Calibration of RH Sensor

The saturated salt solutions for the calibration can be prepared in different ways. In the procedure used by (Nielsen-Kellerman, 2014) only pure distilled water was used to make up solutions. A liquid dropper was used to add the distilled water to the bottle used for the salt. The salt was stirred well after each addition until the salt can absorb no more water as will be evidenced by excess liquid in the bottle. The excess liquid is kept to a minimum in order to get best results (Figure 2.18).

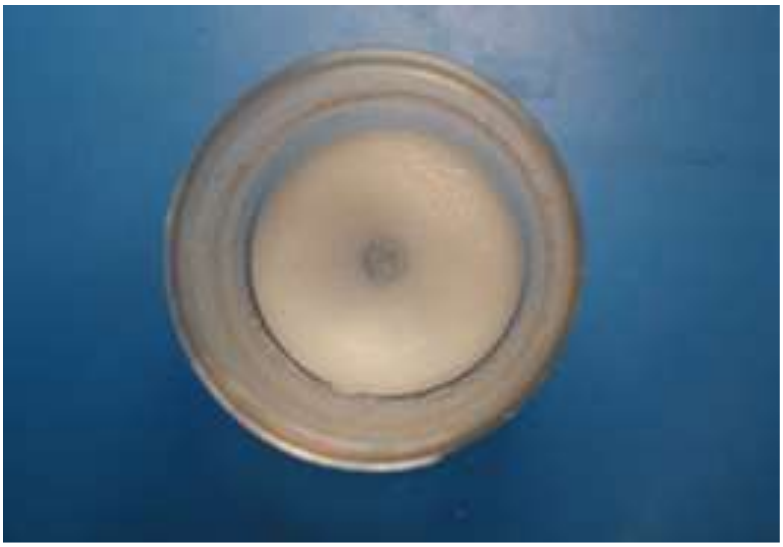

Figure 2.18 Saturated salt solution (Nielsen-Kellerman, 2014)

The bottle was closed after mixing and inserted in a foam block for temperature stabilization. New solutions should be prepared at least 12 hours prior to first-time use.

2.14.2 RH Sensor Calibration Procedure

Genovese provided three steps for checking and calibrating a humidity sensor as follows:

1. to evaluate the sensor performance using reference standards

In Genovese, 2017 description, a solution is made in a sealed jar to preserve the atmosphere and the connected sensor is placed in the sealed jar (Figure 2.19). Subsequently, the sensor is repeatedly read and the values recorded. By repeating the procedure using several different salts, each producing a different relative humidity, a profile for the sensor under test can be developed. Since the relative humidity of each micro-environment is known, the deviations of the relative humidity sensor readings can be assessed from the known humidity values of the saturated salts.

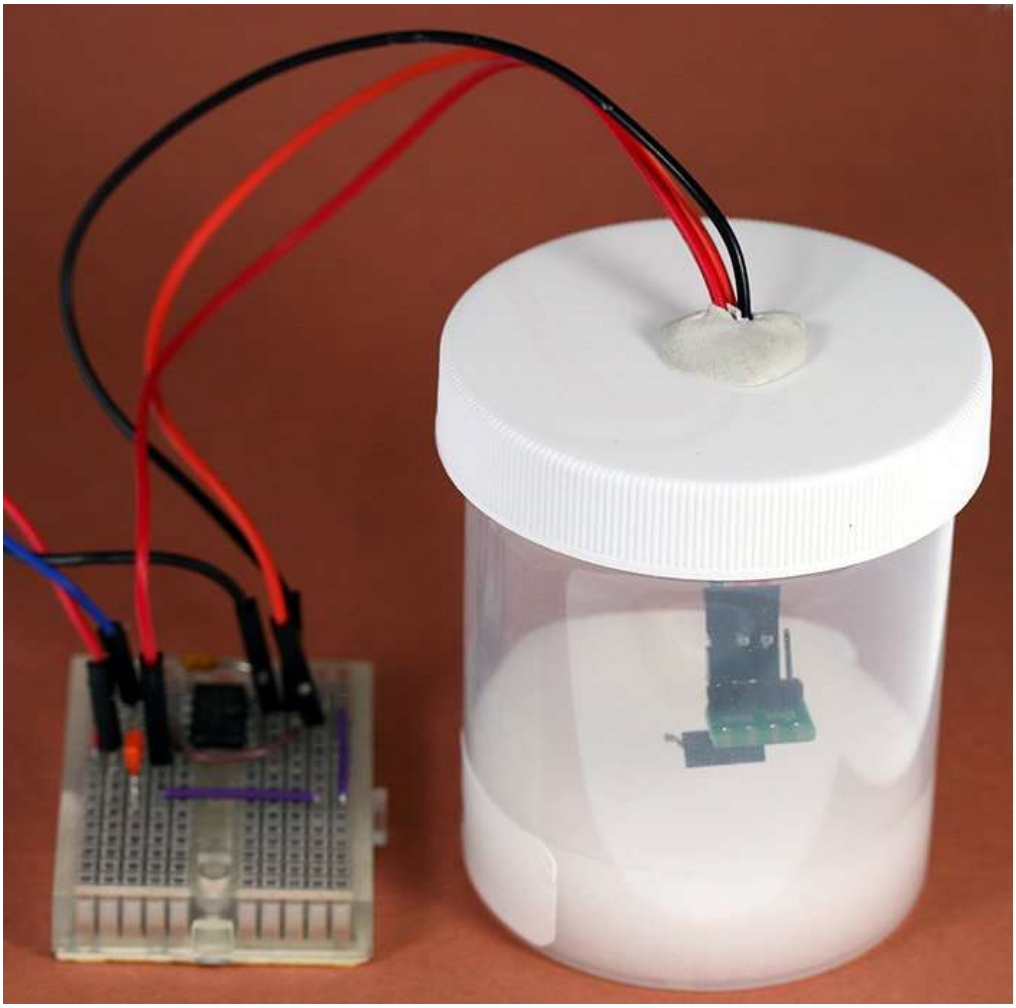

Figure 2.19 A sensor on a carrier board inside a micro-environment containing sodium chloride (Genovese, 2017).

The accuracy of the RH sensor is then evaluated. Evaluating the accuracy of the RH sensor in each of the micro-environments implies calculating the error and the root mean square error (RMSE) in measurement of the relative humidity by the Test Sensor. Error is the difference between the observed value (OBS) and the standard value.

$$\text{RMSE} = \sqrt{\frac{\sum_{i-1}^{n}(O_i - I_i)^2}{n}} \qquad 2.14$$

where O_i is the observed sensor value for micro-environment i and I_i is the ideal sensor value (i.e., the reference standard) for the micro-environment i (Genovese, 2017). The root mean square error (RMSE) is used to characterize the sensor's accuracy.

Once the accuracy of the sensor is characterized, the RMSE is used to decide whether it is necessary to calibrate the sensor. In some cases, the RMSE is small and completely acceptable for the application and no calibration may be required. If RMSE is less than 1 % and all sample points have an error less than 2 %, there may be no need for calibration of the sensor. However, the accuracy of the sensor can be improved by calibration.

2. to perform linear regression to determine a function that relates the ideal RH value (from the standards) to the observed value from the sensor readings:

This step involves calibrating the sensor by mathematically determining the function that relates the ideal values to the observed values. A linear regression procedure can be used to determine the function. The three polynomial functions shown represent linear regression:

i. $y = ax + b$ (first degree, linear) 2.15

ii. $y = ax^2 + bx + c$ (second degree, quadratic) 2.16

iii. $y = ax^3 + bx^2 + cx + d$ (third degree, cubic) 2.17

where y in 2.15 – 2.17 is the calibrated value, x is the sensor reading and a, b, c and d are the coefficients to be determined (Genovese, 2017).

In theory, the polynomial that best fits the data is used. That is, the polynomial that produces the smallest coefficient of determination, r^2 (or R^2). The closer r^2 is to 1, the better the fit. The observed values can be modified using the calculated functions. The polynomials will produce a

significant decrease in the RMSE, compared to the observed measures. A graph can be used to illustrate the improvement in the accuracy of the sensor readings.

3. to modify the sensor values using the polynomial to calculate the calibrated values

The modifications (calibrations) are implemented in software, which translates the sensor readings to their calibrated equivalents.

2.15 ARNUINO Nano ATmega 328 Microcontroller

A microcontroller is a computer-on-a-chip, or, it may be considered as a single-chip computer (Hussain *et al.*, 2016). It is a small device that controls objects, processes or events. Microcontroller and its support circuits are often built into or embedded in the devices they control. Hence, a microcontroller can be seen as an embedded controller. It consists of a Processor (CPU), Memory (RAM / ROM / Flash) and I/O ports (USB, I2C, SPI, ADC). Common microcontroller families include Intel: 4004, 8008, etc., Atmel: AT and AVR, Microchip: PIC, ARM: (multiple manufacturers). Microcontrollers are used in cellphones, toys, household appliances, cars and cameras.

Arduino boards include Arduino Uno, Arduino Leonardo, Arduino LilyPad, Arduino Mega, Arduino Nano, Arduino Mini, Arduino Mini Pro and Arduino BT. Arduino Nano is a Microcontroller board based on ATmega 328p or Atmega168. The description on Arduino Nano microcontroller given in this work is based on the description given by Circuits Today, 2018. Table 2.2 shows Arduino Nano ATmega 328 specification.

Table 2.2 Arduino Nano ATmega 328 specification (Circuits Today, 2018)

Arduino Nano	Specifications

Microcontroller	ATmega328
Architecture	AVR
Operating Voltage	5 Volts
Flash Memory	32 KB of which 2 KB used by Bootloader
SRAM	2KB
Clock Speed	16 MHz
Analog I/O Pins	8
EEPROM	1 KB
DC Current per I/O Pins	40 milliAmps
Input Voltage	(7-12) Volts

2.15.1 Arduino Nano Pin Descriptions

Figure 2.20 shows the five categories of Arduino pins. These include

1. Digital I/O , PWM = 14 Pins
2. For Analog Functions = 9 Pins
3. Power = 7 Pins
4. SPI (Apart from Digital I/O Section) = 3 Pins
5. Reset = 3 Pins

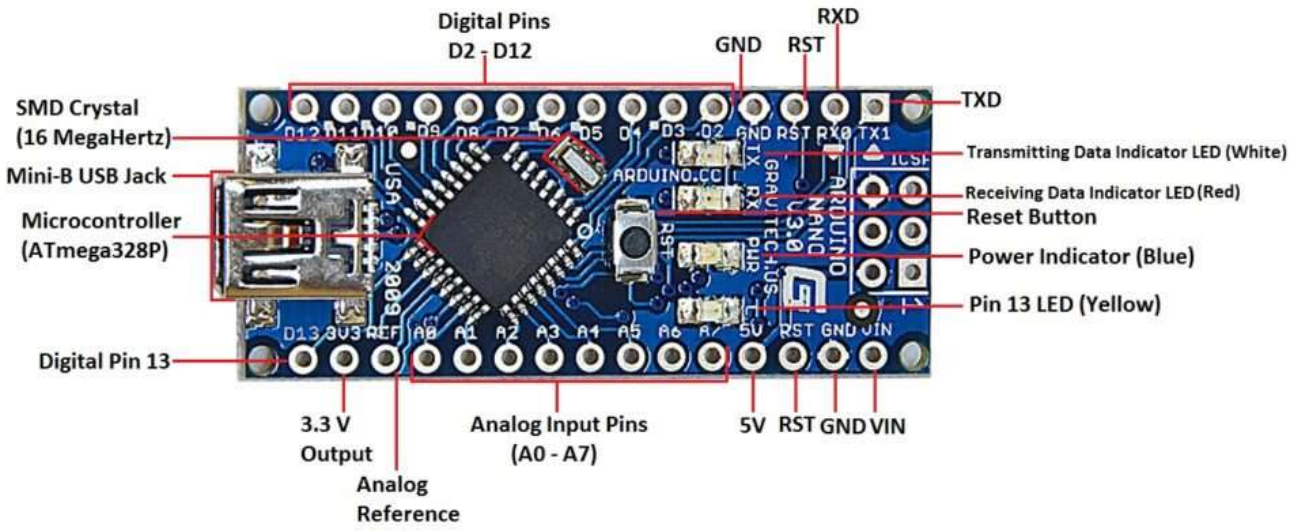

Figure 2.20 Arduino nano V3.0 pinout

Figure 2.21 gives a complete structure and pin arrangement of the 36 Arduino Nano pins. Table 2.3 shows the descriptions of pins 1 to 30 giving the pin number and their names, types and functions while Table 2.4 shows the description of ICSP pins giving the pin name, type and function.

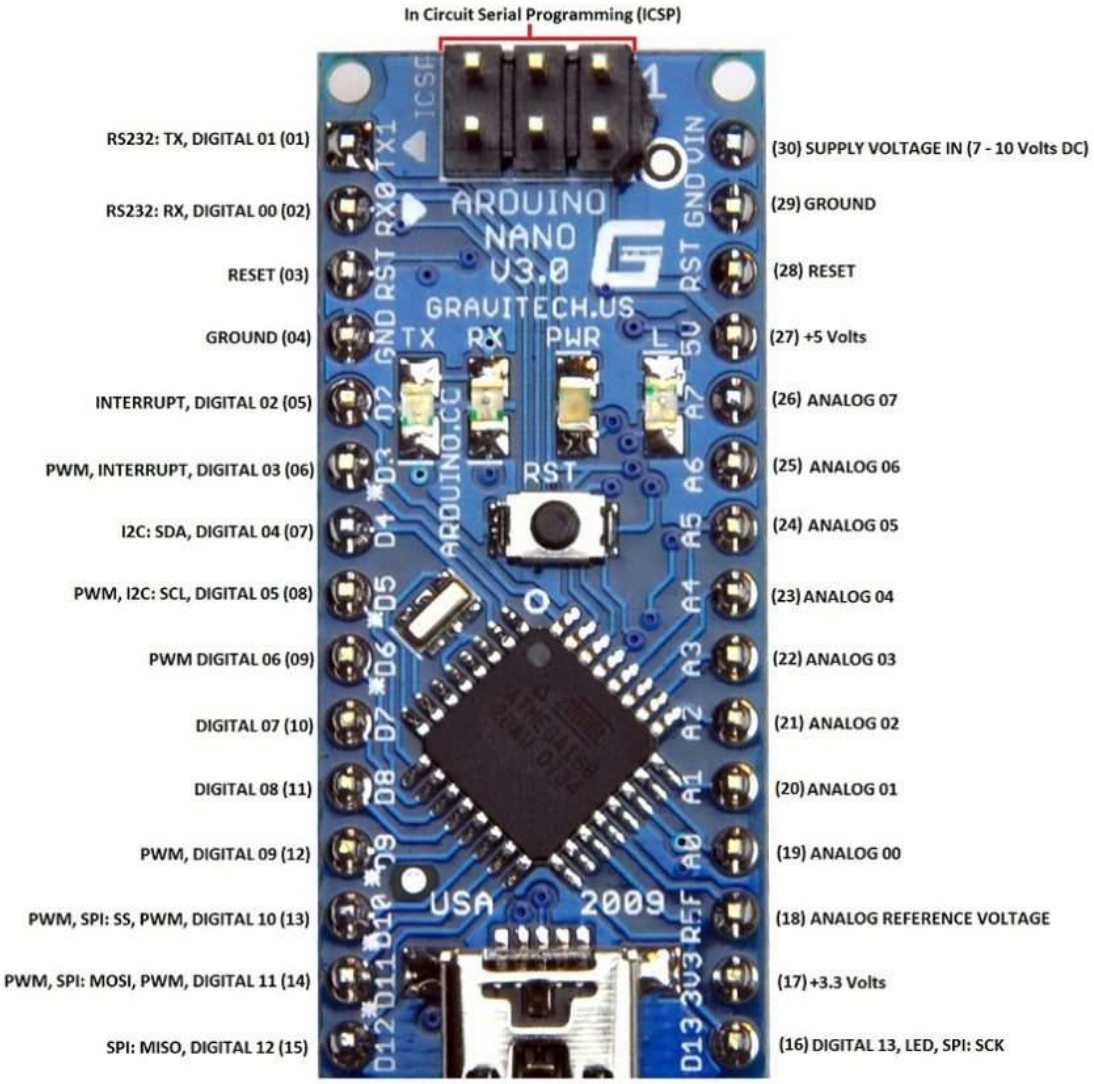

Figure 2.21 Arduino nano V3.0 pin description

www.CircuitsToday.com

Table 2.3 Pin 1 to 30 Descriptions

Arduino Nano Pin	Pin Name	Type	Function
1	D1/TX	I/O	Digital I/O Pin Serial TX Pin
2	D0/RX	I/O	Digital I/O Pin Serial RX Pin
3	RESET	Input	Reset (Active Low)
4	GND	Power	Supply Ground
5	D2	I/O	Digital I/O Pin
6	D3	I/O	Digital I/O Pin
7	D4	I/O	Digital I/O Pin
8	D5	I/O	Digital I/O Pin
9	D6	I/O	Digital I/O Pin
10	D7	I/O	Digital I/O Pin
11	D8	I/O	Digital I/O Pin
12	D9	I/O	Digital I/O Pin
13	D10	I/O	Digital I/O Pin
14	D11	I/O	Digital I/O Pin
15	D12	I/O	Digital I/O Pin
16	D13	I/O	Digital I/O Pin
17	3V3	Output	+3.3V Output (from FTDI)
18	AREF	Input	ADC reference
19	A0	Input	Analog Input Channel 0
20	A1	Input	Analog Input Channel 1
21	A2	Input	Analog Input Channel 2
22	A3	Input	Analog Input Channel 3
23	A4	Input	Analog Input Channel 4
24	A5	Input	Analog Input Channel 5
25	A6	Input	Analog Input Channel 6
26	A7	Input	Analog Input Channel 7
27	+5V	Output or Input	+5V Output (From On-board Regulator) or +5V (Input from External Power Supply
28	RESET	Input	Reset (Active Low)
29	GND	Power	Supply Ground
30	VIN	Power	Supply voltage

Table 2.4 ICSP Pins description

Arduino Nano ICSP Pin Name	**Type**	**Function**
MISO	Input or Output	Master In Slave Out
Vcc	Output	Supply Voltage
SCK	Output	Clock from Master to Slave
MOSI	Output or Input	Master Out Slave In
RST	Input	Reset (Active Low)
GND	Power	Supply Ground

2.15.2 Arduino Nano Digital Pins

Arduino digital pins are pins 1, 2, 5, 6, 7, 8, 9, 10, 11, 12, 13, 14, 15, and 16. They work with 5 V voltage as maximum, i.e., digital high is 5 V and digital low is 0 V. Each pin can provide or receive a current of 20 mA, and has a pull-up resistance of about 20-50 kilo Ohms. Each of the 14 digital pins on the Nano pinout can be programmed in a circuit as an input or output, using pinMode (pin, INPUT), digitalWrite (pin, value) and digitalRead (pin, value) functions. The digital pins have some additional functionality as well. pin represents the number of the pin whose mode is to be set; mode represents INPUT, OUTPUT or INPUT - PULLUP. The digitalWrite (pin, value) function is used to write a value to a digital pin. The value can be digital HIGH or digital LOW. Arduino is able to detect whether there is a voltage applied to one of its pins and report it through the digitalRead (pin, value) function. The value can be 5 V or 3.3 V on 3.3 V boards for HIGH, 0 V (ground) for LOW.

Pins 1 and 2 also function as serial communication pins, RX and TX respectively. Pin RX- receive and TX- transmit are used for TTL serial data communication and are connected to the corresponding pins of the USB-to-TTL Serial chip.

Pins 6, 8, 9, 12, 13, and 14 are used for Pulse Width Modulation (PWM). Each of the digital pins provide Pulse Width Modulation signal of 8-bit resolution. The PWM signal can be generated using analog Write (pin, value) function.

Pins 5 and 6 provide an external interrupt to other processor or controller when necessary. These pins can be used to enable interrupts INT0 and INT1 respectively by using the attachInterrupt

(pin, INT0) function. These pins can be used to trigger three types of interrupts such as interrupt on a low value, a rising or falling edge interrupt and a change in value interrupt.

Serial Peripheral Interface (SPI) Pins include pins 13, 14, 15, and 16. Serial Peripheral Interface pins are used when the data is not to be transmitted asynchronously. The pins support synchronous communication with SCK as the synchronizing clock. LED pin, pin 16, is being connected to the blinking LED on the board.

2.15.3 Arduino Nano Analog Pins

The analog pins are pins 18, 19, 20, 21, 22, 23, 24, 25, and 26. Arduino Nano has 8 analog inputs (19 to 26), marked A0 through A7. Each of the analog pins has an inbuilt analog digital converter (ADC) of resolution of 1024 bits. By default, the pins are measured from ground to 5 V. A reference voltage of 0 V to 3.3 V can be used, 3.3 V is connected to AREF pin (18^{th} Pin) by using the analogReference () function. Other functions of the analog pins are as follows:
I2C pins are pins 23, 24 as A4 and A5. I2C protocol is used for long distance communication. I2C supports multi master and multi slave with only two wires, one for clock (SCL) and another for data (SDA). Analog reference (AREF) pin 18 is used as a reference voltage for analog input for the ADC conversion. Reset Pin 28 is active LOW pin. If the pin value is made LOW i.e., 0V, it will reset the controller. It is usually connected with switches to use as reset button.

2.15.4 Arduino Nano ISCP

ICSP stands for In Circuit Serial Programming, which represents one of the several methods available for programming Arduino boards. Ordinarily, an Arduino bootloader program is used to program an Arduino board, but if the bootloader is missing or damaged, ICSP can be used

instead. ICSP can be used to restore a missing or damaged bootloader. Figure 2.22 shows the Arnuino nano ISCP.

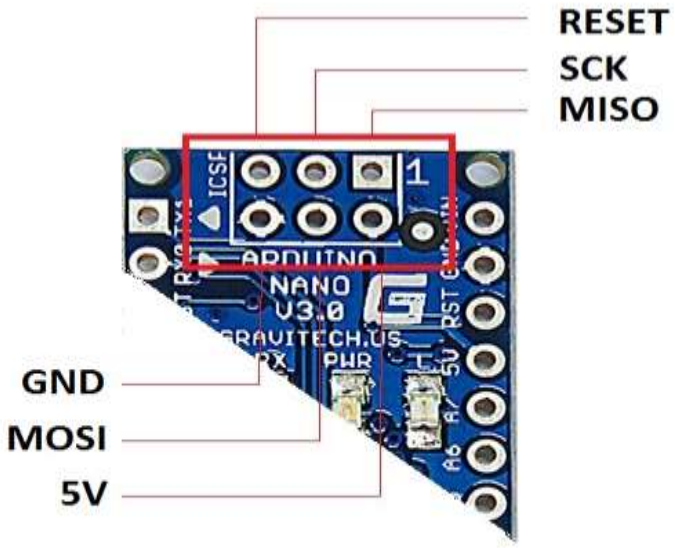

Figure 2.22 Arduino Nano ISCP

www.CircuitsToday.com

Each ICSP pin usually is cross-connected to another Arduino pin with the same name or function. For example, MISO on Nano's ICSP header is connected to MISO / digital pin 12 (Pin 15); MOSI on the ISCP header is connected to MOSI / digital pin 11 (Pin 16); and so forth (the table 2.4). MISO, MOSI, and SCK pins taken together make up most of an SPI interface. Reset pins in ICSP are pins 3, 28 and 5 while the power pins are pins 4, 17, 27, 28, 30 and 2 & 6. One Arduino can be used to program another Arduino using ICSP.

2.16 Gap in Literature

The literature review revealed that low or high humidity has adverse effect on the environment as a result of low or high condensation of water vapour on the environment. Some of these adverse effects include high corrosion and damage of equipment, discomfort and health hazard to human beings and animals, low rate of production and poor storage of crops in agriculture and drop in optimal performance and reliability of data from data centres or computer rooms in industries and institutions.

Literature showed that many researches have been carried out on humidity and its measurement using humidity sensors. It was discovered that the greatest challenge in humidity measurement, monitoring and control using relative humidity sensors especially electronic sensors is high condensation of moisture on the sensors during humidity measurement which results in the damage of the sensors. This challenge is more obvious in countries under the tropical savanna climates such as Nigeria with very high relative humidity values and high temperatures.

It is obvious from literature that high condensation of water vapour (moisture) on relative humidity sensors remains a great challenge in humidity measurement, monitoring and control. This is a serious gap in literature which this research tends to bridge by fabricating a capacitive relative humidity sensor that will be resistant to condensation (moisture). The capacitive relative humidity sensor will be able to measure relative humidity in the range of 5 % RH to 100 % RH with operating temperature of 5 ^{0}C to 100 ^{0}C and target accuracy of ± 1 %RH with little or no condensation effect.

CHAPTER THREE

MATERIALS AND METHODS

3.1 Materials and Equipment

The synthesis of Zinc Oxide (ZnO) Nanoparticles was carried out at NAMIROCH Laboratory Nig. Ltd., Plot 52B Oversea Quarters Extension, Kwali, Abuja using Zinc Acetate ($Zn(O_2CCH_3)_2(H_2O)_2$), Sodium Lauryl Sulphate (SLS) ($CH_3(CH_2)_{10}CH_2(OCH_2CH_2)_nOSO_3Na$) by Sigma Aldrich; Diethylene glycol (DEG) $(HOCH_2CH_2)_2O$, linear alkylbenzene sulphonate (LAS or LABS) ($C_{11}.6H_{24}.2)C_6H_4SO_3Na$), methanol ($CH_3OH$), propanol ($C_3H_8O$) by Kestrel and water.

The equipment used in the synthesis include magnetic stirrer hotplate (Pec Medicals USA 78-1), magnetic stirrer bar, temperature control system, electronic centrifuge, mantle heater, thermocouple, stopwatch, round bottom flask, crucible boat, electric oven and plastic container. The equipment used in characterization of the synthesized ZnO nanoparticles includes Raman Spectroscope (Model No. Pro Raman-L-785-BIS), Thermogravimetric Analysis (TGA) instrument (PerkinElmer), Multi-Point Brunauer Emmett Teller (BET) (Quantachrome Instrument Version 11.03), Malvern Instrument (Zetasizer Version 7.01) and stylus profilometer (Veeco, ektat 150, Vintage: 2010 software)

The materials used in design and fabrication of interdigitated electrodes (IDEs) and the nanostructured ZnO capacitive relative humidity sensor were computer aided design software (PROTEUS Design suite), propanol by Kestrel, hydrochloric acid, Ferric Chloride ($FeCl_2$),

Sodium Lauryl Sulphate (SLS) and acetone (CH_3CO) by Sigma Aldrich, photographic paper, immersion tinning agent with composition of Tin (II) Chloride, Thiourea, Benzene and HCl, distilled water, glass slide, printed circuit board (PCB), masking tape, solder, soldering iron electric wires, smooth sandpaper, nanostructured ZnO ink, H_2SO_4, sodium hydroxide (NaOH), 1kΩ resistor, power regulator, Arduino Nano ATmega 328 microcontroller, light emitting diode (LED) and DHT11 sensor. The equipment used includes ***hp*** Deskjet F2280 laser printer, laminating machine, air blower machine, and soldering iron, electronic centrifuge and temperature controlled hotplate, Hielscher's ultrasonic sonicator and petri dish.

The materials used for the calibration of the nanostructured ZnO capacitive relative humidity sensor include Arduino Nano ATmega 328 microcontroller operational circuit, Lithium Chloride (LiCl) with reference relative humidity of 11.30 %RH, Potassium Carbonate (K_2CO_3) with reference relative humidity of 43.16 %RH, Sodium Chloride (NaCl) by JHD Laboratory Reagents with reference relative humidity of 75.30 %RH, Potassium Chloride (KCl) by Fisher Scientific with reference relative humidity of 84.34 %RH, Potassium Sulphate (K_2SO_4) by Molychem with reference relative humidity of 97.3 %RH and distilled water. The equipment used include humidity chamber and laptop computer.

3.2 Solvothermal Synthesis of Zinc Oxide (ZnO) Nanoparticles

A round bottom flask was washed and dried using mantle heater connected to a temperature control system. A solution of 0.5 mol (which is 8.7 g) of SLS was made in 60 ml of diethylene glycol at a dissolution temperature of 120 ^{0}C on a magnetic stirrer hotplate. The mixture was stirred continuously using magnetic stirring bar until the SLS was completely dissolved in

diethylene glycol. 1.0 mol which is 13.2 g of $Zn(O_2CCH_3)_2(H_2O)_2$ was added to the solution and stirred continuously until it was completely dissolved in the solution. The mixture was heated on the mantle heater and the temperature was maintained at 190 ^{0}C for 1 hour with the temperature control system. Figure 3.1shows the set up for the synthesis of ZnO nanoparticles.

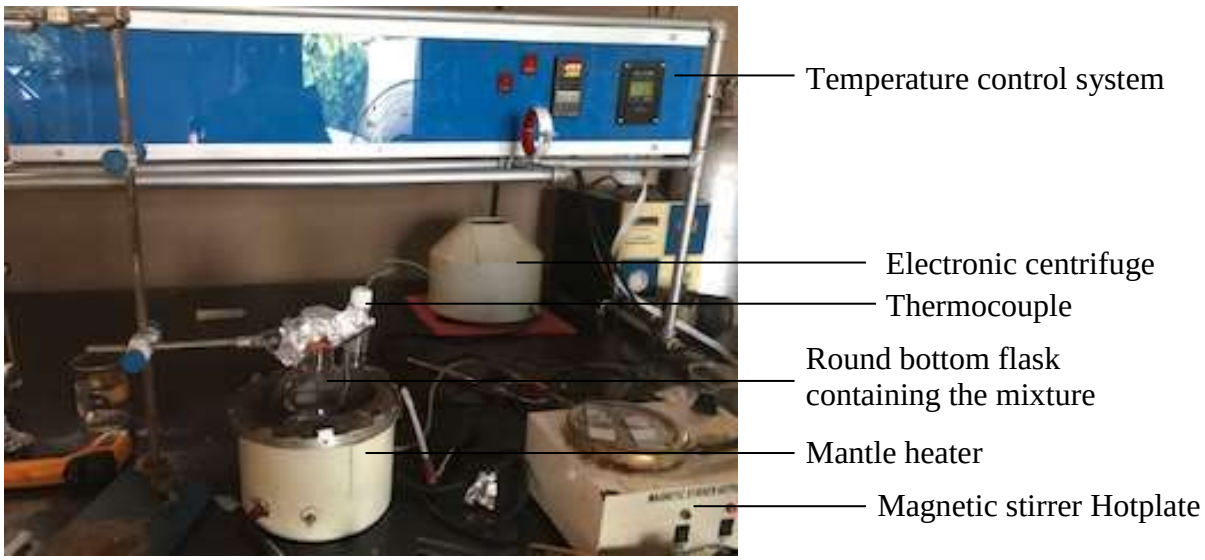

Figure 3.1 Set up for the synthesis of ZnO nanoparticles

The solvothermal synthesis of ZnO nanoparticles was completed at 190 ^{0}C. The product was centrifuged to separate the ZnO nanoparticles from the mixture using an electronic centrifuge. Methanol was used to wash excess ZnO nanoparticles that grew on the flask. Propanol was used for precipitation and segmentation of the ZnO nanoparticles. A milky liquid form of the ZnO nanoparticles was produced. Figure 3.2 shows the synthesized ZnO nanoparticles in a plastic container.

Figure 3.2 Synthesized ZnO nanoparticles

The product was transferred to a crucible boat and was dried in an electric oven at 60 ^{0}C for 12 hours. White powder of ZnO nanoparticles was obtained.

Zinc Oxide (ZnO) Nanoparticles were also synthesized with linear alkylbenzene sulphonate (LABS) as the capping agent using the same procedure of solvothermal technique.

3.3 Characterization of the ZnO nanoparticles

The synthesized ZnO nanoparticles with SLS and LABS were characterized at Federal University of Technology (FUT), Minna using the following characterization techniques: Raman Spectroscopy, Thermogravimetric Analysis (TGA), Brunauer–Emmett–Teller (BET) surface area analysis and particle-size distribution (PSD) analysis.

Raman Spectroscopy instrument was used to determine the molecular and crystal structures of the synthesized ZnO nanoparticles. PerkinElmer Thermal Analysis was used to determine the thermal stability, decomposition pathways, viscoelastic and phase changes. Quantachrome Instrument Version 11.03 was used for surface area analysis by Multi-Point BET. Malvern Instrument (Zetasizer Version 7.01) was use to study the synthesized nanoparticles in terms of size, size distribution by intensity, size distribution by volume and size quality.

The ZnO nanoparticles synthesized with SLS and LABS were compared based on their characterization results, that is, their crystalinity, thermal stability, decomposition pathways, viscoelastic properties, phase changes, surface area analysis, size, size distribution and size quality. The ZnO nanoparticles synthesized with LABS yielded better results and were used for the rest of the work.

3.4 Design and Fabrication of Interdigitated Electrodes (IDEs) for the Nanostructured ZnO Capacitive Humidity Sensor

The design and fabrication of IDEs involves giving the IDEs a pattern and transferring it on the PCB. These are shown in the following work.

3.4.1 Design of the Interdigitated Electrode

The method used in the design was the Generic interdigitated array model. The patterns were designed using a computer aided design program/software (PROTEUS Design Suite). The nine IDEs designed for the sensors are shown in Figure 3.3. The pattern or the design of the interdigitated electrodes (IDEs) gave the sensor its design. The same design was used to produce nine sensors of the same structure and geometrical parameters.

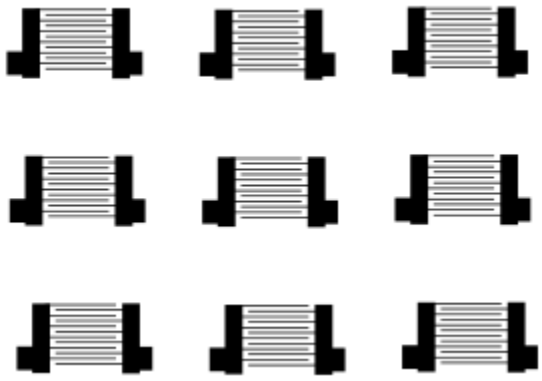

Figure 3.3 Nine IDEs designed for the sensors

Figure 3.4 represents the schematic of the interdigitated electrodes/sensor's structure and geometrical parameters. The two metallic electrodes form the interdigitated capacitive relative humidity sensor with a comb shape. Each finger of the electrodes has a width W (mm) and a length L (mm). The distance between two consecutive fingers is G (mm) and the total width of the IDEs is H (mm).

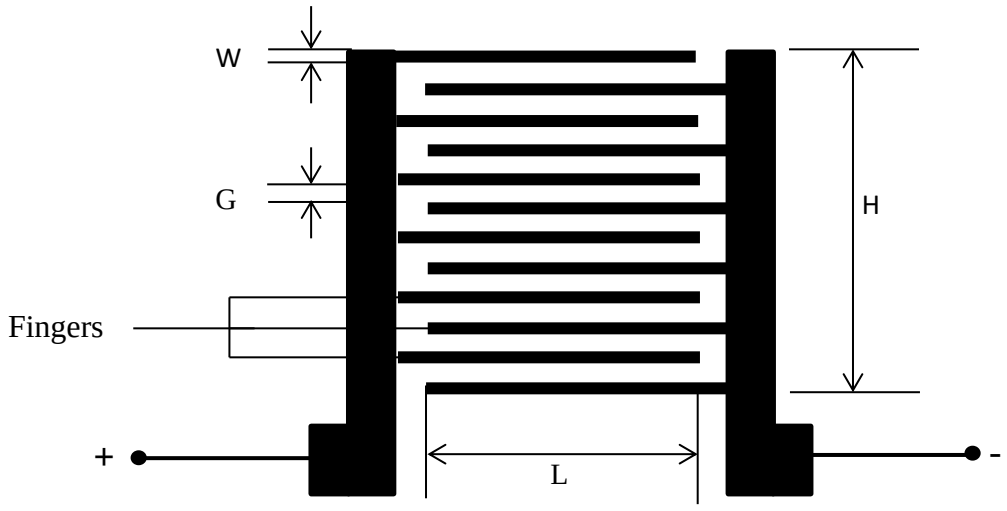

Figure 3.4 The schematic of the IDEs structure and its parameters

The parameters of IDEs designed for the study are as follows:

Number of fingers = 12

Width of a finger (W) = 0.2 mm

Length (x-direction) of a finger (L) = 8.536 mm

Length (y-direction) of the IDEs (H) = 8.536 mm

Spacing/gap between the fingers (G) = 0.5 mm

Area of the IDEs = L x H 3.1

= 8.536 x 8.536

= 72.8633 mm^2

The area covered by IDEs gives the area of the sensor.

The area of a finger = L x W 3.2

= 8.536 mm x 0.2 mm

= 1.7072 mm^2

The total area of the fingers = 12 x 1.7072 mm^2

= 20.4864 mm^2

The total sensing area (A) of the sensor = 11 (G X L). 3.3

= 11(8.536 x 0.5)

$= 46.948\ mm^2$

3.4.2 Transfer of the Interdigitated Electrodes on a printed circuit board (PCB)

The transfer of the designed IDEs on the PCB was achieved through the process of screen printing (digital printing). The following steps were taken.

1. **Screen printing (digital printing) of the designed IDEs on the PCB**

The surface of the PCB was cleaned with dilute HCl and rinsed with water. Propanol was used for final cleaning and drying. The set of nine interdigitated electrodes (IDEs) designed using computer aided design program/software (PROTEUS Design Suite) were printed with ***hp*** Deskjet F2280 laser printer on a photographic paper. The print out (the mask) was soaked in HCl acid water for 25 minutes. The photosensitive layer (photoresist) bearing the designed sensors was detached from the photographic paper. This was done for easy transfer of IDEs on the PCB. The IDEs were printed on the PCB using a laminating machine operated at a temperature of 200 °C.

2. **Etching of the IDEs**

The etching process was done using a mixture of ferric chloride ($FeCl_3$), small amount of HCl and water as the etchant. The Ferric chloride was used because it does not form bubbles or gas. It makes the process faster and preserves the features of the design. The PCB was immersed in the ferric chloride mixture for 20 minutes. This produced the design of IDEs on the PCB such that the IDEs were given a copper pattern, that is, the black design of photoresist was converted to copper. The etched interdigitated electrodes are shown in figure 3.5.

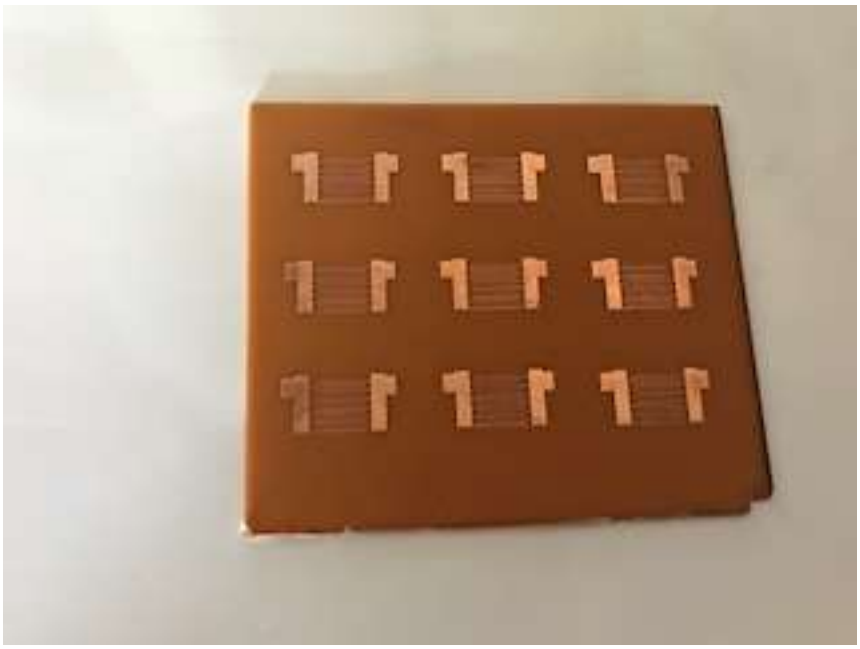

Figure 3.5 Etched interdigitated electrodes

The photoresist was removed using acetone $(CH_3)_2CO$). The sensors were washed with propanol and dried.

3. Tin coating of the electrodes

The process used for the coating of the electrodes was the displacement plating also known as electrochemical plating. Immersion tinning was used to coat the copper interdigitated electrodes (IDEs) with tin (Sn). The IDEs were immersed into the immersion tinning agent of composition 21 gl^{-1} of tin (II) chloride, 90 gl^{-1} of thiourea, 3 gl^{-1} of benzene disulfonic acid and 0.3 M of HCl. In the displacement plating process, as copper ions replace Sn ions in solution, Sn metal replaces copper metal on the surface. Hence, the electrodes were coated with tin (Figure 3.6). This was done to protect the IDEs from corrosion or oxidation and to give it a better contact and make soldering easier.

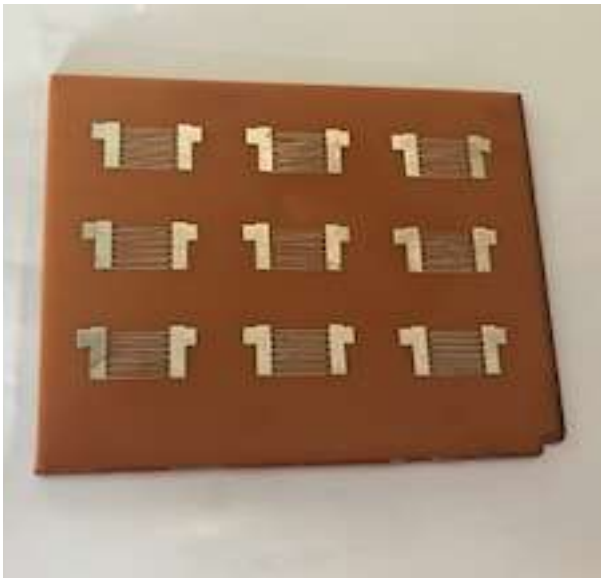

Figure 3.6 Tin coated interdigitated electrodes

The nine sensors on the PCB were separated using a cutting machine. 5 gm of sodium lauryl sulphate was dissolved in 100 ml of water and the solution was used to wash the sensors. The sensors were rinsed with distilled water. Propanol was used for the final rinsing to ensure the production of contamination free sensors. The sensors were blown dry using air blower machine. Figure 3.7 shows a magnified structure of the sensor after tinning.

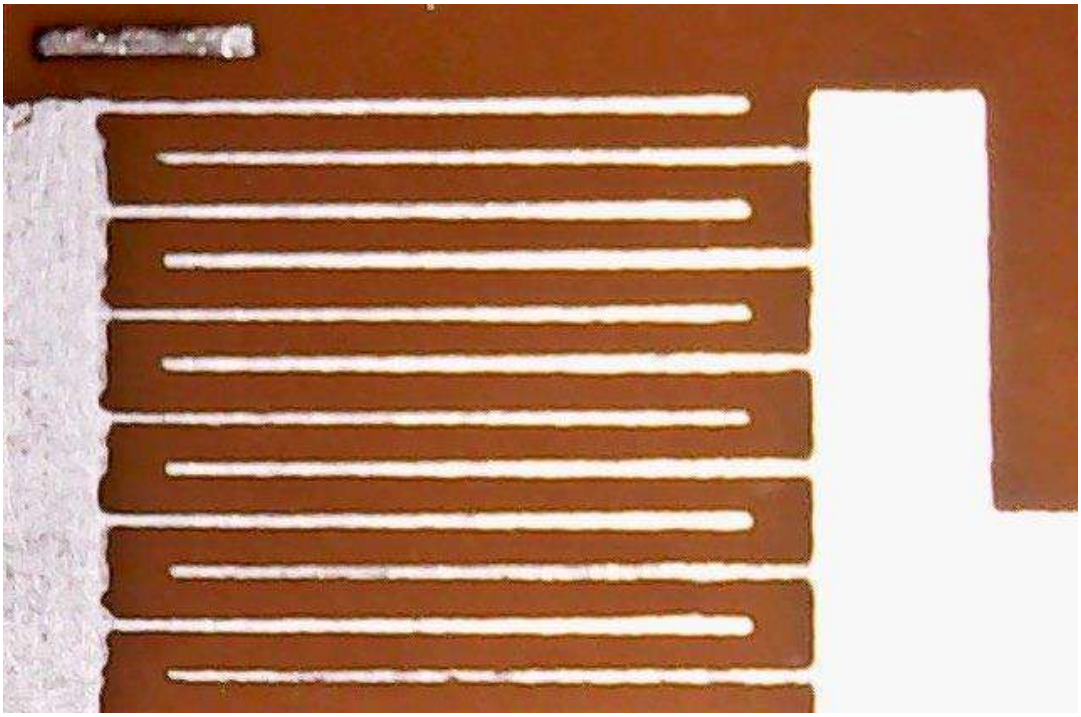

Figure 3.7 Interdigitated Electrode after Immersion Tinning

The ambient capacitance of the sensor was tested. The value of the capacitance with air as the dielectric was 0.51 μF.

3.5 Fabrication of the Nanostructured ZnO Capacitive Relative Humidity Sensor

The fabrication processes for the nanostructured ZnO capacitive relative humidity sensor are presented as follows:

3.5.1 Preparation of nanostructured ZnO ink

The nanostructured ZnO ink was produced by dissolving the powder of the synthesized ZnO nanoparticles in propanol. The agglomerate of the nanostructured ZnO ink was sonicated for 30

minutes using Hielscher's ultrasonic sonicator. The agglomerate of nanostructured ZnO ink was sonicated to ensure uniformly dispersed/deagglomerated ZnO nanoparticles and to obtain precise of ZnO nanoparticles.

3.5.2 Deposition of ZnO nanoparticles on IDEs

The terminals of the sensors were covered with masking tape to prevent spillage of the ZnO nanoparticles on the terminals during spin coating. Figure 3.8 shows some of the sensors in a petri dish with their terminals masked.

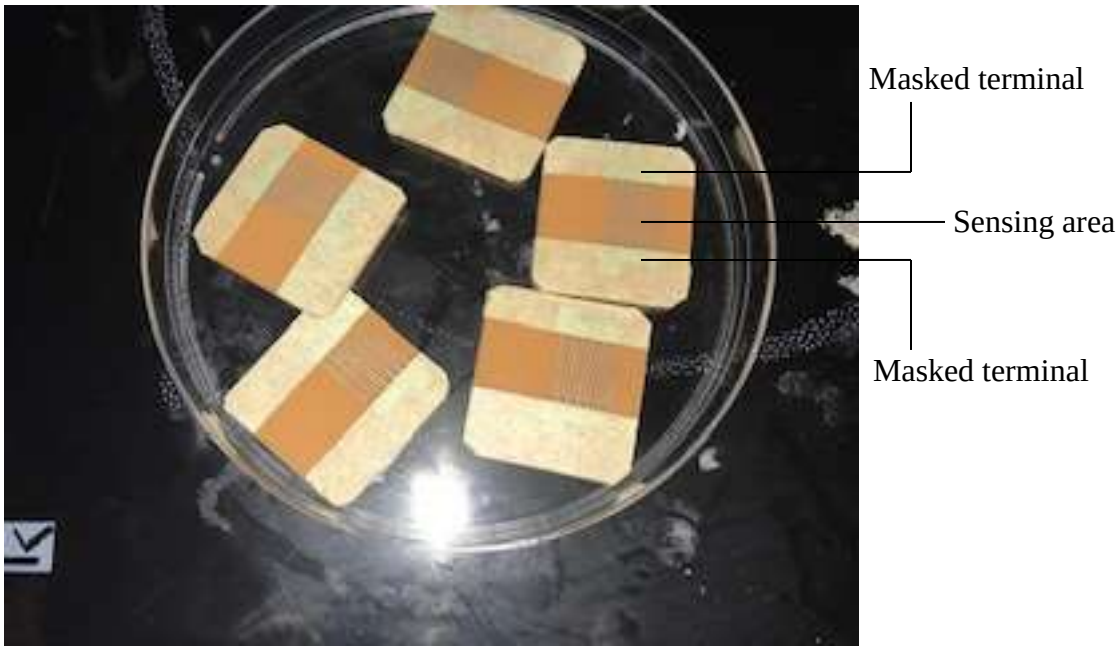

Figure 2.8 Some sensors with masked terminals

Spin coating technique was used for the deposition of the nanostructured ZnO ink on the sensors' IDEs. The spin coater used for the spin coating was set at the speed of 4000 RPM (revolutions per minute). An IDE was carefully put in the spin coater. A small puddle of the nanostructured

ZnO ink was deposited onto the centre of the IDE and spun by the centrifugal force for 20 seconds. Figure 3.9 shows the spinning of the sensor in the spin coater. The IDE was placed on a temperature controlled hot plate at 150 ^{0}C for 5 minutes to allow the nanostructured ZnO ink to solidify so that it does not dissolve during the deposition of another layer. The process of the spin coating was repeated four times to obtain five layers of nanostructured ZnO deposited on the IDE. The fabrication of the nanostructured ZnO capacitive relative humidity sensor is now completed. Figure 3.10 shows some of the nanostructured ZnO capacitive relative humidity sensors. The remaining eight IDEs were spin coated using the same processes already describe.

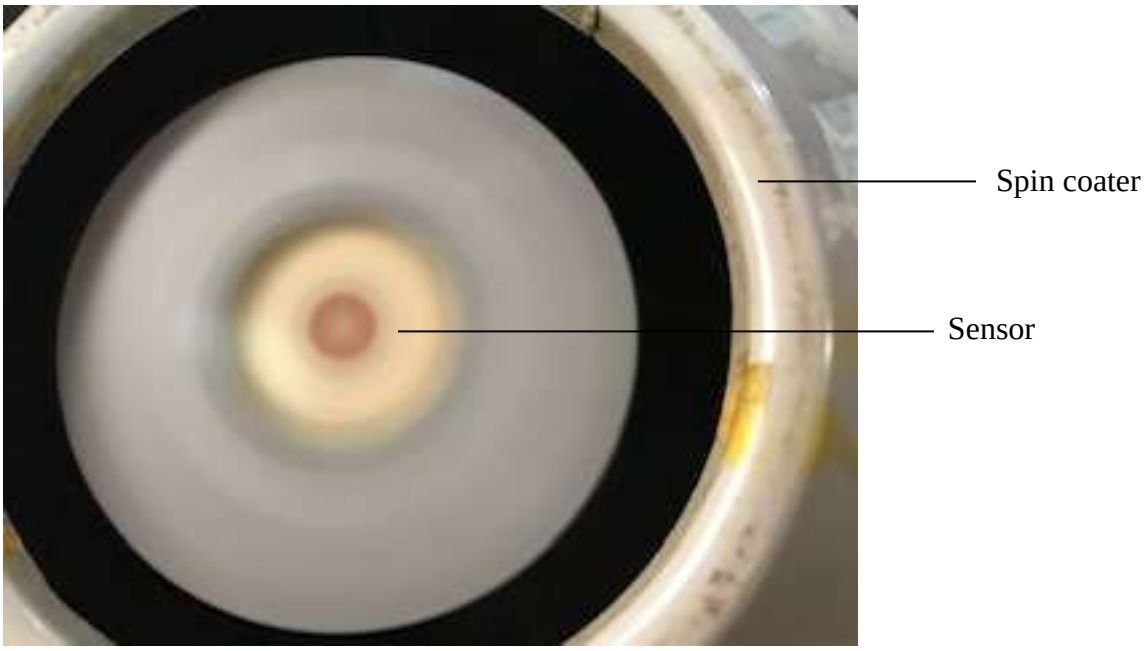

Figure 3.9 Spin coating of the sensor

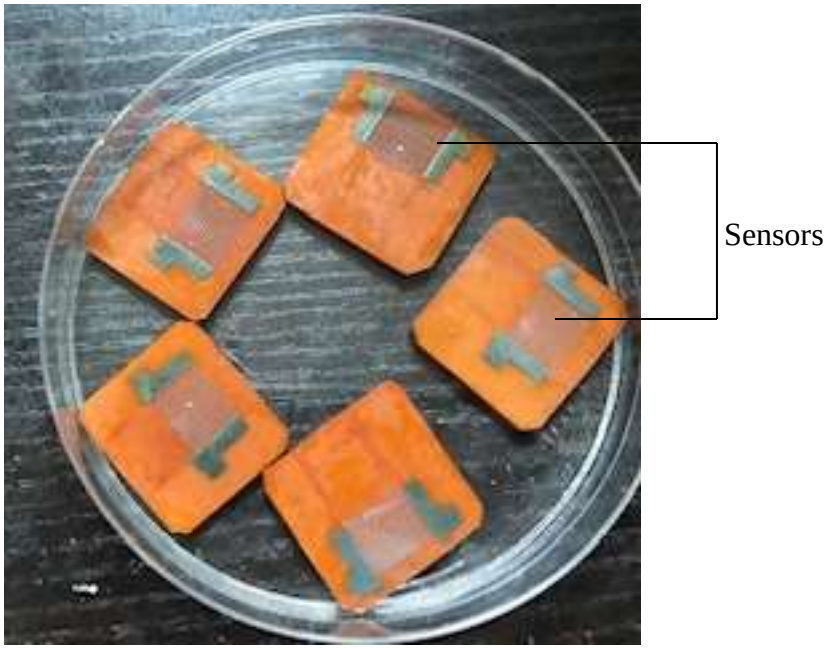

Figure 3.10 Some of the Nanostructured ZnO Capacitive Relative Humidity

3.5.3 Annealing of the sensors

Nine sensors were produced. In order to test the effect of annealing temperature on the performance of the sensor, one of the sensors was annealed by heating them on a temperature controlled hot plate at 150^0C for 30minutes. Another sensor was annealed at 200^0C for 30minutes while the rest were unannealed.

3.5.4 Soldering of Electric Wires on the Sensor Terminals

The oxide stain and impurities on the terminals of the sensors were removed using smooth sandpaper. Wires were soldered on the two terminals of the sensors. This will allow easy connection of the sensor in an electrical circuit. Figure 3.11 shows three sensors with wires

solder on their terminals. Figure 3.11a represents the unannealed sensor, Figure 3.11b represents the sensors annealed at 150 ^{0}C; and Figure 3.11c represents the sensors annealed at 200 ^{0}C.

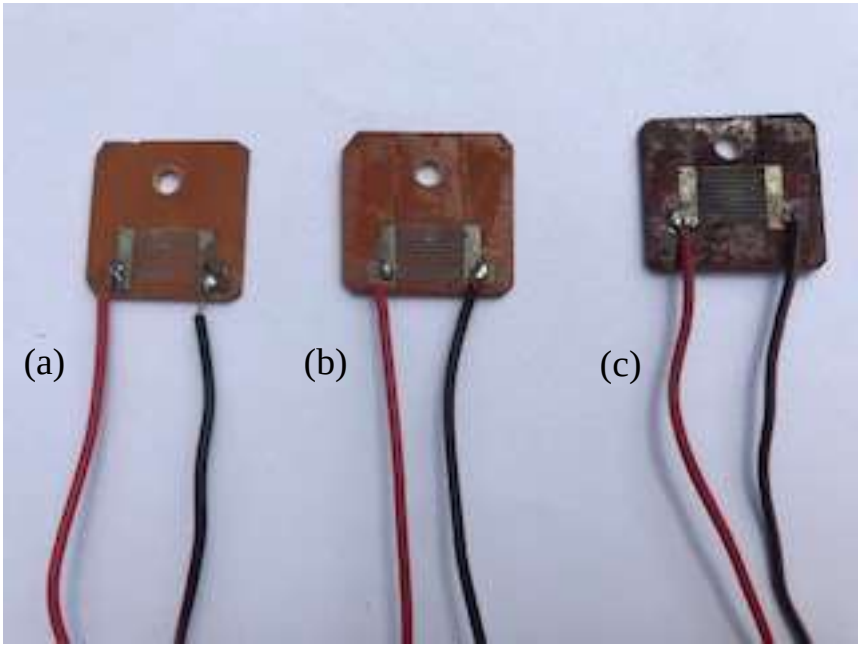

Figure 3.11 Sensors annealed at different temperatures and connected to their terminals

3.6 Programming of ARDUINO NANO ATMEGA 328 microcontroller

The ARDUINO NANO ATMEGA 328 microcontroller was programmed to process and measure the capacitance of the nanostructured ZnO capacitive relative humidity sensor, the resistance of the DHT11 resistive sensor and their corresponding humidity values after every second at a specified temperature of the environment. It was programmed to operate at 0 V and 5 V, where 0 V is the digital low (0) and 5 V is the digital high (1).

The nanostructured ZnO capacitive relative humidity sensor was connected to pin A_0 and pin A_2, which was connected to pin 5 V. Its operating voltage is 5 V. The DHT11 resistive sensor was connected to ARDINO Nano pin D_6 and 5 V and ground (GRD). Its operating voltage is 5 V.

The positive terminal of the LED was connected to 5 V pin and its negative terminal to 1 kΩ resistor, then to the GRD.

3.7 ARDUINO Nano ATmega 328 Microcontroller Operational Circuit Design

The electronic components used in designing the circuit include ARDUNO NANO ATMEGA 328 microcontroller with USB 2.0 – Serial, 1kΩ resistor, light emitting diode (LED) and a voltage regulator provided for external power supply when required. The provisions for connecting to the nanostructured ZnO capacitive relative humidity sensor and DHT11 resistive relative humidity sensor which was used as a control sensor were provided.

The ARDUNO NANO ATMEGA 328 microcontroller operational circuit design provides the top silk of the circuit (Figure 3.12), the bottom copper of the circuit (Figure 3.13), the combination of the top silk and the bottom copper of the circuit (Figure 3.14) and operational circuit (Figure 3.15).

Figure 3.12 Top silk of ARDUNO NANO ATMEGA 328 microcontroller operational circuit

Figure 3.13 Bottom copper of ARDUNO NANO ATMEGA 328 microcontroller operational circuit

Figure 3.14 Top silk and bottom copper combination of ARDUNO NANO ATMEGA 328 microcontroller operational circuit

Figure 3.15 ARDUNO NANO ATMEGA 328 microcontroller operational circuit diagram

3.7.1 Transfer of ARDUNO NANO ATMEGA 328 microcontroller operational circuit on PCB

The PCB of dimensions 9.8 cm x 6.0 cm was cleaned with dilute HCl and rinsed with water. Propanol was used for final cleaning and drying.

The bottom copper of the ARDUNO NANO ATMEGA 328 microcontroller operational circuit was printed on a photographic paper using a laser printer. The printout was soaked in a solution of 2 ml of H_2SO_4 and 200 ml of water (H_2O). The photosensitive part of the photographic paper was detached and the designed circuit was transferred on the PCB using a laminating machine operated at a temperature of 200 °C. A mixture of Ferric Chloride (F_eCl_3), small amount of HCl and water was used for the etching. The PCB was neutralized with 1 mole of N_aOH for 1 minute

and rinsed with water. The bottom copper was tinned using immersion tinning technique described in sub-section 3.5.2.

A drilling machine was used to drill the points marked on the PCB for connecting the nanostructured ZnO capacitive relative sensor, DHT11 resistive relative humidity sensor, Arduino nano pins, LED, 1 kΩ resistor and power regulator. The different components in the ARDUINO NANO ATMEGA328 microcontroller operational circuit were assembled and soldered on the PCB as shown in Figure 3.16.

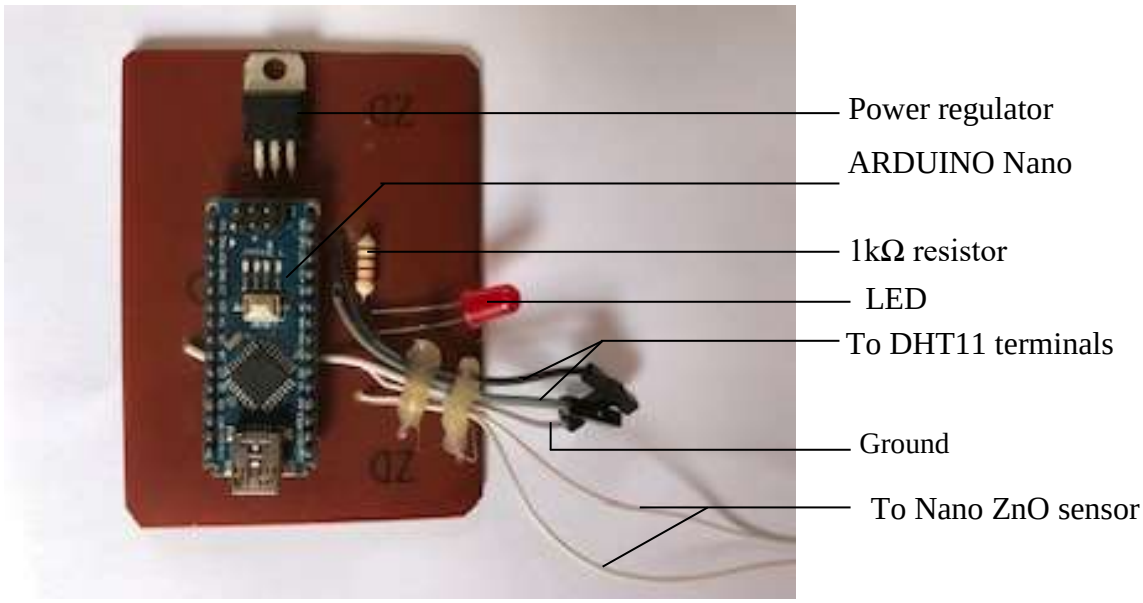

Figure 3.16: ARDUINO Nano microcontroller operational circuit

3.8 Calibration of the Nanostructured ZnO Capacitive Relative Humidity Sensor

The calibration of the nanostructed ZnO capacitive relative humidity sensor was based on the comparison of its humidity values with some reference standards of humidity values of saturated solutions of some salts. The calibration was done at room temperature of 27 ^{0}C to 30 ^{0}C under standard atmospheric pressure. The following salts were used for the calibration:

1. Lithium Chloride (LiCl) with reference relative humidity value of 11.30 %RH
2. Potassium Carbonate (K_2CO_3) with reference relative humidity value of 43.16 %RH
3. Sodium Chloride (NaCl) with reference relative humidity value of 75.3 %RH
4. Potassium Chloride (KCl) with reference relative humidity value of 84.34 %RH
5. Potassium Sulphate (K_2SO_4) with reference relative humidity value of 97.30 %RH

3.9.1 Humidity Chamber Micro Environment for Calibration of the Nanostructured ZnO Capacitive Relative Humidity Sensor

A humidity chamber was used to create a micro humidity environment. The humidity chamber was constructed using a cylindrical plastic container. The height or depth (h) of the chamber is 2.0 cm and the radius (r) is 4.3 cm. The sensors were fixed on the inside part of the cover of the humidity chamber as shown in figure 3.17.

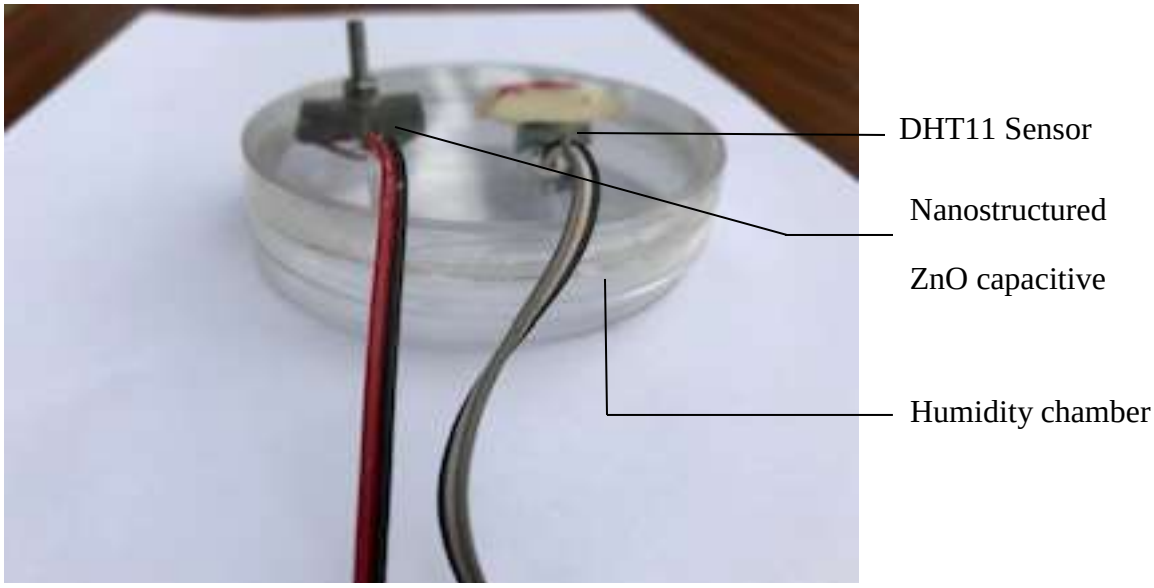

Figure 3.17: Humidity chamber with the sensors fixed on the cover

The volume (V) of the chamber was calculated using the formula,

$V = \pi r^2 h$ 3.4

$\Rightarrow V = \pi \times 4.3^2 \times 2.0$

$= 116.18\ cm^3$

3.8.2 Preparation of the Saturated Salt Solution for Calibraion of the Sensor

A saturated solution of Potassium Carbonate (K_2CO_3) was prepared in the humidity chamber to create a micro humidity environment needed for the calibration. The saturated solution was prepared using distilled water and 20.0 g of the Potassium Carbonate (K_2CO_3). Drops of distilled water were gradually added to the Potassium Carbonate (K_2CO_3) in humidity chamber. It was stirred very well after each addition of distilled water until it could absorb no more water and

excess liquid settles on the saturated salt solution (Figure 3.18). The excess liquid is kept to a minimum in order to get best results.

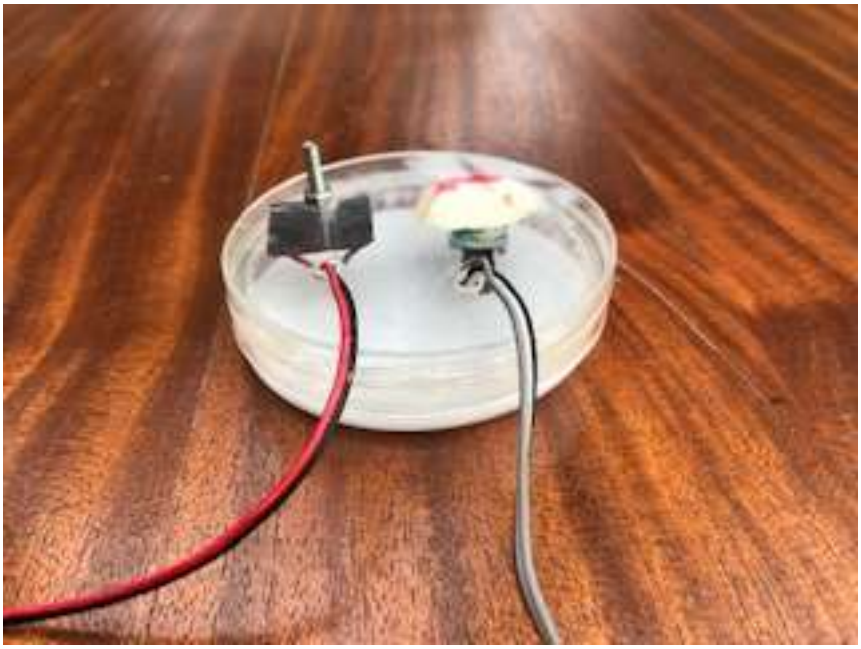

Figure 3.18 Humidity chamber containing saturated solution of K_2CO_3 and the sensors

The humidity chamber was closed and kept for six hours for temperature stabilization. The same preparation process was used in preparing the saturated solutions of Lithium Chloride (LiCl), Sodium Chloride (NaCl), Potassium Chloride (KCl) and Potassium Sulphate (K_2SO_4).

3.8.3 The Sensor System used for Collection of Data

The sensor system used for the calibration comprised the humidity chamber containing the nanostructured ZnO capacitive relative humidity sensor, DHT11 resistive relative humidity sensor and saturated solution of Potassium Carbonate (K_2CO_3); the ARDUINO NANO ATMEGA 328 microcontroller operational circuit; a lap top computer and a reliable power supply. These components or units of the sensor system were connected as shown in figure 3.19.

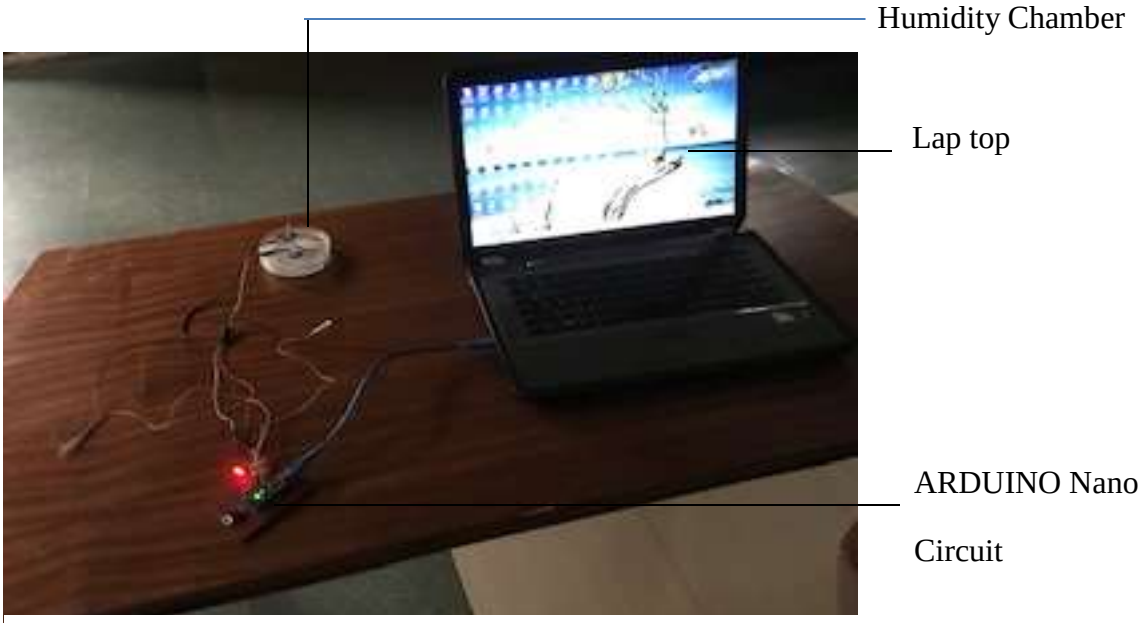

Figure 3.19 The humidity sensor system

When the system was switched on, the signal (moisture) from the micro humidity environment was adsorbed by the nanostructured ZnO capacitive relative humidity sensor and the DHT11 relative humidity sensor. The signal from each of the sensors was sent to the ARDUINO Nano ATMEGA 328 microcontroller. The signal from the sensors were processed by the microcontroller and displayed on the computer. The computer displayed the relative humidity values of the micro humidity environment and the corresponding capacitance values measured by the nanostructured ZnO capacitive relative humidity sensor, the temperature measured by the DHT11 sensor and the time for variations in RH and capacitance. The system was left on until the two sensors attained their constant values which were the observed values (OBS) of the sensors. The data displayed on the computer were stored and used for further analysis (see appendix E).

The same system was used to collect data from each micro humidity environment from the saturated solutions of lithium chloride (LiCl), sodium chloride (NaCl), potassium chloride (KCl) and potassium sulphate (K_2SO_4). The data collected from the different micro humidity environments were used to the nanostructured ZnO capacitive relative humidity sensors and to determine the effect of annealing temperature on the nanostructured ZnO capacitive relative humidity sensors.

3.8.4 The effect of the annealing temperatures on the accuracy/performance of the nanostructured ZnO capacitive relative humidity sensor

The root mean square error (RMSE) was used to characterize the sensors' accuracies. The accuracies of the unannealed sensor and sensors annealed at 150 ^{0}C and 200 ^{0}C were evaluated using each of the micro humidity environments. The error and the root mean square error (RMSE) or root mean square deviation (RMSD) in measurements of the relative humidity by the sensors were determined. The error was calculated by finding the difference between the observed values (OBS) and the standard values (relative humidity values of the saturated salts). The RMSE was calculated using equation 2.14. A RMSE of less than 1 % implies a high accuracy of the sensor. Thus, if the RMSE of the sensor is low, the accuracy of the sensor is high and vice versa. In a situation where by the RMSE was high, the sensor had to be calibrated. The same method was used to evaluate the performance of the sensors annealed at 150 ^{0}C and 200 ^{0}C.

3.8.5 Calibration of the Nanostructured ZnO Capacitive Relative Humidity Sensor

The calibration of the nanostructured ZnO capacitive relative humidity sensor was done using linear regression. The linear regression was performed to determine the linearity of the relationship between the variations in relative humidity measured by DHT11 and the variations in capacitance measured by nanostructured ZnO capacitive RH sensor. In situations of low linearity, a function that relates the ideal RH value (from the standards RH values) to the observed value from the nanostructured ZnO capacitive RH sensor readings was determine. This function was determined based on the fact that in linear regression the dependent variable is directly proportionality to the independent variable. In this research, the capacitance measured by the nanostructured ZnO capacitive RH sensor depends on the relative humidity measured by DHT11. Thus, the relationship between the reference RH values (I) of the saturated salt solutions and the corresponding capacitance value (C_I) was obtained using a simple linear equation:

$$C_I \propto I$$

$$\Rightarrow C_I = SI \qquad 3.5$$

where S is the constant of proportionality. Equation 3.5 was used to calibrate the nanostructured ZnO capacitive RH sensor to obtain 100 % linearity of its output. The calibration was done in order to eliminate the RMSE.

3.8.6 Characterization of the Nanostructured ZnO Capacitive Relative Humidity Sensor

The micro humidity environment of potassium nitrate was used for the characterization of the sensor. It was used because it produces the highest humidity level.

1. **Accuracy of the Sensor**

The accuracy of the sensor was determined using the root mean square error (RMSE).

2. **Response and Recovery Times**

The sensor was in turn taken from a humidity environment filled with air and fixed inside each of the micro humidity environments and connected in the sensor system. The system was switched on and the time (response time) it took the sensor to attain the required RH level was determined. The sensor was then removed and returned inside humidity environment filled with air. The time (recovery time) it took the sensor to attain the RH level of the environment was determined.

In each case, a graph of capacitance against time was plotted to show the response and recovery times for the RH range. The maximum and minimum values of the capacitance were used to calculate the sensitivity and range of the sensor.

3. **The Sensitivity of the Sensor**

The sensitivity (S) of the sensor was calculated using the equation below (Hengchang *et al*., 3013):

$$S = \frac{C_H - C_L}{RH_H - RH_L} \qquad 3.6$$

where S is the sensitivity of the sensor to relative humidity variation, RH_H and RH_L are the highest and lowest RH values in the variation range (Hengchang *et a*l., 2013).

.

4. **Range of the sensor**

The range of the sensor was obtained by finding the difference between the maximum and minimum capacitance values measured by the sensor or the difference between their corresponding humidity levels.

CHAPTER FOUR

RESULTS AND DISCUSSIONS

The characterization results from Raman Spectroscopy, Thermogravimetric Analysis (TGA), Brunauer–Emmett–Teller (BET) surface area analysis and particle-size distribution (PSD) analysis were discussed as follows:

4.1 Raman Spectroscopy

Raman spectroscopy examined the ZnO nanoparticles by scattering a high intensity laser light in which few photons interacted with the molecules of the ZnO nanoparticles in their vibrational states emitting light of slightly different wavelengths. The laser light with Raman excitation wavelength of 785 nm was used for the inelastic scattering of the molecules of the ZnO nanoparticles samples at room temperature. The scattered light occurred at wavelengths that were shifted (Raman shifts or wavenumbers) from the incident light by the energies of the molecular vibrations.

4.1.1 Raman Spectroscopy of ZnO Nanoparticles Produced with Sodium Lauryl Sulphate (SLS).

The sample of ZnO nanoparticles produced with SLS was analyzed using Raman spectroscopy. Figure 4.1 shows the Raman spectrum of ZnO nanoparticles produced with SLS. The Raman peaks prominently present in the Raman spectrum were observed at 408 cm^{-1}, 426 cm^{-1}, 854 cm^{-1}, 874 cm^{-1} and 2878 cm^{-1}. In this work, the observed Raman shift or peak of 408cm^{-1} and 426 cm^{-1} fall within the region of the functional group (vibration) of 150 cm^{-1} to 450 cm^{-1} for metal (zinc) oxides (HORIBA, 2019).

Figure 4.1 Raman spectrum of ZnO nanoparticles produced with SLS.

The main peak E_2(high) at 426 cm^{-1} has strong and sharp Raman band with the highest intensity which indicates a high concentration of ZnO nanoparticles. E_2(low) was 408 cm^{-1}). The E_2(high) mode obtained is in agreement with E_2(high) zinc phonon mode between 370 cm^{-1} and 440 cm^{-1} (Schumm, 2008). In Raman spectroscopy, the E_2 mode is nonpolar with two modes, namely a high-frequency E_2(high) and low-frequency E_2 (low) modes, which are the characteristic of wurtzite-structured ZnO (Khan, 2014). Hence, the Raman prominent peak observed at 426 cm^{-1} is a characteristic peak of the Raman active dominant E_2(high) mode of Wurtzite ZnO with red shift of 11 cm^{-1}. The E_2(high) peak for the synthesized ZnO nanoparticles was within wurtzite hexagonal phase with good crystallinity though the value was shifted from the theoretical Raman vibrational frequency for bulk ZnO nanoparticles wurzite crystal structure for E_2(high) symmetry of 437 cm^{-1} (Dakhlaoui *et al.*, 2009 & Khan, 2010). Basically red shift means that frequency of phonons interacting with the incident photon decreased due to the improved crystallinity of the material (Pooder, 2018). The result differed from the Raman peaks at 434 cm^{-1} and 432 $cm^{-1}$for

ZnO nanoparticles synthesized at room temperature and 100 ^{0}C respectively (Isah *et al*., 2016) and Raman shift at nearly 435 cm^{-1} for wurtzite structure of zinc oxide nanorods (Bhunia *et al.*, 2016). The red shift can also be attributed to either phonon confinement within the nanocrystal boundaries or the localization of phonons due to defects in ZnO nanoparticles samples (Taziwa *et al.*, 2017) or high excitation wavelength of the laser light. The observable bands situated at 854 cm^{-1} and 874 cm^{-1} assigned to O–O stretching vibration mode from intermolecular bonding of oxygen in acetate salt which is associated to O–O stretching vibration mode of oxygen in zinc acetate salt (Tapan *et al*., 2001). It can also be as a result of weaker bands which correspond to C-H vibration of the aromatic ring. The peak at 2878 cm^{-1} is a strong and sharp band with high intensity which could be associated with the C-H stretching vibrations. This is consistent with bands 2970 to 2850 cm^{-1}, 2990 cm^{-1} and 2420 cm^{-1} corresponding to C–H stretching vibration mode of methyl groups (Phoohinkong *et al*., 2017). The C-H stretching mode obtained is also in agreement with C-H stretching modes between about 2800 cm^{-1} and 3100 cm^{-1} (Schumm, 2008).

4.1.2 Raman Spectroscopy of ZnO Nanoparticles (NPs) Produced with linear alkylbenzene sulphonate (LAS or LABS)

The ZnO nanoparticles sample produced with LABS was analyzed using Raman spectroscopy. Figure 4.2 shows the Raman spectrum of ZnO nanoparticles with LABS. The Raman shift or peaks observed in the spectrum also fall within three functional groups or vibrations.

Figure 4.2 Raman spectrum of ZnO nanoparticles produced with LABS.

The bands at 408 cm^{-1} and 424 cm^{-1} fall within the functional group of metal oxide (150 cm^{-1} and 450 cm^{-1}). This shows the sample contained ZnO with wurtzite (hexagonal) crystal structure, which is the stable structure of ZnO. The peak at 424cm^{-1} has the intensity of 1400 a.u which indicates the highest concentration of ZnO nanoparticles present in the sample. The bands at 854 cm^{-1} and 874 cm^{-1} fall within the functional group of O-O stretching vibration mode of oxygen present in zinc acetate salt. The observed peak at 2878 cm^{-1} corresponds to C–H stretching vibration mode which can be associated with the presence of propanol in the sample. This suggests the presence of impurity in the ZnO nanoparticles produced.

4.1.3 Comparison of the Raman active modes of the ZnO nanoparticles synthesized with SLS and LABS with the theoretical and experimental results

Tables 4.3 compared results of the analysis based on the theoretical and experimental results of Raman active modes of ZnO NPs.

Table 4.1 A comparison of the Raman active modes of the ZnO nanoparticles synthesized with SLS and LABS with the experimental results of Dakhlaoui *et al.*, 2009 & Khan, 2010

Symmetry	**Peaks (cm^{-1}) (Dakhlaoui et al, 2009 &Khan, 2010)**	**ZnO NPs SLS**		**ZnO NPs LABS**	
		Peak (cm^{-1})	**Shift (cm^{-1})**	**Peak (cm^{-1})**	**Shift (cm^{-1})**
E_1(TO)	407	408	+1	408	+1
E_2(High)	437	426	-11	424	-13

In Table 4.1, the Raman vibrational frequency for bulk ZnO NPs wurzite crystal structure for E_2 high symmetry is 437 cm^{-1} (Dakhlaoui *et al.*, 2009 & Khan, 2010). The E_2(High) peaks for the synthesized ZnO NPs with SLS and LABS were 426 cm^{-1} and 424 cm^{-1} respectively and were within wurtzite hexagonal phase with good crystallinity though the values were shifted from the theoretical value. The E_2(High) peaks were red shifted by 11 cm^{-1} and 13 cm^{-1} for ZnO NPs with SLS and LABS respectively. The redshift indicated that the scattered light shifted towards the lower frequencies or towards the red end of the electromagnetic spectrum. The red-shifts were observed due to the improved crystallinity of the material (Podder, 2018). The E_1(TO) peaks was 408 cm^{-1} for both ZnO NPs with SLS and LABS which was blue shifted by +1 cm^{-1}. The blueshift indicated that the scattered light shifted towards the higher frequencies or towards the blue end of the electromagnetic spectrum.

In comparison with experimental bulk ZnO NPs in Table 4.2 (Khan, 2010) , E_2(High) peaks are red shifted by 10 cm^{-1} and 12 cm^{-1} for ZnO NPs with SLS and LABS respectively. It was also observed that E_1(TO) are blue shifted by 1 $cm^{-1}$for both ZnO NPs with SLS and LABS when compared with theoretical values and are both red shifted by 2 cm^{-1} when compared with the experimental values.

Table 4.2 Raman spectra of ZnO nanoparticles synthesized with SLS and LABS compared with the experimental bulk ZnO.

Symmetry	**Peak (cm^{-1}) (Khan, 2010)**	**ZnO NPs SLS**		**ZnO NPs LABS**	
		Peak (cm^{-1})	**Shift (cm^{-1})**	**Peak (cm^{-1})**	**Shift (cm^{-1})**
E_1(TO)	410	408	-2	408	-2
E_2(High)	436	426	-10	424	-12

The different shifts can be attributed to either phonon confinement within the nanocrystal boundaries or the localization of phonons due to defects in ZnO nanoparticles samples (Taziwa *et al.*, 2017).

The results of the analysis when compared on the basis of fingerprint regions and functional group/vibrations within the Raman region of 150 to 450 cm^{-1} for metal oxides were consistent with the Raman shift at 434 cm^{-1} and 432 $cm^{-1}$for ZnO nanoparticles synthesized at room temperature and 100 ^{0}C respectively by Isah *et al*. (2016) in their study of the effect of metallic Zn film substrate temperature on the optical, morphological and structural properties of thermally oxidized Zn films, Raman shift at nearly 435 cm^{-1} for wurtzite structure of zinc oxide nanorods (Bhunia *et al.*, 2016), Raman shift at 438.63 cm^{-1} for Wurtzite ZnO crystal structure for doped ZnO sample and Raman shift at 432 cm^{-1} belonging to Wurtzite ZnO structure for carbon modified ZnO sample (Taziwa *et al.*, 2017).

4.2 Brunauer-Emmett-Teller (BET) surface area analysis

The single point BET surface area (specific surface area), the multipoint BET surface area (total surface area, S_{BET}), Barret-Joyner-Halenda (BJH) pore volume and pore diameter of the synthesized ZnO nanoparticles were determined by nitrogen (N_2) adsorption at 77.350 K. The

molecular weight of N_2 adsorbate used was 28.013g/mol with cross-section of 16.2 $Å^2 mol^{-1}$ and liquid density of 0.080 g/cm^3.

4.2.1 BET Surface Area Analysis of ZnO Nanoparticles Produced with SLS

BET surface area analysis was used to determine the specific surface area and multipoint BET surface area of dry powders of ZnO nanoparticles synthesized using SLS.

The specific surface area of the sample from the single-point BET plot and the multipoint BET equation was 220.9 m^2/g. Figure 4.3 shows the multipoint BET plots of the ZnO nanoparticles sample produced with SLS. It was observed that the graph in Figure 4.3 is a linear graph and has five data points in the $\frac{P}{P_0}$ range of 0.0466 to 0.2967. The multipoint BET analysis showed that the graph has a positive slope of 10.600, positive intercept of 1.650, positive correlation coefficient of 0.9905 and a positive constant of 7.423. The positive values indicated that the graph is a graph of the BET equation and can successfully be used to determine the surface area of the ZnO nanoparticles sample.

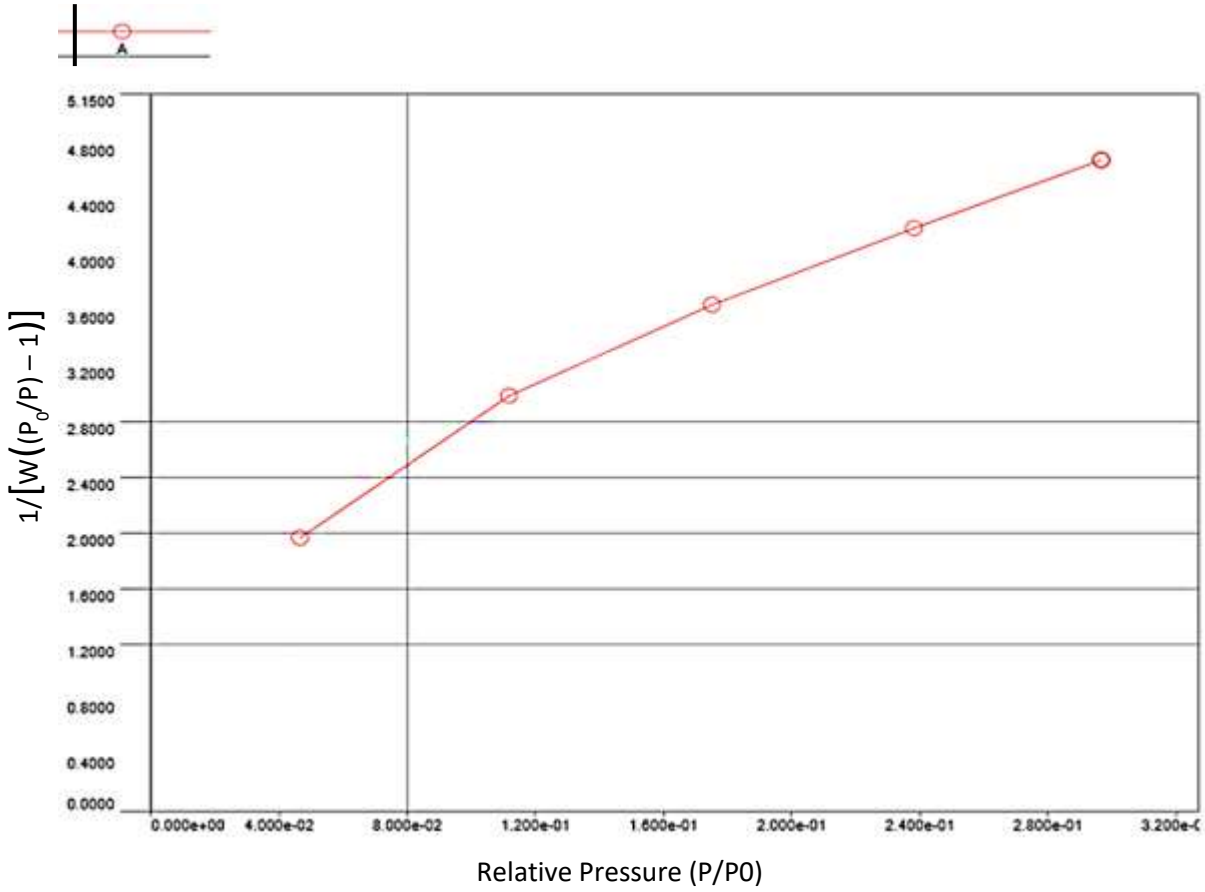

Figure 4.3 the multipoint BET plots of ZnO nanoparticles with SLS

The multipoint BET surface area of the ZnO nanoparticles of the sample was 284.286 m^2/g. It was also observed that monolayer started to form just after the knee while multilayers were formed as the pressure reached a medium value. The graph does not show capillary condensation at higher pressures which indicated that ZnO is not affected by condensation.

The N_2 adsorption isotherm of ZnO nanoparticles with SLS is shown in Figure 4.4. The isotherm displayed the type IV isotherm which was attributed to the predominance of mesopores in the sample which provided the sensor with high area structures with a very precise shape.

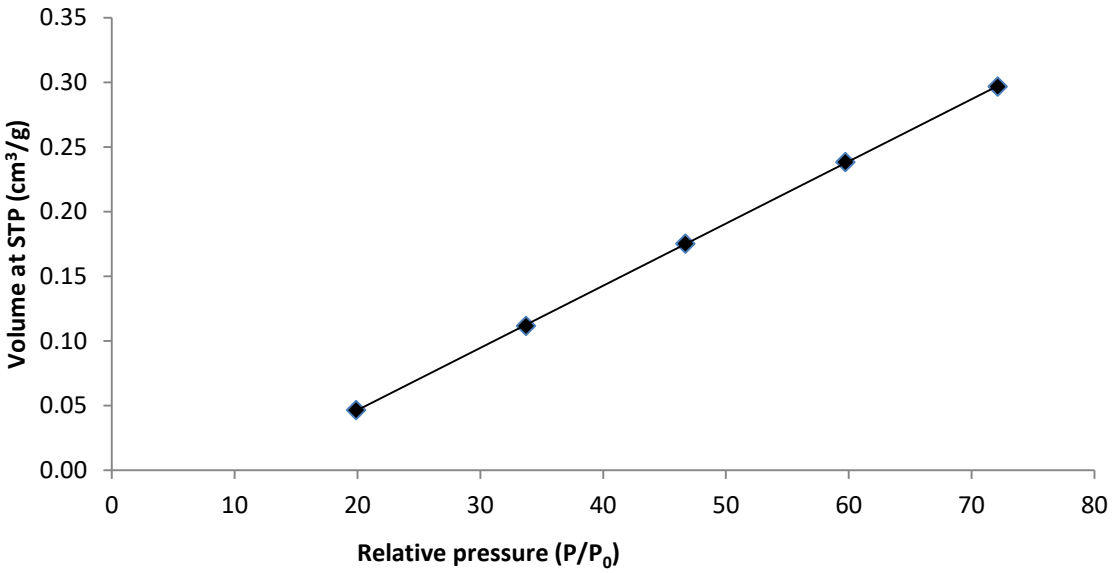

Figure 4.4 N_2 adsorbtion isotherm of ZnO nanoparticles with SLS

The isotherm showed that the mesopores were filled with the gas at extremely low pressure. The analysis equally revealed that the BJH adsorption pore diameter of the sample was 2.411 nm which fell within the IUPAC range of 2 nm to 50 nm for mesopores. The BJH cumulative adsorption volume of the ZnO nanoparticles sample was 0.181 cm^3/g which showed good porosity.

4.2.2 BET Surface Area Analysis of ZnO Nanoparticles Produced with LABS

Figure 4.5 shows the multipoint BET plots of ZnO nanoparticles with LABS. The graph in Figure 4.5 is linear with five data points in the $\frac{P}{P_0}$ range of 0.0485 to 0.3011. The BET analysis indicates that the graph has a positive slope of 10.494, positive intercept of 1.681, positive correlation coefficient of 0.9918 and a positive constant of 7.183.

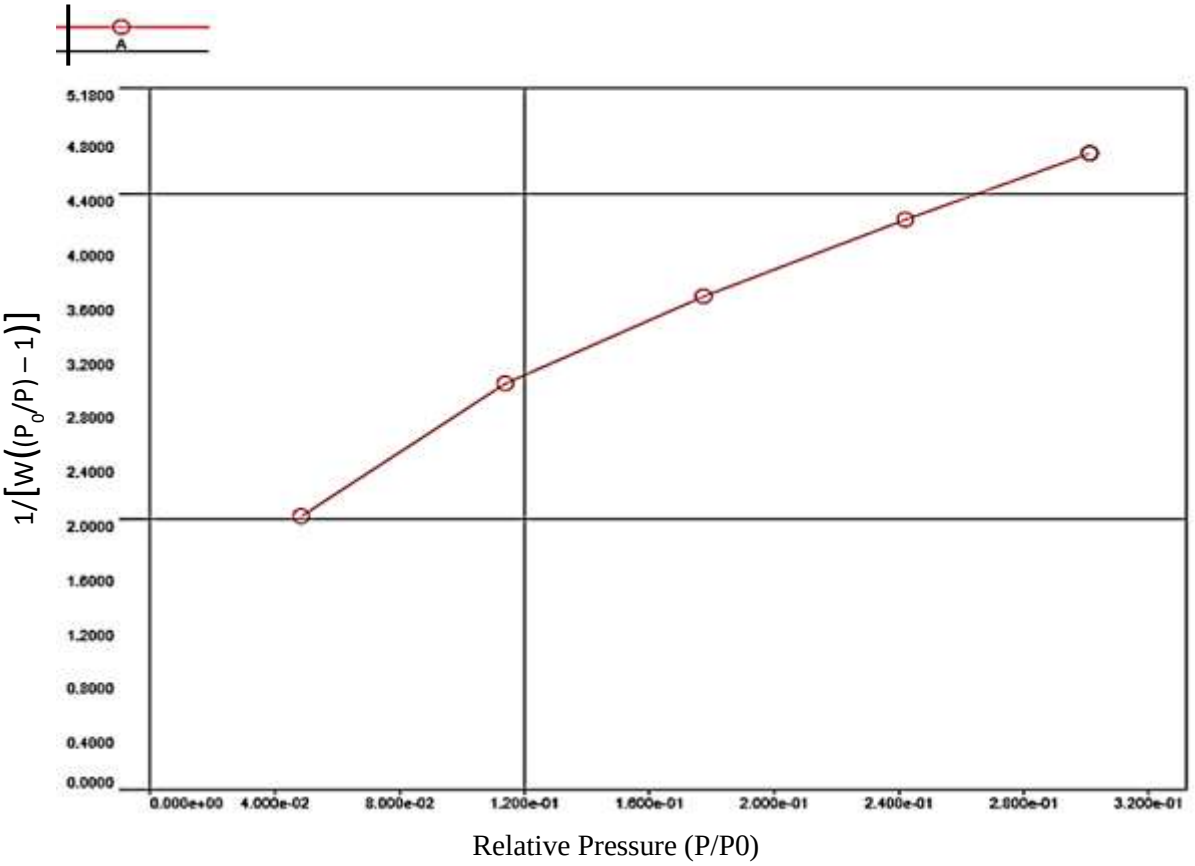

Figure 4.5 The multipoint BET plots of ZnO nanoparticles with LABS

The specific surface area of the sample was 223.0 m^2/g. Thus, the graph can successfully be used to determine the surface area of the ZnO nanoparticles in the sample. The multipoint BET surface area of the sample was 288.421 m^2/g. It equally had good porosity with BJH cumulative adsorption volume of 0.184 cm^3/g and BJH adsorption pore diameter of 2.433 nm. The sample exhibited mesopores characteristic structure. Figure 4.6 shows the N_2 adsorption isotherm of the ZnO nanoparticles produced with LABS. The isotherm is type IV isotherm which confirmed the mesopores structure of the ZnO nanoparticles sample.

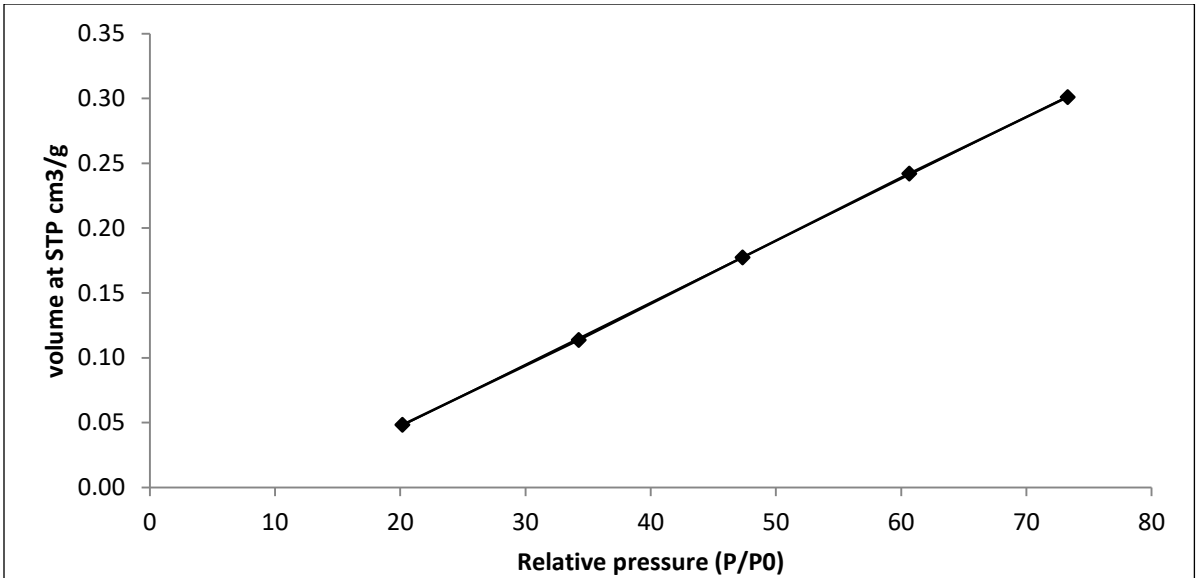

Figure 4.6 N2 adsorption isotherm for ZnO nanoparticles with LABS

In comparison with the results from other researches, Ramin *et al.* (2018) in their investigation on the enhanced anti-bacterial activities of ZnO nanoparticles and ZnO/CuO nanocomposites synthesized using *Vaccinium arctostaphylos* L. fruit extract discovered that ZnO nanoparticles powder in water had specific surface area of 29.3 m^2/g with mean pore diameter of 27.0 nm and total pore volume of 0.1981 cm^3/g. Their BET results revealed that the samples showed typical IV isotherms, indicating they had mesopores structure as obtained in this research. The surface area, the pore diameter and the pore volume differ appreciably from the values obtained in this research because different synthesis technique was used. Ismail *et al.* (2018) studied the BET analysis of ZnO nanoparticles annealed at different temperature and observed a reduction in the surface area of ZnO samples from 25.3641 to 8.7781 m^2/g and pore volume from 0.3536 to 0.0270 cm^3/g as the temperature was increased from 275 to 600 °C. The surface areas and the pore volumes are much smaller than 284.286 m^2/g and 288.421 m^2/g surface areas and pore volumes of 0.181 cm^3/g and 0.184 cm^3/g obtained in this research. The disparity could be

attributed to the annealing of the ZnO nanoparticles that might have resulted in the collapse of the pores and agglomeration of the nanoparticles. In agreement with the findings of this research, however their BJH average of pores diameter were less than 50 nm, which coincided with type IV isotherm and was consistent with mesoporous material characteristics. Mohammad *et al.* (2018) also observed type IV isotherm from BET analysis of ZnO nanoparticles. They observed BET mean particle size of ZnO nanoparticles of 9.7 nm and the specific surface area of 101.32 m^2/g. The surface area of the particles and the pore volume obtained by Herrera-Rivera *et al.* (2017) in their BET analysis of ZnO nanopowders were $19.1\ m^2g^{-1}$ and $0.025\ m^3g^{-1}$ for ZnO nanorods and 18.2 m^2g^{-1} and 0.022 m^3g^{-1} for ZnO flowers respectively. Generally, the surface area decreases with decreasing particle size of the ZnO nanoparticles.

4.3 Thermogravimetric Analysis (TGA) of the Synthesized ZnO nanoparticles

The three most important signals that TGA collected when it was analyzing the samples were the weight, rate of weight change (differential thermogravimetry) and temperature. The TGA was performed to study the thermal stability and the quantitative properties of the original samples of ZnO nanoparticles samples produced with SLS and LABS. The two samples were heated from 30.0 ^{0}C to 950.0 °C at the rate of 10 °C/ min.

4.3.1 TGA of ZnO nanoparticles Produced with SLS

Figure 4.7 shows the TGA graph of ZnO nanoparticles produced with SLS. The graph revealed no weight loss between 27.03 ^{0}C and 200 ^{0}C. This implies that the ZnO nanoparticles sample was thermally stable within the temperature range. Above 200 ^{0}C, the ZnO nanoparticles experienced some significant weight loss until the temperature reached 475 ^{0}C. The weight loss

could be as a result of evaporation of moisture, volatile solvent desorption and degradation of the sample. The major weight loss occurred at the temperatures above 475 ^{0}C to 725 ^{0}C. The huge weight loss was an indication of thermal decomposition of the ZnO nanoparticles. The thermal decomposition was almost completed at about 725 ^{0}C which implies that it would be a satisfactory temperature for the decomposition of ZnO nanoparticles in the sample.

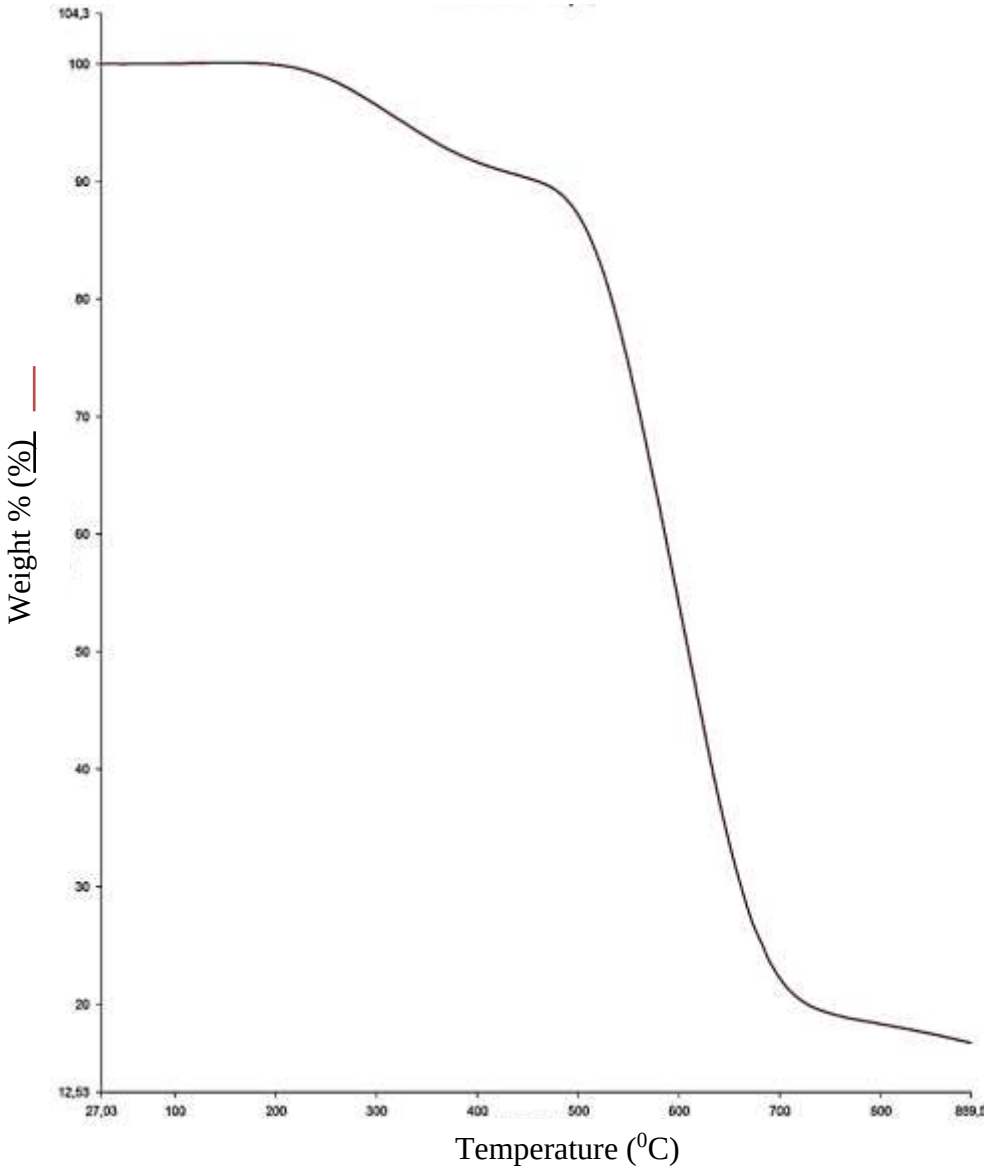

Figure 4.7 TGA graph of ZnO nanoparticles with

Figure 4.8 shows a differential thermogravimetric (DTG) curve which was generated as the first derivative of the weight with respect to time. DTG curve was plotted on the same temperature axis with TGA graph. Two peaks were observed in the DTG curve. The two peaks correspond to the number of degradation stages in the ZnO nanoparticles sample. Peak 1 indicated that the sample experienced its first maximum degradation at about 325 ^{0}C. The second stage of degradation had its maximum degradation at 600 ^{0}C. The TGA and DTG curves showed that the sample had its best quantity properties and thermal stability at temperatures between 27.03 ^{0}C

and 325^0C.

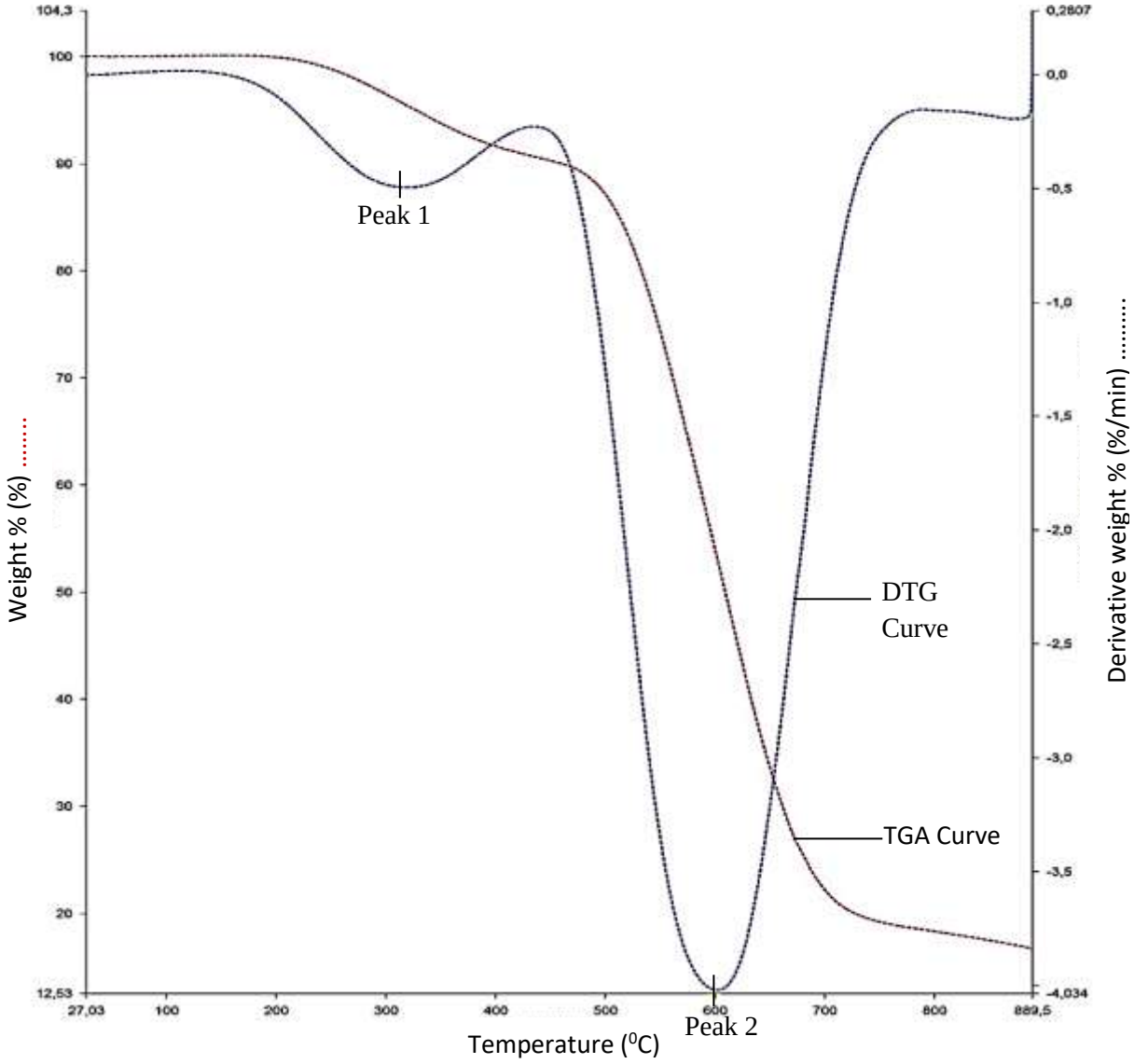

Figure 4.8 Differential thermogravimetric (DTG) curve

4.3.2 TGA of ZnO Nanoparticles Produced with LABS

Figure 4.9 shows the TGA graph of ZnO nanoparticles produced with LABS. At temperatures of 26.52 ^{0}C to 300 ^{0}C, ZnO nanoparticles experienced a slight weight loss due to moisture evaporation and desorption of volatile solvent in the sample. At 300 ^{0}C about 98.7 % of ZnO nanoparticles were left in the sample. It implies that temperature range the ZnO nanoparticles is thermally stable and has it best quantitative properties. Above 300 ^{0}C, the ZnO nanoparticles experienced major weight loss up to 560 ^{0}C. Hence, the thermal decomposition was completed at 560 ^{0}C.

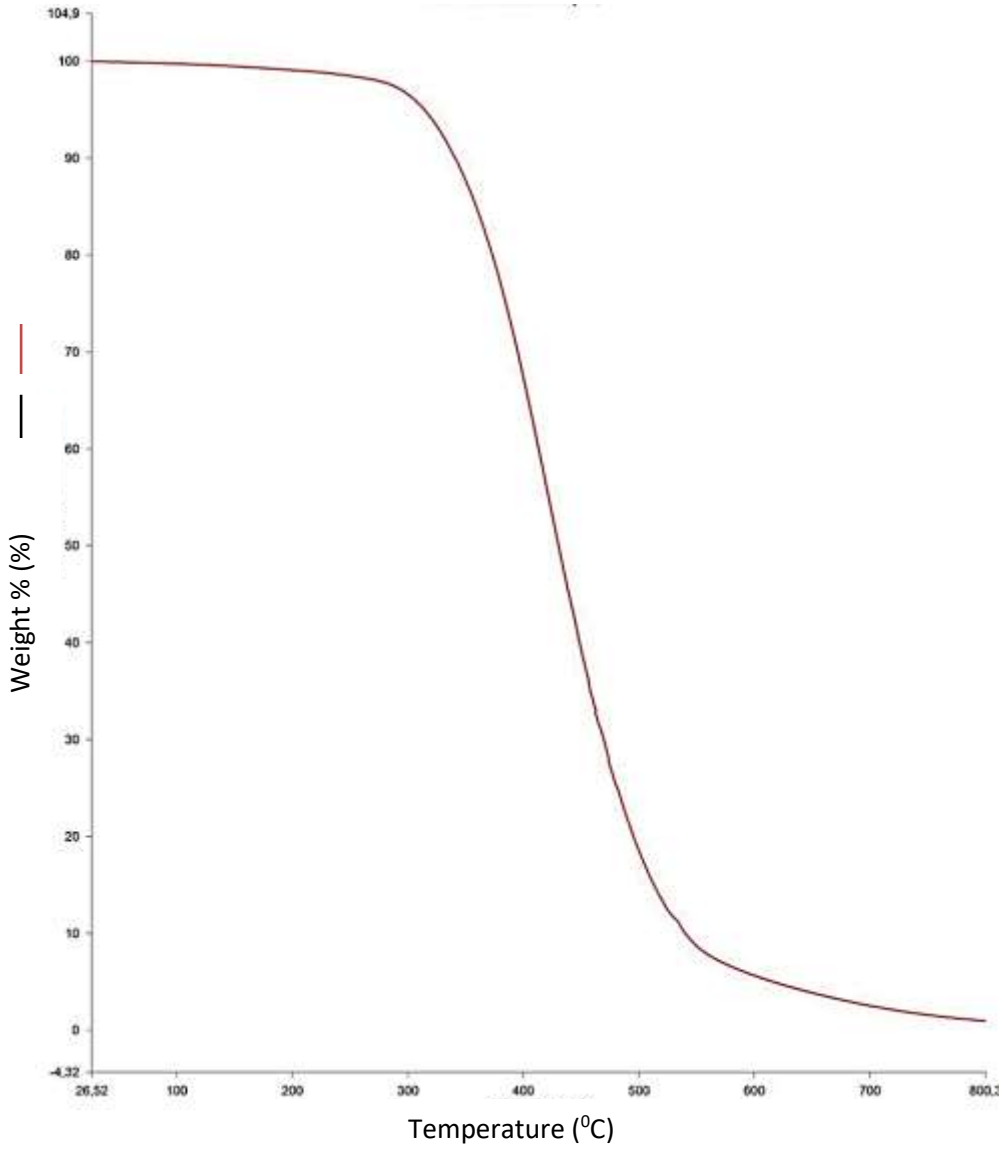

Figure 4.9 TGA of ZnO nanoparticles with LABS

In figure 4.10, only one stage of maximum degradation was observed on the DTG curve of ZnO nanoparticles. The maximum degradation occurred at 420 ^{0}C. Thus, the ZnO nanoparticles sample has it best reliable, thermal stability and quantitative properties at temperatures between 26.52 ^{0}C and 420 ^{0}C.

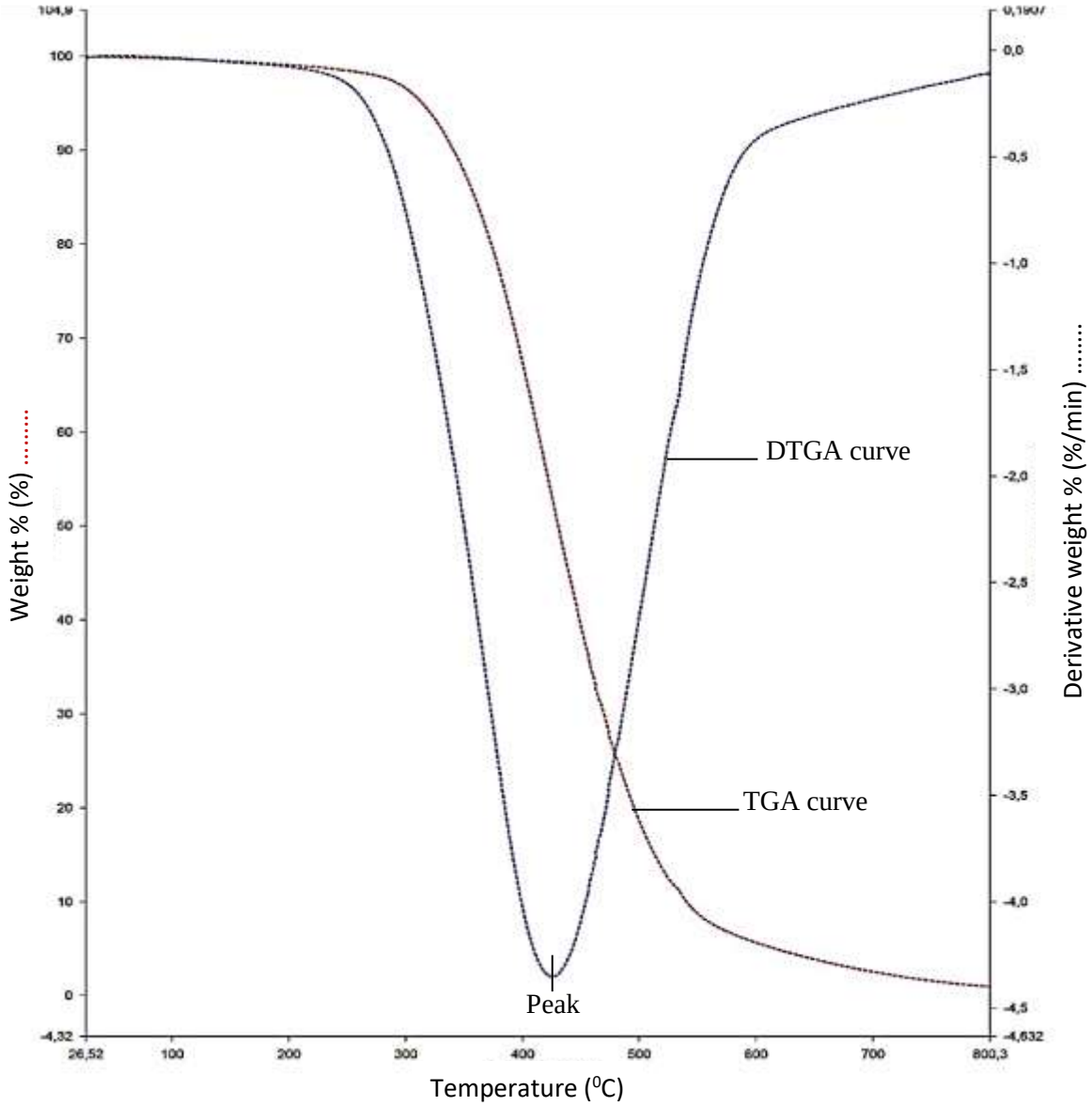

Figure 4.10 DTG of ZnO nanoparticles with LABS

In this analysis, ZnO nanoparticles produced with SLS experienced two stages of decomposition from 200 ^{0}C to 475 ^{0}C and from 475 ^{0}C to 725 ^{0}C. The two stages were in agreement with the two successive decomposition stages observed by Mahamuni *et al.* (2019) in DEG and TEG mediated synthesized ZnO nanoparticles in the range of 145 to 270 ^{0}C for initial weight loss observed due to the evaporation of surface adsorbed water and moisture and in the range of 452–

490 °C due to loss of adsorbed DEG/TEG molecules. Salahuddin *et al.* (2015) also observed two stages of decomposition in studying the synthesis and characterization ZnO Nanoparticles via precipitation method in the range of 50 °C to about 190 °C and in the range of 190 °C to about 320 °C with no further weight loss up to 600 °C temperature. Deak *et al.* (2019) synthesised ZnO nanoparticles for water treatment applications in studying the thermal behaviour of the obtained ZnO nanoparticles noticed two mass loss steps, one before 200 °C and the second one in the interval 200 – 600 °C.

The result of ZnO nanoparticles with LABS was almost stable up to about 420 ^{0}C with minor weight loss. This was consistent with the result obtained by Arora *et al.* (2014) in their study of synthesis and characterization of ZnO nanoparticles with a loss of 2.4 % up to 434 ^{0}C. The two results differed in the sense that ZnO synthesized with LABS degraded at 434 ^{0}C while ARORA *et al*. (2014) reported that there was no considerable loss of weight observed from 434 ^{0}C up to 1000 ^{0}C. The one stage decomposition obtained with LABS was consistent with one stage decomposition obtained from the study of ZnO nanoparticles surface and x-ray profile analysis conducted by Ismail *et al.* (2018). They observed a minor weight loss (≈ 5 %) at around 200 ^{0}C owing to moisture and volatile solvent desorption and a major weight loss in the temperature range of 236 ^{0}C to 289 ^{0}C and the thermal decomposition was almost completed before 300 ^{0}C was attained.

Generally, the disparities in temperature ranges, losses of weight and stages of decomposition could be attributed to the differences in the synthesis techniques, precursors and other materials used during the synthesis.

4.4 Particle Size Distribution Analysis (PSD) of ZnO Nanoparticles

The particle size distribution analysis was used to indicate the sizes of ZnO nanoparticles present and their proportions in the two samples (ZnO nanoparticles produced with SLS and ZnO nanoparticles produced with LABS). The analyses were done based on particle size distribution by volume, particle size distribution by intensity and size quality. The dispersant used in both cases was water. Size distributions of the nanoparticles were determined with a Malvern Zetasizer (Nano Range) by the Dynamic Light Scattering (DLS) technique. Suitable parameters (viscosity, absorption and refractive index) were chosen for each of ZnO samples and the dispersant. ZnO samples had absorption of 0.010 and refractive index of 1.59. The water used as dispersant had viscosity 0.8872 cP and refractive index of 1.33. The samples were dispersed at 25 ^{0}C for 60 seconds (1 minute).

4.4.1 PSD of ZnO Nanoparticles Produced with SLS

The ZnO nanoparticles produced with SLS was analyzed based on size distribution by volume, intensity and size quality.

1. **PSD Analysis by Volume**

The solution of the sample had Z-average particle size of 354nm with polydispersity index of 0.605. Samples had size distribution with polydispersity index values less than 0.7 made it which suitable for the dynamic light scattering (DLS) technique. It shows that the synthesized zinc oxide nanoparticles produced with SLS are monodispersed in nature. The dominant ZnO nanoparticles in the sample had the diameter of 722.3 nm and occupied 68.5 % of the entire volume. This portion of the ZnO nanoparticles is represented in peak 1 of Figure 4.11 that shows a histogram of the particle size distribution by volume of the ZnO nanoparticles produced with

SLS. The results of the analysis indicated the ZnO nanoparticles produced with SLS was of good quality. Peak 2 contains ZnO nanoparticles with diameter of 121.5 nm which occupied 16.8 % of the entire volume. Peak 3 contains ZnO particles of diameter 4967.0 nm which occupied 14.7 % of the entire volume.

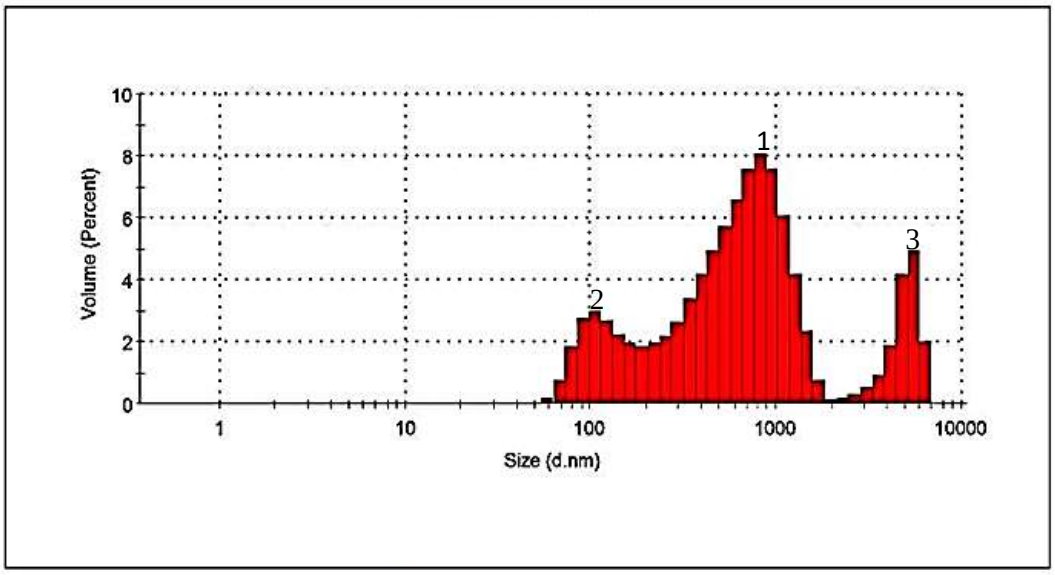

Figure 4.11 Size distributions by volume

2. Particle Size Distribution (PSD) Analysis by Intensity

The PSD by intensity was also obtained from the analysis. The results were based on the intensity of each particle size. Figure 4.12 shows the histogram of the particle size distribution by intensity of the ZnO nanoparticles produced with SLS. The dominant ZnO nanoparticle in the sample had the diameter of 523.1nm and occupied 66.3 % of the entire volume. This portion of the ZnO nanoparticles is represented by peak 1 of Figure 4.12. Peak 2 represents the ZnO nanoparticles with diameter of 136.0 nm which occupied a volume of 23.6 %. Peak 3 represents

the ZnO particles with diameter of 4581.0 nm occupying 10.0 % of the entire volume of the sample.

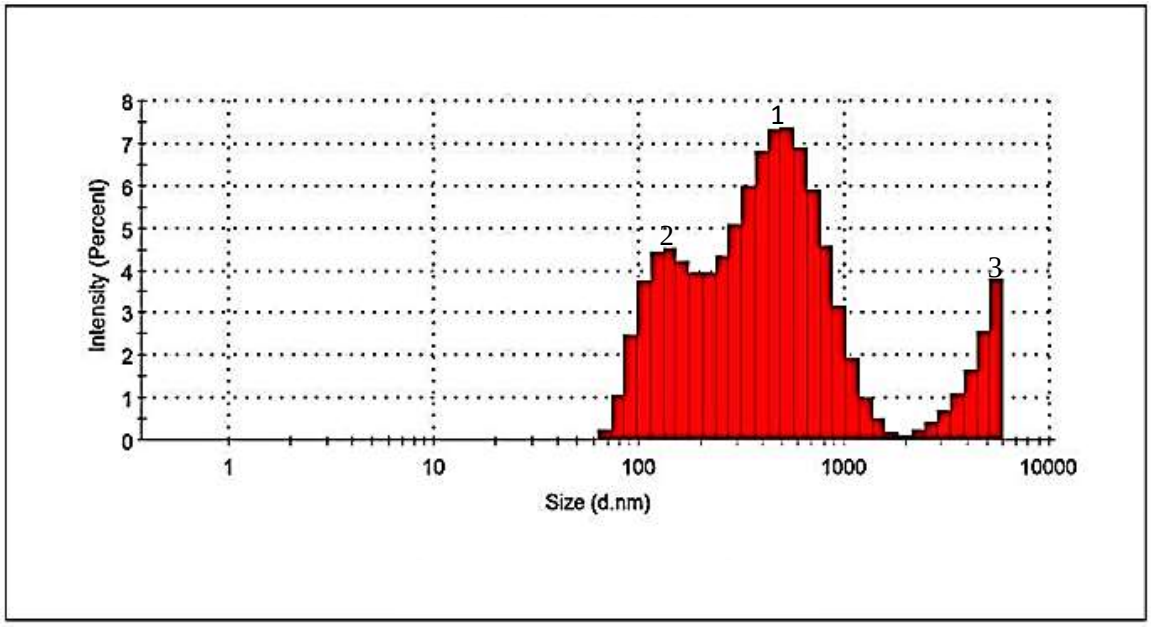

Figure 4.12 Size distributions by intensity

3. **Size Quality Analysis of ZnO Nanoparticles produced with SLS**

The quality of the size distribution of the ZnO nanoparticles obtained from the analysis was verified. Correlation analysis was used to evaluate the strength of the relationship between the size (diameter) and the intensity of the ZnO nanoparticles. Figure 4.13 shows the graph of size distribution by intensity of the ZnO nanoparticles while Figure 4.14 shows the graph of raw correlation data for the distribution.

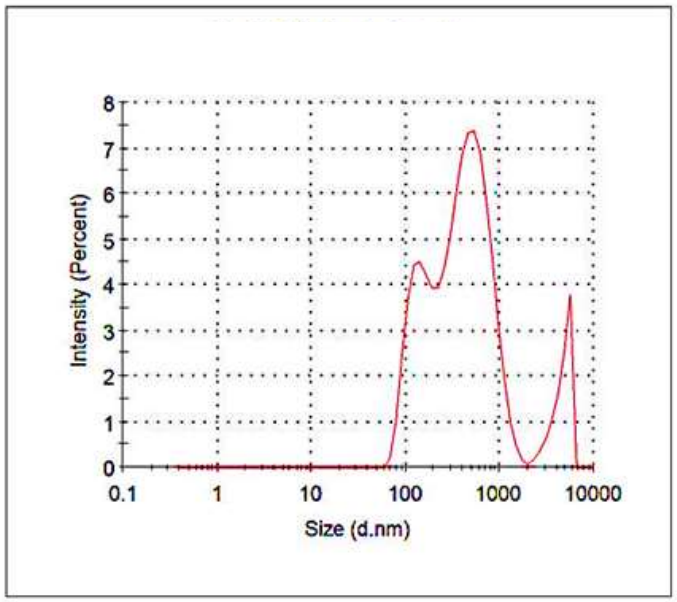

Figure 4.13 Graph of size distribution by intensity

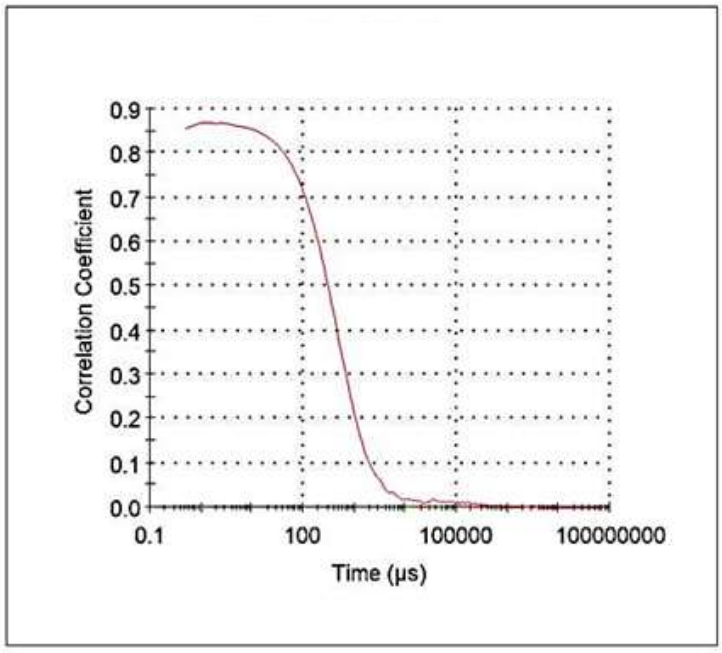

Figure 4.14 Graph of raw correlation data

Figures 4.13 and 4.14 indicated that there was a relationship between the size distribution of the ZnO nanoparticles and the intensity of the nanoparticles. The correlation coefficients were all

positive values which implied that there was a positive linear relationship between the size distribution and intensity of the ZnO nanoparticles present in the sample. The result of the analysis proved that the ZnO nanoparticles synthesized with SLS met the quality criteria.

4.4.2 PSD of ZnO Nanoparticles Produced with LABS

1. **PSD of ZnO Nanoparticles by Volume**

The Z-average diameter for the distribution was 715.2 nm and Polydispersity index (PdI) was 0.431. Thus, the solution of ZnO nanoparticles from the sample contained average particle size of 715.2 nm with polydispersity index of 0.431 which was a clear indication that the synthesized ZnO nanoparticles with LABS were monodispersed in nature.

Figure 4.15 demonstrated the size distribution by volume of the ZnO nanoparticles produced with LABS. Three peaks (1, 2 and 3) were observed from the distribution. The particles within peak 1 occupied 97.3 % of the entire volume of the ZnO nanoparticles in the sample. Peaks 2 and 3 occupied 1.8 % and 0.9 % respectively. The results indicated that ZnO nanoparticles of 981.1 nm were predominantly present in the sample.

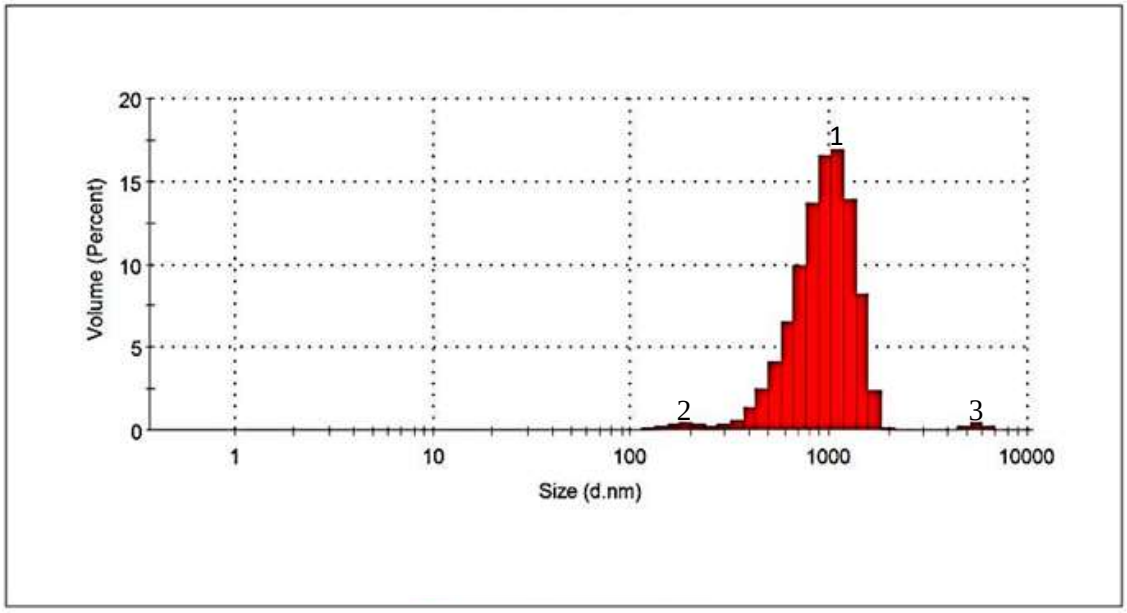

Figure 4.15 Size distribution by volume of ZnO nanoparticles produced with LABS

The results of the size distribution by volume proved that ZnO nanoparticles synthesized with LABS were of good quality.

2. PSD by Intensity of ZnO Nanoparticles Produced with LABS

Figure 4.16 shows the size distribution by intensity of ZnO nanoparticles produced with LABS. Three peaks were observed. Peak 1 has 90.9 % of the particles with average diameter of 787.1nm. Peaks 2 and 3 have intensities of 8.2 % and 0.9 % and average diameters of 202.3 nm and 5478.0 nm respectively. The results demonstrated that the ZnO nanoparticles produced with LABS were of good quality.

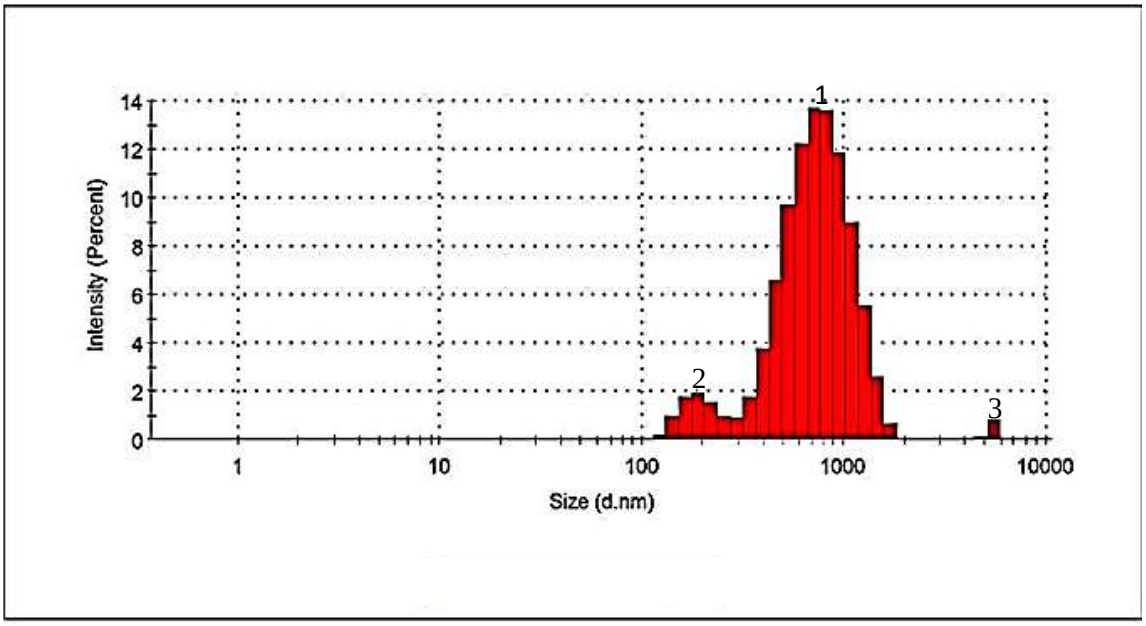

Figure 4.16 Size distributions by intensity of ZnO nanoparticles with LABS

3. Size Quality Analysis of ZnO Nanoparticles produced with LABS

Figure 4.17 is a graph of size distribution by intensity of ZnO nanoparticles produced with LABS. Figure 4.18 is a graph of raw correlation data of the distribution. It was evident that there was a relationship between the size distribution and the intensity of the ZnO nanoparticles. The positive correlation coefficients indicate a positive linear relationship between the size distribution and intensity of the ZnO nanoparticles present in the sample. Hence, the result met the quality criteria.

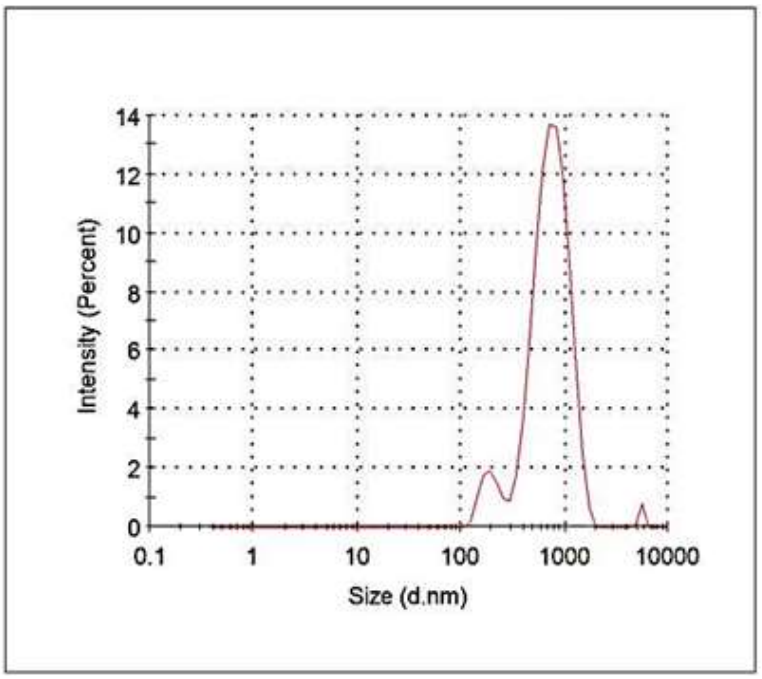

Figure 4.17 Graph of particles size distribution by intensity of ZnO nanoparticles produced with LABS

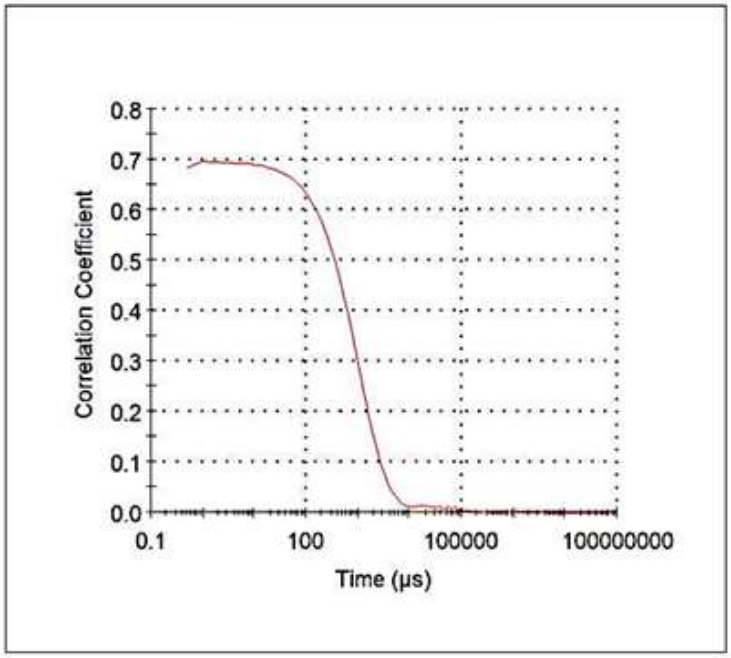

Figure 4.18 Graph of raw correlation data

The value of Z-average of the sample with LABS was very close to Z-average 735 nm of ZnO nanoparticles dispersed in water. Z-average of 354 nm was close to Z-average of 340 nm for ZnO nanoparticles dispersed in ethylene glycol (Marsalek, 2014) and 386.4 nm for pure ZnO nanofluid (Chai *et al.*, 2018). However, the results differ greatly from Z-average of 145.1 nm with PdI of 0.189 for ZnO particles synthesized Using Ixora Coccinea Leaf Extract (Yedurkar *et al.*, 2016), Z-Average size of 46.61 nm and Polydispersity index of 0.552 from extracellular synthesis of zinc oxide nanoparticle using seaweeds o*f* gulf of Mannar, *India* (Nagarajan *et al.*, 2013), Z-average size of 62.94 nm for surface modified ZnO nanofluid (Chai *et al.*, 2018) and Z-average of 64.4 nm and PdI of 0.418 from ZnONPs from Vitis vinifera Peel Extract (Divya *et al*., (2018).

The disparities in Z-averages and Polydispersity Indices could be because the results depended on the dispersant used, its refractive index and viscosity, the measurement technique, synthesis techniques and the purpose for which the ZnO nanoparticles was be used.

4.5 Comparison of ZnO Nanoparticles Synthesized with SLS and LABS

Table 4.3 was used for the comparison of the qualities of ZnO nanoparticles produced with SLS and the ZnO nanoparticles produced with LABS. The table shows the results of all the characterizations using the different characterization techniques. The results revealed that the ZnO nanoparticles produced with SLS and LABS were both of good quality but the ZnO particles produced with LABS yielded better results

Table 4.3 Summary of results from the characterization techniques used for the analysis of ZnO nanoparticles produced with SLS and LABS

ZnO Sample	Characterization Technique									
	Raman		BET		TGA		PSD			
	Material /structure	Intensity (a. u.)	Surface area (m^2/g)	Pore diameter (d.nm)	Degradation temperature (^0C)	Thermal stability	Z-average (nm)	PdI	% vol	% intensity
SLS	ZnO NPs/ wurtzite crystal	1300	284.286	2.411	325	high	354.0	0.605	68.5	66.3
LABS	ZnO NPs/ wurtzite crystal	1400	288.421	2.433	420	higher	715.2	0.431	97.3	90.9

In both ZnO samples, Raman results indicated that the two samples were ZnO nanoparticles of wurtzite crystal structure. The difference in the Raman results was that the ZnO nanoparticles in LABS sample had higher intensity revealing that it had greater concentration of ZnO nanoparticles. Therefore, it had greater yield of the ZnO nanoparticles.

BET results demonstrated that the ZnO nanoparticles produced with LABS had greater surface area and larger pore size diameter. It implied that ZnO nanoparticles in LABS sample had better adsorption properties.

TGA results discovered that degradation temperature of ZnO nanoparticles produced with LABS was higher than that of ZnO particles produced with SLS. It depicted that the ZnO nanoparticles in LABS sample had higher thermal stability and was more reliable than the ZnO nanoparticles in SLS sample.

PSD results show that Z-average diameter of ZnO nanoparticles produced with LABS was higher with less PdI than the Z-average of the ZnO nanoparticles produced with SLS. Considering the percentage volumes and percentage intensities of the two samples, the ZnO nanoparticles in LABS sample exhibited similar identities in terms of their size properties.

97.3 % by volume and 90.9 % by intensity of the ZnO particles in LABS sample fell within the same size range compared to 68.5 % by volume and 66.3 % by intensity in SLS sample. The analysis showed that the ZnO particles produced with LABS had better particle size distribution.

The Raman, BET, TGA and PSD analyses of the ZnO nanoparticles produced with SLS and LABS demonstrated that the ZnO nanoparticles produced with LABS had good structure with higher concentration of ZnO nanoparticles, larger surface area and pore diameter, higher thermal stability and reliability, and better size properties than the ZnO nanoparticles produced with SLS. Based on this analysis the ZnO nanoparticles produced with LABS was used in the subsequent parts of this research.

4.6 Calibration of the Nanostructured ZnO Capacitive Relative Humidity Sensors

The nanostructured ZnO capacitive humidity sensors were calibrated at room (laboratory) temperatures ranging from 27 ^{0}C to 30 ^{0}C. Stable relative humidity environments were maintained using saturated solutions of lithium Chloride (LiCl), Potassium carbonate (K_2CO_3), potassium chloride (KCl), potassium sulphate (K_2SO_4) and sodium chloride (NaCl). Each of the humidity environments was used to calibrate the unannealed sensor and the sensors annealed at 150 ^{0}C and 200 ^{0}C. Linear regression equation (equation 3.5) was used for the calibration of the sensors (Hsuan-Yu and Chiachung, 2019).

$$y = b_0 + b_1x \qquad 4.4$$

where y is the standard humidity value measured by DHT11, x is the capacitance value measure by nanostructured ZnO capacitive RH sensor, b_0 and b_1 are constants. In each case, the calibration equation was established to build the relationship between the standard RH (reference

RH) values measured by DHT11 RH sensor and the corresponding capacitance values of the nanostructured ZnO capacitive relative humidity sensors. The capacitance corresponding to the standard %RH of each of the saturated salt solutions were determined from the adsorption curve. Desorption curve was also obtained. The coefficient of determination (R^2) for each calibration equation was determined for each set of data. Positive values of R^2 indicated good linearity, which showed good linear relationship between the capacitance values and relative humidity values. Negative values of R^2 indicated poor linearity. The standard deviation was used to determine how widely the capacitance values were dispersed from the mean capacitance of the sensor. The sensitivity, the response and recovery times and the accuracy of the sensors were also determined.

4.6.1 Calibration of the Unannealed Nanostructured ZnO Capacitive Relative Humidity (RH) Sensor

The unannealed nanostructured ZnO capacitive relative humidity sensor was calibrated using the saturated salt solutions of LiCl, K_2CO_4, NaCl, KCl and K_2SO_4.

1. **Calibration of the Unannealed Nanostructured ZnO Capacitive RH Sensor Using Saturated Solution Of Lithium Chloride (LiCl)**

Saturated solution of LiCl was used in a humidity chamber as a micro humidity environment. Figures 4.19a and 4.19b show the relationship between the capacitance values of the unannealed nanostructured ZnO capacitive RH sensor and the RH values of DHT11 RH sensor in LiCl micro humidity environment. Figure 4.19a shows the adsorption curve while Figure 4.19b shows the desorption curve of the sensor. During adsorption of moisture in LiCl micro humidity

environment, it was observed that the output capacitance of the unannealed sensor decreased with decreasing RH level of the DHT11 sensor. The implication was that the adsorbed moisture reduced the dielectric constant and the capacitance of the unannealed ZnO capacitive RH sensor. Desorption curve (Figure 4.19b) shows that the desorbed moisture increased the dielectric constant and the capacitance of the unannealed ZnO capacitive RH sensor. Hence, the capacitance of the unannealed nanostructured ZnO RH sensor was a function of relative humidity. The relationship was that of direct proportionality. The relative humidity decreased from 69 %RH until it attained a minimum humidity of 13 %RH. Similarly, the capacitance decreased from 11.1 pF to 9.4 pF. Therefore the relative humidity and capacitance corresponding to the RH reference of LiCl were 13 %RH and 9.4 pF (see Figure 4.19a).

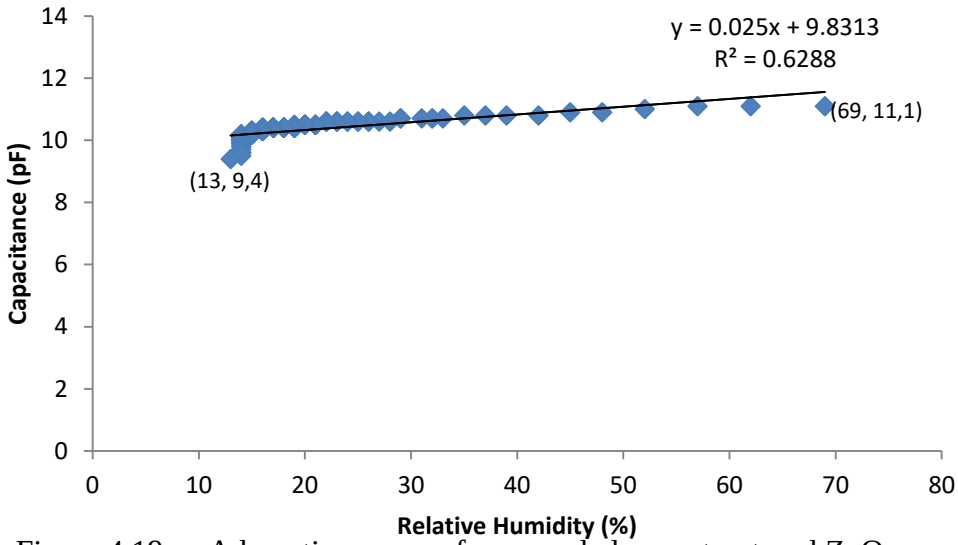

Figure 4.19a Adsorption curve of unannealed nanostructured ZnO capacitive RH sensor in LiCl micro humidity environment

The calibration equation for adsorption of moisture (Figure 4.19a) was expressed as

$y = 0.025x + 9.8313$. 4.1

The standard deviation (SD) of the capacitance values was 0.3003. The coefficient of determination (R^2) was 0.6288. This indicated that 62.88 % of points on the graph fell within the regression line of humidity range of 13 %RH to 69 %RH and capacitance range of 9.4 pF to 11.1 pF. The percentage of the points within the regression line depicted good linearity of the unannealed sensor during adsorption.

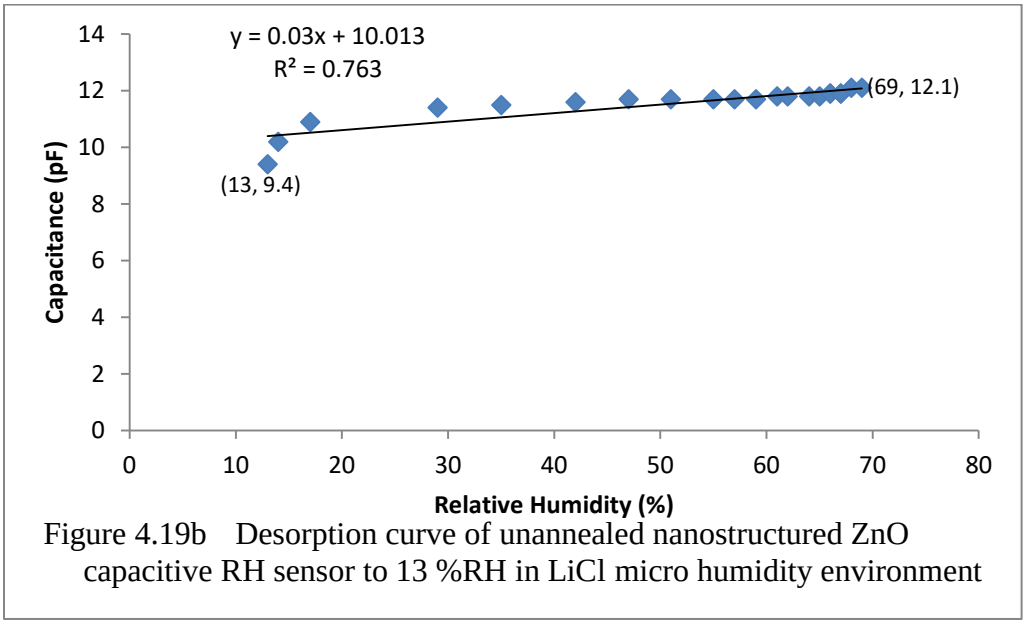

Figure 4.19b Desorption curve of unannealed nanostructured ZnO capacitive RH sensor to 13 %RH in LiCl micro humidity environment

The fitted curve for desorption (Figure 4.19b) of moisture was determined by the equation:

$y = 0.03x + 10.013.$ 4.2

The data distribution had a standard deviation of 0.6472 which showed a wider dispersion of the capacitance values from the mean capacitance compared to what was obtained during adsorption. The equation was a linear equation with a positive coefficient of determination (R^2) of 0.763. Thus, 76.3 % of the points fell within the regression line of humidity range of 13 %RH to 69 %RH and capacitance range of 9.4 pF and 12.1 pF. The desorption curve had better linearity and wider range of capacitance values compared to the adsorption curve.

The response and recovery times of the unannealed nanostructured ZnO capacitive RH sensor for humidity levels between 13 %RH and 69 %RH are shown in Figures 4.20a and 4.20b respectively.

.

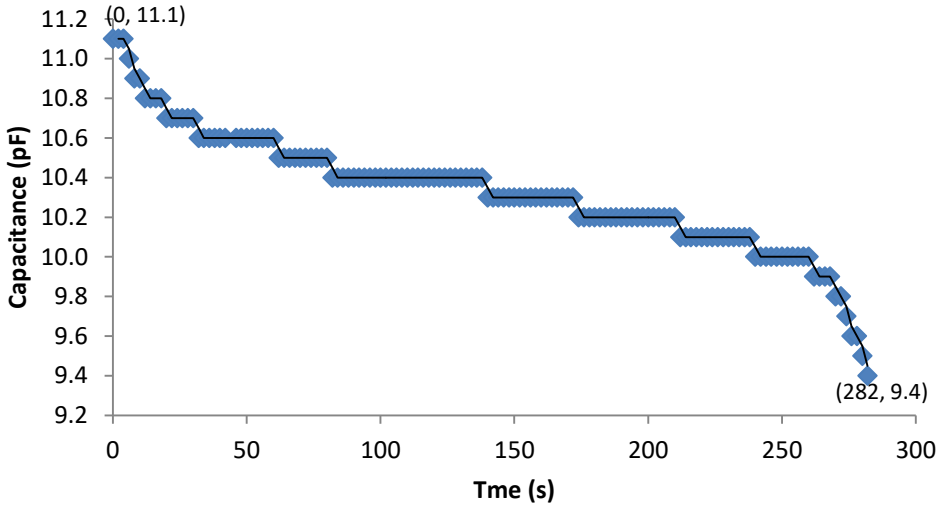

Figure 4.20a Response time of unanneled nanostructured ZnO capacitive RH sensor to 69 %RH in LiCl micro humidity environment

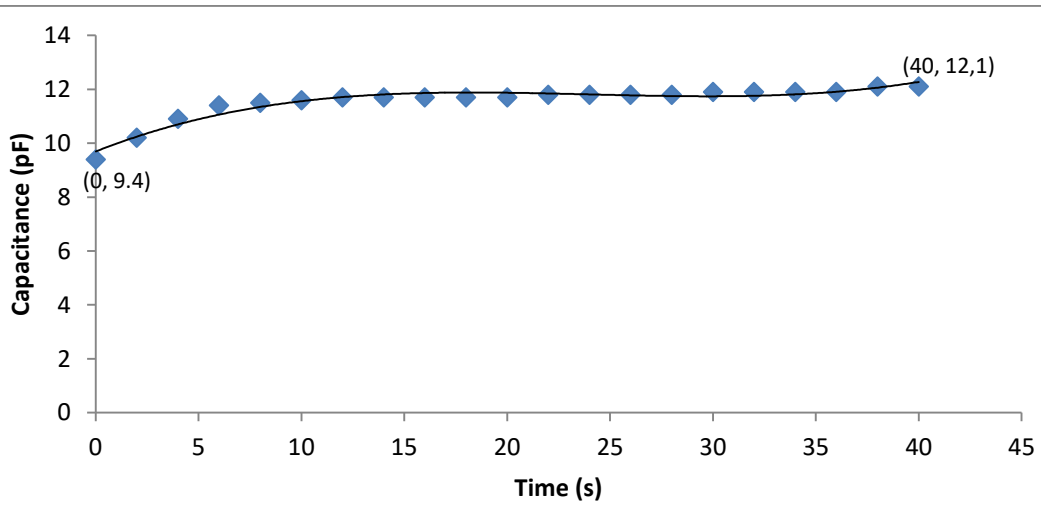

Figure 4.20b Recovery time of unannealed nanostructured ZnO capacitive RH sensor in LiCl micro humidity environment

Response time for the unannealed nanostructured ZnO capacitive RH sensor was 282 s or 4.7 minutes. The recovery time was 40 s or 0.67 minutes which was shorter than the response time. It was also observed that the variation in capacitance was higher during desorption than during adsorption of moisture.

2. **Calibration of the Unannealed Nanostructured ZnO Capacitive Relative Humidity Sensor Using Saturated Solution of Potassium Carbonate (K_2CO_3)**

Figure 4.21a shows the adsorption curve of unannealed nanostructured ZnO capacitive RH sensor in K_2CO_3 micro humidity environment. The DHT11 recorded a continuous decrease in humidity from 93 %RH to 57 %RH. In a similar way the nanostructured ZnO capacitive RH sensor recorded a reduction in capacitance from 23.8 pF to a constant capacitance of 11.1 pF. The RH and capacitance corresponding to the K_2CO_3 micro humidity environment were 57 %RH and 11.1 pF respectively. A curved graph was obtained from the data for desorption of the moisture. The line best fit for the curve (Figure 4.21a) was a polynomial curve with polynomial equation 4.3. The linear series 1 shows the linear relationship between capacitance and RH which was represented by equation 4.4. The R^2, SD and S_A were determined and their values were recorded.

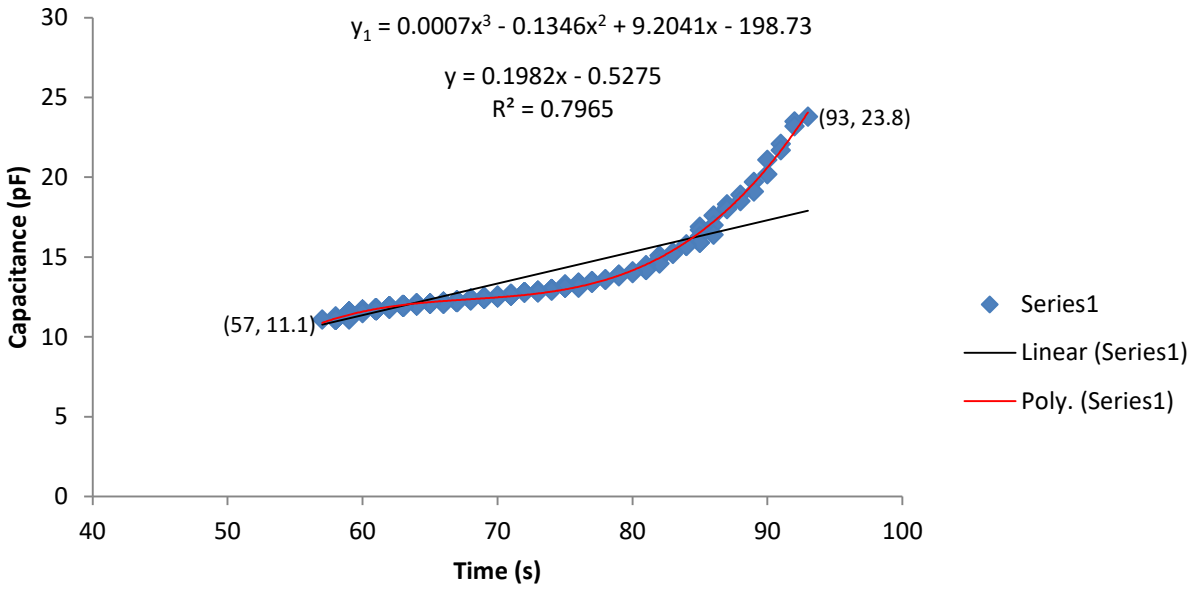

Figure 4.21a Adsorption curve of unannealed nanostructured ZnO capacitive RH sensor in K_2CO_3 micro humidity environment

$y_1 = 0.0007x^3 - 0.1346x^2 + 9.2041x - 198.73$ 4.3

$y = 0.1982x - 0.5275.$ 4.4

$R^2 = 0.7965$, SD = 1.772155

R^2 was 0.7965 which revealed a linear relationship of 79.65 %. Figure 4.21b shows the desorption curve of the unannealed nanostructured ZnO capacitive RH sensor in K_2CO_3 micro humidity environment. The fitted curve for desorption of moisture was determined by the forth order polynomial equation displayed on the graph. The calibration equation (4.5), R^2, SD and S_D were determined.

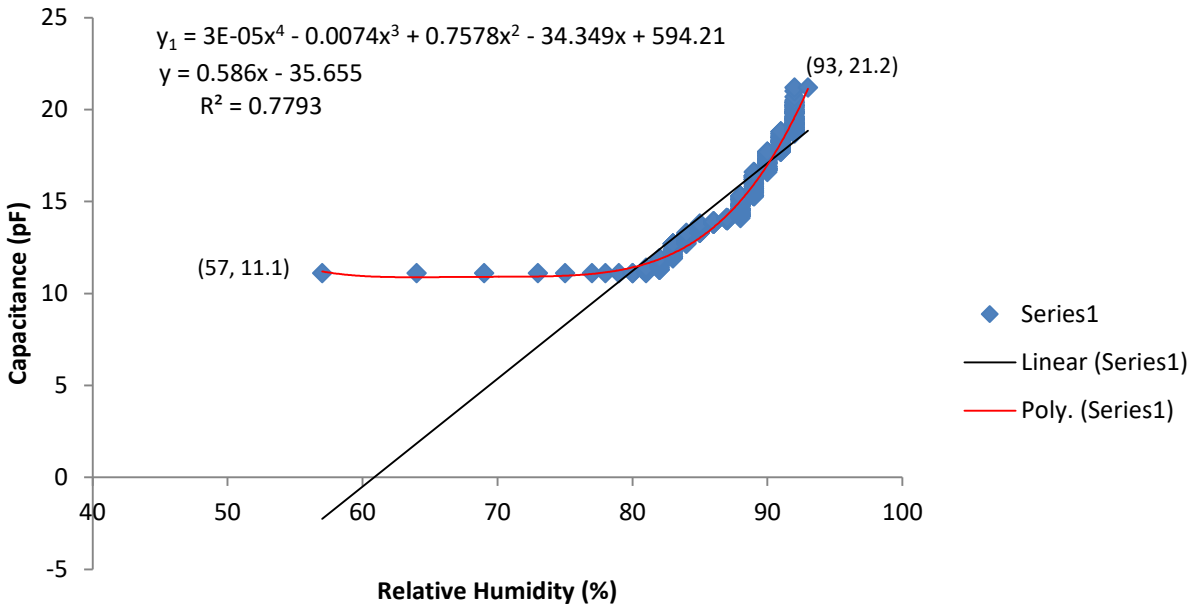

Figure 4.21b Desorption curve for unanneled nanostructured ZnO capacitive RH sensor in K_2CO_3 micro humidity environment

$y = 0.586x - 35.655$ 4.5

$R^2 = 0.7793$, SD = 2.750076, $S_D = 0.910$

The high value of R^2 was an indication of a very good linearity. There was 77.93 % linear relationship between the capacitance and RH. The SD was 2.750076 which designated high dispersion of data obtained from the capacitive sensor. In comparison with the behaviour of the sensor during adsorption, the unannealed ZnO capacitive RH sensor showed lower linearity, lower sensitivity and higher dispersion of data during desorption.

The response time and recovery time of the sensor were determined from Figure 4.22a and Figure 4.22b respectively. The response time was 858 s or 14.3 minutes between 57 %RH and 93 %RH and between capacitance of 11.1 pF and 23.8 pF. The recovery time was 802 s or 13.37 minutes for the same RH range and capacitance range of 11.1 pF and 20.7 pF. The recovery time was shorter than the response time but with shorter capacitance range.

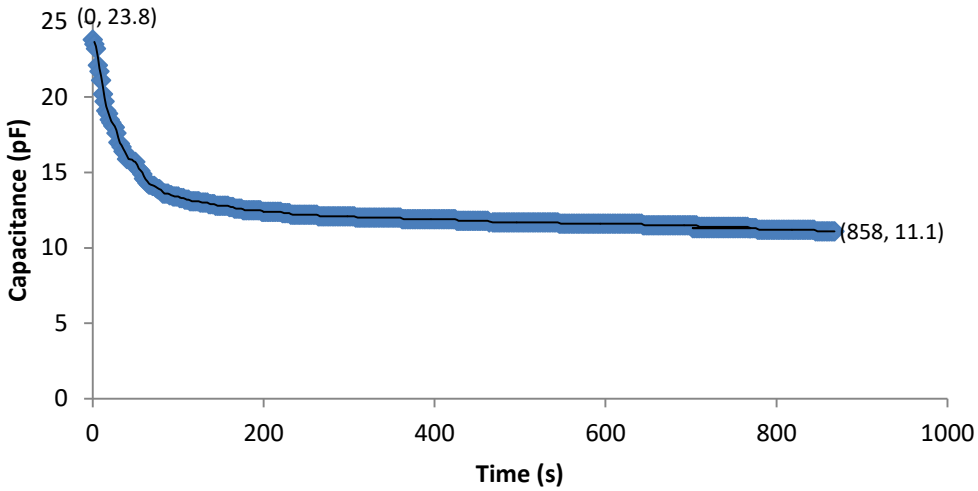

Figure 4.22a Response time of unannealed nanostructured ZnO capacitive RH sensor in K_2CO_3 micro humidity environment

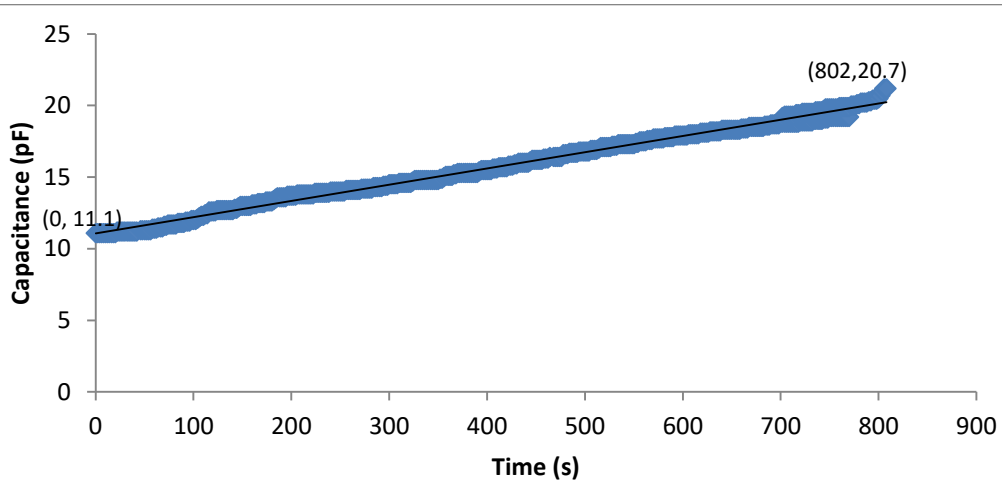

Figure 4.22b Recovery time for unannealed nanostructured ZnO capacitive capacitive RH sensor in K_2CO_3 micro humidity environment

3. Calibration of the Unannealed Nanostructured ZnO Capacitive Relative Humidity Sensor using saturated solution of Sodium Chloride (NaCl)

Figure 4.23a shows adsorption curve of unannealed nanostructured ZnO capacitive RH sensor in NaCl micro humidity environment. The DHT11 sensor attained a final humidity of 86 %RH which corresponded to the reference humidity of the saturated solution of NaCl. The unannealed

nanostructured ZnO capacitive RH sensor had a capacitance of 13.9 pF corresponding to the same reference relative humidity. Figure 4.23b shows the desorption curve of the same sensor. The equation for calibration (4.6) was established. R^2, SD and S_A where found and recorded.

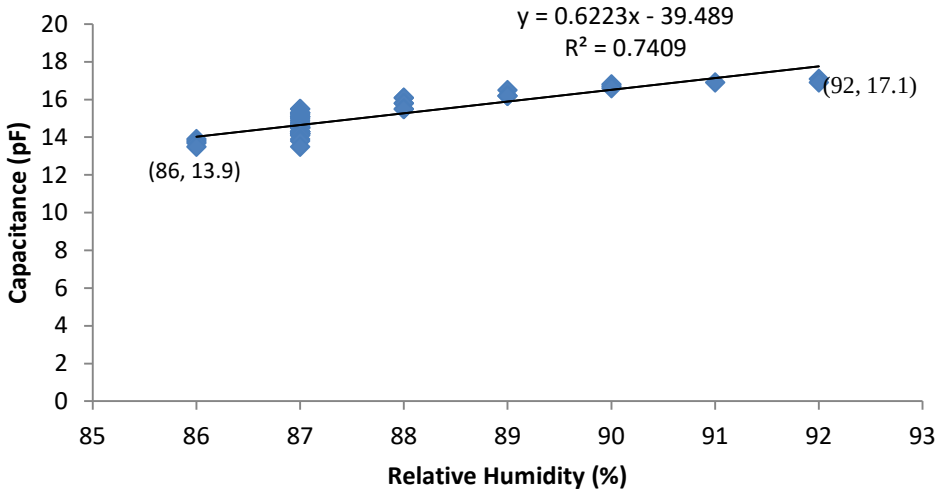

Figure 4.23a Adsorption curve of unannealed nanostructured ZnO capacitive RH sensor in NaCl micro humidity environment

$$y = 0.6223x - 39.489 \qquad 4.6$$

$R^2 = 0.7409$, SD = 0.9657149, $S_A = 0.230$

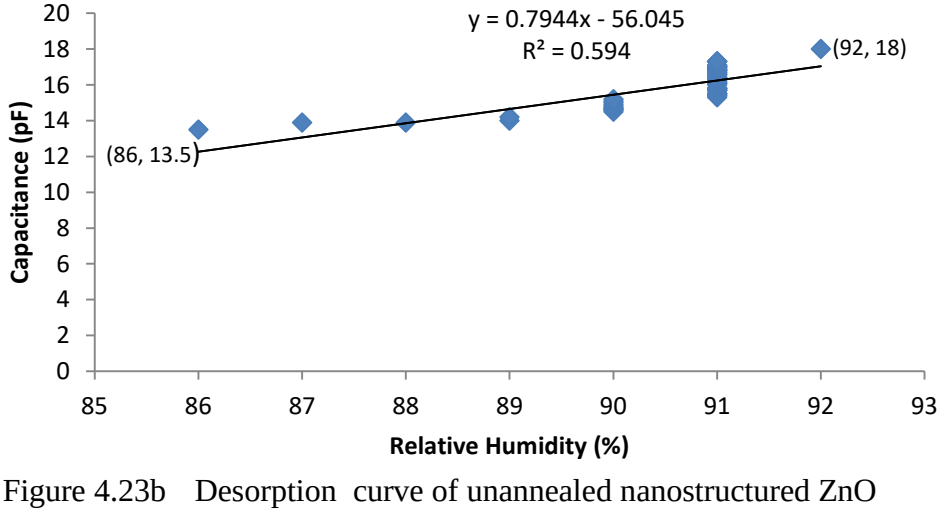

Figure 4.23b Desorption curve of unannealed nanostructured ZnO capacitive RH sensor in NaCl micro humidity environment

$y = 0.7944x - 56.045$ 4.7

$R^2 = 0.594$, SD = 1.012979, $S_D = 0.333$

The variation of capacitance with RH during adsorption was 74.09 % linear while it was 59.40 % during desorption when NaCl micro humidity environment was used. Thus, the unannealed ZnO capacitive RH sensor demonstrated a more linear variation of capacitance with RH during adsorption of moisture than in desorption of moisture. The sensor experienced wider dispersion and greater sensitivity in desorption than during adsorption.

Figures 4.24a and 4.24b respectively shows the response and the recovery times of the unannealed ZnO capacitive RH sensor. The response time was 106 s or 1.77 minutes for RH humidity range of 86 %RH and 92 %RH and for capacitance range of 13.9 pF and 17.1 pF. The recovery time was 124 s or 2.07 minutes for the same humidity range and capacitance range of 13.5 pF and 18 pF. The response time was shorter though with a shorter capacitance range.

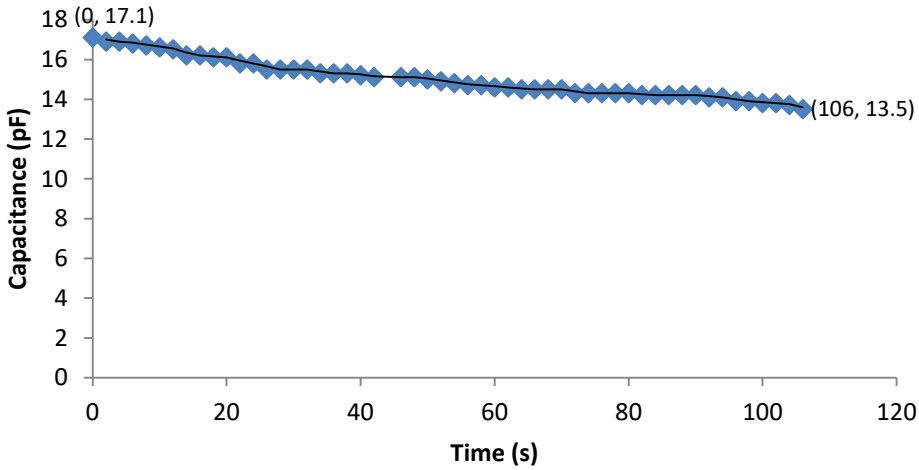

Figure 4.24a Response time of unannealed nanostructured ZnO capacitive RH sensor in NaCl micro humidity environment

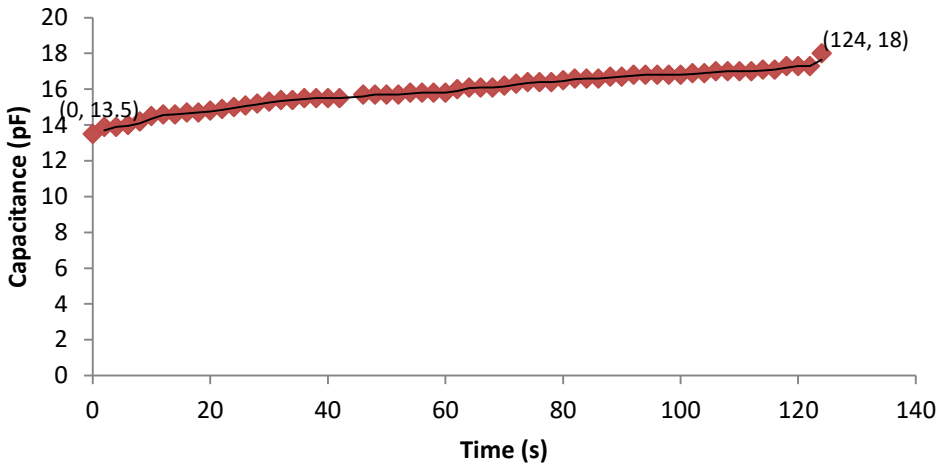

Figure 4.24b Recovery time of unannealed nanostructured ZnO capacitive RH in NaCl micro humidity environment

4. Calibration of the Unannealed Nanostructured ZnO Capacitive Relative Humidity Sensor Using Saturated Solution of Potassium Chloride (KCl)

During adsorption from the KCl micro humidity environment the DHT11 sensor reached a stable relative humidity of 87 %RH while the unannealed nanostructured ZnO RH sensor reached a stable capacitance of 17.1 pF equivalent to the reference humidity of KCl. The adsorption curve was shown in figure 4.25a. The calibration equation (4.7) for adsorption of moisture, R^2, SD and S_A were determined. The coefficient of determination (R^2) indicated that the relationship between the RH and capacitance was 65.25 % linear during adsorption with SD of 0.337085. The sensitivity (S_A) of the unannealed capacitive sensor was 0.051 which was low. Figure 4.25b shows the desorption curve of unannealed nanostructured ZnO capacitive RH sensor in KCl micro humidity environment. The calibration equation (4.8), R^2, SD and S_D were determined as shown on the graph.

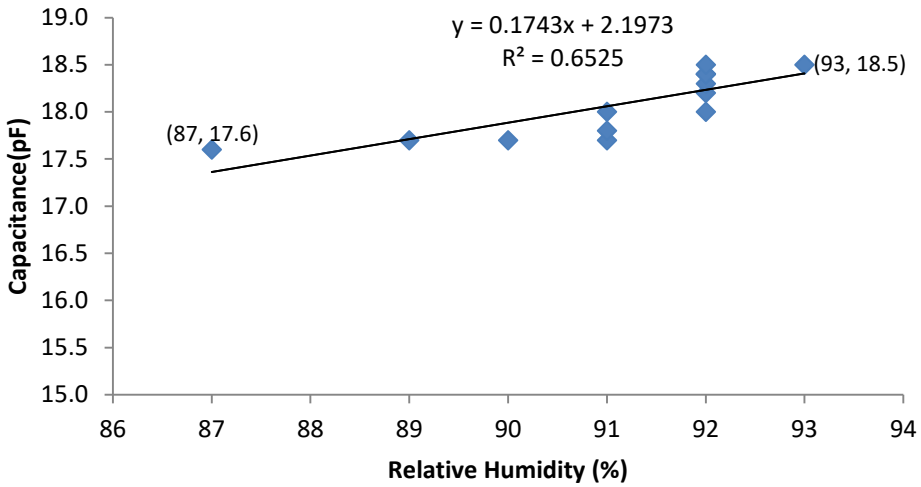

Figure 4.25a Adsorption curve of unannealed nanostructured ZnO RH sensor in KCl micro humidity environment

$$y = 0.1743 + 2.1973 \qquad 4.7$$

$R^2 = 0.6525$, SD = 0.337085, $S_A = 0.051$

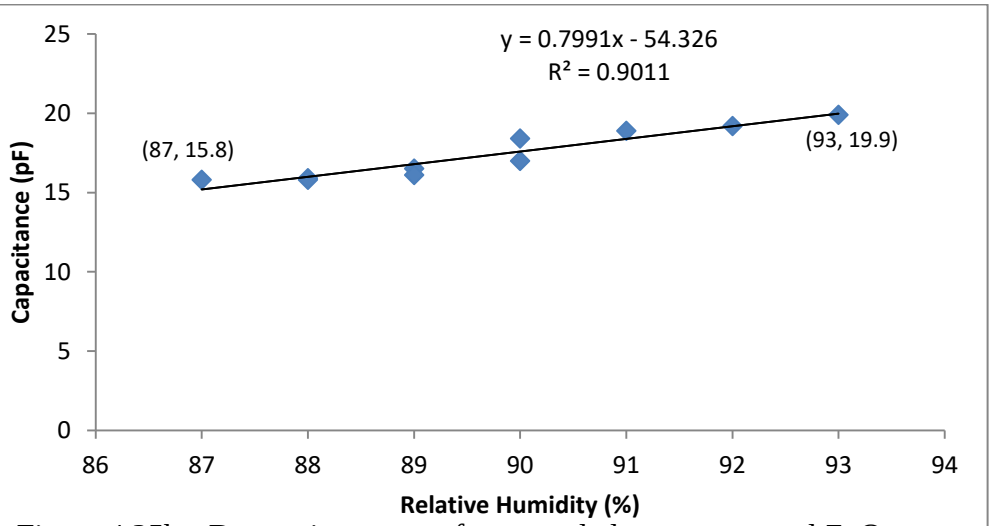

Figure 4.25b Desorption curve of unannealed nanostructured ZnO capacitive RH sensor in KCl micro humidity environment

$$y = 0.7991x - 54.326 \qquad 4.8$$

$R^2 = 0.9011$, SD = 1.5897, $S_D = 0.2595$

The equation demonstrated a linear relationship which was 90.11 % linear with SD of 1.5897. The unannealed capacitive sensor had sensitivity of 0.2595 during desorption. It was observed that the sensor had a very good linearity, higher standard deviation and higher sensitivity during desorption that during adsorption.

Figures 4.26a and 4.26b respectively illustrated the response time and recovery time of the unannealed nanostructured ZnO capacitive RH sensor in KCl micro humidity environment. The response time was 26 s for RH level of 87 %RH to 93 %RH and capacitance variation of 17.6 pF to 18.5 pF. The recovery time was 18 s for the same RH range of 15.8 pF to 19.9 pF. Recovery of the sensor was faster and for wider capacitance range compared to the sensor response to relative humidity changes which confirmed the higher sensitivity of the sensor during desorption.

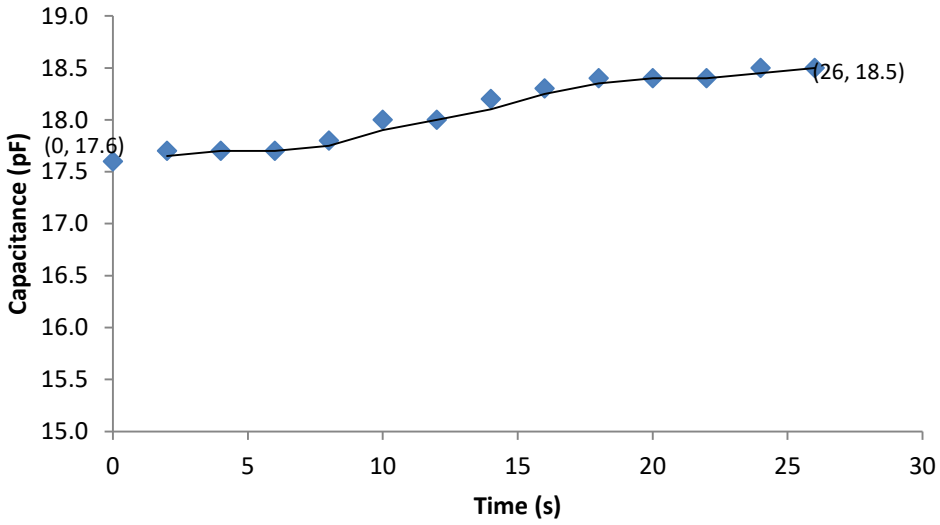

Figure 4.26a Response time of unannealed nanostructured ZnO capacitive RH sensor in KCl micro humidity environment

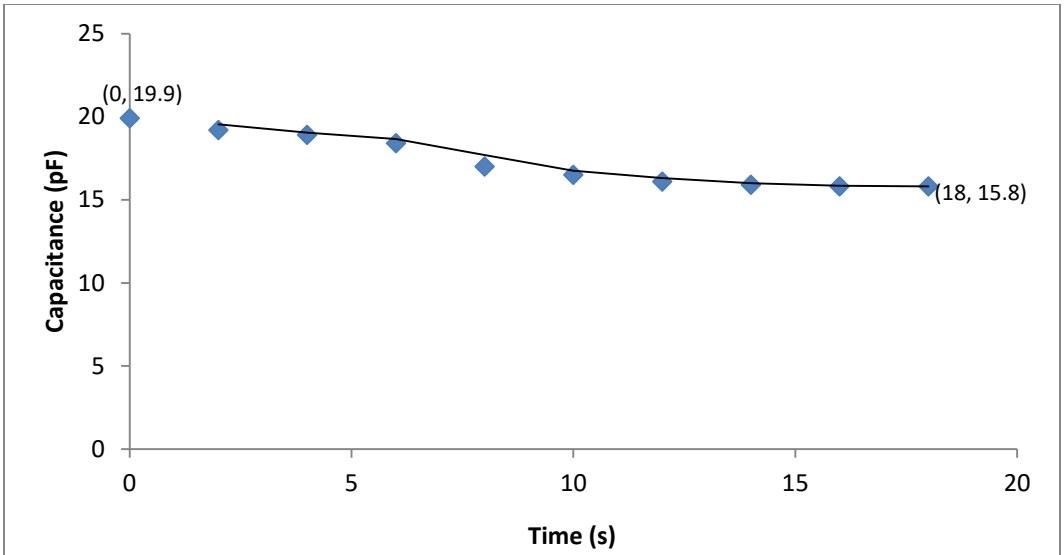

Figure 4.26b Recovery time of unannealed nanostructured ZnO capacitive RH sensor in a KCl micro humidity environment

5. Calibration of the Unannealed Nanostructured ZnO Capacitive Relative Humidity Sensor Using Saturated Solution of Potassium Sulphate (K_2SO_4)

The unannealed nanostructured ZnO capacitive RH sensor experienced increase in capacitance from 87 %RH and above. The DHT11 relative humidity sensor could not read more than 95 %RH. Hence, the corresponding values of capacitance above 95 %RH could not be recorded. 95 %RH was taken as the reference relative humidity for K_2SO_4 micro humidity environment and the corresponding capacitance was 22.6 pF. Figure 4.27a illustrated the relationship between the capacitance and RH during adsorption. Figure 4.27b illustrated the relationship between RH and capacitance during desorption. The calibration equations (4.9 and 4.10), R^2, SD, S_A and were determined from the graphs. R^2 indicated that the adsorption graph was 62.22 % linear with SD deviation of 1.342577 and S_A of 0.378 while desorption curve was found to be 93.18 % linear with SD of 1.873067 and S_D of 0.404. The performance of the sensor at desorption was better than its performance at adsorption in K_2SO_4 micro humidity environment.

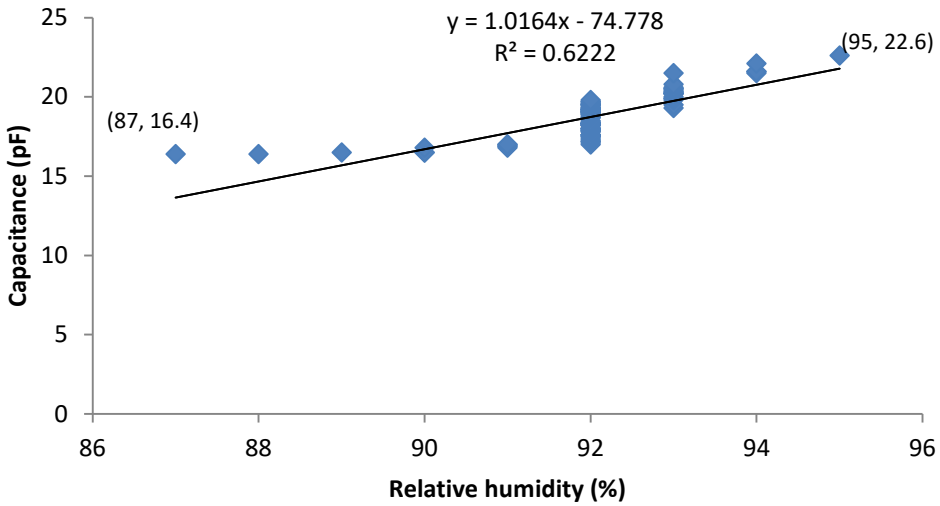

Figure 4.27a Adsorption curve of unannealed nanostructured ZnO capacitive RH in K_2SO_4 micro humidity environment

$$y = 1.0164x - 74.778 \quad (4.9)$$

$R^2 = 0.6222$, SD = 1.342577, $S_D = 0.378$

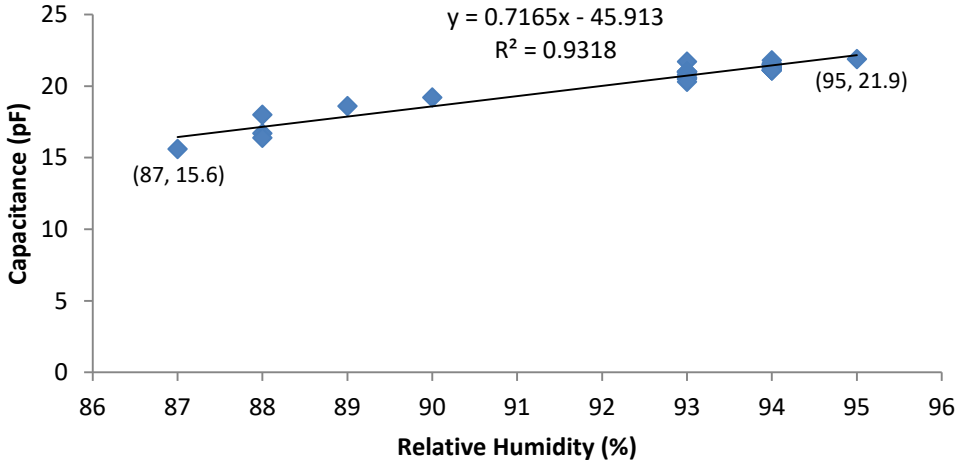

Figure 4.27b Desorption of unannealed nanostructured ZnO capacitive RH sensor in K_2SO_4 micro humidity environment

$$y = 0.7165x - 45.913 \quad (4.10)$$

$R^2 = 0.9318$, SD = 1.873067, $S_D = 0.404$

The response and recovery times of the unannealed capacitive sensor were illustrated in Figure 4.28a and Figure 4.28b respectively. The response time was 204 s or 3.4 minutes for RH of

87 %RH to 95 %RH and capacitance 16.4 pF to 22.6 pF. The recovery time was 64 s or 1.07 minutes for the same RH range and capacitance of 15.6 pF to 21.9 pF. The recovery time was faster than the response time of the unannealed capacitive sensor in the K_2SO_4 micro humidity environment.

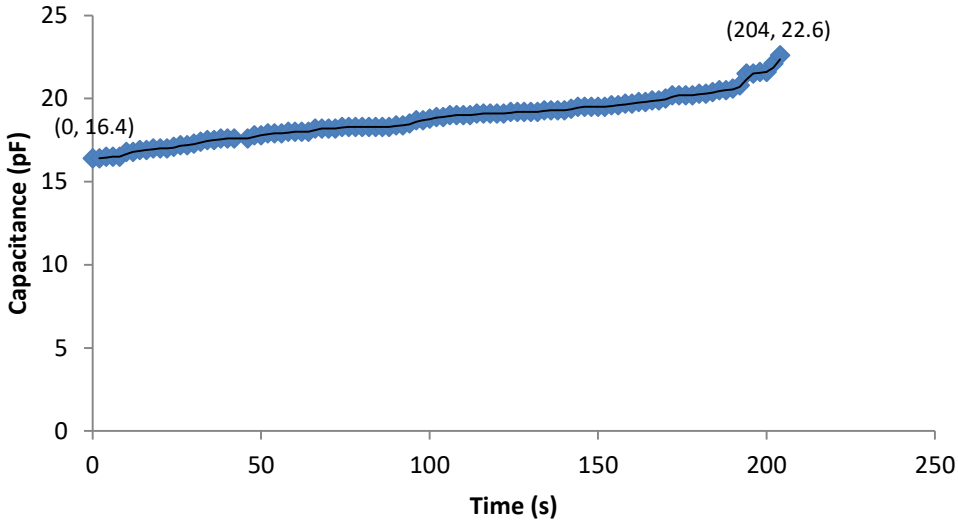

Figure 4.28a Response time of unannealed ZnO nanostructured capacitive RH sensor in K_2SO_4 micro humidity environment

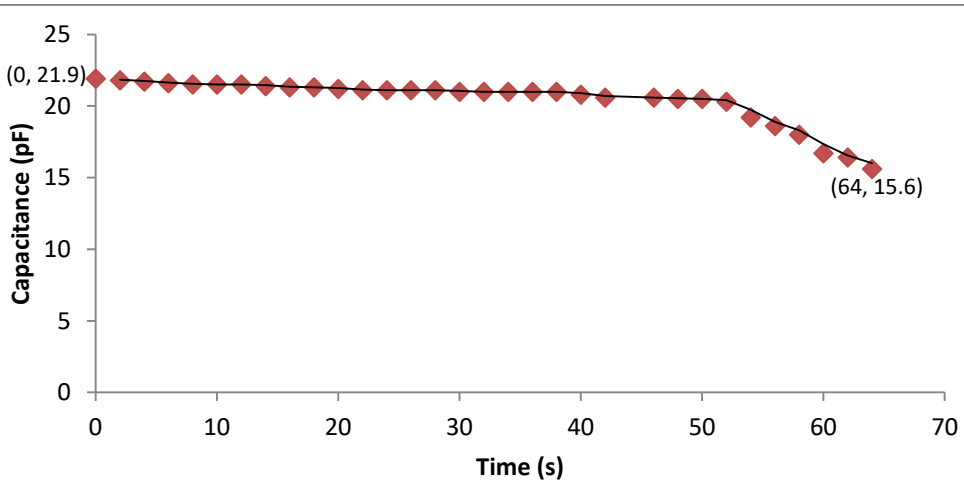

Figure 4.28b Recovery time of unannealed nanostructured ZnO capacitive RH sensoe in K_2SO_4 micro humidity environment

The characteristics of capacitive humidity sensors are widely variable due to the different manufacturing processes used, RH humidity ranges and RH environments among others. The results of the calibration of the unannealed sensor for instance showed different response ranging from 26 s for KCl to 858 s for KCO_3 and recovery time of 18 s for KCl to 802 s for KCO_3 for different humidity values ranging from 13 %RH to 95 %RH. This is also evident in the findings of some researchers. Yang *et al*. (2017) in the research on stable and fast-response capacitive humidity sensors based on a ZnO nanopowder/PVP-RGO Multilayer discovered that capacitive ZnO sensors exhibited the highest sensitivity (~0.044) at middle and high RH (>40%) with response and recovery times of 21.3 s and 0.9 s respectively. The ZnO capacitive RH sensor produced by Narimani *et al*. (2016) showed higher response time of 250 s for RH changes of 55 %RH to 90 %RH. Graphene oxide capacitive relative RH sensor by Hengchang *et al*. (2013) had response time was 10.5 s and the recovery time if 41.0 s for RH range of 86 % RH to 23 %RH. Capacitive Humidity Sensor Applications of Lead-Free Ca,Mg,Fe,Ti-Oxides-Based Electro-Ceramics with Improved Sensing Properties via Physisorption developed by Tripathy *et al* observed a response time of 14.5 s and recovery 34.27 s for 33%–95 % relative humidity range. However, capacitive humidity sensors present sensitivity in the range from 0.005 pF/% RH to 0.077 pF/% RH, with response times between 4 s and 47 s (Du *et al*., 2004, Lee *et al*., 2011 and Hernández-Rivera *et al*., 2017).

6. Calibration of the Unannealed Nanostructured ZnO capacitive RH Sensor Using the Five Saturated Salt Solutions

Table 4.12 summarized the capacitance values and the corresponding relative humidity values measured by the unannealed nanostructured ZnO capacitive RH sensor in the five micro

humidity environments. Figure 4.29 is a graph of capacitance (pF) versus corresponding relative humidity (%).

Table 4.12 Capacitance and corresponding RH measured by unannealed nanostructured ZnO capacitive RH sensor in saturated salt solutions (micro humidity environment)

Saturated Salt Solutions	**Capacitance (pF)**	**Relative Humidity (%)**
Lithium Chloride	9.4	13
Potassium Carbonate	11.3	58
Sodium chloride	13.9	86
Potassium Chloride	17.6	87
Potassium Sulphate	22.6	95

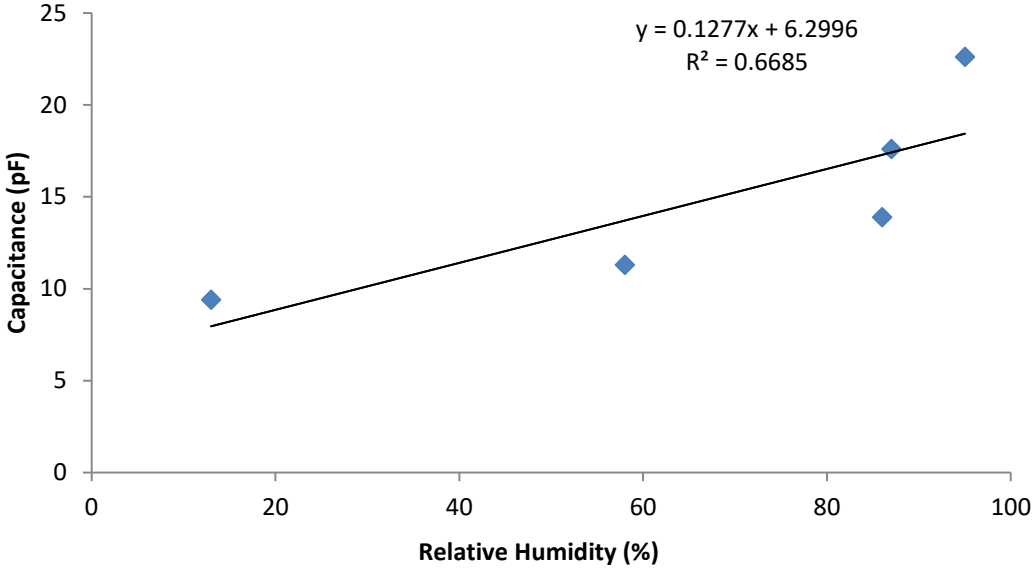

Figure 4.29 Capacitance versus RH measured by unannealed nanostructured ZnO capacitive RH sensor in LiCl, K_2CO_3, NaCl, KCl and K_2SO_4 in micro humidity environments

$y = 0.1277x + 6.2996$ 4.11

$R^2 = 0.6685$

The graph displays a linear relationship between the capacitance and relative humidity. R^2 specified that the linearity of the sensor was only 66.85 %. The fact that the relationship was not 100 % linear necessitated a kind of error analysis or determination of the accuracy of the unannealed sensor and its sensitivity.

7. Determination of the accuracy and sensitivity of the unannealed nanostructured ZnO capacitive RH sensor

The root mean square error (RMSE) was used to characterize the sensor's accuracy. The RMSE of the unannealed nanostructured ZnO capacitive RH sensor was calculated using equation 3.5. Table 4.5 compares the reference relative humidity values of the saturated salt solutions and relative humidity values measured by the unannealed nanostructured ZnO capacitive relative humidity sensor and the associated errors in measurement.

Table 4.5 Reference RH and RH measured by unannealed nanostructured ZnO capacitive RH sensor and the associated errors

Reference RH		**Unannealed Sensor**	
Saturated Salt Solution	**I (%)**	**O (%)**	**Error**
Lithium Chloride	11.30	13	1.70
Potassium Carbonate	43.16	58	14.84
Sodium chloride	75.30	86	10.70
Potassium Chloride	84.34	87	2.66
Potassium Sulphate	97.30	95	2.30
RMSE			**8.367**

The RMSE was high which depicted low accuracy of the sensor as revealed in Figure 4.29.

The sensitivity of the unannealed nanostructured ZnO capacitive relative humidity sensor to relative humidity variations was determined using equations 3.6.

$$\Rightarrow S = \frac{22.6-9.4}{95-13}$$

$$= 0.161$$

It implies therefore that the unannealed sensor experienced 0.161 pF change in capacitance per 1 % change in relative humidity. The sensitivity of the unannealed nanostructured ZnO capacitive relative humidity sensor was improved when compared with 0.005 pF/ % RH to 0.077 pF/ % RH for capacitive RH sensors recorded by Du *et al*. (2004), Lee *et al*. (2011) and

Hernández-Rivera *et al*. (2017) in investigation on capacitive humidity sensor based on an electrospun PVDF/graphene membrane.

8. Error Correction and Calibration of the Unaanealed Nanostructured ZnO Relative Humidity Sensor

The RMSE error in the unannealed nanostructured ZnO capacitive RH sensor was corrected using the sensitivity (S) of the sensor. Equation 3.5 was used to form Table 4.6 which contains the reference RH of each saturated salt solution and their correct corresponding capacitance values.

Table 4.6 Reference RH and capacitance for final calibration of unannealed nanostructured ZnO capacitive relative humidity sensor

Saturated Slat Solution	Reference RH (I)	Capacitance (C_I) pF
Lithium Chloride	11.30	1.81930
Potassium Carbonate	43.16	6.94876
Sodium chloride	75.30	12.12330
Potassium Chloride	84.34	13.57874
Potassium Sulphate	97.30	15.66530

Figure 4.30 displays the calibration curve of unannealed nanostructured ZnO capacitive RH sensor. The value of R^2 was 1 which confirmed 100 % linearity of the sensor. The slope of the graph was equal to the sensitivity(S) which confirmed it as the constant of proportionality. The intercept was 1.0×10^{-14} pF/ %RH which implied that error in the sensor was very negligible.

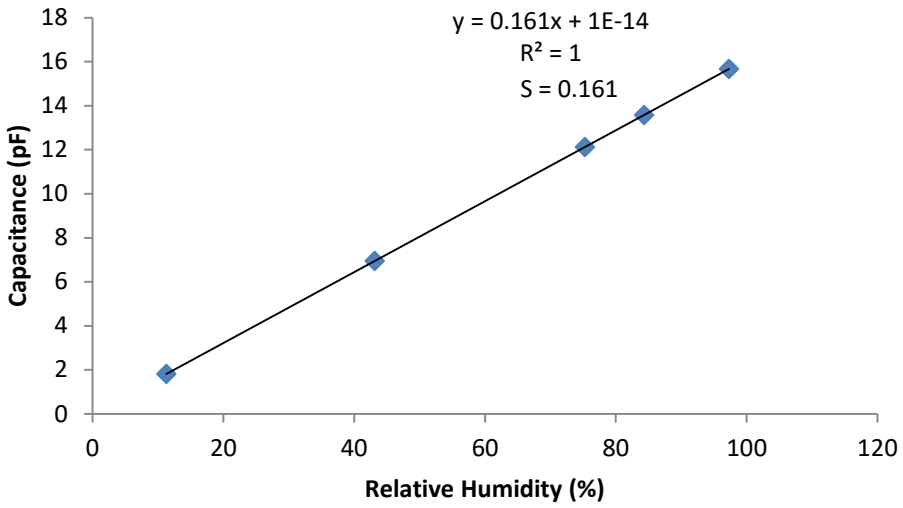

Figure 4.30 Calibration curve of unannealed nanostructured ZnO capacitive RH sensor

The scale was expanded to accommodate RH values ranging from 0 %RH to 100 %RH using Table 4.7. Table 4.7 was developed using arbitrary values of relative humidity and finding their equivalent values using equation 4.14. The calibration curve for humidity range of 0 %RH of 100 %RH for unannealed nanostructured ZnO capacitive RH sensor is shown in Figure 4.31.

Table 4.7 Expanded scale for the calibration of unannealed nanostructured ZnO capacitive RH sensor

Capacitance (pF)	0	1.61	3.22	4.83	6.44	8.05	9.66	11.27	12.88	14.49	16.10
Relative Humidity (%)	0	10	20	30	40	50	60	70	80	90	100

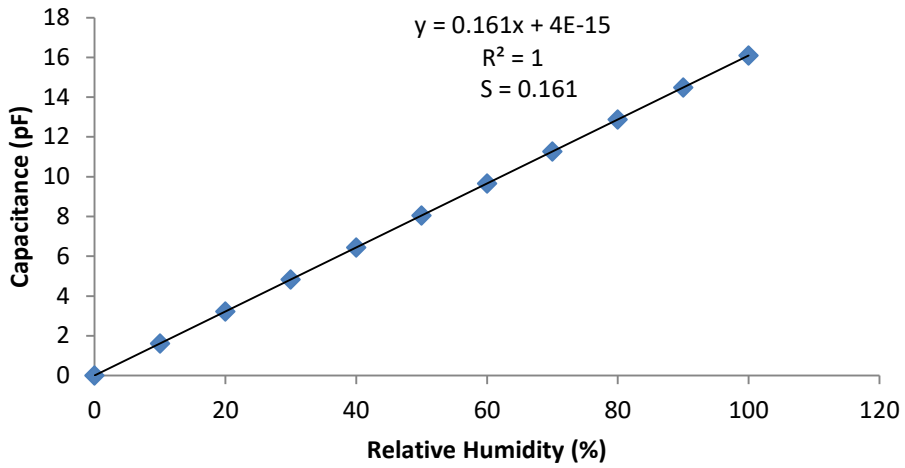

Figure 4.31 Calibraion curve of unannealed nanostructured ZnO capcitive RH sensor for RH range of 0 %RH to 100 %RH

The graph can be used to read any relative humidity value ranging from 0 % to 100 %.

4.6.2 Calibration of Nanostructured ZnO Capacitive Relative Humidity Sensor Annealed at 150 ^{0}C

The nanostructured ZnO capacitive relative humidity sensor was calibrated using the five micro humidity environments and analyzed in terms of its linearity, response and recovery times, standard deviation, accuracy and sensitivity.

1. **Calibration of the Nanostructured ZnO Capacitive RH Sensor Annealed at 150 ^{0}C Using Saturated Solution of Lithium Chloride (LiCl)**

Figures 4.32a and 4.32b show the capacitance of the nanostructured ZnO capacitive relative humidity sensor annealed at 150 ^{0}C as a function of relative humidity values using saturated solution of LiCl. The equations of adsorption (4.12) and desorption (4.13) curves were linear

The coefficient of determination (R^2) of 0.5097 indicated that 50.97 % of the points plotted fell within the regression line of humidity range of 14 %RH to 69 %RH and capacitance range of

8.7 pF and 10.5 pF. The standard deviation (SD) = 0.31595. The sensitivity (S_A) was 0.207. The sensor at adsorption stage experienced reduction in humidity from 69 %RH to constant value of 14 %RH. Hence the observed humidity value corresponding to the reference relative humidity was 14 %RH.

The coefficient of determination (R^2) during desorption was 0.8511 showing that 85.11 % of the points were within the regression line of humidity range of 14 %RH and 79 %RH and capacitance range of 9.4 pF and 10.7 pF. The standard deviation (S) was 0.32298. The sensitivity (S_D) was 0.138. The sensor exhibited a better performance during desorption than during adsorption with higher linearity, better spacing of capacitance values and higher sensitivity.

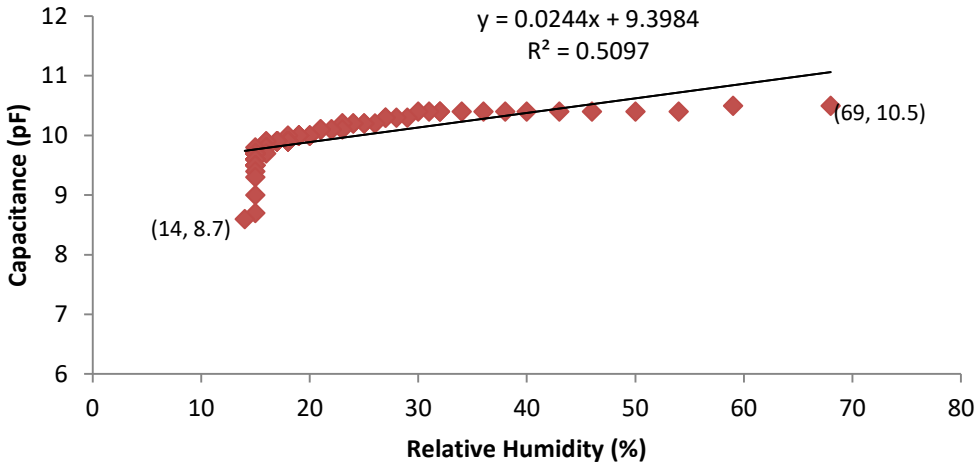

Figure 4.32a Adsorption curve of nanostructured ZnO capacitve RH sensor annealed at 150 ^{0}C in LiCl micro humidity environment

$$y = 0.0244 + 9.3984 \qquad 4.12$$

$R^2 = 0.5097$, SD = 0.31595, $S_A = 0.207$

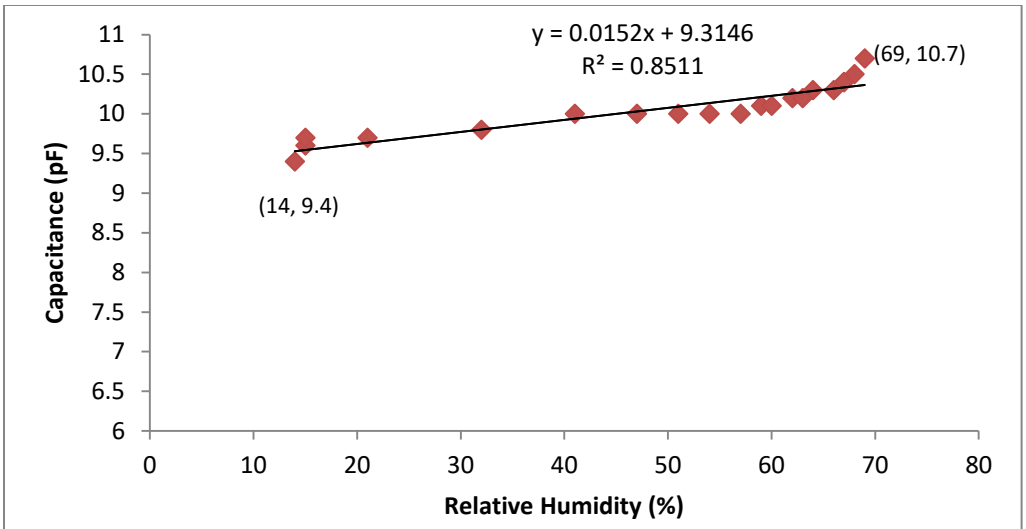

Figure 4.32b Desorption curve of nanostructured ZnO capacitive RH sensor annealed at 150 ^{0}C in LiCl micro humidity environment

$y = 0.0152x + 9.3146$ 4.13

$R^2 = 0.8511$, SD = 0.32298, $S_D = 0.138$

Figures 4.33a and 4.33b respectively show the response and recovery times of nanostructured ZnO capacitive relative humidity sensor annealed at 150 ^{0}C. The response time was 240 s or 4minutes within RH levels from 69 %RH to 14 %RH and capacitance variations of 8.6 pF and 10.5 pF.

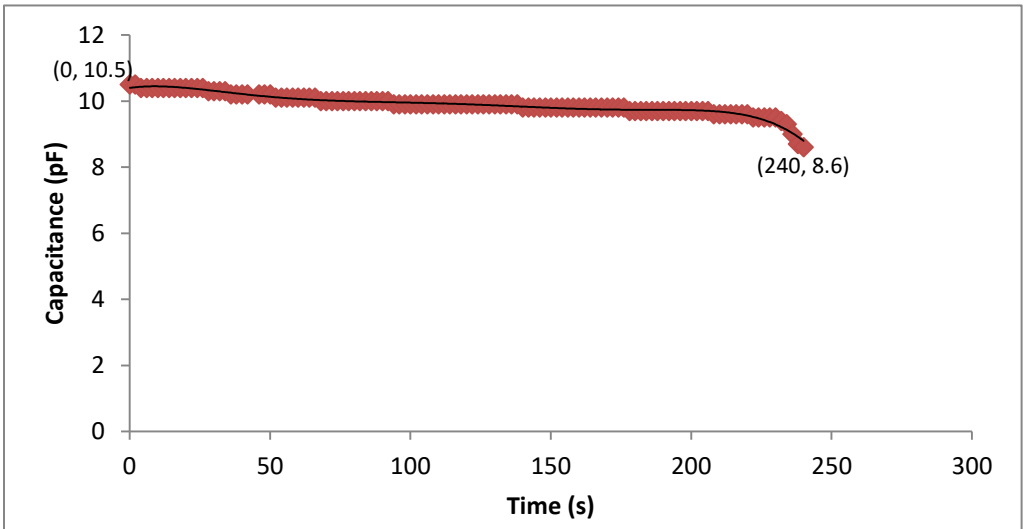

Figure 4.33a Response time of nanostructured ZnO capacitive RH sensor annealed at 150 ^{0}C in LiCl micro humidity environment

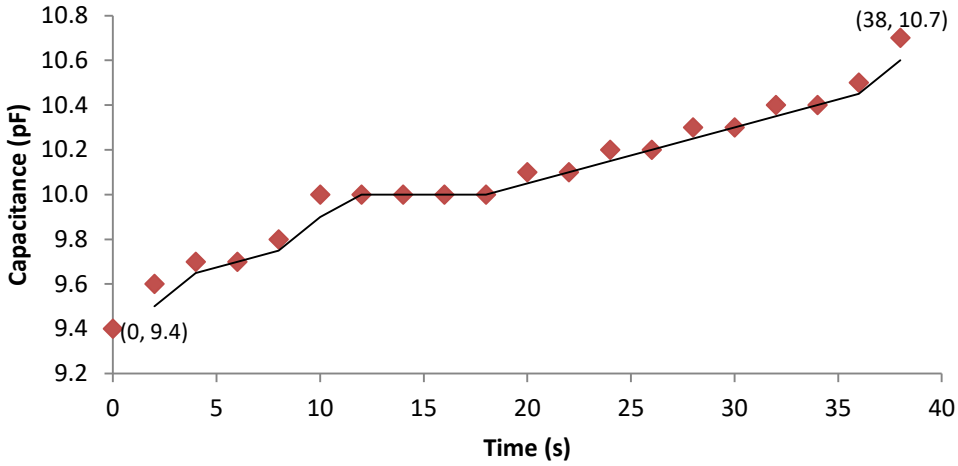

Figure 4.33b Recovery time of nanostructured ZnO capacitive RH sensor annealed at 150 ^{0}C in LiCl micro humidity environment

The recovery time was 38 s for the same RH range and capacitance range of 8.6 pF to 10.5 pF. The recovery of the sensor was faster compared to its response to humidity variations.

2. Calibration of the Nanostructured ZnO Capacitive Relative Humidity Sensor Annealed at 150 ^{0}C Using Saturated Solution of Potassium Carbonate (K_2CO_3)

The humidification of the sensor took place from 90 %RH to 57 %RH and from capacitance of 40.1 pF to 5.5 pF. The resultant relative humidity was 57 % and the capacitance was 5.5 pF. The adsorption curve was shown in Figure 4.34a. The fitted curve for desorption of moisture was determined by the fifth order polynomial equation displayed on the graph. The calibration equation (4.14) was established and R^2, SD and S_A were calculated from the graph. The sensor behaviour proved 72.56 % linear with SD of 3.263578 and sensitivity of 6.291. Figure 4.34b shows the behaviour of the sensor from 57 %RH to 90 %RH and capacitance of 5.5 pF to 40.9 pF during desorption. The sensor's behaviour was expressed in equation 4.15. The sensor

was found to be 99.49 % linear at desorption. The SD of the capacitance values was 13.87764 and had sensitivity of 6.436.

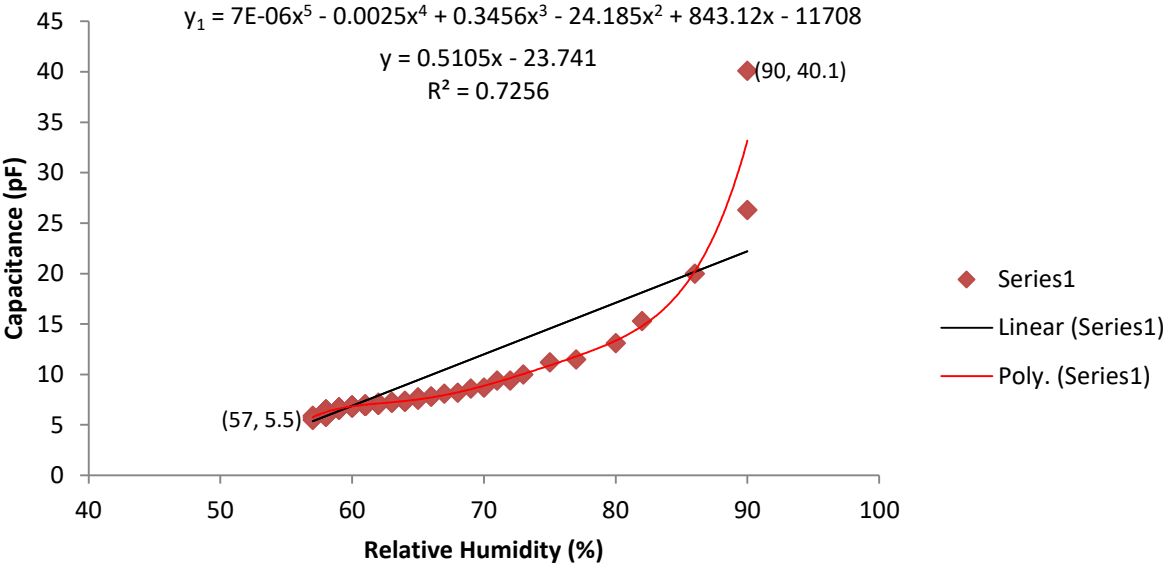

Figure 4.34a Adsorption curve of nanostructured ZnO capacitive RH sensor annealed at 150 ^{0}C in K_2CO_3 micro humidity environment

$$y = 0.5105x - 23.741 \qquad 4.14$$

$R^2 = 0.7256$, SD = 3.263578, $S_A = 6.291$

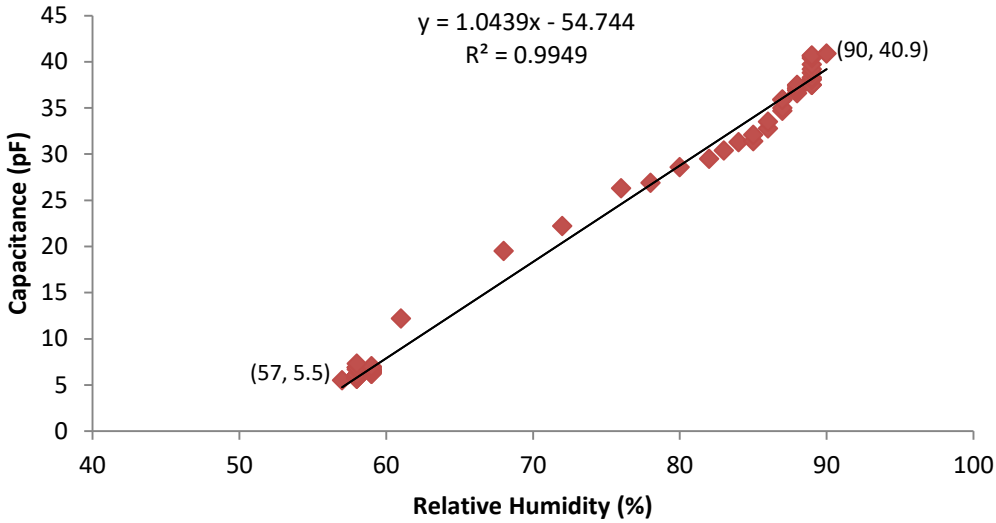

Figure 4.34b Desorption curve of nanostructured ZnO capacitive RH sensor annealed at 150 ^{0}C in K_2CO_3 micro humidity environment

$y = 1.0439x - 54.744$ 4.15

$R^2 = 0.99.49$, SD = 13.87764, $S_D = 6.436$.

The sensor's performance during desorption was much better than during adsorption with higher linearity, higher standard deviation and higher sensitivity.

The response time was shown in Figure 4.35a whereas the recovery time was shown in figure 4.35b. The response time was 352 s or 5.87 minutes for RH changes of 90 % to 57 % and capacitance changes of 40.1 pF to 5.5 pF. The sensor recovered from humidification in 188 s or 3.13 minutes for the same humidity range and capacitance range of 5.5 pF to 40.9 pF. The recovery of the sensor was faster than its response to humidity variations during adsorption.

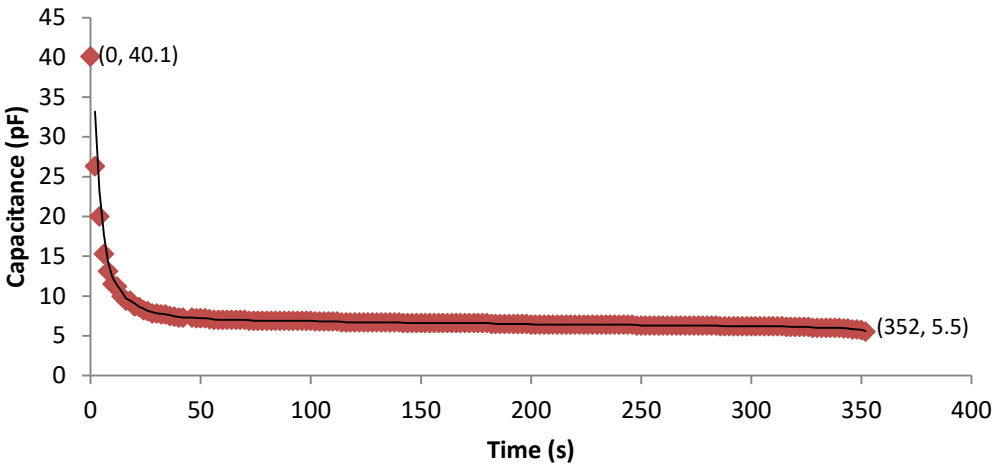

Figure 4.35a Response time of nanostructured ZnO capacitive RH sensor annealed at 150 ^{0}C in K_2CO_3 micro humidity environment

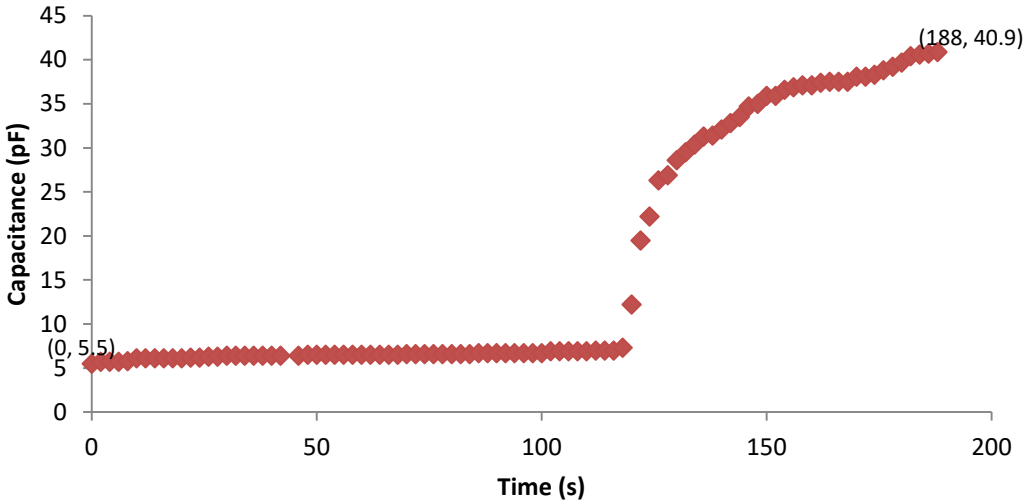

Figure 4.35b Recovery time of nanostructure ZnO capacitive RH sensor annealed at 150 ^{0}C in K_2CO_3 micro humidity environment

3. Calibration of the Nanostructured ZnO Capacitive Relative Humidity Sensor Annealed at 150 ^{0}C in NaCl micro humidity environment

Figure 4.36a shows the adsorption curve of nanostructured ZnO capacitive RH sensor annealed at 150 ^{0}C in NaCl micro humidity environment. Equation 4.16 expresses the relationship

between the RH measured by DHT11 sensor and capacitance measured by the nanostructured ZnO capacitive RH sensor. R^2 of 0.8318 demonstrated that the relationship was 83.18 % linear with standard deviation of 1.780087 and sensitivity of 0.453. Figure 4.36b shows the desorption curve of the sensor, the calibration equation (4.17) and R^2. The relationship between the RH and capacitance was 85.26 % linear. The standard deviation was 4.453518 and sensitivity was 0.670. The observed humidity value was 87 %RH and capacitance equivalent was 26.7 pF. Desorption of moisture was more linear with higher spacing of values and greater sensitivity than adsorption of moisture by the sensor.

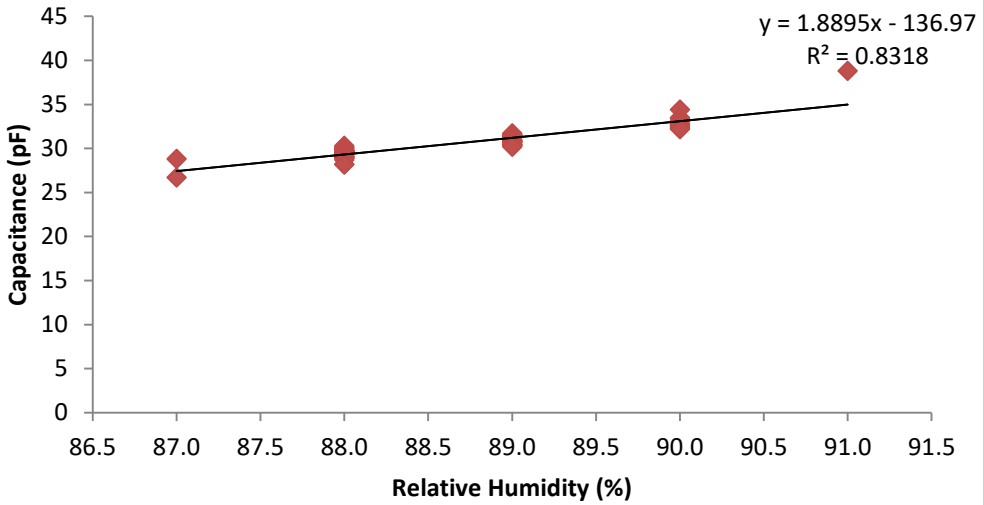

Figure 4.36a Adsorption curve of nanostructure ZnO capacitive RH sensor annealed at 150 ^{0}C in NaCl micro humidity environment

$$y = 1.8895x - 136.97 \qquad 4.16$$

$R^2 = 0.8318$, SD = 1.780087, $S_A = 0.453$

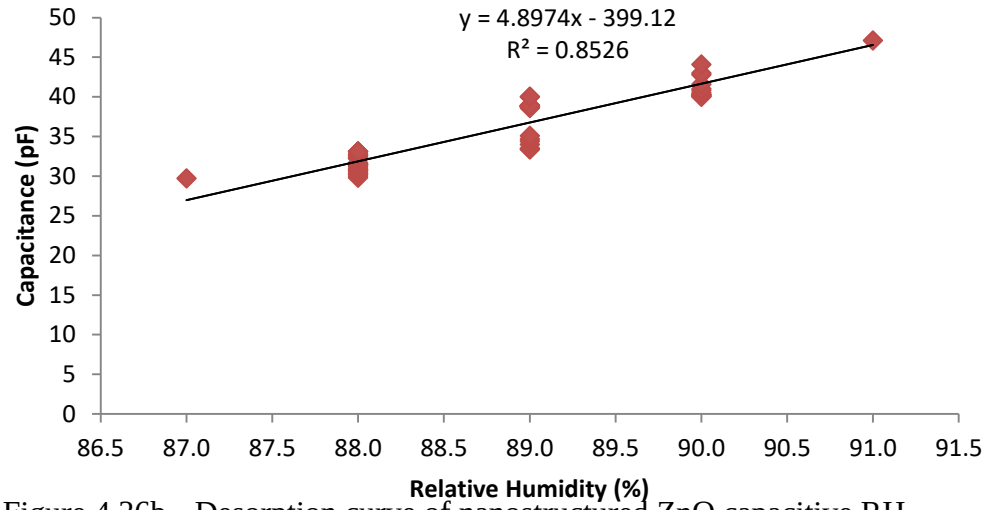

Figure 4.36b Desorption curve of nanostructured ZnO capacitive RH sensor annealed at 150 ^{0}C in NaCl micro humidity environment

$$y = 4.8974X - 399.12 \qquad 4.17$$

$R^2 = 0.8526$, SD = 4.453518, $S_D = 0.670$

Figures 4.37a and 4.37b respectively represent the response time and recovery time of the sensor. It took the sensor 138s or 2.3minutes to attain the required RH level from 91 %RH to 87 %RH for capacitance range of 38.8 pF to 26.7 pF.

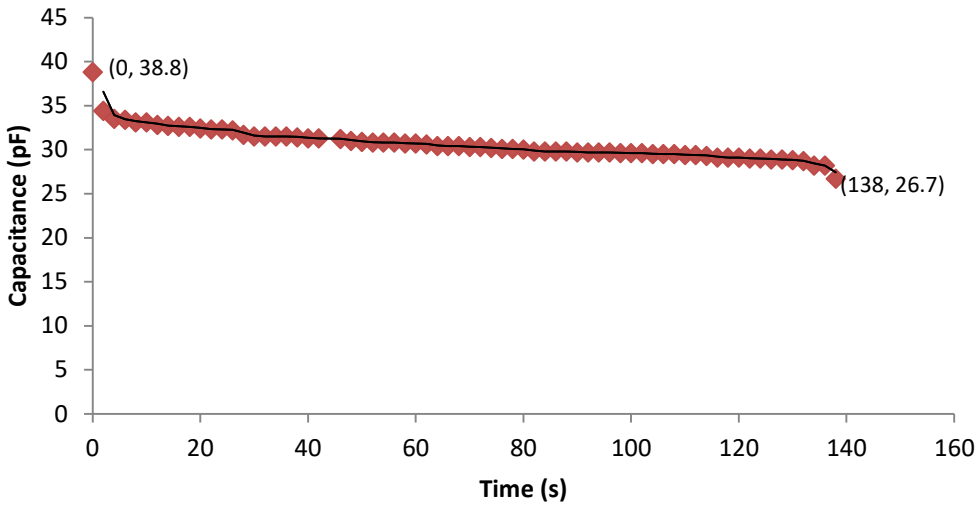

Figure 4.37a Response time of nanostructured ZnO capacitive RH sensor annealed at 150 ^{0}C in NaCl micro humidity environment

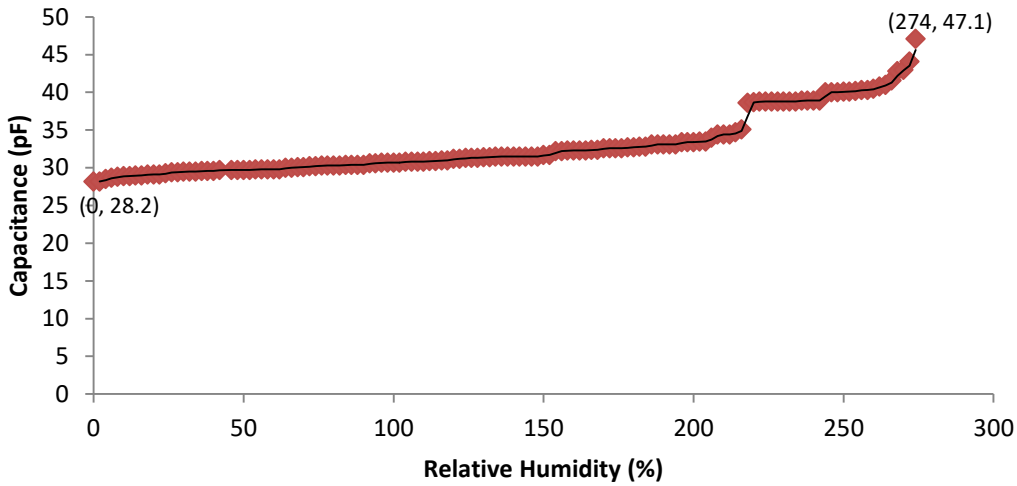

Figure 4.37b Recovery time of nanostructure ZnO capacitive RH sensor annealed at 150 ^{0}C in NaCl micro humidity environment

It took the sensor 274 s or 4.57 minutes to recover from 87 %RH to 91 %RH for capacitance range of 29.9 pF to 47.1 pF. The response time was shorter than the recovery time though with a shorter range of capacitance values.

4. Calibration of the Nanostructured ZnO Capacitive Relative Humidity Sensor Annealed at 150 ^{0}C Using Saturated Solution of Potassium Chloride (KCl)

The performance of the sensor during the adsorption of moisture was shown in Figure 4.38a. The calibration equation (4.18) and the parameters R^2, SD and S_A were determined and recorded. The graph was 91.54 % linear with SD of 4.489021 and S_A of 2.143. The observed RH was 87 %RH with capacitance equivalent of 33.0 pF.

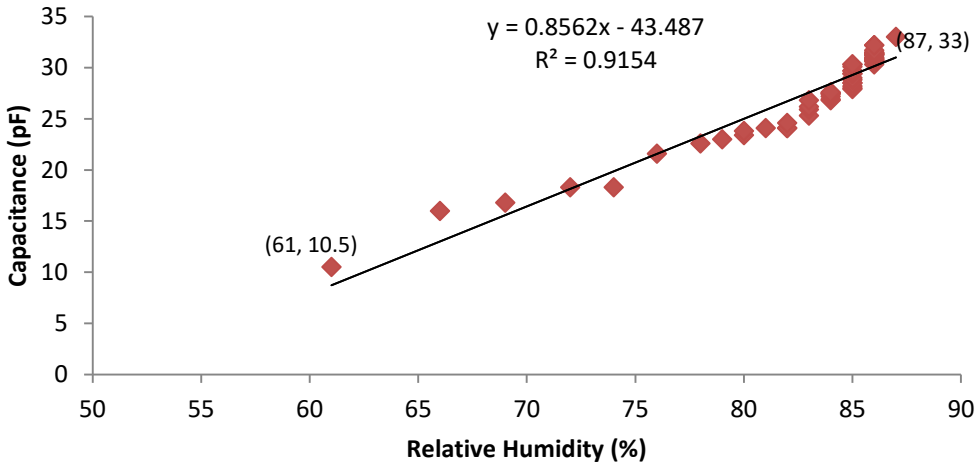

Figure 4.38a Adsorption curve of nanostructured ZnO capacitive RH sensor annealed at 150 ^{0}C in KCl micro humidity environment

$y = 0.8562 – 43.487$ 4.18

$R^2 = 0.9154$, SD = 4.489021, $S_A = 2.143$

Figure 4.38b illustrated the behaviour of the nanostructured capacitive RH sensor annealed at 150 ^{0}C during desorption. The best fit for the curve is established by fifth order polynomial equation displayed on the graph. The equation for the calibration was expressed in equation 4.19. R^2, SD and S_D were determined and are listed below. The correlation between the RH and

capacitance of the sensor was 85.18% linear with SD of 6.462520 and S_D of 3.853. The variation of the RH with capacitance was more linear during adsorption compared to the variation during desorption. The higher SD and S_D during desorption showed better spacing of capacitance values and greater sensitivity of the sensor during desorption.

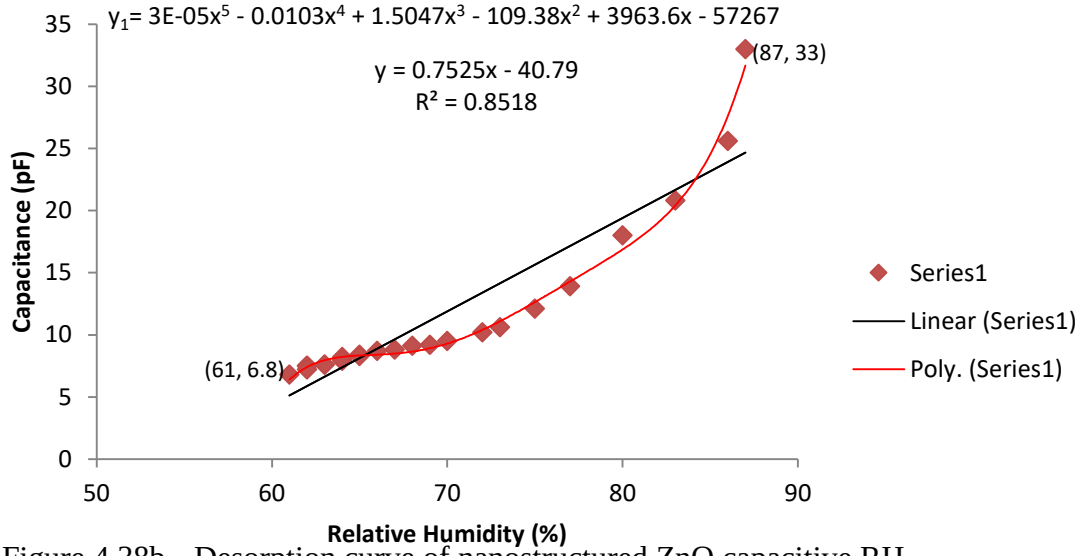

Figure 4.38b Desorption curve of nanostructured ZnO capacitive RH sensor annealed at 150 ^{0}C in KCl micro humidity environment

$$y = 0.7525 – 40.79 \qquad 4.19$$

$R^2 = 0.8518$, SD = 6.462520, $S_D = 3.853$

The response and recovery times were demonstrated in Figures 4.39a and 4.39b respectively. The time taken by the sensor to respond to the required RH values from 61 %RH to 87 %RH and capacitance variations from 10.5 pF to 33 pF was 126 s or 2.1 minutes. The recovery time was 50 s or 0.83 minute for the same RH range and capacitance range of 6.8 pF to 33.0 pF. The recovery time was faster and it covered wider range of capacitance values.

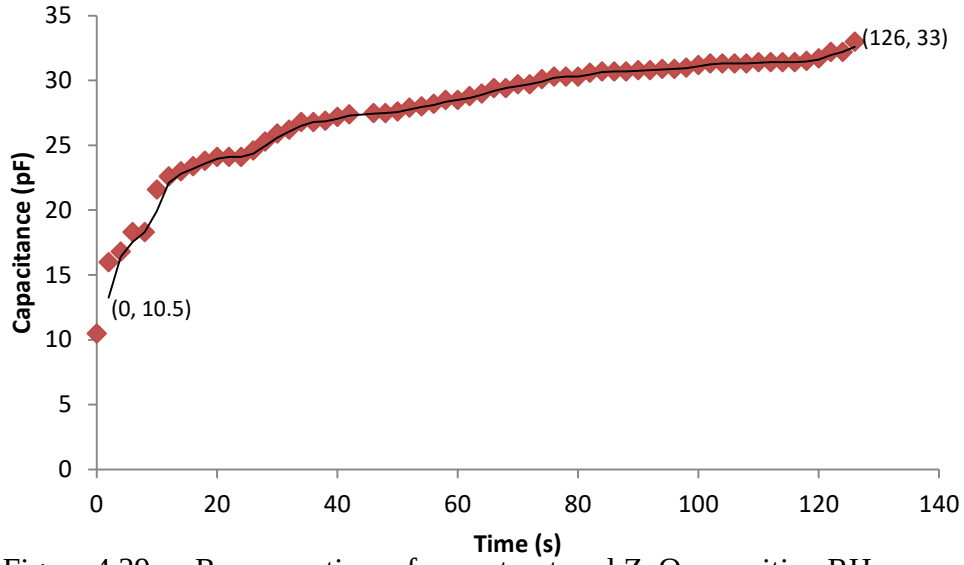

Figure 4.39a Response time of nanostructured ZnO capacitive RH sensor annealed at 150 ^{0}C in KCl_2 micro humidity environment

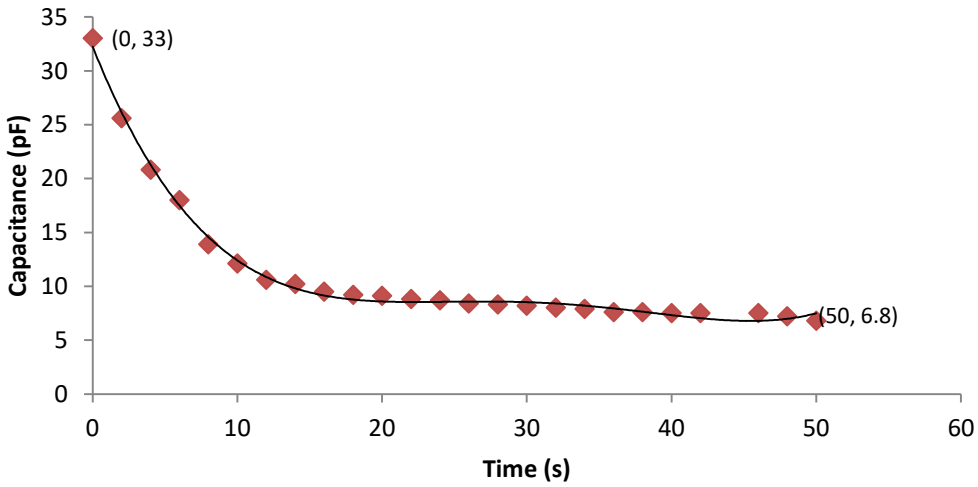

Figure 4.39b Recovery time of nanostructured ZnO capacitive RH sensor annealed at 150 ^{0}C in KCl micro humidity environment

5. Calibration of the Nanostructured ZnO Capacitive Relative Humidity Sensor Annealed at 150 ^{0}C Using Saturated Solution of Potassium Sulphate (K_2SO_4)

Figure 4.40a shows the adsorption curve of nanostructured ZnO capacitive relative humidity sensor annealed at 150 ^{0}C in K_2SO_4 micro humidity environment. Equation 4.20 expressed the relationship between the capacitance and relative humidity during adsorption of moisture. R^2 for the curve was 0.957 showing 95.7 % linearity of the curve. SD was 20.72181 which showed a very good spacing of the capacitance values. S_A was found to be 4.197. The required RH humidity corresponding to the reference RH was 95 %RH.

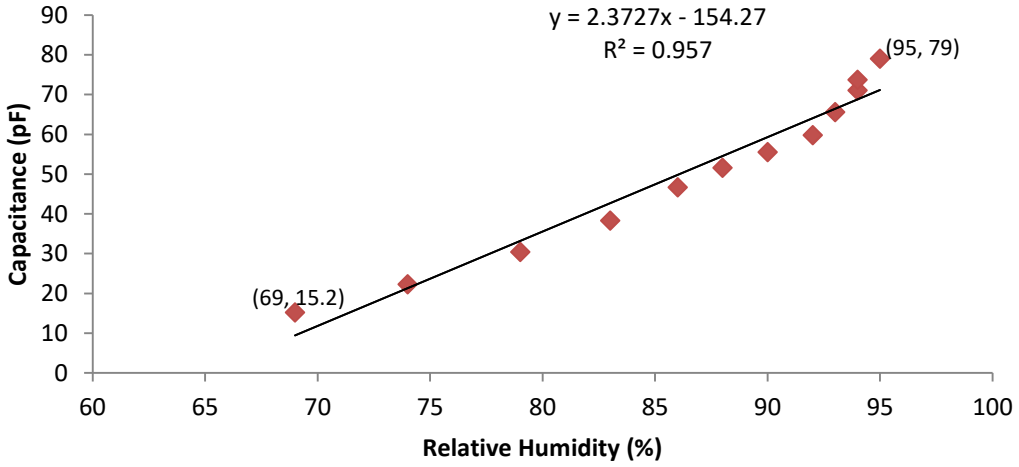

Figure 4.40a Adsorption curve of nanostructured ZnO capacitive RH humidity sensor annealed at 150 ^{0}C in K_2SO_4 micro humidity environment

$$y = 2.3727x - 154.27 \qquad 4.20$$

$R^2 = 0.957$, SD = 20.72181, $S_A = 4.197$

Figure 4.40b is the desorption curve of nanostructured ZnO capacitive RH sensor annealed at 150 ^{0}C in K_2SO_4 micro humidity environment. The fitted curve for desorption of moisture was determined by the second order polynomial equation displayed on the graph. The calibration equation (4.21) was linear by 89.24 % as specified by R^2 of 0.8924. It had wide dispersion of capacitance values, hence SD of 20.12253. S_D was 6.823 which gave a good sensitivity of the sensor.

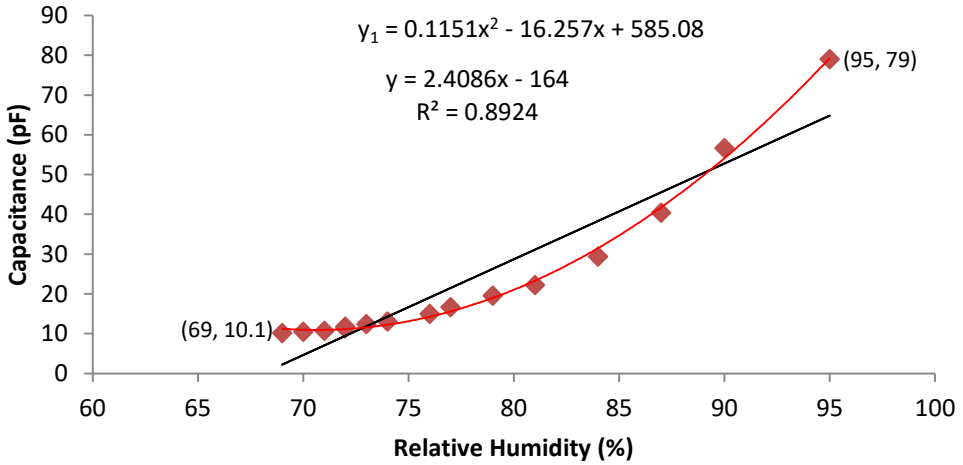

Figure 4.40b Desorption curve of nanostructured ZnO capacitive RH sensor annealed at 150 ^{0}C in K_2SO_4 micro humidity environment

$$y = 2.4086x - 164 \qquad 4.21$$

$R^2 = 0.8924$, SD = 20.12253, $S_D = 6.823$

Comparing the performances of the sensor in adsorption and desorption, it was observed that the sensor had an excellent and better linearity and wider spacing of capacitance values in adsorption. However, the sensitivity of the sensor was higher during desorption.

Figure 4.41a shows the response time of the nanostructured ZnO capacitive RH sensor annealed at 150 ^{0}C for RH range of 69 %RH and 95 %RH and capacitance variations of 15.2 pF and

79 pF. The response time was 22 s. Figure 4.41b displays the recovery time of the sensor for the same RH range and capacitance variations of 10.1 pF and 79 pF. The sensor recovered from humidification in 28 s. The response time was shorter than the recovery time though with shorter capacitance range.

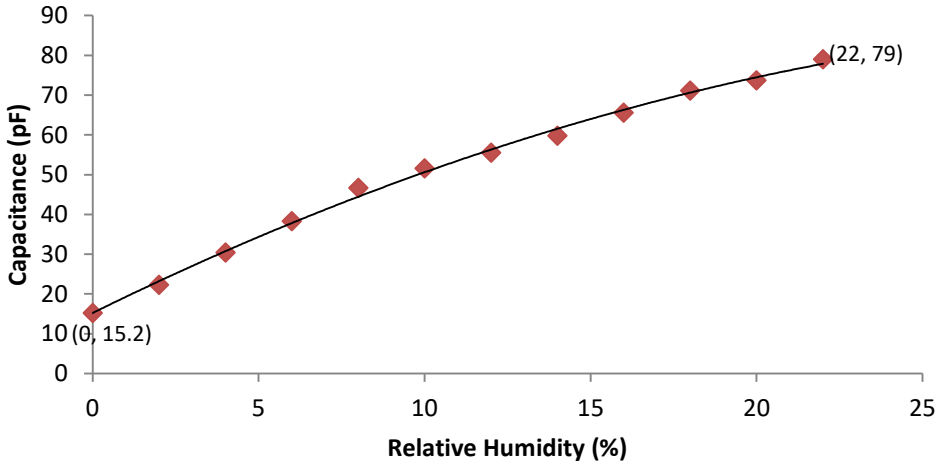

Figure 4.41a Response time of nanostructure ZnO capacitive RH sensor annealed at 150 ^{0}C in K_2SO_4 micro humidity environment

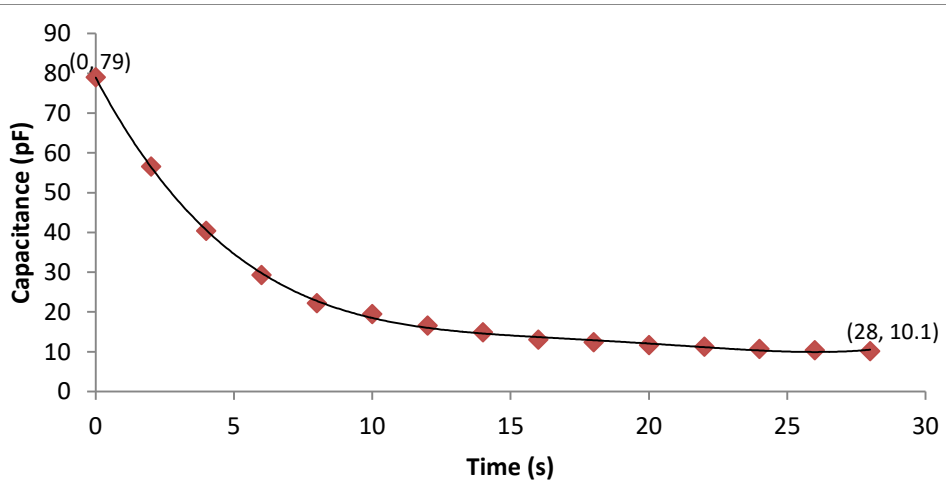

Figure 4.41b Recovery time of nanostructured ZnO capacitive RH sensor annealed at 150 ^{0}C in K_2SO_4 micro humidity environment

The results showed different response times ranging from 22 s for K_2SO_4 352 s for K_2CO_3 and recovery time of 28 s for K_2SO_4 to 188 s for K_2CO_3 for different humidity values ranging from 14 %RH to 95 %RH. This differs from the findings of Hong *et al*. (2019) that capacitive humidity sensor with a shielding electrode under the interdigitated electrode (SIDE) based on polyimide (PI) had the response and recovery times of 20 s and 22 s respectively. It differs greatly from response time of 1s and recovery time of 15 s of high sensitivity capacitive humidity sensor with a novel polyimide reported by Kim *et al*. (2009). The disparities in response and recovery times are as a result of variations in manufacturing processes used, RH humidity ranges and RH environments among others.

6. Calibration of the Nanostructured ZnO Capacitive RH Sensor Annealed at 150 ^{0}C Using the Five Micro Humidity Environments

The observed RH values in the five micro humidity environments and their equivalent capacitance values were used for the actual calibration of the nanostructured ZnO capacitive RH sensor annealed at 150 ^{0}C. Table 4.8 contains the capacitance and corresponding RH measured in LiCl, K_2CO_3, NaCl, KCl and K_2SO_4 micro humidity environments recorded by nanostructured ZnO capacitive RH sensor annealed at 150 ^{0}C. The table was used to plot the graph in Figure 4.42 which shows how the capacitance varied with humidity.

Table 4.8 Capacitance and corresponding RH measured in the micro humidity environments by nanostructured ZnO capacitive RH sensor annealed at 150^{0}C

Micro Humidity Environment	**Capacitance (pF)**	**Relative Humidity (%)**
Lithium Chloride	8.7	14
Potassium Carbonate	5.7	57
Sodium chloride	28.8	87
Potassium Chloride	33.0	87
Potassium Sulphate	79.0	95

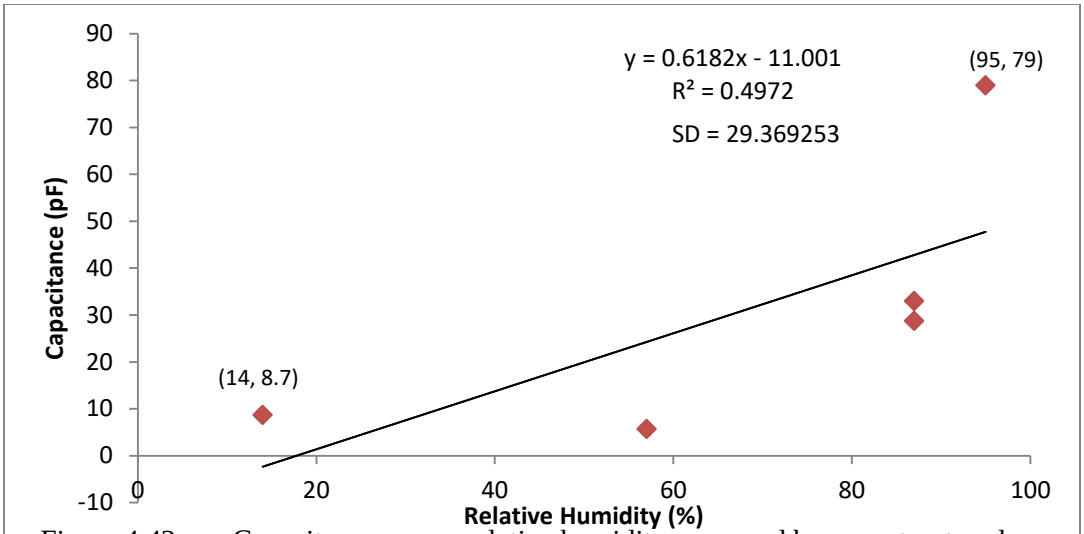

Figure 4.42 Capacitance versus relative humidity measured by nanostructured ZnO capacitive RH sensor in LiCl, K_2CO_3, NaCl, KCl and K_2SO_4 micro humidity environments

The calibration equation, R^2 and SD were determined and displayed on the graph. The R^2 of 0.4972 implied that linear relationship existed between the capacitance and RH values but only to 49.72 %. An error analysis was needed since the result was not 100 % linear. The high standard deviation (SD) of 29.369253 specified good spacing of the capacitance values of the sensor.

7. Determination of the Accuracy (RMSE) and Sensitivity of the Nanostructured ZnO Capacitive RH Sensor Annealed at 150^{0}C.

The reference RH values of the saturated salt solutions used in the study were compared with the observed or corresponding RH values measured by nanostructured ZnO capacitive RH sensor annealed at 150 ^{0}C. The related errors were calculated. The accuracy of the sensor was determined using RMSE. Table 4.9 gives the reference RH and RH recorded by nanostructured ZnO capacitive RH annealed at 150 ^{0}C and the associated errors.

Table 4.9 Reference RH and RH recorded by nanostructured ZnO capacitive RH annealed at 150 ^{0}C and the associated errors.

Reference RH		**Annealed Sensor (150 ^{0}C)**	
Saturated Salt Solution	**I (%)**	**O (%)**	**Error**
Lithium Chloride	11.30	14	2.70
Potassium Carbonate	43.16	57	13.84
Sodium chloride	75.30	87	11.70
Potassium Chloride	84.34	87	2.66
Potassium Sulphate	97.30	95	2.30
RMSE			**8.34**

The RMSE was 8.344. The high value of RMSE shows low accuracy of the sensor. Hence, the sensor required calibration to improve on its accuracy and obtain 100 % linearity.

The sensitivity (S) of the nanostructured ZnO capacitive relative humidity sensor annealed at 150 ^{0}C was determined using equation 3.12 and the value obtained was 0.868 /%RH. The sensitivity was high and good for the sensor compared to the sensitivity of the unannealed nanostructured ZnO capacitive relative humidity sensor and 0.005 pF/ % RH to 0.077 pF/ % RH for capacitive RH sensors recorded by Du *et al*. (2004), Lee *et al*. (2011) and Hernández-Rivera *et al*. (2017).

8. Error Correction and Calibration of the Nanostructured ZnO Capacitive Relative Humidity Sensor Annealed at 150^{0}C

The RMSE was corrected using equation 3.5. Equation 3.5 was also used to obtain the capacitance equivalents of the reference RH for the calibration of the nanostructured ZnO capacitive RH sensor. Table 4.10 was used for calibration of the sensor. Figure 4.43 shows the calibration curve for nanostructured ZnO capacitive RH sensor annealed at 150 ^{0}C.

Table 4.10 Reference RH and capacitance for the calibration of nanostructured ZnO capacitive relative humidity sensor annealed at 150 ^{0}C

Saturated Slat Solution	Reference RH (I)	Capacitance (C_I) pF
Lithium Chloride	11.30	9.80840
Potassium Carbonate	43.16	37.46288
Sodium chloride	75.30	65.36040
Potassium Chloride	84.34	73.20712
Potassium Sulphate	97.30	84.45640

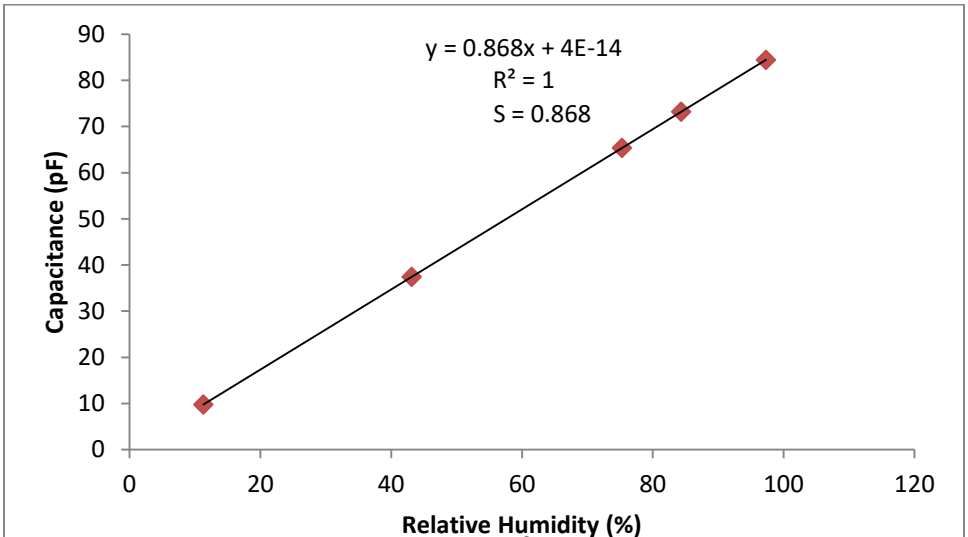

Figure 4.43 Calibration curve of nanostructured ZnO capacitive RH sensor annealed at 150 ^{0}C

$$y = 0.868 + 4E\text{-}14 \qquad (4.22)$$

R^2= 1, SD = 30.215562, S = 0.868

The correlation between the capacitance and the relative humidity was expressed in equation 4.22. R^2 was equal to 1which indicated that the graph was a perfect linear graph of 100 % linearity. This was confirmed with the sensitivity (s) of the sensor which had equal value with the slope of the graph with a very insignificant intercept of 4.0 x 10^{-14} pF/ %RH. The SD was 30.215562 which gave a very good variation of values for the sensor.

The scale of the sensor was expanded to read the humidity values of 0 %RH to 100 %RH. This was done by using arbitrary values of RH humidity and finding the equivalent values of capacitance using equation 3.5. The values were tabulated in Table 4.11 Figure 4.44 shows the calibration curve of nanostructured ZnO capacitive RH sensor annealed at 150 ^{0}C for RH range of 0 %RH and 100 %RH. The sensor can be used to record any RH variations within the range.

Table 4.11 Expanded scale for the calibration of nanostructured ZnO capacitive RH sensor annealed at 150 ^{0}C

Capacitance (pF)	0	8.68	17.36	26.04	34.72	43.4	52.08	60.76	69.44	78.12	86.8
Relative Humidity (%)	0	10	20	30	40	50	60	70	80	90	100

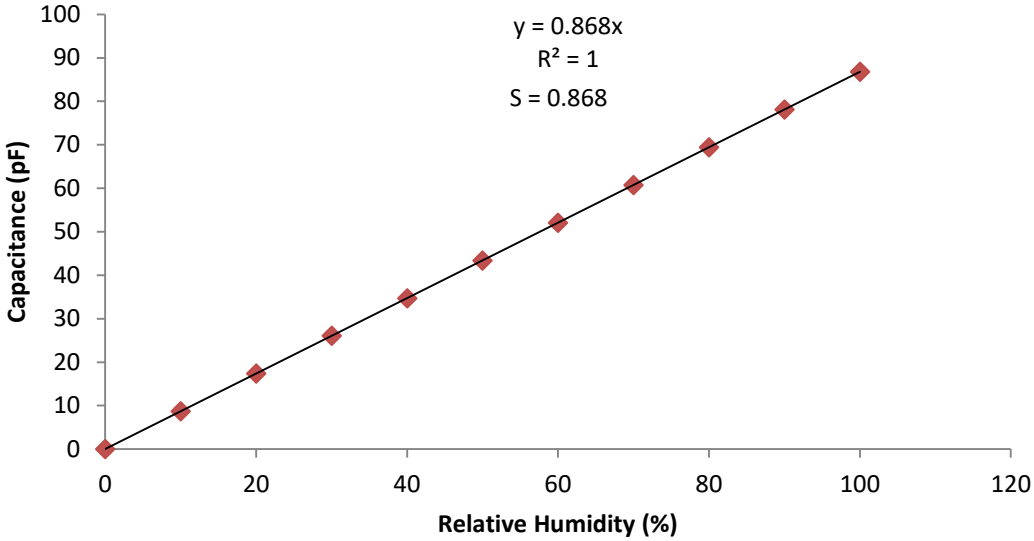

Figure 4.44 Calibration curve of nanostructured ZnO capacitive RH sensor annealed at 150 ^{0}C for RH range of 0 %RH and 100 %RH

4.6.3 Calibration of Nanostructured ZnO Capacitive Relative Humidity Sensor Annealed at 200 ^{0}C

The nanostructured ZnO capacitive relative humidity sensor annealed at 200 ^{0}C was calibrated using LiCl, K_2CO_3, NaCl, KCl, and K_2SO_4 micro humidity environments. The performance of

the sensor was analyzed in terms of its linearity, response time, recovery time, accuracy and sensitivity.

1. **Calibration of the Nanostructured ZnO Capacitive Relative Humidity Sensor Annealed at 200 ^{0}C Using LiCl Micro Humidity Environment**

Figures 4.45a and 4.45b explained the relationships between the variations of the capacitance values of the nanostructured ZnO capacitive relative humidity sensor annealed at 200 ^{0}C and the relative humidity values. Figure 4.46a shows the behavior of the sensor during the adsorption of moisture while Figure 4.46b shows its behavior during desorption.

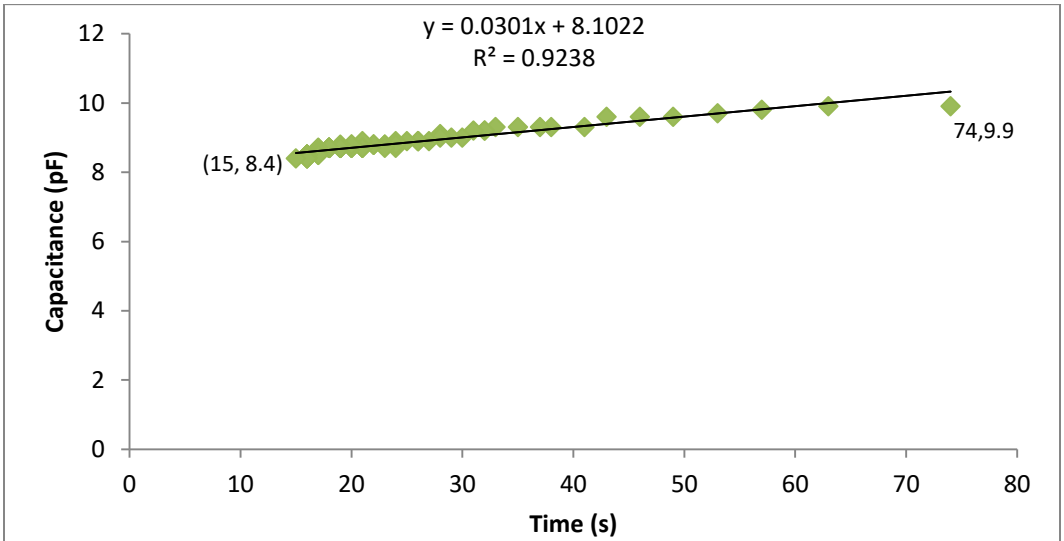

Figure 4.45a Adsorption curve of nanostructured ZnO capacitive RH sensor annealed at 200 ^{0}C in LiCł·micro humidity environment

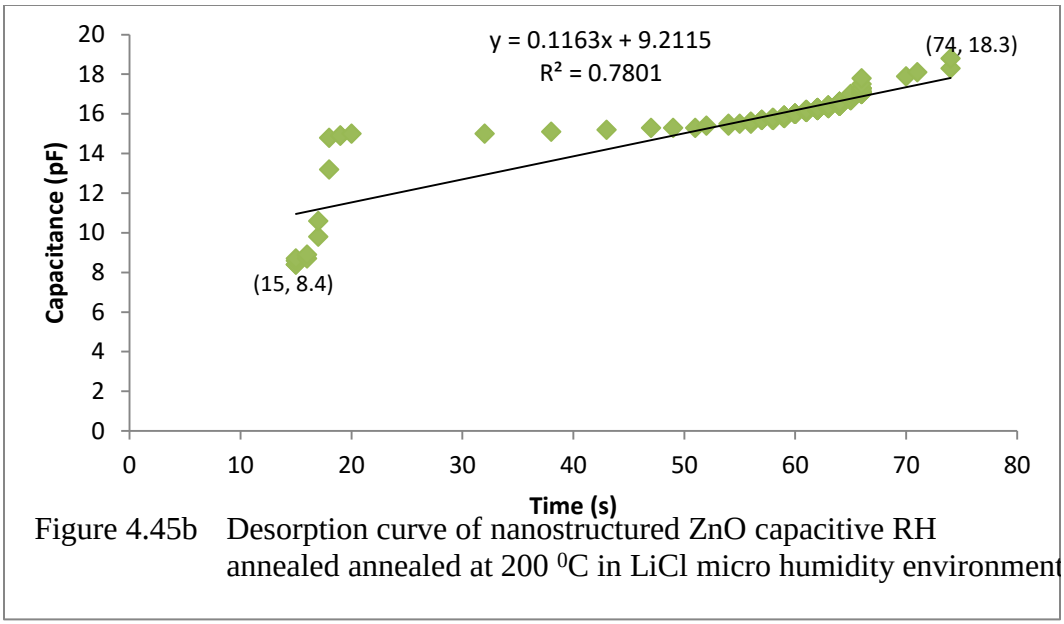

Figure 4.45b Desorption curve of nanostructured ZnO capacitive RH annealed annealed at 200 ^{0}C in LiCl micro humidity environment

The calibration equations are displayed on the graphs. The standard deviation (SD) and the sensitivity of the sensor were determined.

The calibration equation for adsorption of moisture was a linear equation. R^2 specified that the capacitance variation with changes in RH humidity was 92.38 % linear at adsorption. On the other hand, the capacitance variation with changes in RH was 78.01 % linear at desorption. Hence, the linearity was lower. The SD of the capacitance values was 0.333161 during adsorption compared to SD of 1.910764 for desorption for RH range of 15 %RH to 74 %RH. S_A was 0.179 compared to S_D of 1.179. The higher standard deviation and sensitivity during desorption presented wider and better variation of capacitance values during desorption of moisture. The required (observed) RH value of the sensor in LiCl micro humidity environment was 15 %RH with corresponding capacitance of 8.4 pF.

The response and recovery times are shown in Figures 4.46a and 4.46b respectively. The response time was 234 s or 3.9 minutes for RH range of 15 %RH to 74 %RH and capacitance

changes of 8.4 pF to 9.9 pF. The recovery time was 260 s or 4.3 minutes for the same RH range and capacitance changes of 8.4 pF to 18.8 pF. The response time of the sensor was faster.

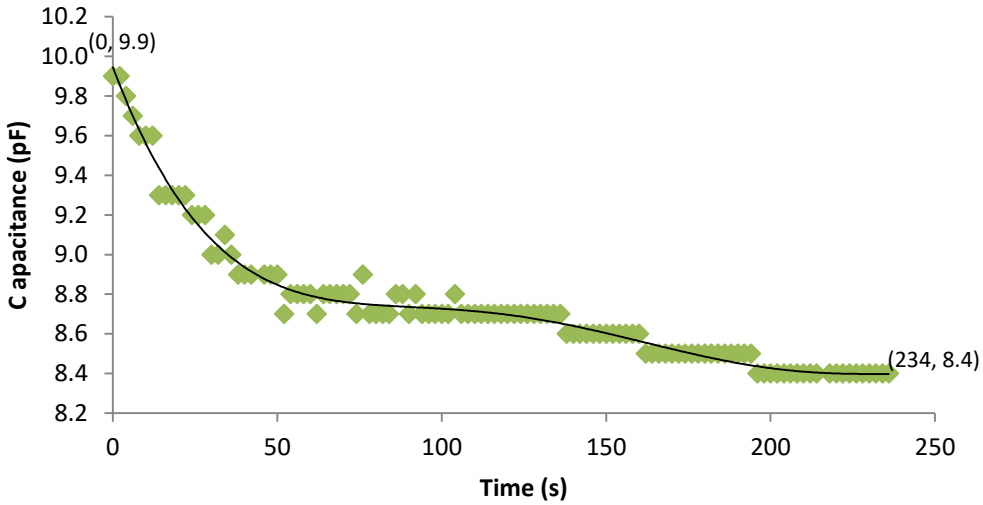

Figure 4.46a Response time of nanostructured ZnO capacitive RH sensor annealed at 200 ^{0}C in LiCl micro humidity environment

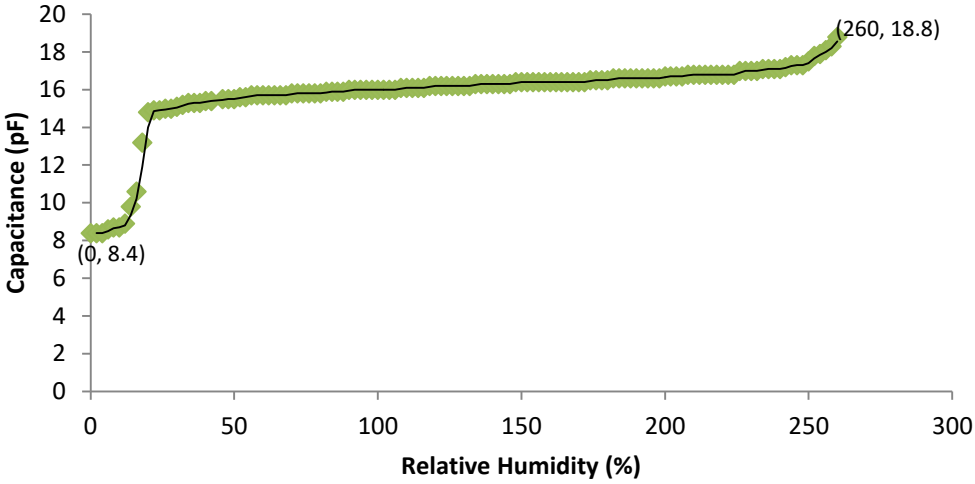

Figure 4.46b Recovery time for nanostructured ZnO capacitive RH sensor annealed at 200 ^{0}C in LiCl micro humidity environmen

2. Calibration of the Nanostructured ZnO Capacitive Relative Humidity Sensor Annealed at 200 ^{0}C Using K_2CO_3 Micro Humidity Environment

Figure 4.47a is the adsorption curve of nanostructured ZnO capacitive RH sensor annealed at 200 ^{0}C in K_2CO_3 micro humidity environment. Figure 4.47b shows the desorption curve. The fitted curve for desorption of moisture was determined by the forth order polynomial equation displayed on the graph. The calibration equations and R^2 values are presented on the graphs. R^2 adsorption curve was 0.9407 which specified that the graph was 94.07 % linear while R^2 for desorption curve was 0.6148 meaning that the curve was 61.48 linear. Therefore the linearity of the sensor was higher at adsorption. The SD and the sensitivity were calculated. The SD during adsorption was 5.381758 with sensitivity of 0.996. The SD during desorption was 18.501880 with sensitivity of 3.440. The sensor experienced higher sensitivity and wider dispersion at desorption.

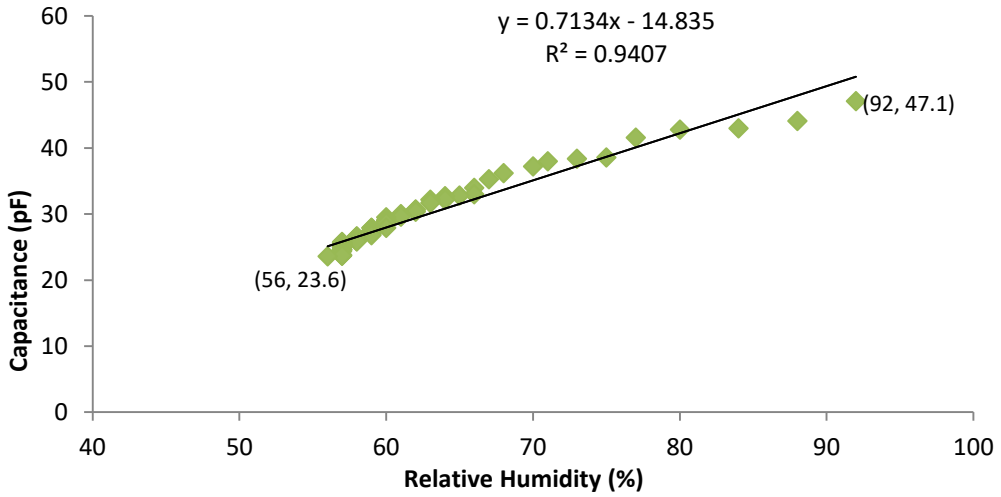

Figure 4.47a Adsorption curve of nanostructured ZnO capacitive RH sensor annealed at 200 ^{0}C in K_2CO_3 micro humidity environment

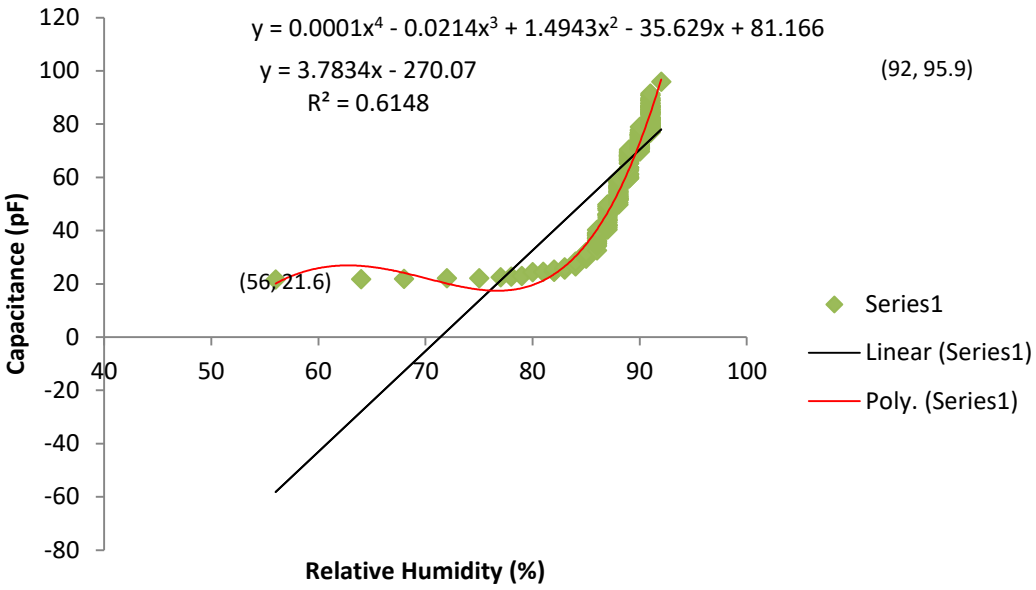

Figure 4.47b Desorption of nanostructure ZnO capacitive RH sensor annealed at 200^0C in K_2CO_3 micro humidity environment

Figure 4.48a presents the time it took the sensor to respond to RH changes from 92 %RH to 56 %RH. Figure 4.48b represents the time it took the sensor to recover from 56 %RH to 92 %RH. The response time was 152 s or 2.53 minutes while the recovery time was 562 s or 9.37 minutes. It took the sensor a longer time to recover but with higher capacitance values.

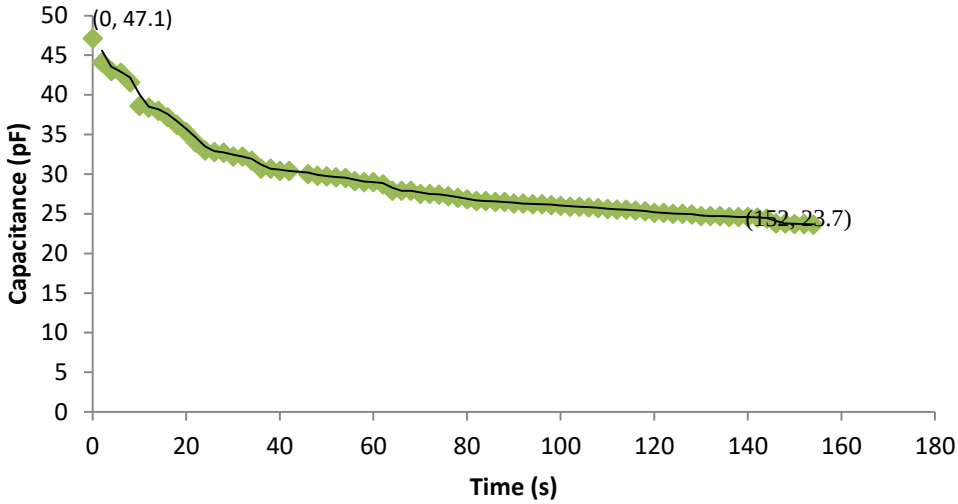

Figure 4.48a Response time of nanostructured ZnO capacitive RH sensor annealed at 200 ^{0}C in K_2CO_3 micro humidity environment

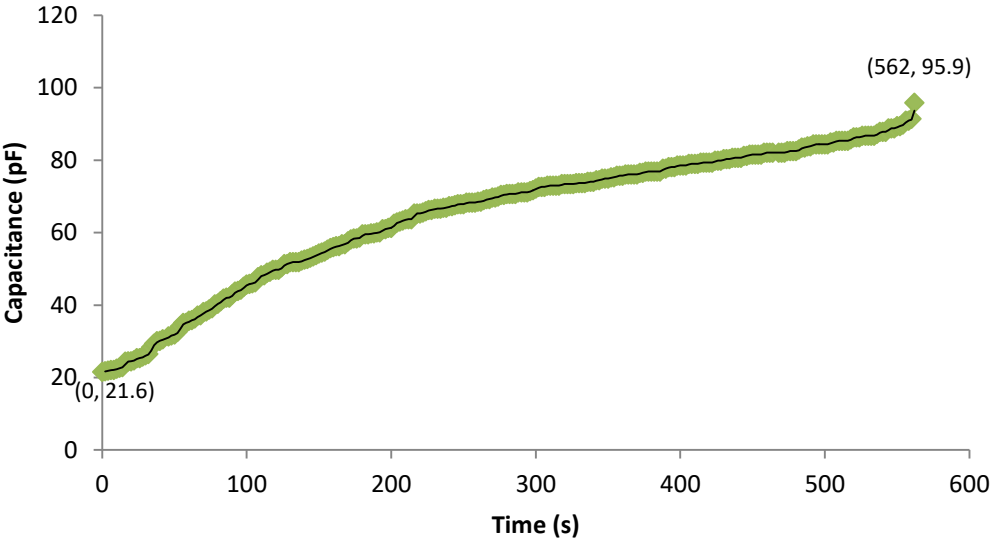

Figure 4.48b Recovery time of nanostructured ZnO capacitive RH sensor annealed at 200 ^{0}C in K_2CO_3 micro humidity environment

3. Calibration of the Nanostructured ZnO Capacitive Relative Humidity Sensor Annealed at 200 ^{0}C Using NaCl Micro Humidity Environment

The adsorption curve showing the relationship between capacitance and RH when the nanostructured ZnO capacitive RH sensor was used in NaCl micro humidity environment was

shown in Figure 4.49a. The fitted curve for adsorption of moisture was determined by the sixth order polynomial equation displayed on the graph. The relationship was expressed in equation 4.23. R^2 was 0.4285 which implied that the adsorption was only 42.85 % linear. SD was 4.448729 while S_A was 1.9611. Figure 4.49b shows the desorption curve of the sensor. Equation 4.24 expressed the relationship between capacitance and RH during desorption. R^2 indicated that the relationship was 89.89 % linear during adsorption. SD was 3.313640 which showed a lower dispersion of values of capacitance compared to what was obtained during adsorption. S_D was 0.657. The sensitivity of the sensor was also found higher during adsorption than what was obtained during desorption. The required (observed) RH in NaCl micro humidity environment recorded by the sensor was 85 %RH with associated capacitance of 35.3 pF.

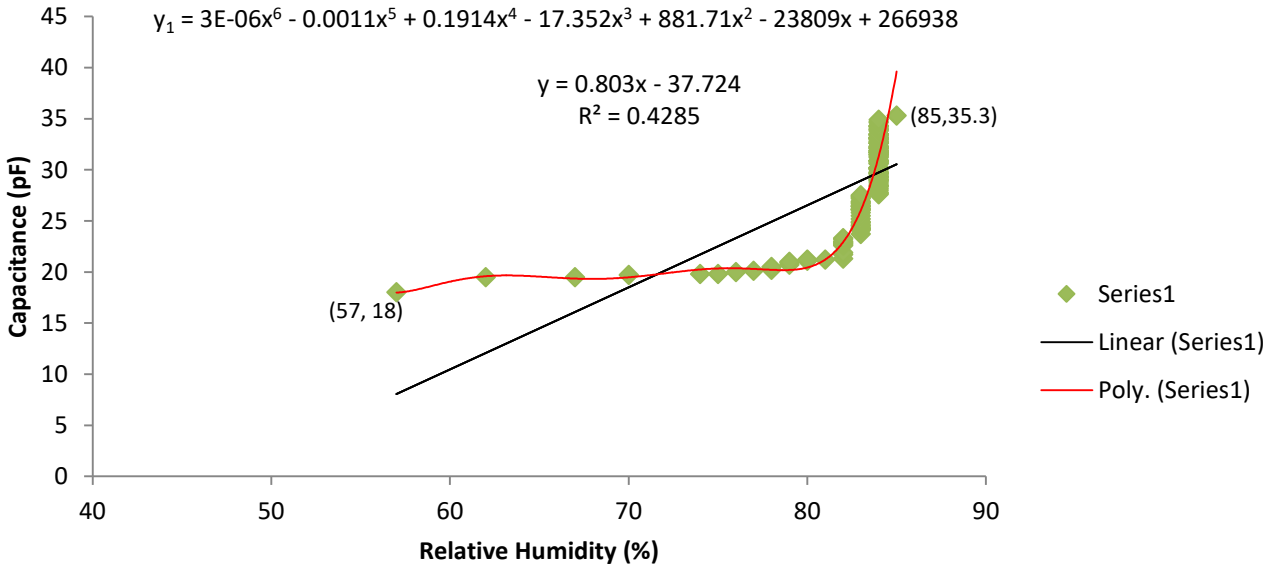

Figure 4.49a Adsorption curve of nanostructured ZnO capacitive RH sensor annealed at 200 ^{0}C in NaCl micro humidity environment

$$y = 0.803x - 37.724 \qquad 4.23$$

$R^2 = 0.4285$, SD = 4.448729, $S_A = 1.9611$

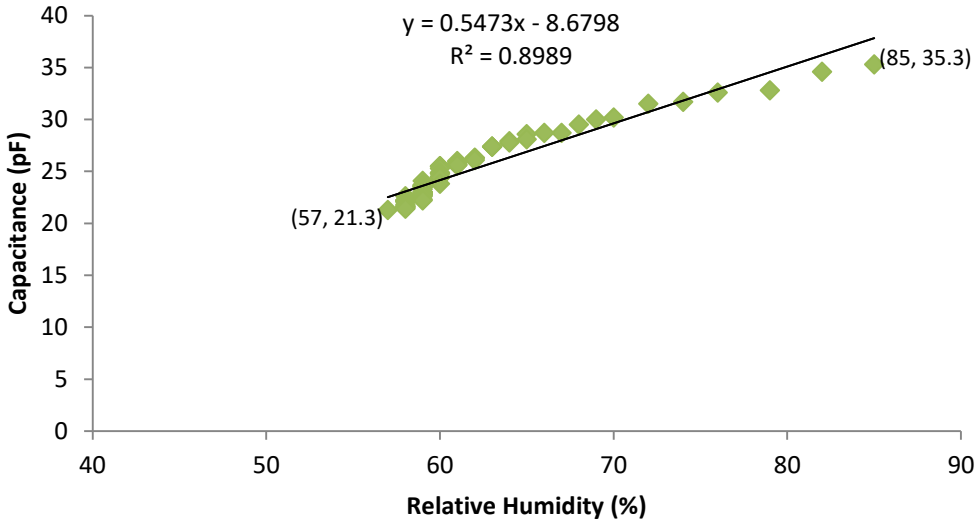

Figure 4.49b Desorption curve of nanostructured ZnO capacitive RH sensor annealed at 200 ^{0}C in NaCl micro humidity environment

$y = 0.5473x - 8.6798$ 4.24

$R^2 = 0.8989$, SD = 3.313640, $S_D = 0.657$

The response and recovery times are shown in Figure 4.50a and Figure 4.50b respectively. The response time was 302 s or 5.03 minutes for humidity range of 57 %RH to 85 %RH and capacitance variation of 18.0 pF to 34.7 pF. The recovery time was 142 s or 2.37 minutes for the same RH range and capacitance variation of 21.4 pF and 35.3 pF. The recovery time was faster but for smaller range of capacitance.

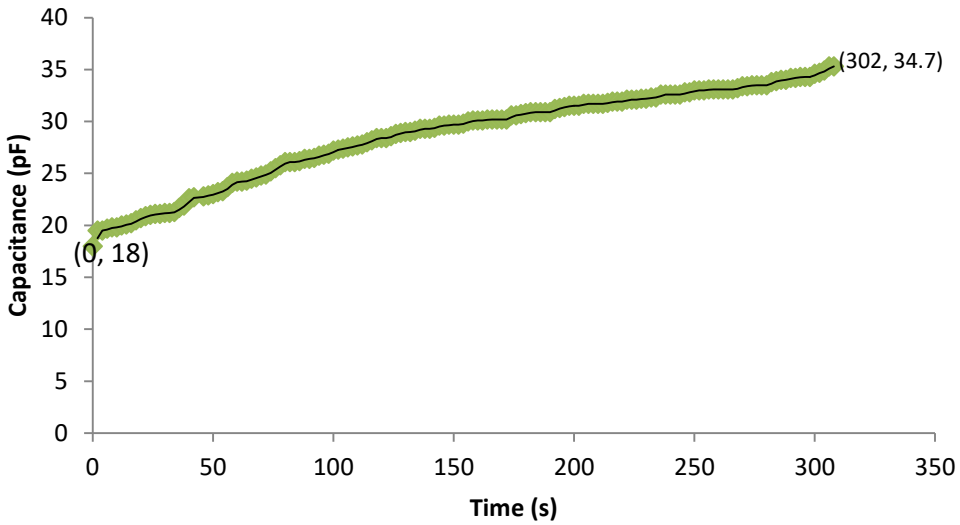

Figure 4.50a Response time of nanostructured ZnO capacitive RH sensor annealed at 200 ^{0}C in NaCl micro humidity environment

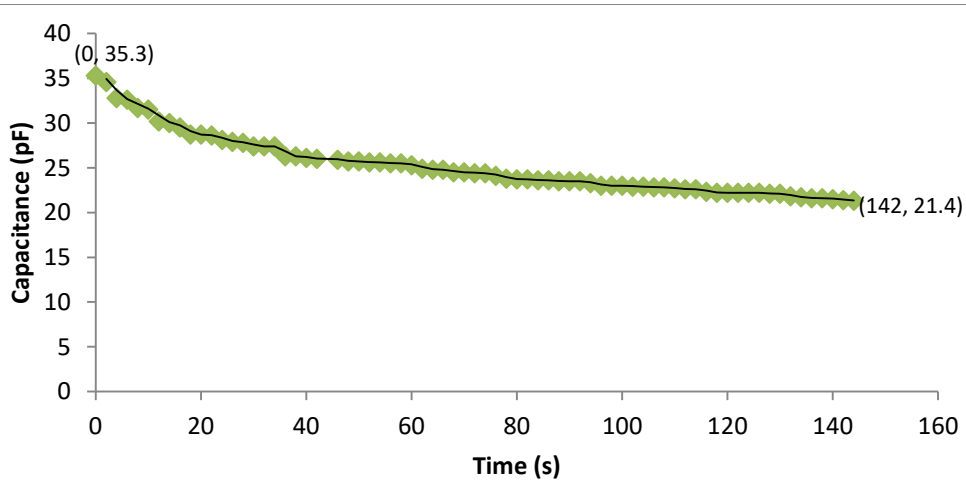

Figure 4.50b Recovery time of nanostructured ZnO capacitive RH sensor annealed at 200 ^{0}C in NaCl micro humidity environment

4. Calibration of the Nanostructured ZnO Capacitive Relative Humidity Sensor Annealed at 200 ^{0}C Using KCl Micro Humidity Environment

Figures 4.51a and 4.51b respectively demonstrate the adsorption and desorption of moisture in the KCl micro humidity environment by the sensor. Calibration equation for adsorption was

represented by equation 4.25 whereas that for desorption was represented by equation 4.26. During adsorption of moisture RH increased from 59 %RH to 87 %RH with corresponding capacitance of values increasing from 24.4 pF to 35.3 pF. In other words the required humidity level attained by the sensor was 87 %RH and its equivalent capacitance was 35.3 pF. The changes can be described to be 90.71 % based on R^2. SD and $\mathbf{S_A}$ were calculated and the values were 3.019785 and 0.447 respectively.

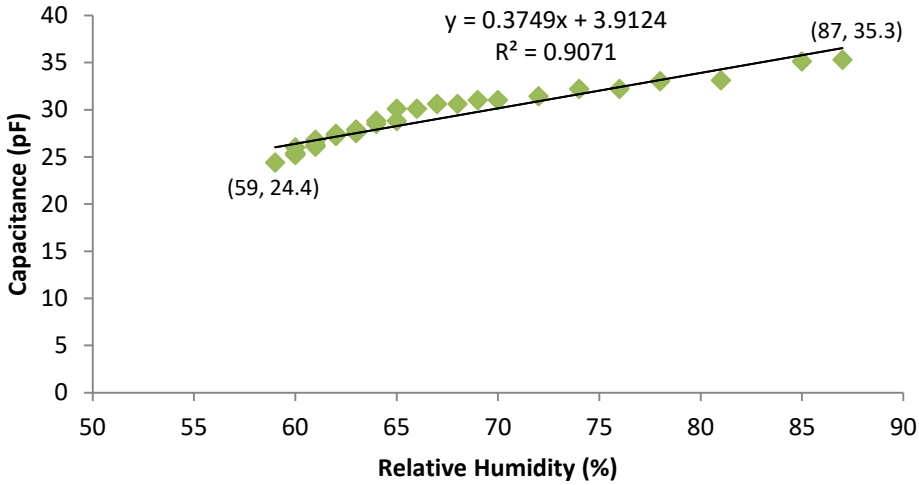

Figure 4.51a Adsorption curve in KCl micro humidity environment of nanostructured ZnO capacitive RH annealed at 200 ^{0}C

$$y = 0.3749x + 3.9124 \qquad 4.25$$

$R^2 = 0.9071$, SD = 3.019785, $S_A = 0.447$

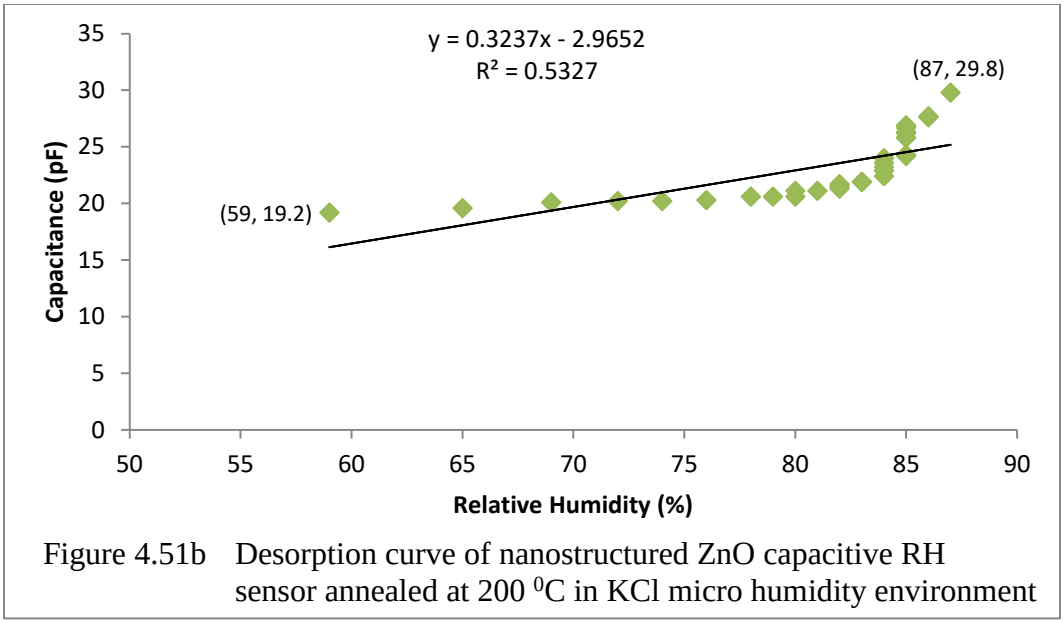

Figure 4.51b Desorption curve of nanostructured ZnO capacitive RH sensor annealed at 200 ^{0}C in KCl micro humidity environment

$y = 0.3237x - 2.9652$ 4.26

$R^2 = 0.5327$, SD = 2.869207, $S_D = 0.552$

R^2 was found to be 0.5327 suggesting that the correlation of the capacitance and RH was 53.27 % linear. SD of 2.869207 and S_D of 0.552 were recorded. Considering the behaviour of the sensor in adsorption and desorption it was discovered that the sensor had high linearity and wider spacing of the values at adsorption than at desorption. However, the sensitivity of the sensor was higher during desorption of moisture.

Figure 4.52a shows how long it took the nanostructured ZnO capacitive RH sensor annealed at 200 ^{0}C to respond from 57 %RH and attain the required humidity level of 87 %RH. Thus, the response time was 64 s or 1.07 minutes. Figure 4.52b shows the time taken by the sensor to recover from the RH level of 87 %RH to 57 %RH. The recovery time was 64 s or 1.07 minutes. The response and recovery time were the same but with different capacitance variations.

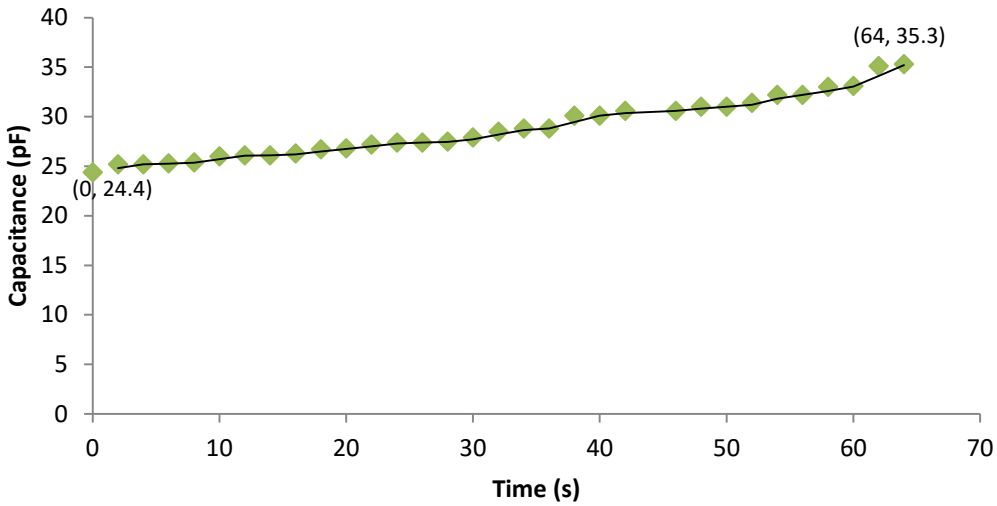

Figure 4.52a Response time in KCl micro humidity environment of nanostructured ZnO capacitive RH sensor annealed at 200 ^{0}C

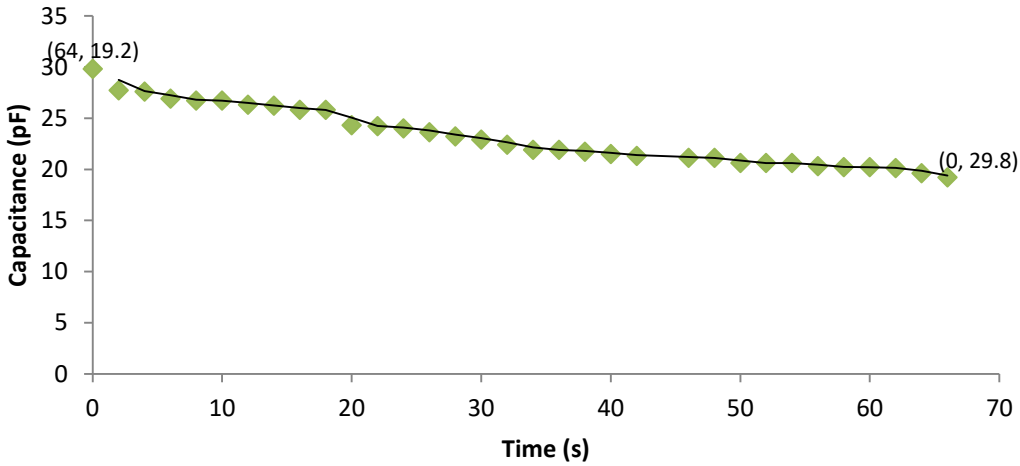

Figure 4.52b Recovery time of nanostructured ZnO capacitive RH sensor annealed at 200 ^{0}C in KCl micro humidity environment

5. Calibration of the Nanostructured ZnO Capacitive Relative Humidity Sensor Annealed at 200 ^{0}C Using K_2SO_4 Micro Humidity Environment

The behaviour of the sensor in K_2SO_4 micro humidity environment in relation to capacitance and RH variations was investigated. Figure 4.54a shows its behaviour at adsorption while Figure

4.53b shows its behaviour at desorption. The fitted curve for desorption of moisture was determined by the forth order polynomial equation displayed on the graph. In Figure 4.53a, the calibration equation (4.27) was linear and R^2 of 0.9807 specified that it was 98.07 % linear. SD of 4.653115 was obtained and S_A of 0.176 was equally calculated. In Figure 4.53b the equation (4.28) was linear. R^2 of 0.9072 confirmed that it was 90.72 % linear. SD of 13.551500 and S_D of 0.773 were calculated. In comparison the behaviour of the sensor was more linear during adsorption than during desorption. However, the sensor had wider deviation and higher sensitivity during desorption than during adsorption.

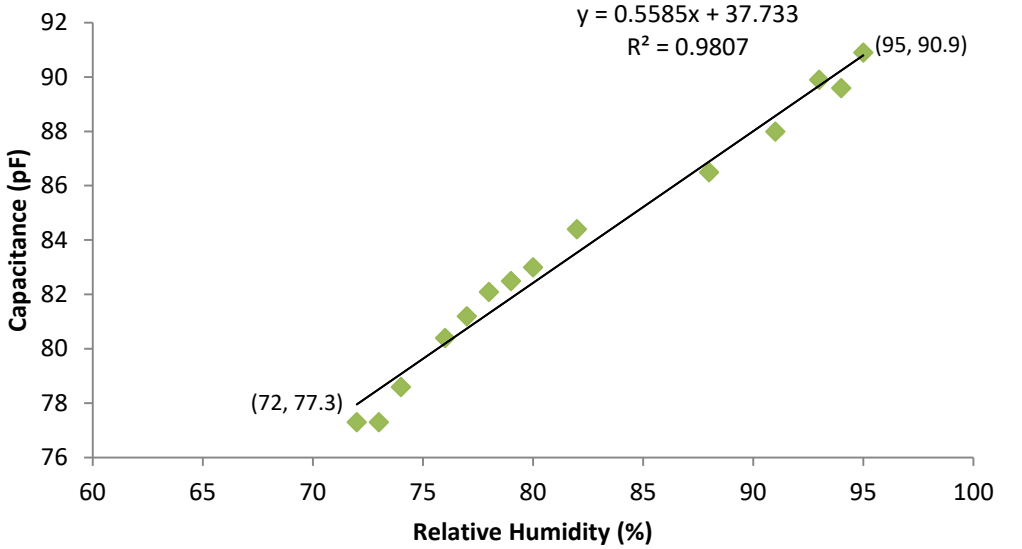

Figure 4.53a Adsorption curve of nanostructured ZnO capacitive RH sensor annealed at 200 ^{0}C in K_2SO_4 micro humidity environment

$$y = 0.5585x + 37.733 \qquad 4.27$$

$R^2 = 0.9807$, SD = 4.653115, $S_A = 0.176$

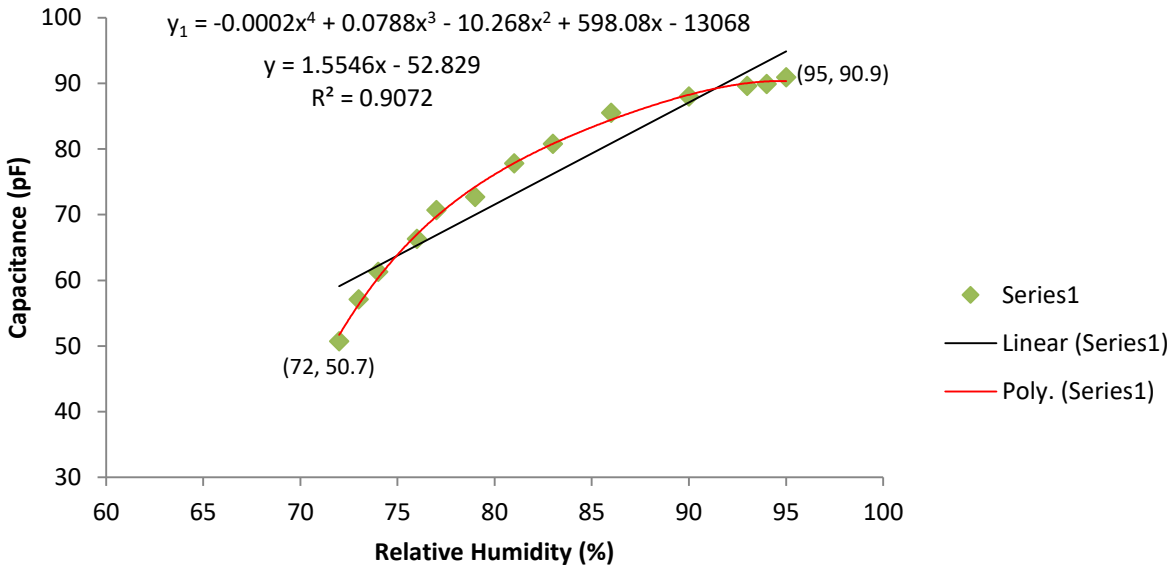

Figure 4.53b Desorption curve of nanostructured ZnO capacitive RH sensor annealed at 200 ^{0}C in K_2SO_4 micro humidity environment

$y = 1.5446x – 52.829$ 4.28

$R^2 = 0.9072$, SD = 13.551500, $S_D = 0.773$

The response and recovery times are shown in Figures 4.54a and 4.54b respectively. The response time from RH level of 72 %RH to 95 %RH was 26 s for capacitance variation of 77.3 pF to 90.9 pF. The time for the sensor to recover from 95 %RH to 72 %RH was 24 s for capacitance variations of 90.9 pF to 50.7 pF. The recovery time was only 2 s higher than response time but for a wider capacitance range.

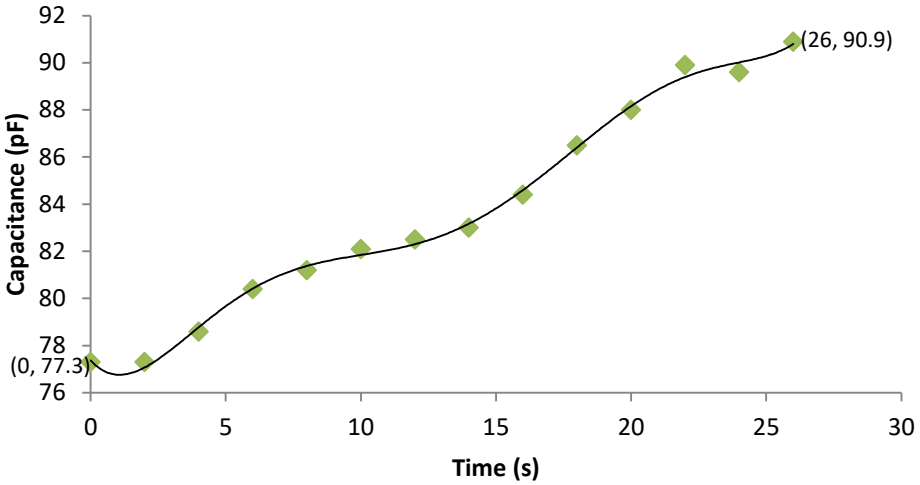

Figure 4.54a Response time of nanostructured ZnO capacitive RH sensor annealed at 200 ^{0}C in K_2SO_4 micro humidity environment

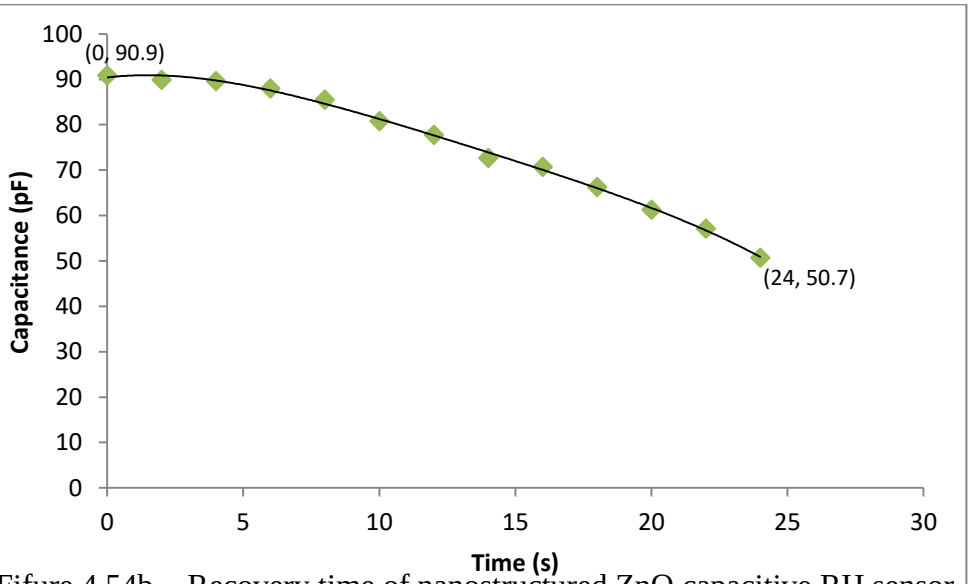

Fifure 4.54b Recovery time of nanostructured ZnO capacitive RH sensor annealed at 200 ^{0}C in K_2SO_4 micro humidity environment

Capacitive humidity sensors exhibit wide range of characteristics due to the different manufacturing processes, RH humidity ranges and RH environments. The nanostructured ZnO capacitive relative humidity sensor annealed at 200 ^{0}C showed different response times ranging

from 26 s for K_2SO_4 to 302 s for NaCl and recovery time of 24 s for K_2SO_4 to 562 s for K_2CO_3 for different humidity values ranging from 14 %RH to 95 %RH. The results are different from the findings of Hengchang *et al*. (2013) with response time of 10.5 s and the recovery time of 41.0 s for RH range of 86 % RH to 23 % RH, Tripathy *et al*. (2016) with response time of 14.5 s and recovery 34.27 s for 33 % – 95 % relative humidity range, Hong *et al*. (2019) with response and recovery times of 20 s and 22 s respectively and Kim *et al*. (2009) with1s and recovery time of 15 s for high sensitivity capacitive humidity sensor with a novel polyimide.

6. Calibration of the Nanostructured ZnO Capacitive RH Sensor Annealed at 200 ^{0}C Using the Five Micro Humidity Environments

Table 4.12 shows the capacitance values and the equivalent RH humidity values recorded by the nanostructured ZnO capacitive RH sensor annealed at 200 ^{0}C for the micro humidity environments of LiCl, K_2CO_3, NaCl, KCl and K_2SO_4. The table was used to a graph of capacitance against RH shown in Figure 4.55.

Table 4.12 Capacitance and corresponding RH measured in the micro humidity environments by nanostructured ZnO capacitive RH sensor annealed at 200 ^{0}C

Micro Humidity Environment	**Capacitance (pF)**	**Relative Humidity (%)**
Lithium Chloride	8.4	15
Potassium Carbonate	23.6	57
Sodium chloride	35.3	85
Potassium Chloride	35.3	87
Potassium Sulphate	90.9	95

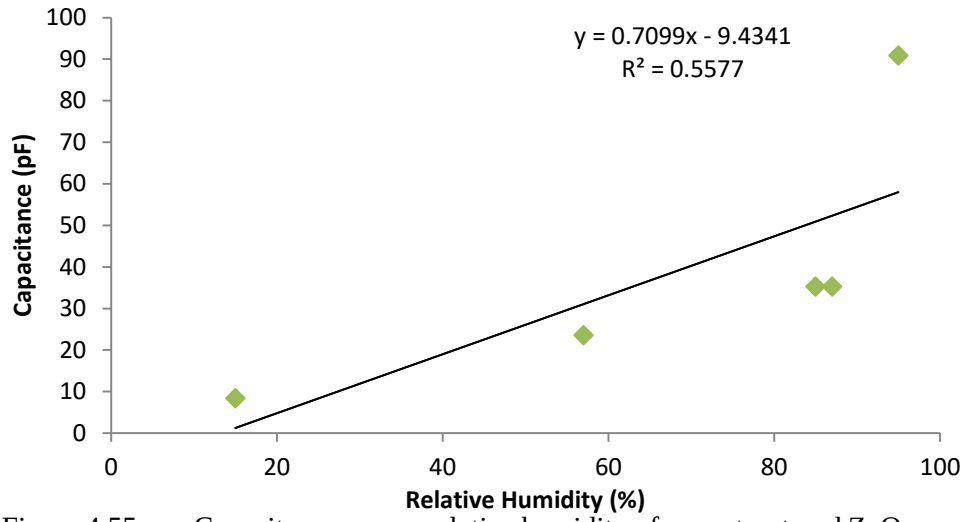

Figure 4.55 Capacitance versus relative humidity of nanostructured ZnO capacitive RH sensor annealed at 200 ^{0}C in LiCl, K_2CO_3, NaCl, KCl and K_2SO_4 micro humidity environments

$y = 0.7099x – 9.4341$ 4.29

$R^2 = 0.5577$, SD = 31.201200, S = 1.031

The graph was 55.77 % linear as confirmed with R^2 of 0.5577. The linearity of the sensor was not high enough which means that the sensor needed to be calibrated. The SD of 31.2012 and S of 1.031 were determined. The high standard deviation and high sensitivity were an indication that the capacitance values measured by the sensor had a very good distribution.

7. Determination of the Accuracy (RMSE) and Sensitivity of the Nanostructured ZnO Capacitive RH Sensor Annealed at 200 ^{0}C.

The RMSE was ascertained to confirm whether the sensor needed calibration or not. The RMSE was calculated from equation 2.14. Table 4.13 shows the reference RH and the RH measured by nanostructured ZnO capacitive RH sensor annealed at 200 ^{0}C. RMSE was 7.170. The RMSE was high which confirmed the need for the calibration of the sensor.

Table 4.13 Reference RH and RH recorded by nanostructured ZnO capacitive RH annealed at 200 ^{0}C and the associated errors.

Reference RH		**Annealed Sensor (150 ^{0}C)**	
Saturated Salt Solution	**I (%)**	**O (%)**	**Error**
Lithium Chloride	11.30	15	3.70
Potassium Carbonate	43.16	57	13.84
Sodium chloride	75.30	85	9.70
Potassium Chloride	84.34	87	2.66
Potassium Sulphate	97.30	95	2.30
RMSE			**7.170**

8. Error Correction and Calibration of the Nanostructured ZnO Capacitive Relative Humidity Sensor Annealed at 200 ^{0}C

The sensitivity of the sensor was determined from equation 4.12 and the value obtained was 1.031. The sensitivity of the sensor was also very good. It indicated that a capacitance of 1.031 pF is equivalent to relative humidity of 1 %RH as measured by the sensor. There was great improvement on the sensitivity of the nanostructured ZnO capacitive relative humidity compared to the sensitivity of 0.005 pF/% RH to 0.077 pF/% RH for capacitive relative humidity sensors reported by Du *et al*. (2004), Lee *et al*. (2011) and Hernández-Rivera *et al*. (2017).

The high RMSE and low linearity were handled by finding the capacitance values corresponding to the reference RH using the calibration equation (3.5). The values obtained were tabulated in Table 4.14. Table 4.14 was used to calibrate the nanostructured ZnO capacitive RH sensor annealed at 200 ^{0}C. Figure 4.56 shows the calibration curve for the sensor. The calibration equation was linear.

Table 4.14 Reference RH and capacitance for the calibration of nanostructured ZnO capacitive relative humidity sensor annealed at 200 ^{0}C

Saturated Slat Solution	Reference RH (I)	Capacitance (C_I) pF
Lithium Chloride	11.30	11.6503
Potassium Carbonate	43.16	44.4980
Sodium chloride	75.30	77.6343
Potassium Chloride	84.34	86.9545
Potassium Sulphate	97.30	100.3163

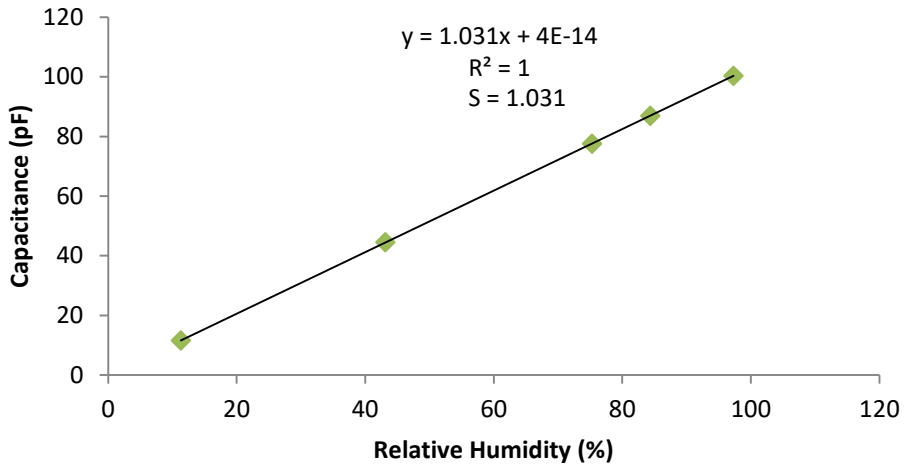

Figure 4.56 Calibration curve of nanostructured ZnO capacitive RH sensor annealed at 200 ^{0}C.

The value of R^2 was 1 showing that the correlation of capacitance variations with RH variations was 100 % linear. The slope of the graph was equal to the sensitivity of the graph confirming the linearity of the sensor. There was an intercept was 4.0 x 10^{-14} pF/ %RH which was very negligible. It also indicated that the error in the sensor was very negligible.

The scale of the sensor was expanded to record the RH values within 0 % and 100 %RH. This was done using arbitrary values of RH within the required RH range and finding their corresponding capacitance values from equation 3.5. The values were recorded in Table 4.15 and

the required graph was plotted as in Figure 4.57. It was obvious from the graph that the sensor can be used to measure any humidity from 0 %RH to 100 %RH with practically zero error.

Table 4.15 Expanded scale for the calibration of nanostructured ZnO capacitive RH sensor annealed at 200 ^{0}C

Capacitance (pF)	0	10.31	20.62	30.93	41.24	51.55	61.86	72.17	82.48	92.79	103.10
Relative Humidity (%)	0	10	20	30	40	50	60	70	80	90	100

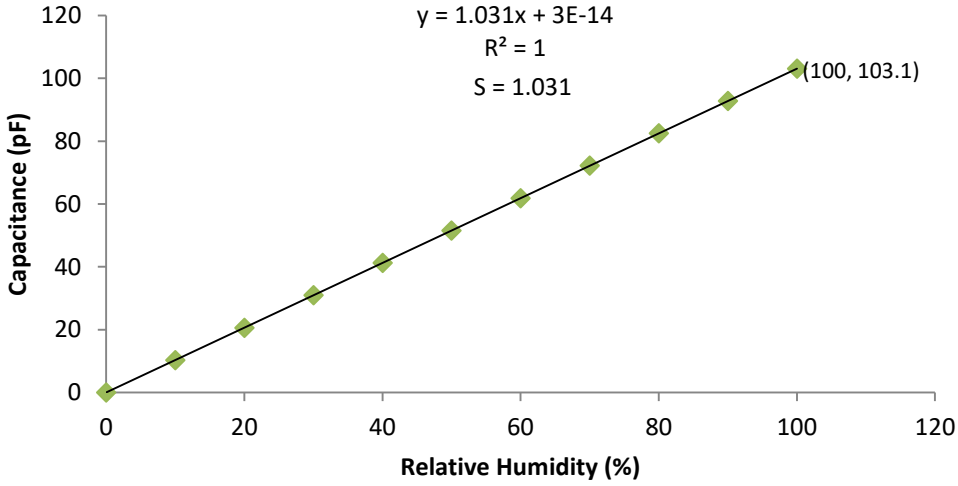

Figure 4.57 Calibration curve of nanostructured ZnO capacitive RH sensor annealed at 200 ^{0}C for RH range of 0 %RH to 100 %RH

4.6.4 Comparison of the Calibrated Sensors

The sensors were compared based on the RMSE obtained before the calibration of the sensors. Table 4.16 contains the reference relative humidity values of the saturated salt solutions and humidity values measured by the unannealed sensor and the sensors annealed at 150 ^{0}C and 200 ^{0}C in each of the five micro-environments.

Table 4.16 Reference relative humidity values of the saturated salt solutions and humidity values measured by the three sensors

Reference RH		**Unannealed Sensor**		**Annealed (150 ^{0}C)**		**Annealed (200 ^{0}C)**	
Saturated Salt Solution	I (%)	O (%)	Error	O (%)	Error	O (%)	Error
Lithium Chloride	11.30	13	1.70	14	2.70	15	3.70
Potassium Carbonate	43.16	58	14.84	57	13.84	57	13.84
Sodium chloride	75.30	86	10.70	87	11.70	85	9.70
Potassium Chloride	84.34	87	2.66	87	2.66	87	2.66
Potassium Sulphate	97.30	95	2.30	95	2.30	95	2.30
RMSE			**8.37**		**8.34**		**7.17**

The unannealed nanostructured ZnO capacitive RH sensor had the largest RMSE followed by the nanostructured ZnO capacitive RH sensor annealed at 150 ^{0}C. The nanostructured ZnO capacitive RH sensor annealed at 200 ^{0}C had the lowest RMSE which showed that it had the highest accuracy.

The performance of the sensors was again compared based on capacitance range (R), sensitivity (S) and standard deviation (SD). Figure 4.58 gives a pictorial view of the performance of the unannealed nanostructured capacitive RH sensor, the nanostructured ZnO capacitive RH sensor annealed at 150 ^{0}C and nanostructured ZnO capacitive RH sensor annealed at 200 ^{0}C after their calibrations. The linearity of each of the sensors was 100 %. The capacitance range (R), sensitivity (S) and standard deviation (SD) were derived from Figure 4.58 and were summarized in Table 4.17.

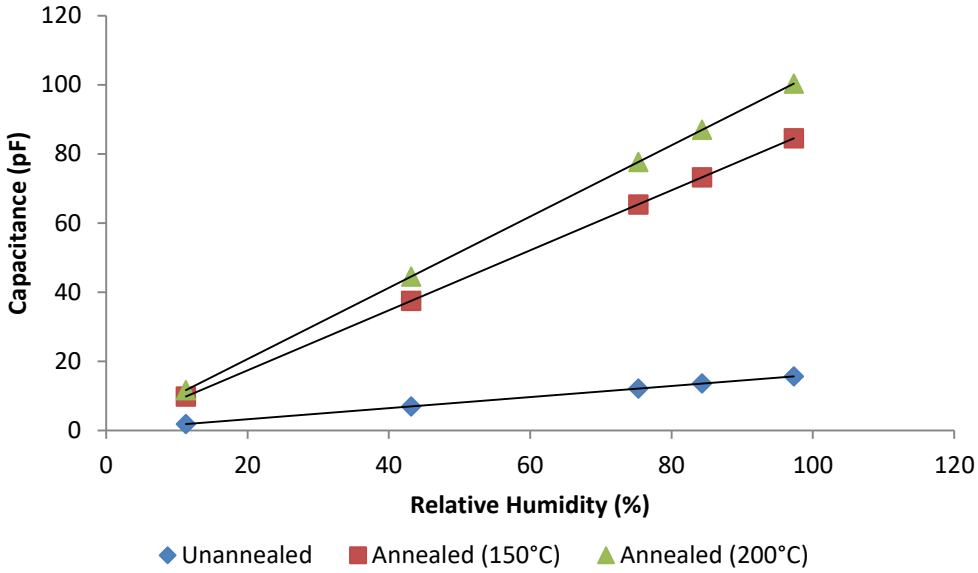

Figure 4.58 Calibration curves of the three nanostructure ZnO sensors capacitive RH sensors

Table 4.17 Comparison of the sesnors based on capacitance range (R), sensitivity (S) and standard deviation (SD)

Nanostructured ZnO Capacitive Sensor	**Range (R) (pF)**	**Sensitivity (S)**	**Standard Deviation (SD)**	**Remark**
Unannealed	13.85	0.161	5.805	3rd
Annealed (150 ^{0}C)	74.65	0.868	30.216	2nd
Annealed (200 ^{0}C)	88.67	1.031	35.890	1st

It can be concluded from the graphs and the table that the nanostructured ZnO capacitive RH sensor annealed at 200 ^{0}C had the best performance out of the three sensors due to its highest range, sensitivity and standard deviation. The next best was the sensor annealed at 150 ^{0}C. The unannealed sensor had the least performance. The results also revealed that the annealing temperatures had effect on the performance of the sensors. It can be established that the higher the annealing temperature the higher the performance of the sensor.

CHAPTER FIVE

SUMMARY, CONCLUSIONS AND RECOMMENDATIONS

5.1 Summary

The study was to fabricate a capacitive relative humidity sensor using nanostructured zinc oxide (ZnO) produced by solvothermal synthesis technique as a dielectric. Two samples of ZnO nanoparticles were successfully synthesized by solvothermal synthesis technique using sodium lauryl sulphate (SLS) and linear alkylbenzene sulphonate (LAS or LABS) as capping agents. The solvothermal synthesis was done at 190 ^{0}C using zinc acetate as the precursor and diethylene glycol as the solvent.

Raman Spectroscopy, Thermogravimetric Analysis (TGA), Brunauer–Emmett–Teller (BET) surface area analysis and particle-size distribution (PSD) analysis were used for characterization of the synthesized ZnO nanoparticles. The Raman spectrum of ZnO nanoparticles produced with SLS showed a prominent peak observed at 426 cm^{-1}, that is, characteristic peak of the Raman active dominant E_2(high) mode of Wurtzite ZnO with red shift of 11 cm^{-1}. The Raman spectrum of ZnO nanoparticles produced with LABS showed a prominent peak observed at 424 cm^{-1} which was also a characteristic peak of the Raman active dominant E_2(high) mode of Wurtzite ZnO with red shift of 13 cm^{-1}. The results showed that the ZnO synthesized were of stable structure. The multipoint BET surface area of the ZnO nanoparticles produced with SLS was 284.286 m^2/g with BJH adsorption pore diameter of 2.411 nm and BJH cumulative adsorption volume of 0.181 cm^3/g. The BET surface area of the ZnO nanoparticles produced with LABS was 288.421 m^2/g with BJH cumulative adsorption volume of 0.184 cm^3/g and BJH adsorption pore diameter of 2.433 nm. Both samples exhibited mesopores characteristic structure which

showed good porosity. Their isotherms displayed the type IV isotherm which was accredited to the prevalence of mesopores in the sample. The results from TGA analysis showed that ZnO nanoparticles produced with SLS had degradation temperatures of 325 ^{0}C while ZnO nanoparticles produced with LABS had 420 ^{0}C which were of good thermal stability for the sensors. The PSD analysis showed that the sample with SLS had Z-average particle size of 354nm with polydispersity index of 0.605 and the dominant ZnO nanoparticles in the sample had the diameter of 722.3 nm and occupied 68.5 % of the entire volume. The sample with LABS had Z-average diameter particle size of 715.2 nm and Polydispersity index (PdI) of 0.431; nanoparticles of 981.1 nm were predominantly present in the sample and occupied 97.3 % of the entire volume. The particle sizes of both samples were discovered to be of good quality. The properties of the ZnO nanoparticles produced with sodium lauryl sulphate (SLS) and linear alkylbenzene sulphonate (LAS or LABS) were compared and it was found that the sample with LABS was of better quality. The ZnO nanoparticles produced with LABS was used for the fabrication of the sensor.

The interdigitated electrodes (IDEs) were designed using computer aided design program/software (PROTEUS Design Suite) and printed on Printed Circuit Board (PCB) using screen printing technique. The total sensing area of each of the IDEs is 46.948 mm^2. The nanostructured ZnO capacitive relative humidity sensors were fabricated by depositing the ZnO nanoparticles on the IDEs using spin coating technique. The ZnO nanoparticles deposited on the IDEs was the dielectric material for the capacitive sensors. Three sensors including unannealed nanostructured ZnO capacitive RH sensor and nanostructured ZnO capacitive RH sensors annealed at 150 ^{0}C and 200 ^{0}C were successfully produced. The ARDUINO NANO ATMEGA 328 microcontroller was programmed to operate at 0 V (digital low) and 5 V (digital high) and to

process the signals (stimuli) from DHT11 and the nanostructured ZnO capacitive relative humidity sensors. ARDUNO NANO ATMEGA 328 microcontroller operational circuit was designed for the electronic sensor system.

The sensors were calibrated using the RH standards of saturated solutions of lithium Chloride (LiCl), Potassium carbonate (K_2CO_3), potassium chloride (KCl), potassium sulphate (K_2SO_4) and sodium chloride (NaCl) micro humidity environments. The RMSE associated with the sensors were 8.367, 8.344 and 7.170 for the unannealed sensor, sensor annealed at 150 ^{0}C and sensor annealed at 200 ^{0}C respectively. The high RMSE necessitated the calibration of the sensor to achieve 100 % linearity and to take care of the error. The sensitivity (S) of the sensors to 1 %RH change in relative humidity were 0.161 for unannealed sensor, 0.868 for sensor annealed at 150 ^{0}C and 1.031 for sensor annealed at 200 ^{0}C. The disparities in the RMSE and the sensitivity of the three sensors are indications of the positive effect of annealing temperature on the sensor performance. The performance of the sensor improved with increase in annealing temperature. A model equation for the calibration of sensors was derived based on sensitivity. The model equation was used to calibrate the sensors. Each sensor was successfully calibrated to measure any relative humidity variation from 0 %RH to 100 %RH with very negligible error.

5.2 Conclusions

The study has proved that sodium lauryl sulphate (SLS) and linear alkylbenzene sulphonate (LAS or LABS) can be used as good capping agents for the synthesis of ZnO nanoparticles. It equally revealed that the linear alkylbenzene sulphonate is a better capping agent compared to sodium lauryl sulphate. These are evident from the Raman Spectroscopy, Thermogravimetric

Analysis (TGA), Brunauer–Emmett–Teller (BET) surface area analysis and particle-size distribution (PSD) analysis characterization of the synthesized ZnO nanoparticles which showed that the two samples are of stable wurtzite structure with good surface area, mesopores characteristic structure for excellent sensing, good thermal stability and good size quality and size distribution by volume and intensity. The study demonstrated that the synthesized ZnO nanoparticles is a high quality dielectric material for fabrication of capacitive relative humidity sensors which is obvious in the linearity, accuracy, sensitivity to relative humidity changes and response and recovery times of the sensors. The three nanostructured ZnO capacitive relative humidity sensors (unannealed sensor, sensor annealed at 150 ^{0}C and sensor annealed at 200 ^{0}C) fabricated are of good quality but characterization and calibration of the sensors showed that the sensor annealed at 200 ^{0}C is of best quality. The implication is that increase in annealing temperature improves the performance of nanostructured ZnO capacitive relative humidity sensor. A model linear equation was used to calibrate the sensors to achieve 100 % linearity such that the sensor can be used to measure relative humidity variations ranging from 0%RH to 100 %RH for wide temperature range of 0 ^{0}C to 420 ^{0}C as specified in TGA analysis. The nanostructured ZnO capacitive RH sensors will be found suitable for relative humidity measurements.

5.3 Recommendations for Further Studies

The following study may be carried out on the nanostructured ZnO capacitive relative humidity sensor for more suitable applications:

- Effect of aging on the performance of nanostructured ZnO capacitive relative humidity sensor.

5.4 Contributions to Knowledge

The major contributions of this study are as follows:

1. Sodium lauryl sulphate (SLS) can be used as a capping agent in synthesis of ZnO nanoparticles.
2. Utilization of linear alkylbenzene sulphonate (LAS or LABS) as a capping agent in synthesis of ZnO nanoparticles.
3. Application of ZnO nanoparticles produced with linear alkylbenzene sulphonate (LABS) as good sensing material for relative humidity sensor.
4. Calibration of relative humidity sensor using linear regression analysis.
5. Incorporation of ARDUNO NANO ATMEGA 328 microcontroller circuit in electronic relative humidity sensing system.

REFERENCES

Academic, (2017, October 17). Aspiration psychrometer. Academic Dictionaries and Encyclopedias. 6 pages. Retrieved from *http://deacademic.com/dic.nsf/dewiki/439240*

Ahrens, D. C. (2012). Meteorology today: an introduction to weather, climate, and the environment (10th ed). USA, Brooks/Cole Cengage Learning. 578 pages.

Aijazi, A. T. (2014). Printing Functional Electronic Circuits and Components. Dissertations Graduate College. Western Michigan University. 131 pages.

Antikainen, V., Paukkunen, A. and Jauhiainen, H. (2002). Measurement Accuracy and Repeatability of Vaisala RS90 Radiosonde. Vaisala News. 159, 11-13.

Arafat, M. M., Dinan, B., Akbar, A. S. and Haseeb, A. S. M. A. (2012). Gas Sensors Based on One Dimensional Nanostructured Metal-Oxides: A Review. Sensors, 12(6), 7207-7258; DOI:10.3390/s120607207

Arora, A. K., Devi, S., Jaswal, J. S., Kinger, M. and Gupta, V. D. (2014). Synthesis and Characterization of ZnO Nanoparticles. Oriental Journal of Chemistry. 30 (4): 1671-1679. http://dx.doi.org/10.13005/ojc/300427

Balasubramanian, A. (2016). Measurement of Meteorological Variables. DOI: 10.13140/RG.2.2.21633.66405.

Beaubien, D. J (2005, May 1). The chilled mirror hygrometer: How it works, where it works-and where it doesn't. Sensors Magazine. Framingham, 2019 Questex LLC. 13 pages.

Bekkari, R., Jaber, B., Labrim,H., Ouafi, M., Zayyoun, N. and Laânab, L. (2019). Effect of Solvents and Stabilizer Molar Ratio on the Growth Orientation of Sol-Gel-Derived ZnO Thin Films, International Journal of Photoenergy, 7 pages. DOI.10.1155/2019/3164043

Bekkari, R., Laânab, L.,Boyer, D., Mahiou,R., and Jaber, B. (2017). Influence of the sol gel synthesis parameters on the photoluminescence properties of ZnO nanoparticles. Materials Science in Semiconductor Processing, 71, 181–187.

Bhat, S., Shrisha, B. V. and Naik, K. G. (2013). Synthesis of ZnO nanostructures by solvothermal method. Archives of Physics Research, 4 (2):61-70

Bhunia, A. K., Jha, P. K., Rout, D. and Saha, S. (2016). Morphological Properties and Raman Spectroscopy of ZnO Nanorods. Journal of Physical Sciences, 21, 111-118

Bramer, I., Anderson, B. J., Bennie, J., Bladon, A. J., De Frenne, P., Hemming, D., Hill R. A., Kearney, M., R., Körner, C., Korstjens, A. H., Lenoir, J., Maclean, I. M. D., Marsh, C.D., Morecroft, M. D., Ohlemüller, R., Slater, H. D. , Suggitt, A. J., Zellweger, F. and

Birnie, D.P., Aegerter, M.A. and Mennig, M. (eds). Spin Coating Technique. Sol-Gel Technologies for Glass Producers and Users. Boston. Springer. pp 49-55.

Brenner, J. P. (2010). Design Specifications for Wet-Bulb Aspirator Apparatus. Thesis: University of Wisconsin-Madison. 259 pages.

Campbell, C. B. (1969). Dew point hygrometer with constant resistance humidity transducer. All Graduate Theses and Dissertations. Logan, Utah State University. 94 pages

Cancela, J.J., Martinez, E. M., Cuesta, T. S. and Neira, X. X. (2011). Review. Use of psychrometers in field measurements of plant material: accuracy and handling difficulties. Spanish Journal of Agricultural Research. 1695-971-X, 2171-9292, 9(1), 313-328

Chang, S.P.; Chang, S.J.; Lu, C.Y.; Li, M.J.; Hsu, C.L.; Chiou, Y.Z.; Hsueh, T.J.; Chen, I.C. (2010). A ZnO nanowire-based humidity sensor. Super lattices Microstruct. 47, 772–778.

Chang, T. H.; Chou, J. C.; Sun, T. P.; Hsiung, S. K. (2010). A device for skin moisture and environment humidity detection. Sens. Actuators B Chem. 134, 206–212.

Chen, Z. and Lu, C. (2005). Humidity sensors: A review of materials and mechanisms. Sensors. Letters. 3, 274–295.

Chia-Yen, L. and Gwo-Bin, L. (2005). Humidity Sensors: A Review. Sensor Letters. 3(1). DOI:10.1166/sl.2005.001. 15 pages.

Chou, K. S. and Lee, CH. (2014). Fabrication of silver interdigitated electrode by a stamp method. Advances in Materials Science and Engineering. Volume 2014, Article ID 514508,. http://dx.doi.org/10.1155/2014/514508. 5 pages

Ciprian, R., & Lehman, B. (2009). Modeling effects of relative humidity, moisture, and extreme environmental conditions on power electronic performance. 2009 IEEE Energy Conversion Congress and Exposition, 1052-1059.

Corey, P. L. (2016). Dew-point measurements for water in compressed CO2. USA, National Institute of Standards and Technology (NIST). 5 pages.

Circuits Today (2018, February 17). Arduino Nano Tutorial – Pinout & Schematics. Retrieved from *http://www.circuitstoday.com/arduino-nano-tutorial-pinout-schematics*

Cracknell, R. and Bolton, P. (2009). Statistical literacy guide: What is a billion? And other units. UK, House of Commons Library. 3 pages

Dakhlaoui, A., Jendoubi, M., Smiri, L.S., Kanaev, A. and Jouini, N. (2009) Synthesis, Characterization and Optical Properties of ZnO Nanoparticles with Controlled Size and

Morphology. Journal of Crystal Growth, 311, 3989-3996. http://dx.doi.org/10.1016/j.jcrysgro.2009.06.028

Dario, C. & Vito, F. (2010). How to measure temperature and relative humidity Instruments and instrumental problems. 10.13140/2.1.2270.0169.

Deak, G., Dumitru, F.D., Moncea, M., Ana-Maria, P., Baraitaru, A., Viorel, O., Marius, B. and Stanciu, S. M. (2019). Synthesis of ZnO Nanoparticles for Water Treatment Applications. 10 (2), 343-350

Demazeau, G. (2008). Solvothermal reactions: an original route for the synthesis of novel materials. Journal of Materials Science, Springer Verlag, 43 (7), 2104-2114.

Divya, R., Supraja, N. and David, E. (2018). Synthesis and Characterization of ZnONPs from Vitis Vinifera Peel Extract and Its Antimicrobial Efficacy. Advancements Bioequiv Availab. 2(2). 8 pages. DOI: 10.31031/ABB.2018.02.000535

Dubourg, G., Segkos, A., Katona, J., Radovi´, M., Savi´, S., Niarchos, G., Tsamis, C. and Crnojevi´-Bengin, V. (2017). Fabrication and characterization of flexible and miniaturized humidity sensors using screen-printed TiO_2 nanoparticles as sensitive layer. Sensors . 17(854). DOI:10.3390/s17081854. 13 pages

Dumey, B. (2014, June 11). Four reasons to use and not to use psychrometers. Retrieved from *www.davis.com/blog/2014/06/11/four-reasons-to-use-and-not-to-use-psychrometers/*

Electronicshub.org (2018, October 22). Humidity Sensor – Types and Working Principle. Retrieved from *https://www.electronicshub.org/humidity-sensor-types-working-principle/*

Emslie, A. G., Bonner, F. T., and Peck, L. G. (1958). Flow of a Viscous Liquid on a Rotating Disk, J. Appl. Phys. 29, 858-862.

Farahani, H., Wagiran, R., and Hamidon, M. N. (2014). Humidity sensors principle, mechanism, and fabrication technologies: A comprehensive review. Sensors. 14, 7881-7939; doi:10.3390/s140507881.

Fenner, R. and Zdankiewicz, E. (2001). Micromachined Water Vapor Sensors: A Review of Sensing Technologies. IEEE Sensors Journal. 2001 (1) 309–317.

Fong, J. and Youwen, L. (2016). Screen printing. In: Chin J. (ed). Numbers and Niches. National Library Board (HIB), Singapore, pp 3.

Fraden, J. (2004). Handbook of modern sensors: Physics designs and applications, third edition. Springer-Verlag New York, Inc., New York, USA, 2004: 608 pages.

Gallicchio, N. and Teague, K. A. (2017). Inventions of Weather Instruments (1400–1800). New Jersey, John Wiley & Sons, Inc. 9781119136170, 9781119136149, 11 – 17. DOI: 10.1002/9781119136170.ch2

Gammel, J. (2013). Simplifying Humidity Measurement with Single-Chip Relative Humidity Sensors. Sensors Magazine. Framingham, 2019 Questex LLC. 9 pages.

Garza, M., López, I., Aviña, F. and Gómez, I. (2013). Microwave-assisted solvothermal synthesis of porous zinc oxide nanostructures. Journal of Ovonic Research. 9(4), 89 – 94.

GE Measurement and Control (2015). Model 1311XR General Eastern Chilled Mirror Hygrometer Installation and Operational Manual. EU, General Electric Company. A 40186181 Rev. C. 40 pages.

Genovese, R. (2017). How to Check and Calibrate a Humidity Sensor. All About Circuits. USA, EETech Media, LLC. 17 pages

Gersten, B. (2018). Solvothermal Synthesis of Nanoparticles. Chemfiles–Sigma Aldrich. 5(13). 5 pages

Ghanem, S., Telia, A., Boukaous, C., and Aida, M. S. (2015). Humidity sensor characteristics based on ZnO nanostructure grown by sol-gel method. International Journal of Nanotechnology. 12 (8), 697. DOI:10.1504/IJNT.2015.068890.

Ghoshal, T., Biswas, S., Paul M., and De, S. K. (2009). Synthesis of ZnO nanoparticles by solvothermal method and their ammonia sensing properties. Journal of Nanoscience and Nanotechnology. 9, 5973–5980.

Gillingham, P. K. (2018). Advances in monitoring and modelling climate at ecologically relevant scales. Next generation biomonitoring: part 1 58, 101-161. DOI: 10.1016/bs.aecr.2017.12.005

Greenspan, L. (1977). Humidity Fixed Points of Binary Saturated Aqueous Solutions. Journal of Research of the National Bureau of Standards-A. Physics and Chemistry. 81 A (1), 89 – 96.

Griesel, S., Theel M., Niemand, H. and Lanzinger, E. (2012). Acceptance Test Procedure for Capacitive Humidity Sensors in Saturated Conditions. WMO CIMO TECO-2012, Conference Contribution. 7 pages.

Gu, L., Huang, Q.A. and Qin, M. (2004). A novel capacitive-type humidity sensor using CMOS fabrication technology. Sensors. Actuators B Chem. **2004** (99) 491–498.

Gupta, N. (2015) Humidity sensor. Engineering. 55359601, 24 pages.

Gusatti, M., Barroso, G. S., Carlos, E. M. C., Daniel, A. R. S., Jeane, A. R., Raquel, B. L., Camila, C. M., Laura A. S., Humberto G. R. and Nivaldo C. K. (2011). Effect of

different precursors in the chemical synthesis of ZnO nanocrystals. Materials Research. 14(2): 264-267. DOI: 10.1590/S1516-14392011005000035

Han, K. I., Kim, S., Lee, I. G., Kim, J. P., Kim, J., Hong, S. W., Cho, B. J. and Hwang, W. S. (2017). Compliment Graphene Oxide Coating on Silk Fiber Surface via Electrostatic Force for Capacitive Humidity Sensor Applications. Sensors. 17 (407). DOI: 10.3390/s17020407. 7 pages.

Haq, A. N. U., Nadhman, A., Ullah, I., Mustafa, G., Yasinzai, M. and Khan, I. (2017). Synthesis approaches of zinc oxide nanoparticles: The dilemma of ecotoxicity. Journal of Nanomaterials. 2017, ID 8510342, 14 pages.

Harun, N. H., Ali, R. M., Ali, A. M. M. B., Yahya, M. Z. A. (2012). Resistive-type Humidity Sensor Based on CA-NH4BF4-PEG600 Thin Films. Physics Procedia. 25, 221 – 226. DOI: 10.1016/j.phpro.2012.03.075

Hassan, M. J., Yusoff, M. A. and Vengadesh, P. (2016). Humidity influenced capacitance and resistance of an Al/DNA/Al Schottky diode irradiated by alpha particles. Scientific Reports. 6, 25519. DOI: 10.1038/srep25519. 13 pages

Heat – tech (2018, October 12). The principle of the Psychrometer. Retrieved from *http://heater.heat-tech.biz/air-blow-heater/science-of-the-drying/basic-knowledge-of-the-drying/property-of-the-humid-air/9840.html*

Hellstrom, S.L. (2007). Published course work for physics 210. Autumn 2007. Stanford University.

Hernández-Rivera, D., Rodríguez-Roldán, G., Mora-Martínez, R. and Suaste-Gómez, E. (2017). A Capacitive Humidity Sensor Based on an Electrospun PVDF/Graphene Membrane. 17 (1009). DOI: 10.3390/s17051009. 11 pages

Hengchang, B., Kuibo, Y., Xiao, X., Jing, J., Shu, W., Litao, S., Mauricio, T. and Mildred, S. D. (2013). Ultra high humidity sensitivity of graphene oxide. Scientific Reports. 3, 2714. 7 pages. DOI: 10.1038/srep02714.

Herrera-Rivera, R., Olvera, M. and Maldonado, A.(2017). Synthesis of ZnO Nanopowders by the Homogeneous Precipitation Method: Use of Taguchi's Method for Analyzing the Effect of Different Variables. Journal of Nanomaterials. Vol (2017), 9 pages. https://doi.org/10.1155/2017/4595384

Hillel, D. (1998). Environmental Soil Physics (1st Edition). USA, Academic Press. 9780123485250, 9780080544151, 771 pages.

Hong, L., Wang, Q., Wenjie, S., Xubo, W., Zhang, K., Lin, D., and Jia, Z. (2019). Humidity Sensors with Shielding Electrode Under Interdigitated Electrode. Sensors. 19 (659). 11 pages. DOI:10.3390/s19030659

HORIBA, (2019, October 30). Raman data analysis: Raman bands. Raman application note. 2pages. Retrieved from https://www.horiba.com/fileadmin/uploads/Scientific/Documents/Raman/bands.pdf

Horikoshi, S. and Serpone, N. (ed) (2013). Introduction to Nanoparticles. Microwaves in Nanoparticle Synthesis, First Edition. Wiley-VCH Verlag GmbH & Co. KGaA. pp 1-24

Hsuan-Yu, C. and Chiachung, C. (2019). Determination of Optimal Measurement Points for Calibration equations—Examples by RH Sensors. Sensors, 19 (1213), 1 -18. doi:10.3390/s19051213

Hussain, A., Hammad, M., Hafeez, K. and Zainab, T. (2016). Programming a Microcontroller. International Journal of Computer Applications. 155(1),6 pages.

Ilican, S. (2016). Improvement of the crystallinity and optical parameters of ZnO film with aluminum doping. Anadolu University Journal of Science and Technology A- Applied Sciences and Engineering. 17 (1), 181 – 190

Isah, K. U., Ramalan, A. M., Ahmadu, U., Ibrahim, S. O., Yabagi, A. and Jolayemi, B. J. (2016). Effect of Zn Film Substrate Temperature on Optical, Structural and Vibrational Characteristics of Thermally Oxidized Zn Films. Asian Journal of Applied Sciences. ISSN 1996-3343. 11 pages. DOI: 10.3923/ajaps.2016.

Ismail, M. S. Muhammad, H. H. C., Norlaili, A. and Noorhana, Y. (2018). Characterization and Colloidal Stability of Surface Modified Zinc Oxide Nanoparticle. Journal of Physics: Conference Series 1123, doi :10.1088/1742-6596/1123/1/012007 ISSN: 2350-0352

Jadhav, N. A., Singh, P. K., Rhee, H. W. and Bhattacharya, B. (2004). Effect of variation of average pore size and specific surface area of ZnO electrode (WE) on efficiency of dye-sensitized solar cells. Nanoscale Research Letters. 9, 575. DOI: 10.1186/1556-276X-9-575

Jayaraj, M. K., Aneesh, P. M. and Vanaja, K. A. (2017). Synthesis of ZnO nanoparticles by hydrothermal method. Nanophotonic Materials IV, Proc. of SPIE. 6639, 66390J, DOI: 10.1117/12.730364

Jifang, T., Yu, L., Li ,W., Hong, C., Tao, S., Junfeng, S., Hui, L. and Yuandong, G. (2016). An ultrahigh-accuracy Miniature Dew Point Sensor based on an Integrated Photonics Platform. Scientific Report. 6:29672 | DOI: 10.1038/srep29672. 7 pages.

Jillavenkatesa, A., Dapkunas, S. J. and Lin-Sien, L. (2001). Particle Size Characterization. National Institute of Standards and Technology *(*NIST). U.S. Government Printing Office, Washington, DC, USA. pp 49.

Kalantar-Zadeh, K. (2013). Sensor characteristics. Sensors: An Introductory Course. 12, 196 pages.

Karthick, R., Babu, S.P.K., Abirami, A. R. and Kalainila, S. (2011). Design of Mems Based High Sensitivity and Fast Response Capacitive Humidity Sensor. The Proceedings of the 2011 COSMOL Conference in Bangore. Periyar Maaniammai University. 24 pages.

Kestrel (2012, September 27). What is psychrometer? Retrieved form *https://kestrelmeters.com/blogs/news/6638286-what-is-a-psychrometer*

Khalil, M. I., Al-Qunaibit, M. M., Al-zahem, A. M., and Labis, J. P. (2014). Synthesis and characterization of ZnO nanoparticles by thermal decomposition of a curcumin zinc complex. Arabian Journal of Chemistry. 7, 1178–1184.

Khan, A. (2010). Raman Spectroscopic Study of the ZnO Nanostructures. J Pak Mater Soc. 4(1), 5-9

Khan, T. and Irfan, M. (2014). Studies on the complex behavior of optical phonon modes in wurtzite (ZnO)1−x (Cr2O3) x. Applied Physics A. 117. Doi:10.1007/s00339-014-8518-9.

Kim, J.H., Hong, S.M., Moon, B.M., and Kim, K. (2010). High-performance capacitive humidity sensor with novel electrode and polyimide layer based on MEMS technology. Microsyst. Technol. 2009 (16), 2017–2021

Kolekar, T. V., Bandgar, S. S., Shirguppikar, S. S., Ganachari, V. S., (2013). Synthesis and Characterization of ZnO nanoparticles for efficient gas sensors. Arch. Appl. Sci. Res. 5 (6), 20-28.

Kolpakov, S. A., Gordon, N. T., Mou, C. and Zhou, K. (2014). Toward a New Generation of Photonic Humidity Sensors. Sensors. 14, 3986-4013. DOI:10.3390/s140303986.

Korotcenkov, G. (2018). Handbook of Humidity Measurement. Spectroscopic Methods of Humidity Measurement. 1: 978-1-138-30021-7. 111 pages.

Krepcik, H. (2010). Psychrometrics from Start to Finish. RSES Journal. 0410, 10 – 12.

Kumar, K. S and Sharada, S. (2015). Development Synthesis of Zinc Oxide Nano Particles and Its Application in Water Treatment Technology. National Research Organization, India. 2(12), 2393-8374, pp 83 – 86.

Lars, E. N. and Elmarsson, B. (1994). Fukthandbok: praktik och teori (Moisture handbook: practice and theory, in Swedish). Svensk byggtjanst, Solna, Sverige, 35 pages.

Lawrence, C.J. & Zhou, W. (1991). Spin Coating of Non-Newtonian Fluids. Journal of Non-Newtonian Fluid Mechanics. 39. 137–187. DOI:10.1016/0377-0257(91)80010-H.

Lee, H., Lee, S., Jung, S., Lee, J. (2011). Nano-grass polyimide-based humidity sensors. Sensors Actuators B Chem. 2011 (154) 2–8.

Lester, G. E. (2006). Environmental regulation of human health nutrients (ascorbic acid, carotene, and folic acid) in fruits and vegetables. HortScience. 41:59–64

Lewis, R.J. (ed) (2004). Sax's Dangerous Properties of Industrial Materials. 11th Edition. New Jersey, Wiley- Interscience, Wiley & Sons, Inc. pp 3725

Lewis, R.J. Sr. (ed) (2007) Hawley's Condensed Chemical Dictionary 15th Edition. New York John Wiley & Sons, Inc. pp 1347

Liu, MQ., Wang C. and Kim NY. (2017). High-Sensitivity and Low-Hysteresis Porous MIM-Type Capacitive Humidity Sensor Using Functional Polymer Mixed with TiO_2 Microparticles. Sensors (Basel). 17(2): 284. DOI: [10.3390/s17020284].

Luptáková, N., Pešlová, F. and Kliber, J. (2015). The Study and Microstructure Analysis of Zinc and Zinc Oxide. METABK 54(1) 43-46.

Luurtsema, G. A. (1997). Spin Coating for Rectangular Substrates. Thesis. University of California, Berkeley. 39 pages.

Mahamuni, P. P., Pooja, M. P., Maruti, J. D., Manohar, V. B., Prem, G. S., Abhishek, C. L. and Raghvendra, A. B. (2019). Synthesis and characterization of zinc oxide nanoparticles by using polyol chemistry for their antimicrobial and antibio film activity. Biochemistry and Biophysics Reports. 17, 71 – 80.

Maheshwari, G. (2014). Solar Drying – Psychrometry. IOSR Journal of Applied Chemistry (IOSR-JAC). 2278-5736, 54-57

Marina, P., Menditto, A. and Magnusson, B. (2007). Understanding the meaning of accuracy, trueness and precision. Accreditation and Quality Assurance. DOI 10.1007/s00769-006-0191-z. 4 pages.

Marsalek, R (2014). Particle size and Zeta Potential of ZnO. Asia-Pacific Chemical, Biological & Environmental Engineering (APCBEE) Society Procedia 9 (2014) 13 – 17

Massaroni, C., Nicolò, A., Presti, D. L., Sacchetti, M., Silvestri, S. and Schena, E. (2019). Contact-Based Methods for Measuring Respiratory Rate. Sensors. 19 (908). DOI: 10.3390/s19040908. 47 pages

Mayer, S., Reuder, J. and Schween, J. (2005). Calibration of capacitive humidity sensors for atmospheric sounding by remotely piloted vehicles. Meteorological Institute, Department of Physics, LMU Munich. pp 5.

Misra, S. K., Abhishek, P. and Narendra, K. P(2018). Doped and undoped zinc oxide as humidity sensor. International Journal of Engineering Sciences and Research Technology, *7*(1), 179-185.

Mitzi, D.B., Kosbar, L.L., Murray, C.E., Copel, M. and Atzali, A. (2004). High mobility ultrathin semiconducting films prepared by spin coating. Nature. 428, 299-303.

Mogera, U., Sagade, A. A., George, S. J. and Kulkarni, G. U. (2014). Ultrafast response humidity sensor using supramolecular nanofibre and its application in monitoring breath humidity and flow. Scientific Reports. **4**, 1–9.

Mohammad, S., Nuraqeelah, S., Wee, B.C., Kok, S.,K.Y. (2018). Synthesis and Characterization of Zinc Oxide Nanoparticles with Small Particle Size Distribution. Acta Chimica Slovenica. 65. 578-585. 10.17344/acsi.2018.4213.

More, R. N., Chanshetti, U., Aurangabad, B., Dnyaneshwar, S. and Newasa, M. (2018). Review Article on ZnO thin films by Spray Pyrolysis. International Journal of Chemical and Physical Sciences. 7(Special issue), 2319-6602. 5 pages.

Morris, A. S. (2001). Measurement and Instrumentation Principles. Great Britain, Planta Tree. ISBN 0 7506 5081 8. 491 pages.

Nagarajan, S. and Kuppusamy, K. A. (2013). Extracellular synthesis of zinc oxide nanoparticle using seaweeds o*f* gulf of Mannar, India. Journal of Nanobiotechnology. 11: 39.

Naik, S. (2018). Humidity Sensing and Flow Sensing: Lecture 10. ECE 5900/6900 Fundamentals of Sensor Design. Weber State University. 29 pages.

Najeeb, N. M., Ahmad, Z. and Shakoor, R. (2018). Organic Thin-Film Capacitive and Resistive Humidity Sensors: A Focus Review. Advanced Materials Interfaces. 10.1002/admi.201800969. 19 pages

Narimani K., Nayeri F.D., Kolahdouz M. and Ebrahimi P. Fabrication, modeling and simulation of high sensitivity capacitive humidity sensors based on ZnO nanorods. Sens. Actuators B Chem. 2016 (224), 338–343. doi: 10.1016/j.snb.2015.10.012.

Nasco (2018, December 12). Sling Psychrometer Kit. Retrieved from https://www.enasco.com/p/Sling-Psychrometer-Kit%2BSB51739M

NIOSH (2005) Pocket Guide to Chemical Hazards & Other Databases. National Institute for Occupational Safety & Health, DHHS (NIOSH) Publication No.2005-151. 1335 pages.

Nishinaka, H. (2002). The effects of the environmental conditions of some Zener voltage references. Conference Digest. 166 pages.

Nielsen-Kellerman (2014). Relative Humidity Calibration Kit. Kestrel – Meters. USA

16 pages

Nunes, C. (2008). Impact of environmental conditions on fruit and vegetable quality. Stewart Postharvest Review. DOI: 4. 1-14. 10.2212/spr.2008.4.4.

O'Brien, F. E. M (1948). The Control of Humidity by Saturated Salt Solutions. Journal of Scientific Instruments, 25(3), 73-76. DOI:10.1088/0950-7671/25/3/305

Pandey, N. K., Tiwari, K. and Akash, R. (2012). ZnO–TiO2 nanocomposite: Characterization and moisture sensing studies. Bull. Mater. Sci. 35(3) 347–352.

Pooder, J. (2018, November 11). Red and Blue shift in Raman Spectra. What is the explanation? ResearchGate. Retrieved from https://www.researchgate.net/post/Red_and_Blue_shift_in_Raman_Spectra_What_is_the explanation

Poole, C. P. Jr. and Owens, F. J. (2003). Introduction to Nanotechnology. U.S.A., John Wiley & Sons, Inc. 0-471 -07935-9. 400 pages.

Prem P. S. B.,Vikaram S. R. and Anshul, B. (2019). Advancements in Micro-Nano-Mechatronics sensors controller and actuators. IJARIIE. 5 (1), 185 – 189.

Ramin, M., Aziz, H., Abolfazl, B., Saeid, L. and Asadollah, A. (2018). Enhanced anti-bacterial activities of ZnO nanoparticles and ZnO/CuO nanocomposites synthesized using *Vaccinium arctostaphylos* L. fruit extract, Artificial Cells, Nanomedicine, and Biotechnology. 46 (1), 1200-1209. DOI: 10.1080/21691401.2018.1448988

Raut, S. B. and Thorat, P. V. (2015). Review on Preparation, Characterization and Application of Zinc Oxide (ZnO) Nanoparticles by Green Synthesis Method. International Journal of Emerging Technology and Advanced Engineering. 5 (3), 2250-2459, ISO 9001:2008. 521 - 524

Regtien, P. P. L. (2012) Sensors for mechatronics. Elsevier. ISBN: 9780123944092, 322 pages

Rittersma, Z (2002). "Recent achievements in miniaturised humidity sensors - a review of transduction techniques," Sensors and Actuators A: Physical, 96 (2-3), 196 – 210.

Rosa, C. and Brad, L. (2009). Modeling effects of relative humidity, moisture, and extreme environmental conditions on power electronic performance. Institute of Electrical and Electronics Engineers (IEEE). 978-1-4244-2893-9/09/$25.00, 1052-1059.

Rotronic, (2014). Part One: Theory, Humidity Accuracy. Humidity theory. ROTRONIC Measurement Solutions. pp 1 – 28.

Roveti, D.K.. (2001). Choosing a humidity sensor: A review of three technologies. Sensors (Peterborough, NH). 18. 54-58.

Sahu, N., Parija, B. and Panigrahi, S. (2009). Fundamental understanding and modeling of spin coating process : A review. Indian Journal of Physics. 83 (4) 493-502.

Salahuddin, N. A., El-Kemary, M., Ebtisam, M. I. (2015). Characterization of ZnO Nanoparticles via Precipitation Method: Effect of Annealing Temperature on Particle Size. Nanoscience and Nanotechnology. 5(4): 82-88. DOI: 10.5923/j.nn.20150504.02

Sandhu, S. K. and Dhaliwal, L. K. (2016). Crop geometry effects on relative humidity variation within wheat crop. Asian Journal of Environmental Science. 11(1), 94-101. 0976- 8947. 94-101. DOI: 10.15740/HAS/AJES/11.1/94-101

Santhaveesuk, T., Siwawongkasem, K., Pommek, S. and Choopun, S. (2016) . High performance Humidity Sensor Based on ZnO nanoparticles synthesized by co-precipitation method. Applied Mechanices and Materials. 848, 99-102.

Saric, A., Stefanic, G., Drazic, G., Gotic, M. (2015). Solvothermal synthesis of zinc oxide microspheres. Journal of Alloys and Compounds. 652, 91-99.

Schultz, G. (2015). Chilled Mirror Hygrometry, a Technology for Process and Lab: Gases and Instrumentation. Feature. 23 – 26.

Schumm, M. (2008). ZnO-based semiconductors studied by Raman spectroscopy: semimagnetic alloying, doping, and nanostructures. Doctoral thesis: Julius-Maximilians Universit¨at W¨urzburg. 93 pages

Shelton, D. P. (2008). Air Properties: Temperature and Relative Humidity. NebGuide, Institute of Agriculture and Natural Resources. G1849, 4 pages.

Sherwood, M. (2010). Vapourisation and Vapourisers. World Federation of Societies of Anesthesiologists Anesthesia Tutorial of the Week. 171, 9 pages.

Shamshiri, R. (2007). Principles of Greenhouse Control Engineering: Theories & Concepts Institute of Advanced Technology Universiti Putra Malaysia. 2006-2007. 87 pages**.**

Shukla, R. K., Anchal, S. A. C. Pandey, S. A., Kamakhya, P. M., Mamta, P. (2015). Sensitivity of polyaniline-zinc oxide composite to Humidity. Sensors & Transducers.188(5), 26-32.

Sigma-Aldrich, (2013). Material Safety Data Sheet for Zinc Oxide. Product Number: 204951, Version 4.2.

Sin, N. D. Md., Kamel, M. F., Alip, R. I., Mohamad, N., and Rusop, M. (2011). The electrical characteristics of aluminum doped zinc oxide thin film for humidity sensor applications. Hindawi Publishing Corporation Advances in Materials Science and Engineering. 2011, Article ID 974906, 5 pages

Sin, N. D. Md., Mohamad, F. T., Mamat, M. H., and Rusop, M. (2014). Enhancement of nanocomposite for humidity sensor application. Recent Trends in Nanotechnology and Materials Science, Engineering Materials, DOI: 10.1007/978-3-319-04516-0_2: 15-30

Singh, H., Kumar, A., Bansod, S. B., Singh, T., Thakur, A., Singhe, T. and Sharma, J. (2018). Enhanced moisture sensing properties of a nanostructured ZnO coated capacitive sensor. The Royal Society of Chemistry Advances. 2018 (8), 3839–3845.

Singh, A., Kumar, R., Malhotra, N. and Suman, (2012). Preparation of ZnO nanoparticles by solvothermal process. International Journal for Science and Emerging Technologies with Latest Trends 4(1): 49-53.

Sinha, G. R. (2017). Introduction and classification of sensors. Lecture 02. Myanmar Institute of Information Technology Mandalay Myanmar. 321625555. 15 pages.

Smith, R., Inomata, H. and Peters, C. (2013). Chemical Information and Know-How. Supercritical Fluid Science and Technology. 4, 121-174. DOI.org/10.1016/B978-0-444-52215-3.00004-0

Sonntag, D. (1987). WMO Assmann Aspiration Psychrometer Intercomparison. Instruments and Observing Methods Report No 34. Potsdam, World Meteorological Organization. 186 pages.

Spooner, E. (2019). Spin Coating: A Guide to Film Thickness. UK, Ossila Ltd. 7 pages.

Sureshkumar and Rajesh (2018). The Analysis of Different Types of IoT Sensors and security trend as Quantum chip for Smart City Management. IOSR Journal of Business and Management (IOSR-JBM). 20 (1,4), 55-60. 2278-487X, 2319-7668 DOI: 10.9790/487X-2001045560

Tanner, K., Tschulik, R., Tahany, K., Jurkschat, C., Batchelor-McAuley, and Compton, R. G.(2015) Nanoparticle capping agent dynamics and electron transfer: polymer-gated oxidation of silver nanoparticles. The Journal of Physical Chemistry C. 119(32), 18808–18815.

Tapan, K. D., Manon, C., Yannick, O., Michel. G., and Denis, L. R. (2001). Simultaneous observation of the O-O and Fe-O2 stretching modes in oxyhemoglobins. PNAS. 98 (2), 479–484

Taziwa R., Luyolo N. and Edson M (2017). Structural, Morphological and Raman scattering Studies of Carbon Doped ZnO nanoparticles Fabricated by PSP Technique. Journal of Nanoscience & Nanotechnology Research. 1(1:3). 8 pages

Tennermann, J. (2011). Capacitive Humidity Sensors: Advantages and Disadvantages. Pharma Automation Sensors. Canada, Jim Baker, Publisher. 4 pages.

TDK (2018, August 8). Humidity Sensors. Humidity Sensors CHS Series. TDK Product Center. 7 (2), 6 pages. https://product.tdk.com/info/de/products/sensor/sensor/humidity/technote/tpo /index.html

Traversa, E. and Bearzotti, A. (1995). A Novel Humidity-Detection Mechanism for ZnO Dense Pellets. Sens. Actuators B Chem. *23*, 181–186.

Tripathy, A., Pramanik, S., Manna, A., Bhuyan, S., Shah, N. F. A., Radzi, Z. and Osman, N. A. (2016). Design and development for capacitive humidity sensor applications of lead-free Ca,Mg,Fe,Ti-Oxides-Based Electro-Ceramics with improved sensing properties via physisorption. Sensors. 16, 1135; DOI:10.3390/s16071135, 18 pages.

Tyona, M. D. (2013). A theoritical study on spin coating technique. Advances in Materials Research. 2(4) (2013) 195-208 DOI: 10.12989/amr.2013.2.4.195

Vining, K. C. (1990) Effects of weather on agricultural crops and livestock: an overview, International Journal of Environmental Studies. 36(1-2), 27-39, DOI: 10.1080/00207239008710581

Voutilainen, J. (2005). Methods and Instrumentation for Measuring Moisture in Building Structures. Dissertation, Helsinki University of Technology Finland. 951-22-7522-8, 951-22-7523-6, 1459-1111. 157 pages.

Wang, Y. (2013). Fabrication of Relative Humidity Sensors based on Polyimide Nanoparticles. Dissertation, Simon Fraser University Canada. 88 pages.

Ward, D. R., Kursinski, E. R., Otarola, A. C., Stovern, M., McGhee, J., Young, A., Hainsworth, J., Hagen, J., Sisk, W. and Reed, H. (2019). Retrieval of water vapour using ground-based observations from a prototype ATOMMS active centimeter- and millimeter-wavelength occultation instrument. Atmospheric Measurement Techniques, 12, 1955–1977. doi.org/10.5194/amt-12-1955-2019

Weatherbase (2017, January 24). Travel weather averages. Retrieved from *http://www.weatherbase.com/*.

Wei, Z., Hong, M. and Simon, X. Y. (2016). An Inexpensive, Stable, and Accurate Relative Humidity Measurement Method for Challenging Environments. Sensors. 16 (398), DOI: 10.3390/s16030398. 15 pages.

Wexler, A. and Emil, J. M. (Ed.) (1963). ISA Transducer Compendium. Instrument Society of America. Plenimum Press, New York. pp. 502-508.

Wexler, A., and Hasegawa, S. (1954). Relative humidity-temperature relationships of some saturated salt solutions in the temperature range 0°C to 50 °C. J. Res. Nat. Bur. Stand. (U.S.) 53 (1), 19-26 RP 2512.

Wexler, A., and Hyland, R. W. (1964). The NBS standard hygrometer, Humidity and Moisture, Vol. Ill, A. Wexler (ed.) (Reinhold Publishing Corporation, N.Y., 1964), pp. 389-432.

Widiyastuti, W., Machmudah, S., Nurtono, T., Winardi, S., Balgis, R., Ogib, T. and Okuyam, K. (2017). Morphology and optical properties of zinc oxide nanoparticles synthesised by solvothermal method. Chemical Engineering Transactions. 56, 955-960. DOI: 10.3303/CET1756160.

Wood, W. H., Marshall, S. J., and Fargey, S. E. (2019). Daily measurements of near-surface humidity from a mesonet in the foothills of the Canadian Rocky Mountains, 2005–2010. Earth System Science Data, 11, 23–34. DOI:10.5194/essd-11-23-2019

Writeup M. (2014, October 13). Sling psychrometer. Retrieved from *http://instrumentationandcontrollers.blogspot.com/2010/12/sling-psychrometer.html*

Writeup M. (2018, October 9). Hair hygrometer – Instrumentation and Control Engineering. Retrieved from *http://instrumentationandcontrollers.blogspot.com/2010/12/hair-hydrometer.html*

Yamamoto, T. and Shimizu, H. Some Considerations on Stability of Electrical Resistance of the TiO2/SnO2 Ceramic Moisture Sensor. *IEEE Trans.* Compon. Hybrids Manuf. Technol. **1982**, 5, 238–241.

Yang, H., Ye, Q., Zeng, R., Zhang, J., Yue, L., Xu, M., Qiu, Z. and Wu, D. (2017). Stable and fast-response capacitive humidity sensors based on a ZnO nanopowder/PVP-RGO multilayer. Sensors. 17, 2415; doi:10.3390/s17102415, 11 pages.

Yankee Environmental Systems, (2005). Chilled mirror hygrometers. Bulletin CMHY G1. USA, Yankee Environmental Systems, Inc. 4 pages.

Yasrebi, N. and Moghaddas, J. (2015). Study on the Effect of Humidity on Electrical Properties of Copper-Silica Aerogel. Iranian Journal of Chemical Engineering. 12(2), 11 pages.

Yedurkar, S., Chandra, M. and Prakash, M. (2016). Biosynthesis of Zinc Oxide Nanoparticles Using Ixora Coccinea Leaf Extract—A Green Approach. Open Journal of Synthesis Theory and Applications. 5 (1), 14 pages. Doi:10.4236/ojsta.2016.51001

Yeo, T., Sun, T. and Grattan, K. (2008), Fibre-optic sensor technologies for humidity and moisture measurement. Sensors and Actuators A: Physical, 144 (2), 280-295.

Yiamsawas, D., Boonpavanitchakul, K. and Kangwansupamonkon, W. (2009). Preparation of ZnO Nanostructures by Solvothermal Method. Journal of Microscopy Society of Thailand, 23(1). 75-78.

Young, J. F. (1967). Humidity control in the laboratory using salt solutions—a review. Journal of Applied Chemistry Banner. 17(9) PP. 241-245. doi.10.1002/jctb.5010170901

Zakariyah, S. (2013). Worked Examples on Gas Laws and Kinetic Theory. 37 pages DOI:10.13140/2.1.4809.6965.

Zhang, X., Yu-lian, C. and Xi-qi, H. (1986). The improvement of lithium chloride dew-point hygrometer for direct reading and controlling of relative humidity. Environment International. 12(1–4), 471-474.

Zook, J. D, 2008. Sensors as Information Transducers. Encyclopedia of Sensors, edited by Craig A. Grimes, Elizabeth C. Dickey and Michael V. Pishko, American Scientific Publishers, Stevenson Ranch, California, 9, 329-359

APPENDIX

A. RAMAN DATA FOR SLS AND LABS SAMPLES

LABS Sample		SLS Sample	
Wavenumber	**Intensity**	**Wavenumber**	**Intensity**
408	1122.959023	408	1033.657299
410	1055.127499	410	974.0431141
412	988.4958279	412	909.7613443
414	965.3556553	414	896.7945583
416	992.7775869	416	908.0355441
418	1045.973802	418	932.3340622
420	1117.123653	420	995.3319507
422	1245.412908	422	1116.345873
424	1396.083334	424	1261.499044
426	1370.613204	426	1264.417093
428	1131.756671	428	1076.424466
430	969.6968799	430	915.2376178
432	921.4137114	432	854.0829482
434	914.8904578	434	842.668111
436	919.1702243	436	841.1769296
438	954.9943234	438	866.5596276
440	957.5684536	440	882.269364
442	947.5905566	442	881.0674196
444	946.0260744	444	872.2951924
446	930.4237212	446	856.5632429
448	902.7031506	448	825.7641946
450	873.6371573	450	800.2280264
452	856.7753583	452	789.0417095
454	861.0561512	454	787.5921735
456	883.3119361	456	802.4150449
458	911.6672523	458	830.6351693
460	917.0565107	460	836.1446826
462	894.5011233	462	810.5312823
464	881.8324111	464	803.4038261
466	876.3202831	466	799.5451679
468	875.0573016	468	794.2936641
470	869.390399	470	795.6322898

472	848.0764418	472	795.498992
474	831.5316253	474	763.1730728
476	834.3304143	476	750.8983011
478	857.1233456	478	780.7719576
480	875.5009625	480	802.5571045
482	853.2088022	482	775.9753671
484	863.022573	484	774.7269426
486	888.6689601	486	800.6852347
488	881.8455713	488	812.2029528
490	878.118327	490	817.3024491
492	863.2003141	492	791.1649021
494	832.8635518	494	748.0886155
496	808.3481184	496	722.5668463
498	812.3410238	498	731.6574922
500	832.9389881	500	765.2327986
502	855.9290256	502	794.0648969
504	863.214351	504	793.3498534
506	857.7346414	506	777.0075535
508	879.1321764	508	797.4783746
510	908.5063338	510	828.9888833
512	908.4648178	512	845.82075
514	873.8647443	514	827.398428
516	834.6724386	516	765.0935384
518	796.2381021	518	727.3442092
520	800.4061374	520	737.3707491
522	841.0164151	522	767.6722263
524	869.2303152	524	789.2757733
526	887.7448243	526	811.6842491
528	890.8713653	528	818.7422888
530	885.0696548	530	814.946252
532	879.6072848	532	808.1798123
534	870.6488201	534	791.1592675
536	859.5080621	536	792.0478168
538	865.0559596	538	805.6736242
540	879.6975064	540	810.4509315
542	883.3236161	542	804.9186312
544	894.2218566	544	811.7563766
546	876.3159757	546	802.287497
548	841.5030837	548	775.7280192

550	839.6559586	550	766.741588
552	890.1756672	552	800.1166192
554	959.9419739	554	854.8567149
556	999.5899243	556	902.7706923
558	1000.581233	558	923.7363206
560	990.5830059	560	918.488084
562	979.3891441	562	909.2435872
564	959.3278735	564	888.2145245
566	937.6326351	566	865.8002027
568	928.9085531	568	850.0350573
570	937.2593222	570	839.086173
572	955.2507362	572	868.2979121
574	962.3188693	574	889.4849561
576	951.8799011	576	880.1393975
578	931.9419666	578	859.9325044
580	910.5693566	580	833.5359838
582	902.6955773	582	831.9929399
584	880.2178807	584	822.9840853
586	842.700623	586	784.3536278
588	824.4467856	588	747.4292109
590	803.125515	590	727.478608
592	760.9981683	592	688.9363716
594	741.1377709	594	668.2649787
596	770.3003918	596	698.2256426
598	807.1230009	598	732.5312975
600	845.7909087	600	770.9059919
602	878.9077003	602	809.6540334
604	901.1521572	604	830.8763152
606	914.110023	606	836.1467372
608	923.1200039	608	856.3109287
610	935.2631871	610	859.4838082
612	931.5817547	612	849.170065
614	912.5370739	614	838.5287168
616	919.6804825	616	840.4236095
618	978.5265161	618	887.0173172
620	997.0337182	620	917.7296053
622	995.2696401	622	916.6903877
624	1004.289111	624	911.9980895
626	979.1463697	626	913.5501924

628	946.0767621	628	899.4954409
630	932.9170844	630	872.4633814
632	923.490156	632	846.9892832
634	907.21984	634	830.775109
636	913.0244763	636	824.9827983
638	933.1902214	638	839.8991577
640	937.2258634	640	859.7537676
642	962.7045771	642	884.5749384
644	1028.764177	644	924.3012367
646	1053.997063	646	963.6111384
648	1052.865212	648	975.9323726
650	1035.842953	650	958.8392157
652	1005.729486	652	926.4951823
654	967.118886	654	890.2101044
656	920.1414003	656	849.8613594
658	870.4586791	658	808.9651026
660	854.8201405	660	779.2793754
662	869.5344121	662	776.7358139
664	879.9792725	664	797.9627988
666	890.7715849	666	809.9367838
668	890.4485071	668	812.3160347
670	893.9883256	670	821.2340469
672	913.7758766	672	839.4050786
674	941.582385	674	859.6525758
676	958.4620359	676	877.8990947
678	917.6358484	678	849.6827576
680	874.3632375	680	810.9676311
682	884.9312419	682	809.2233382
684	922.5136972	684	835.5298913
686	929.6054042	686	852.8399613
688	904.8690263	688	843.6637777
690	900.0875891	690	831.1215715
692	935.0934121	692	854.542809
694	977.6104418	694	903.6983734
696	995.3660259	696	901.6450341
698	952.1590068	698	874.4699104
700	926.7196762	700	862.2481144
702	923.4087185	702	853.1272174
704	894.9751328	704	825.8662199

706	922.7915604	706	820.9145901
708	957.6134631	708	856.5743189
710	968.5916561	710	890.5195086
712	956.8302545	712	887.3354408
714	938.6891242	714	861.2484022
716	938.4871878	716	850.0474036
718	936.0761477	718	860.4307819
720	918.4289623	720	850.0052445
722	902.0863798	722	832.1097369
724	903.365551	724	834.7220584
726	909.8260958	726	825.7484479
728	917.9137397	728	841.2130413
730	937.6273283	730	861.2114335
732	965.6161488	732	886.8946355
734	976.1639973	734	909.9895294
736	956.1043208	736	887.1594584
738	945.4133751	738	869.5014704
740	912.9543633	740	846.3062078
742	898.3382174	742	840.2185198
744	917.2748844	744	853.2464423
746	915.4263775	746	845.0665539
748	936.6468345	748	855.0803573
750	936.3864667	750	856.6994041
752	933.4930135	752	854.7236958
754	946.0606911	754	858.1894309
756	948.0003874	756	863.0364626
758	954.2239868	758	887.4233578
760	983.6648663	760	898.2381674
762	996.809361	762	912.1437093
764	991.714054	764	926.939105
766	990.1706649	766	915.2284318
768	974.2388266	768	892.6314756
770	976.7463245	770	895.869551
772	976.1853384	772	910.196396
774	959.288204	774	898.2743666
776	950.8837367	776	876.1557782
778	965.4287912	778	892.5907293
780	964.0695342	780	909.5868332
782	961.0876241	782	907.7360953

784	981.4260297	784	905.9268211
786	990.6320202	786	905.1094947
788	967.7833588	788	899.2163103
790	984.2438126	790	915.976924
792	994.7824189	792	922.5929628
794	1003.737631	794	909.9057983
796	1007.89327	796	906.2230215
798	999.0948004	798	923.619327
800	997.967854	800	933.1312404
802	993.5063529	802	919.5676821
804	967.3210526	804	887.1223661
806	962.2068034	806	879.9688087
808	977.7105027	808	895.4827897
810	984.0091271	810	907.2314027
812	1018.654427	812	943.9253469
814	1022.003708	814	944.6641141
816	990.2225836	816	917.3581973
818	959.7584214	818	890.5471034
820	961.2662637	820	883.1231958
822	987.3042566	822	901.2136562
824	994.9186065	824	917.7945431
826	1022.549329	826	942.2668971
828	1025.789236	828	955.6320778
830	1007.680868	830	950.9174579
832	1009.6198	832	935.4024162
834	995.1243778	834	910.6662842
836	982.5379787	836	923.4376897
838	1002.839254	838	930.1725653
840	1017.70988	840	932.1006258
842	1011.419391	842	934.0471409
844	1011.795065	844	920.7207653
846	1006.493257	846	928.335904
848	1033.919238	848	956.787742
850	1088.941528	850	992.41166
852	1145.776511	852	1036.400983
854	1142.335814	854	1041.060236
856	1055.261188	856	970.2051992
858	1012.314878	858	939.5646104
860	1002.384532	860	928.1157641

862	995.4682851	862	927.3433019
864	989.6621362	864	920.1044045
866	992.0001926	866	909.9408173
868	1008.025201	868	934.9448428
870	1058.560105	870	973.8779377
872	1160.606378	872	1054.137544
874	1217.821284	874	1106.202323
876	1184.977609	876	1086.798659
878	1112.405165	878	1035.757559
880	1046.504817	880	989.2643059
882	1009.879564	882	944.7025998
884	997.8615922	884	927.7321185
886	1001.01472	886	932.9378355
888	1003.472631	888	930.4694711
890	995.4681302	890	915.1780774
892	987.180695	892	907.4066118
894	988.5796287	894	900.6246165
896	995.0176449	896	915.8419716
898	1001.157239	898	920.0922953
900	1002.857505	900	923.2651203

B. BET Equation

BET equation requires a linear plot of $1/(W(P/P_0)-1)$ against P/P_0 from equation 4.1 which is known as BET equation.

$$\frac{1}{W\left(\frac{P_0}{P}\right)-1} = \frac{c-1}{W_m c}\left(\frac{P}{P_0}\right) + \frac{1}{W_m c}$$

where P and P_0 are the equilibrium and the saturation pressure of adsorbate at the temperature of adsorption, W is the weight of gas adsorbed and W_m is the weight of the gas adsorbed as monolayer and c is the BET constant, $c > 1$. The BET equation is a linear equation with the slope (s) of the equation $= \frac{c-1}{W_m c}$ and the intercept (i) = $\frac{1}{W_m c}$. The results of BET surface area analysis depend on BET equation.

C. Multipoint BET data for SLS

Relative pressure (P/P_0)	Volume at STP (cc/g)	$1/(W (P_0/P) -1)$
0.046585	19.8854	1.9660
0.111780	33.7291	2.9853
0.175174	46.7005	3.6386
0.238216	59.7389	4.1882
0.296673	72.1435	4.6781

D. Multipoint BET data for LABS

Relative pressure (P/P_0)	Volume at STP (cm^3/g)	$1/(W (P_0/P) -1)$
0.048471	20.1697	2.0207
0.113852	34.2532	3.0011
0.177322	47.3278	3.6439
0.241993	60.6483	4.2117
0.301092	73.3127	4.7016

E. Data from Unannealed Nanostructured ZnO Capacitive RH Sensor

1. Adsorption in Saturated Solution of Lithium Chloride (LiCl)

RH (%)	Capacitance (pF)	Temperature (0C)	Time (s)
13	9.4	28	0
14	10.2	28	2
17	10.9	28	4
29	11.4	28	6
35	11.5	28	8
42	11.6	28	10
47	11.7	28	12
51	11.7	28	14
55	11.7	28	16
57	11.7	28	18
59	11.7	28	20
61	11.8	28	22
62	11.8	28	24
64	11.8	28	26
65	11.8	28	28
66	11.9	28	30
66	11.9	28	32
67	11.9	28	34

67	11.9	28	36
68	12.1	28	38
69	12.1	28	40

2. Desorption in Saturated Solution of Lithium Chloride (LiCl)

RH (%)	Capacitance (PF)	Temperature (0C)	Time (s)
13	9.4	28	0
14	10.2	28	2
17	10.9	28	4
29	11.4	28	6
35	11.5	28	8
42	11.6	28	10
47	11.7	28	12
51	11.7	28	14
55	11.7	28	16
57	11.7	28	18
59	11.7	28	20
61	11.8	28	22
62	11.8	28	24
64	11.8	28	26
65	11.8	28	28
66	11.9	28	30
66	11.9	28	32
67	11.9	28	34
67	11.9	28	36
68	12.1	28	38
69	12.1	28	40

3. Adsorption in Saturated Solution of Lithium Chloride (K_2CO_3)

RH %	C (pF)	Temp. (°C)	Time (s)	RH %	C (pF)	Temp. (°C)	Time (s)
93	23.8	27	0	82	14.6	28	60
92	23.5	27	2	81	14.5	28	62
92	23.2	27	4	81	14.3	28	64
91	22.1	27	6	81	14.2	28	66
91	21.7	27	8	81	14.2	28	68
90	21.1	27	10	80	14.1	28	70
90	20.2	27	12	80	14.1	28	72
89	19.7	27	14	80	14	28	74
89	19.1	27	16	79	13.9	28	76
88	18.9	27	18	79	13.9	28	78
88	18.5	27	20	79	13.8	28	80
87	18.3	27	22	78	13.6	28	82
87	18.1	27	24	78	13.6	28	84
87	18	27	26	78	13.6	28	86
86	17.6	27	28	78	13.6	28	88
86	17	27	30	77	13.5	28	90
85	16.9	27	32	77	13.5	28	92
85	16.7	27	34	77	13.4	28	94
86	16.4	28	36	77	13.4	28	96
85	16.3	28	38	76	13.4	28	98
85	15.9	28	40	76	13.4	28	100
85	15.9	28	42	76	13.3	28	102
84	15.8	28	46	76	13.3	28	104
84	15.7	28	48	75	13.3	28	106
84	15.7	28	50	76	13.2	29	108
83	15.3	28	52	76	13.2	29	110
83	15.2	28	54	76	13.2	29	112
82	15.1	28	56	76	13.1	29	114
				76	13.1	29	116

RH %	C (pF)	Temp. (^{O}C)	Time (s)	RH %	C (pF)	Temp. (^{O}C)	Time (s)
75	13.1	29	118	70	12.5	29	178
75	13.1	29	120	70	12.5	29	180
75	13.1	29	122	70	12.5	29	182
75	13.1	29	124	70	12.5	29	184
74	13	29	126	70	12.5	29	186
74	13	29	128	70	12.5	29	188
74	13	29	130	69	12.5	29	190
74	13	29	132	69	12.5	29	192
74	13	29	134	69	12.5	29	194
74	12.9	29	136	69	12.5	29	196
73	12.9	29	138	69	12.4	29	198
73	12.9	29	140	69	12.4	29	200
73	12.9	29	142	69	12.4	29	202
73	12.8	29	144	69	12.4	29	204
73	12.8	29	146	68	12.4	29	206
72	12.8	29	148	68	12.4	29	208
72	12.8	29	150	68	12.4	29	210
72	12.8	29	152	68	12.4	29	212
72	12.8	29	154	68	12.4	29	214
72	12.8	29	156	68	12.4	29	216
72	12.8	29	158	68	12.4	29	218
71	12.7	29	160	68	12.4	29	220
71	12.7	29	162	68	12.3	29	222
71	12.7	29	164	67	12.3	29	224
71	12.6	29	166	68	12.3	29	226
71	12.6	29	168	67	12.3	29	228
71	12.6	29	170	67	12.3	29	230
71	12.6	29	172	67	12.2	29	232
70	12.6	29	174	67	12.2	29	234
70	12.5	29	176	67	12.2	29	236

RH %	C (pF)	Temp. (^{O}C)	Time (s)	RH %	C (pF)	Temp. (^{O}C)	Time (s)
67	12.2	29	238	64	12.1	29	298
67	12.2	29	240	64	12.1	29	300
67	12.2	29	242	64	12.1	29	302
67	12.2	29	244	64	12.1	29	304
67	12.2	29	246	64	12.1	29	306
66	12.2	29	248	64	12	29	308
66	12.2	29	250	64	12	29	310
66	12.2	29	252	64	12	29	312
66	12.2	29	254	64	12	29	314
66	12.2	29	256	64	12	29	316
66	12.2	29	258	64	12	29	318
66	12.2	29	260	64	12	29	320
66	12.2	29	262	64	12	29	322
66	12.1	29	264	64	12	29	324
66	12.1	29	266	64	12	29	326
66	12.1	29	268	64	12	29	328
66	12.1	29	270	64	12	29	330
65	12.1	29	272	63	12	29	332
65	12.1	29	274	64	12	29	334
65	12.1	29	276	63	12	29	336
65	12.1	29	278	63	12	29	338
65	12.1	29	280	63	12	29	340
65	12.1	29	282	63	12	29	342
65	12.1	29	284	63	12	29	344
65	12.1	29	286	63	12	29	346
65	12.1	29	288	63	12	29	348
65	12.1	29	290	63	12	29	350
65	12.1	29	292	63	12	29	352
65	12.1	29	294	63	12	29	354
65	12.1	29	296	63	12	29	356

RH %	C (pF)	Temp. (^{O}C)	Time (s)	RH %	C (pF)	Temp. (^{O}C)	Time (s)
63	12	29	358	62	11.9	29	418
63	12	29	360	62	11.9	29	420
63	11.9	29	362	62	11.9	29	422
63	11.9	29	364	62	11.9	29	424
63	11.9	29	366	62	11.8	29	426
63	11.9	29	368	62	11.8	29	428
63	11.9	29	370	62	11.8	29	430
63	11.9	29	372	62	11.8	29	432
63	11.9	29	374	62	11.8	29	434
62	11.9	29	376	62	11.8	29	436
62	11.9	29	378	61	11.8	29	438
62	11.9	29	380	62	11.8	29	440
62	11.9	29	382	62	11.8	29	442
62	11.9	29	384	61	11.8	29	444
62	11.9	29	386	61	11.8	29	446
62	11.9	29	388	61	11.8	29	448
62	11.9	29	390	61	11.8	29	450
62	11.9	29	392	61	11.8	29	452
62	11.9	29	394	61	11.8	29	454
62	11.9	29	396	61	11.8	29	456
62	11.9	29	398	61	11.8	29	458
62	11.9	29	400	61	11.8	29	460
62	11.9	29	402	61	11.8	29	462
62	11.9	29	404	61	11.7	29	464
62	11.9	29	406	61	11.7	29	468
62	11.9	29	408	61	11.7	29	470
62	11.9	29	410	61	11.7	29	472
62	11.9	29	412	61	11.7	29	474
62	11.9	29	414	61	11.7	29	476
62	11.9	29	416	61	11.7	29	478

RH %	C (pF)	Temp. (^{O}C)	Time (s)	RH %	C (pF)	Temp. (^{O}C)	Time (s)
61	11.7	29	500	60	11.6	29	560
61	11.7	29	502	60	11.6	29	562
61	11.7	29	504	60	11.6	29	564
61	11.7	29	506	60	11.6	29	566
61	11.7	29	508	60	11.6	29	568
61	11.7	29	510	60	11.6	29	570
61	11.7	29	512	60	11.6	29	572
61	11.7	29	514	60	11.6	29	574
61	11.7	29	516	60	11.6	29	576
61	11.7	29	518	60	11.6	29	578
60	11.7	29	520	60	11.6	29	580
60	11.7	29	522	60	11.6	29	582
60	11.7	29	524	60	11.6	29	584
60	11.7	29	526	60	11.6	29	586
60	11.7	29	528	60	11.6	29	588
60	11.7	29	530	60	11.6	29	590
60	11.7	29	532	60	11.6	29	592
60	11.7	29	534	60	11.6	29	594
60	11.7	29	536	60	11.6	29	596
60	11.7	29	538	60	11.6	29	598
60	11.7	29	540	60	11.6	29	600
60	11.7	29	542	60	11.6	29	602
60	11.7	29	544	60	11.6	29	604
60	11.6	29	546	60	11.6	29	606
60	11.6	29	548	60	11.6	29	608
60	11.6	29	550	60	11.6	29	610
60	11.6	29	552	60	11.6	29	612
60	11.6	29	554	60	11.6	29	614
60	11.6	29	556	60	11.6	29	616
60	11.6	29	558	60	11.6	29	618

RH %	C (pF)	Temp. (^{O}C)	Time (s)	RH %	C (pF)	Temp. (^{O}C)	Time (s)
60	11.6	29	620	59	11.5	29	696
60	11.6	29	622	59	11.5	29	698
59	11.6	29	624	59	11.5	29	700
59	11.6	29	626	59	11.5	29	702
60	11.6	29	628	59	11.5	29	704
60	11.6	29	630	59	11.5	29	706
59	11.6	29	632	59	11.4	29	708
60	11.6	29	634	59	11.4	29	710
60	11.6	29	636	59	11.4	29	712
60	11.6	29	638	59	11.4	29	714
59	11.6	29	640	59	11.4	29	716
59	11.6	29	642	59	11.4	29	718
59	11.5	29	644	59	11.4	29	720
60	11.5	29	646	59	11.4	29	722
59	11.5	29	648	59	11.4	29	724
59	11.5	29	650	59	11.4	29	726
59	11.5	29	652	59	11.4	29	728
59	11.5	29	654	59	11.4	29	730
59	11.5	29	656	59	11.4	29	732
59	11.5	29	658	59	11.4	29	734
59	11.5	29	660	59	11.4	29	736
59	11.5	29	662	59	11.4	29	738
59	11.5	29	664	59	11.4	29	740
59	11.5	29	666	59	11.4	29	742
59	11.5	29	668	59	11.4	29	744
59	11.5	29	670	59	11.4	29	746
59	11.5	29	672	59	11.4	29	748
59	11.5	29	674	59	11.4	29	750
59	11.5	29	676	59	11.4	29	752
59	11.5	29	678	59	11.4	29	754
59	11.5	29	680	59	11.4	29	756
59	11.5	29	682	59	11.3	29	758
59	11.5	29	684	59	11.3	29	760
59	11.5	29	686	59	11.3	29	762
59	11.5	29	688	59	11.3	29	764
59	11.5	29	690	59	11.3	29	766
59	11.5	29	692	59	11.3	29	768
59	11.5	29	694	59	11.3	29	770

RH %	C (pF)	Temp. (^{O}C)	Time (s)	RH %	C (pF)	Temp. (^{O}C)	Time (s)
58	11.3	29	772	58	11.2	29	820
59	11.3	29	774	59	11.2	29	822
59	11.3	29	776	58	11.2	29	824
59	11.2	29	778	58	11.2	29	826
59	11.2	29	780	58	11.2	29	828
59	11.2	29	782	58	11.2	29	830
58	11.2	29	784	58	11.2	29	832
59	11.2	29	786	58	11.2	29	834
59	11.2	29	788	58	11.2	29	836
58	11.2	29	790	58	11.2	29	840
58	11.2	29	792	58	11.2	29	842
59	11.2	29	794	58	11.2	29	844
58	11.2	29	796	58	11.1	29	846
59	11.2	29	798	59	11.1	29	848
58	11.2	29	800	58	11.1	29	850
58	11.2	29	802	58	11.1	29	852
58	11.2	29	804	58	11.1	29	854
58	11.2	29	806	58	11.1	29	856
58	11.2	29	808	58	11.1	29	858
59	11.2	29	810	58	11.1	29	860
58	11.2	29	812	58	11.1	29	862
58	11.2	29	814	58	11.1	29	864
58	11.2	29	816	58	11.1	29	866
58	11.2	29	818	57	11.1	28	868

4. Desorption in Saturated Solution of Lithium Chloride (K_2CO_3)

RH %	C (pF)	Temp. (^{O}C)	Time (s)	RH %	C (pF)	Temp. (^{O}C)	Time (s)
64	11.1	27	0	81	11.2	27	24
69	11.1	27	2	81	11.2	27	26
73	11.1	27	4	81	11.2	27	28
75	11.1	27	6	81	11.2	27	30
77	11.1	27	8	81	11.2	27	32
78	11.1	27	10	81	11.2	27	34
79	11.1	27	12	81	11.2	28	36
80	11.1	27	14	81	11.2	28	38
80	11.1	27	16	81	11.2	28	40
81	11.1	27	18	81	11.3	28	42

RH %	C (pF)	Temp. (^{O}C)	Time (s)	RH %	C (pF)	Temp. (^{O}C)	Time (s)
82	11.3	28	50	83	12.7	29	126
82	11.3	28	52	83	12.7	29	128
82	11.3	28	54	83	12.7	29	130
81	11.4	28	56	83	12.7	29	132
82	11.4	28	58	83	12.7	29	134
82	11.4	28	60	84	12.7	29	136
82	11.5	28	62	84	12.7	29	138
82	11.5	28	64	84	12.8	29	140
82	11.5	28	66	84	12.8	29	142
82	11.6	28	68	84	12.9	29	144
82	11.6	28	70	84	13	29	146
82	11.7	28	72	84	13	29	148
82	11.7	28	74	84	13	29	150
82	11.7	28	76	84	13	29	152
82	11.7	28	78	84	13	29	154
82	11.7	28	80	84	13	29	156
82	11.8	28	82	84	13.1	29	158
82	11.8	28	84	84	13.1	29	160
82	11.8	28	86	84	13.1	29	162
82	11.8	28	88	84	13.2	29	164
82	11.9	28	90	84	13.2	29	166
82	11.9	28	92	84	13.2	29	168
83	11.9	28	94	84	13.2	29	170
83	12	28	96	84	13.3	29	172
83	12	28	98	85	13.3	29	174
83	12	28	100	85	13.3	29	176
83	12.1	28	102	85	13.3	29	178
83	12.2	28	104	85	13.4	29	180
83	12.3	28	106	85	13.5	29	182
83	12.3	29	108	85	13.6	29	184
83	12.4	29	110	85	13.6	29	186
83	12.4	29	112	85	13.6	29	188
83	12.6	29	114	85	13.6	29	190
83	12.6	29	116	85	13.6	29	192
83	12.6	29	118	85	13.7	29	194
83	12.6	29	120	85	13.7	29	196
83	12.7	29	122	85	13.7	29	198
83	12.7	29	124	85	13.7	29	200

RH (%)	C (pF)	Temp. (ºC)	Time (s)	RH (%)	C (pF)	Temp. (ºC)	Time (s)
85	13.7	29	202	88	14.2	29	276
85	13.8	29	204	88	14.2	29	278
86	13.8	29	206	88	14.2	29	280
86	13.8	29	208	88	14.3	29	282
86	13.8	29	210	88	14.3	29	284
86	13.8	29	212	88	14.3	29	286
86	13.8	29	214	88	14.3	29	288
86	13.8	29	216	88	14.3	29	290
86	13.8	29	218	88	14.4	29	292
86	13.8	29	220	88	14.4	29	294
86	13.9	29	230	88	14.4	29	296
86	13.9	29	232	88	14.5	29	298
86	13.9	29	234	88	14.5	29	300
86	13.9	29	236	88	14.5	29	302
87	14	29	238	88	14.5	29	304
87	14	29	240	88	14.5	29	306
87	14	29	242	88	14.6	29	308
87	14	29	244	88	14.6	29	310
87	14	29	246	88	14.6	29	312
87	14	29	248	88	14.6	29	314
87	14	29	250	88	14.6	29	316
87	14	29	252	88	14.6	29	318
87	14.1	29	254	88	14.6	29	320
87	14.1	29	256	88	14.7	29	322
87	14.1	29	258	88	14.8	29	324
87	14.1	29	260	88	14.8	29	326
87	14.1	29	262	88	14.8	29	328
87	14.1	29	264	88	14.8	29	330
87	14.1	29	266	88	14.8	29	332
88	14.1	29	268	88	14.8	29	334
88	14.2	29	270	88	14.8	29	336
88	14.2	29	272	88	14.8	29	338
88	14.2	29	274	88	14.8	29	340
88	14.8	29	342	89	15.7	29	418
88	14.8	29	344	89	15.8	29	420
88	14.8	29	346	89	15.8	29	422
88	14.8	29	348	89	15.8	29	424

RH (%)	C (pF)	Temp. (ºC)	Time (s)	RH (%)	C (pF)	Temp. (ºC)	Time (s)
88	14.9	29	350	89	15.9	29	426
88	14.9	29	352	89	15.9	29	428
88	15	29	354	89	16	29	430
88	15.1	29	356	89	16	29	432
88	15.1	29	358	89	16	29	434
88	15.1	29	360	89	16	29	436
88	15.1	29	362	89	16	29	438
88	15.2	29	364	89	16	29	440
88	15.2	29	366	89	16.1	29	442
88	15.3	29	368	89	16.2	29	444
88	15.3	29	370	89	16.2	29	446
89	15.3	29	372	89	16.2	29	448
88	15.3	29	374	89	16.2	29	450
88	15.3	29	376	89	16.2	29	452
89	15.3	29	378	89	16.2	29	454
89	15.3	29	380	89	16.3	29	456
89	15.3	29	382	89	16.3	29	458
89	15.3	29	384	89	16.3	29	460
89	15.3	29	386	89	16.4	29	462
89	15.3	29	388	89	16.4	29	464
89	15.4	29	390	89	16.4	29	468
89	15.5	29	392	89	16.4	29	470
89	15.5	29	394	89	16.4	29	472
89	15.5	29	396	89	16.4	29	474
89	15.5	29	398	89	16.6	29	476
89	15.5	29	400	89	16.6	29	478
89	15.5	29	402	90	16.6	29	480
89	15.6	29	404	90	16.7	29	482
89	15.6	29	406	90	16.7	29	484
89	15.6	29	408	90	16.7	29	486
89	15.7	29	410	90	16.7	29	488
89	15.7	29	412	90	16.7	29	490
89	15.7	29	414	90	16.8	29	492
89	15.7	29	416	90	16.8	29	494
90	16.8	29	496	90	17.7	29	572
90	16.8	29	498	90	17.7	29	574
90	16.8	29	500	91	17.7	29	576
90	16.8	29	502	91	17.7	29	578

RH (%)	C (pF)	Temp. (ºC)	Time (s)	RH (%)	C (pF)	Temp. (ºC)	Time (s)
90	16.9	29	504	91	17.8	29	580
90	16.9	29	506	91	17.8	29	582
90	16.9	29	508	91	17.8	29	584
90	16.9	29	510	91	17.8	29	586
90	17	29	512	91	17.8	29	588
90	17.1	29	514	91	17.9	29	590
90	17.1	29	516	91	17.9	29	592
90	17.1	29	518	91	17.9	29	594
90	17.1	29	520	91	17.9	29	596
90	17.1	29	522	91	17.9	29	598
90	17.1	29	524	91	17.9	29	600
90	17.2	29	526	91	17.9	29	602
90	17.2	29	528	91	18	29	604
90	17.2	29	530	91	18	29	606
90	17.3	29	532	91	18	29	608
90	17.3	29	534	91	18	29	610
90	17.3	29	536	91	18	29	612
90	17.3	29	538	91	18	29	614
90	17.3	29	540	91	18.1	29	616
90	17.3	29	542	91	18.1	29	618
90	17.3	29	544	91	18.1	29	620
90	17.3	29	546	91	18.1	29	622
90	17.3	29	548	91	18.1	29	624
90	17.4	29	550	91	18.2	29	626
90	17.4	29	552	91	18.2	29	628
90	17.5	29	554	91	18.2	29	630
90	17.5	29	556	91	18.2	29	632
90	17.5	29	558	91	18.2	29	634
90	17.5	29	560	91	18.2	29	636
90	17.6	29	562	91	18.3	29	638
90	17.6	29	564	91	18.3	29	640
90	17.6	29	566	91	18.3	29	642
90	17.7	29	568	91	18.3	29	644
90	17.7	29	570	91	18.3	29	646
91	18.3	29	648	92	18.9	29	724
91	18.3	29	650	92	18.9	29	726
91	18.3	29	652	92	18.9	29	728
91	18.3	29	654	92	18.9	29	730

RH (%)	C (pF)	Temp. (ºC)	Time (s)	RH (%)	C (pF)	Temp. (ºC)	Time (s)
91	18.3	29	656	92	19	29	732
91	18.4	29	658	92	19	29	734
91	18.4	29	660	92	19	29	736
91	18.4	29	662	92	19	29	738
91	18.4	29	664	92	19	29	740
91	18.5	29	666	92	19.1	29	742
91	18.5	29	668	92	19.1	29	744
91	18.5	29	670	92	19.1	29	746
91	18.5	29	672	92	19.2	29	748
91	18.5	29	674	92	19.2	29	750
91	18.5	29	676	92	19.2	29	752
91	18.5	29	678	92	19.2	29	754
91	18.5	29	680	92	19.2	29	756
91	18.6	29	682	92	19.2	29	758
91	18.6	29	684	92	19.2	29	760
91	18.6	29	686	92	19.2	29	762
91	18.7	29	688	92	19.2	29	764
91	18.7	29	690	92	19.2	29	766
91	18.7	29	692	92	19.2	29	768
92	18.7	29	694	92	19.2	29	770
91	18.7	29	696	92	20	29	772
91	18.8	29	698	92	20	29	774
92	18.8	29	700	92	20.1	29	776
91	18.8	29	702	92	20.1	29	778
91	18.8	29	704	92	20.2	29	780
92	18.8	29	706	92	20.2	29	782
91	18.8	29	708	92	20.2	29	784
91	18.8	29	710	92	20.3	29	788
92	18.8	29	712	92	20.3	29	790
92	18.8	29	714	92	20.4	29	792
92	18.8	29	716	92	20.4	29	794
92	18.9	29	718	92	20.4	29	796
92	18.9	29	720	92	20.5	29	798
92	18.9	29	722	92	20.7	29	800

5. Adsorption in Saturated Solution of Lithium Chloride (NaCl)

RH (%)	C (pF)	Temp. (°C)	Time (s)	RH (%)	C (pF)	Temp. (°C)	Time (s)
90	16.6	28	10	87	14.5	28	66
89	16.5	28	12	87	14.5	28	68
89	16.2	28	14	87	14.5	28	70
89	16.2	28	16	87	14.3	28	72
88	16.1	28	18	87	14.3	28	74
87	15.5	28	30	87	14.3	28	76
87	15.5	28	32	87	14.3	28	78
87	15.3	28	34	87	14.3	28	80
87	15.3	28	36	87	14.2	28	82
87	15.3	28	38	87	14.2	28	84
87	15.2	28	40	87	14.2	28	86
87	15.1	28	42	87	14.2	28	88
87	15.1	28	46	87	14.2	28	90
87	15.1	28	48	87	14.1	28	92
87	15	28	50	87	14.1	28	94
87	14.9	28	52	86	13.9	28	96
87	14.8	28	54	87	13.9	28	98
87	14.7	28	56	86	13.8	28	100
87	14.7	28	58	87	13.8	28	102
87	14.6	28	60	86	13.7	28	104
87	14.6	28	62	87	13.5	28	106
87	14.5	28	64	86	13.5	28	108

6. Desorption in Saturated Solution of Lithium Chloride (NaCl)

RH (%)	C (pF)	Temp. (°C)	Time (s)	RH (%)	C (pF)	Temp. (°C)	Time (s)
86	13.5	28	0	91	15.7	28	20
87	13.9	28	2	91	15.7	28	22
88	13.9	28	4	91	15.7	28	24
89	14	28	6	91	15.7	28	26
89	14.2	28	8	91	15.8	28	28
90	14.5	28	10	91	15.8	28	30
90	14.6	28	12	91	15.8	28	32
90	14.6	28	14	91	15.8	28	34
90	14.7	28	16	91	16	28	36
90	14.7	28	18	91	16.1	28	38

91	16.1	28	40	91	16.5	28	54
91	16.1	28	42	91	16.6	28	56
91	16.2	28	44	91	16.6	28	58
91	16.3	28	46	91	16.6	28	60
91	16.4	28	48	91	16.7	28	62
91	16.4	28	50	91	16.7	28	64
91	16.4	28	52	91	16.8	28	66

7. Adsorption in Saturated Solution of Potassium Sulphate (K_2SO_4)

RH %	Capacitance (pF)	Time (s)
88	16.4	2
89	16.5	4
90	16.5	6
90	16.5	8
90	16.8	10
91	16.8	12
91	16.9	14
91	16.9	16
91	17	18
91	17	20
92	17	22
92	17.1	24
92	17.2	26
92	17.2	28
92	17.3	30
92	17.4	32
92	17.5	34
92	17.5	36
92	17.6	38
92	17.6	40
92	17.6	42
92	17.6	46
92	17.8	48
92	17.8	50
92	17.9	52
92	17.9	54
92	17.9	56
92	18	58

92	18	60
92	18	62
92	18	64
92	18.2	66
92	18.2	68
92	18.2	70
92	18.2	72
92	18.3	74
92	18.3	76
92	18.3	78
92	18.3	80
92	18.3	82
92	18.3	84
92	18.3	86
92	18.3	88
92	18.4	90
92	18.4	92
92	18.5	94
92	18.7	96
92	18.7	98
92	18.8	100
92	18.9	102
92	18.9	104
92	19	106
92	19	108
92	19	110
92	19	112
92	19.1	114
92	19.1	116
92	19.1	118
92	19.1	120
92	19.1	122
92	19.2	124
92	19.2	126
92	19.2	128
92	19.2	130
92	19.2	132
92	19.3	134
92	19.3	136

93	19.3	138
92	19.3	140
92	19.4	142
93	19.5	144
92	19.5	146
92	19.5	148
92	19.5	150
92	19.5	152
92	19.6	154
92	19.6	156
92	19.7	158
92	19.7	160
92	19.8	162
93	19.8	164
93	19.9	166
93	19.9	168
93	20	170
93	20.2	172
93	20.2	174
93	20.2	176
93	20.2	178
93	20.3	180
93	20.3	182
93	20.4	184
93	20.5	186
93	20.5	188
93	20.6	190
93	20.8	192
93	21.5	194
94	21.5	196
94	21.6	198
94	21.6	200
94	22.1	202
95	22.6	204

8. Desorption in Saturated Solution of Potassium Sulphate (K_2SO_4)

RH %	Capacitance (pF)	Time (s)
93	21	0
93	21	2
93	21	4
93	20.8	6
93	20.6	8
93	20.6	10
93	20.5	12
93	20.5	14
93	20.3	16
90	19.2	18
89	18.6	20
88	18	22
88	16.7	24
88	16.4	26
87	15.6	28

E. TGA DATA FOR SLS AND LABS SAMPLES

SLS Sampe		LABS Sample	
Temperature	**Weight (%)**	**Temperature**	**Weight (%)**
188.43	100.02	188.19	99.165
188.58	100.019	188.33	99.164
188.74	100.018	188.46	99.163
188.89	100.017	188.59	99.162
189.05	100.016	188.72	99.161
189.2	100.015	188.84	99.159
189.35	100.014	188.98	99.158
189.5	100.013	189.1	99.157
189.66	100.012	189.24	99.156
189.81	100.011	189.37	99.155
189.97	100.01	189.5	99.154
190.13	100.009	189.63	99.153
190.28	100.008	189.76	99.152
190.44	100.007	189.89	99.151
190.59	100.006	190.03	99.15
190.74	100.005	190.16	99.149
190.9	100.004	190.29	99.147
191.05	100.003	190.42	99.146
191.2	100.002	190.56	99.145
191.36	100.001	190.69	99.144
191.51	100	190.82	99.143
191.67	99.999	190.95	99.142
191.83	99.998	191.08	99.141
191.98	99.996	191.22	99.14
192.14	99.995	191.35	99.139
192.29	99.994	191.48	99.138
192.45	99.993	191.61	99.136
192.6	99.992	191.74	99.135
192.75	99.991	191.88	99.134
192.9	99.99	192.01	99.133
193.05	99.989	192.14	99.132
193.21	99.988	192.28	99.131
193.36	99.986	192.41	99.13
193.52	99.985	192.54	99.129
193.67	99.984	192.67	99.128
193.82	99.983	192.8	99.126

193.98	99.982	192.93	99.125
194.13	99.981	193.06	99.124
194.28	99.979	193.2	99.123
194.43	99.978	193.33	99.122
194.59	99.977	193.46	99.121
194.74	99.976	193.6	99.12
194.9	99.974	193.73	99.119
195.05	99.973	193.86	99.118
195.21	99.972	194	99.116
195.36	99.971	194.13	99.115
195.51	99.969	194.27	99.114
195.67	99.968	194.4	99.113
195.82	99.967	194.53	99.112
195.97	99.966	194.66	99.111
196.13	99.964	194.79	99.11
196.28	99.963	194.92	99.109
196.44	99.962	195.06	99.107
196.59	99.96	195.19	99.106
196.74	99.959	195.32	99.105
196.9	99.958	195.45	99.104
197.05	99.956	195.58	99.103
197.21	99.955	195.71	99.102
197.35	99.954	195.84	99.101
197.51	99.952	195.97	99.1
197.67	99.951	196.1	99.098
197.82	99.95	196.24	99.097
197.97	99.948	196.37	99.096
198.12	99.947	196.5	99.095
198.27	99.945	196.63	99.094
198.43	99.944	196.77	99.093
198.59	99.943	196.9	99.092
198.74	99.941	197.04	99.09
198.9	99.94	197.17	99.089
199.05	99.938	197.31	99.088
199.2	99.937	197.44	99.087
199.35	99.935	197.57	99.086
199.5	99.934	197.7	99.085
199.65	99.932	197.83	99.084
199.81	99.931	197.96	99.082

199.97	99.929	198.1	99.081
200.12	99.928	198.23	99.08
200.27	99.926	198.36	99.079
200.43	99.925	198.49	99.078
200.58	99.923	198.63	99.077
200.73	99.922	198.76	99.075
200.89	99.92	198.89	99.074
201.04	99.919	199.02	99.073
201.19	99.917	199.15	99.072
201.35	99.916	199.27	99.071
201.5	99.914	199.4	99.07
201.66	99.912	199.53	99.068
201.81	99.911	199.66	99.067
201.96	99.909	199.79	99.066
202.12	99.908	199.93	99.065
202.27	99.906	200.06	99.064
202.43	99.904	200.19	99.063
202.58	99.903	200.31	99.061
202.73	99.901	200.44	99.06
202.88	99.899	200.56	99.059
203.04	99.898	200.68	99.058
203.19	99.896	200.81	99.057
203.35	99.894	200.93	99.056
203.5	99.893	201.06	99.054
203.65	99.891	201.18	99.053
203.81	99.889	201.31	99.052
203.96	99.888	201.43	99.051
204.12	99.886	201.57	99.05
204.27	99.884	201.69	99.048
204.42	99.882	201.81	99.047
204.58	99.881	201.94	99.046
204.73	99.879	202.06	99.045
204.88	99.877	202.19	99.044
205.03	99.875	202.31	99.042
205.19	99.874	202.44	99.041
205.34	99.872	202.56	99.04
205.49	99.87	202.69	99.039
205.64	99.868	202.82	99.038
205.8	99.866	202.94	99.036

205.95	99.864	203.07	99.035
206.1	99.863	203.19	99.034
206.25	99.861	203.32	99.033
206.41	99.859	203.44	99.032
206.56	99.857	203.57	99.03
206.72	99.855	203.7	99.029
206.87	99.853	203.83	99.028
207.03	99.851	203.96	99.027
207.18	99.849	204.08	99.025
207.33	99.848	204.21	99.024
207.48	99.846	204.34	99.023
207.64	99.844	204.46	99.022
207.79	99.842	204.59	99.021
207.94	99.84	204.72	99.019
208.1	99.838	204.87	99.018
208.25	99.836	205.02	99.017
208.41	99.834	205.18	99.016
208.56	99.832	205.35	99.014
208.71	99.83	205.53	99.013
208.87	99.828	205.72	99.012
209.02	99.826	205.91	99.011
209.17	99.824	206.1	99.009
209.32	99.822	206.29	99.008
209.48	99.82	206.48	99.007
209.63	99.818	206.66	99.006
209.78	99.816	206.85	99.004
209.94	99.813	207.02	99.003
210.09	99.811	207.21	99.002
210.24	99.809	207.39	99.001
210.39	99.807	207.57	98.999
210.54	99.805	207.75	98.998
210.7	99.803	207.93	98.997
210.85	99.801	208.11	98.996
211.01	99.798	208.29	98.994
211.16	99.796	208.47	98.993
211.32	99.794	208.65	98.992
211.47	99.792	208.82	98.99
211.62	99.79	209	98.989
211.77	99.787	209.18	98.988

211.92	99.785	209.35	98.987
212.07	99.783	209.52	98.985
212.22	99.781	209.7	98.984
212.38	99.778	209.87	98.983
212.54	99.776	210.04	98.981
212.69	99.774	210.21	98.98
212.84	99.772	210.38	98.979
213	99.769	210.55	98.978
213.15	99.767	210.72	98.976
213.3	99.765	210.89	98.975
213.45	99.762	211.05	98.974
213.61	99.76	211.22	98.972
213.76	99.757	211.38	98.971
213.91	99.755	211.54	98.97
214.07	99.753	211.7	98.968
214.22	99.75	211.86	98.967
214.37	99.748	212.02	98.966
214.53	99.745	212.18	98.965
214.68	99.743	212.34	98.963
214.83	99.74	212.49	98.962
214.99	99.738	212.66	98.961
215.14	99.735	212.82	98.959
215.29	99.733	212.97	98.958
215.45	99.73	213.13	98.957
215.6	99.728	213.29	98.955
215.76	99.725	213.44	98.954
215.91	99.723	213.6	98.953
216.06	99.72	213.76	98.951
216.21	99.718	213.91	98.95
216.37	99.715	214.07	98.949
216.52	99.712	214.22	98.947
216.67	99.71	214.37	98.946
216.82	99.707	214.53	98.944
216.98	99.704	214.68	98.943
217.13	99.702	214.84	98.942
217.28	99.699	214.99	98.94
217.44	99.696	215.14	98.939
217.59	99.694	215.29	98.938
217.74	99.691	215.44	98.936

217.89	99.688	215.59	98.935
218.04	99.685	215.74	98.934
218.2	99.683	215.89	98.932
218.35	99.68	216.04	98.931
218.5	99.677	216.19	98.929
218.65	99.674	216.34	98.928
218.81	99.672	216.49	98.927
218.96	99.669	216.63	98.925
219.11	99.666	216.78	98.924
219.27	99.663	216.92	98.922
219.42	99.66	217.06	98.921
219.57	99.657	217.19	98.92
219.73	99.654	217.32	98.918
219.88	99.651	217.43	98.917
220.03	99.649	217.55	98.915
220.19	99.646	217.66	98.914
220.34	99.643	217.78	98.913
220.49	99.64	217.89	98.911
220.64	99.637	218.01	98.91
220.8	99.634	218.13	98.908
220.95	99.631	218.25	98.907
221.1	99.628	218.38	98.906
221.25	99.625	218.5	98.904
221.41	99.622	218.62	98.903
221.56	99.619	218.74	98.901
221.71	99.616	218.86	98.9
221.86	99.613	218.98	98.898
222.02	99.61	219.1	98.897
222.17	99.606	219.23	98.895
222.32	99.603	219.35	98.894
222.47	99.6	219.47	98.893
222.63	99.597	219.6	98.891
222.78	99.594	219.73	98.89
222.93	99.591	219.85	98.888
223.08	99.588	219.98	98.887
223.23	99.585	220.11	98.885
223.39	99.581	220.23	98.884
223.54	99.578	220.36	98.882
223.69	99.575	220.48	98.881

223.85	99.572	220.61	98.879
224.01	99.569	220.74	98.878
224.16	99.565	220.86	98.876
224.32	99.562	220.99	98.875
224.48	99.559	221.12	98.874
224.63	99.555	221.25	98.872
224.78	99.552	221.38	98.871
224.93	99.549	221.51	98.869
225.08	99.546	221.64	98.868
225.22	99.542	221.77	98.866
225.37	99.539	221.9	98.865
225.52	99.536	222.03	98.863
225.67	99.532	222.16	98.862
225.81	99.529	222.29	98.86
225.96	99.525	222.42	98.858
226.11	99.522	222.55	98.857
226.26	99.519	222.68	98.855
226.41	99.515	222.8	98.854
226.56	99.512	222.93	98.852
226.71	99.508	223.06	98.851
226.87	99.505	223.19	98.849
227.02	99.501	223.32	98.848
227.17	99.498	223.45	98.846
227.33	99.494	223.59	98.845
227.48	99.491	223.72	98.843
227.64	99.487	223.85	98.842
227.79	99.484	223.98	98.84
227.95	99.48	224.11	98.839
228.1	99.477	224.24	98.837
228.25	99.473	224.37	98.835
228.41	99.47	224.51	98.834
228.56	99.466	224.64	98.832
228.71	99.462	224.77	98.831
228.86	99.459	224.9	98.829
229.01	99.455	225.03	98.828
229.16	99.451	225.16	98.826
229.31	99.448	225.29	98.824
229.46	99.444	225.42	98.823
229.61	99.44	225.56	98.821

229.76	99.437	225.69	98.82
229.91	99.433	225.83	98.818
230.07	99.429	225.96	98.816
230.22	99.426	226.1	98.815
230.38	99.422	226.23	98.813
230.53	99.418	226.36	98.812
230.68	99.414	226.49	98.81
230.83	99.411	226.62	98.808
230.98	99.407	226.75	98.807
231.13	99.403	226.88	98.805
231.28	99.399	227.01	98.803
231.43	99.395	227.15	98.802
231.58	99.391	227.28	98.8
231.74	99.388	227.41	98.799
231.89	99.384	227.54	98.797
232.04	99.38	227.67	98.795
232.19	99.376	227.81	98.794
232.34	99.372	227.94	98.792
232.49	99.368	228.08	98.79
232.64	99.364	228.21	98.789
232.79	99.36	228.35	98.787
232.95	99.356	228.49	98.785
233.1	99.352	228.63	98.784
233.25	99.348	228.76	98.782
233.4	99.344	228.9	98.78
233.55	99.34	229.03	98.779
233.71	99.336	229.16	98.777
233.86	99.332	229.29	98.775
234.01	99.328	229.42	98.774
234.17	99.324	229.56	98.772
234.32	99.32	229.69	98.77
234.47	99.316	229.82	98.769
234.62	99.312	229.96	98.767
234.77	99.308	230.09	98.765
234.92	99.304	230.23	98.763
235.07	99.3	230.36	98.762
235.22	99.296	230.5	98.76
235.37	99.291	230.63	98.758
235.53	99.287	230.76	98.757

235.67	99.283	230.9	98.755
235.83	99.279	231.03	98.753
235.98	99.275	231.16	98.751
236.13	99.27	231.3	98.75
236.28	99.266	231.43	98.748
236.44	99.262	231.56	98.746
236.59	99.258	231.69	98.744
236.74	99.254	231.83	98.743
236.89	99.249	231.96	98.741
237.04	99.245	232.09	98.739
237.19	99.241	232.22	98.737
237.34	99.236	232.36	98.736
237.5	99.232	232.49	98.734
237.65	99.228	232.62	98.732
237.8	99.223	232.76	98.73
237.95	99.219	232.89	98.729
238.1	99.215	233.02	98.727
238.25	99.21	233.15	98.725
238.4	99.206	233.28	98.723
238.55	99.201	233.42	98.721
238.71	99.197	233.55	98.72
238.86	99.193	233.68	98.718
239.01	99.188	233.82	98.716
239.16	99.184	233.95	98.714
239.31	99.179	234.09	98.712
239.45	99.175	234.22	98.711
239.6	99.17	234.35	98.709
239.75	99.166	234.48	98.707
239.91	99.161	234.62	98.705
240.06	99.157	234.75	98.703
240.21	99.152	234.88	98.701
240.37	99.147	235.02	98.7
240.52	99.143	235.15	98.698
240.67	99.138	235.29	98.696
240.83	99.134	235.42	98.694
240.98	99.129	235.56	98.692
241.13	99.125	235.69	98.69
241.28	99.12	235.82	98.688
241.42	99.115	235.96	98.687

241.57	99.111	236.09	98.685
241.72	99.106	236.22	98.683
241.87	99.101	236.35	98.681
242.02	99.097	236.49	98.679
242.18	99.092	236.62	98.677
242.33	99.087	236.75	98.675
242.48	99.082	236.88	98.673
242.63	99.078	237.02	98.671
242.78	99.073	237.15	98.67
242.93	99.068	237.28	98.668
243.08	99.063	237.41	98.666
243.24	99.058	237.55	98.664
243.39	99.054	237.68	98.662
243.54	99.049	237.82	98.66
243.69	99.044	237.95	98.658
243.84	99.039	238.09	98.656
243.99	99.034	238.22	98.654
244.14	99.029	238.36	98.652
244.3	99.025	238.49	98.65
244.45	99.02	238.62	98.648
244.6	99.015	238.75	98.646
244.75	99.01	238.88	98.644
244.9	99.005	239.01	98.642
245.05	99	239.15	98.641
245.2	98.995	239.29	98.639
245.35	98.99	239.42	98.637
245.51	98.985	239.55	98.635
245.66	98.98	239.69	98.633
245.81	98.975	239.82	98.631
245.96	98.97	239.95	98.629
246.11	98.965	240.08	98.627
246.26	98.96	240.22	98.625
246.41	98.955	240.35	98.623
246.56	98.95	240.49	98.621
246.71	98.945	240.62	98.619
246.87	98.94	240.76	98.617
247.02	98.935	240.9	98.615
247.17	98.929	241.03	98.613
247.32	98.924	241.17	98.611

247.47	98.919	241.3	98.608
247.62	98.914	241.44	98.606
247.77	98.909	241.57	98.604
247.92	98.904	241.7	98.602
248.07	98.899	241.84	98.6
248.23	98.893	241.97	98.598
248.38	98.888	242.1	98.596
248.53	98.883	242.23	98.594
248.68	98.878	242.35	98.592
248.83	98.872	242.47	98.59
248.98	98.867	242.6	98.588
249.13	98.862	242.72	98.586
249.28	98.857	242.84	98.584
249.43	98.851	242.98	98.582
249.58	98.846	243.11	98.58
249.73	98.841	243.24	98.578
249.88	98.835	243.38	98.575
250.04	98.83	243.51	98.573
250.19	98.825	243.64	98.571
250.34	98.819	243.78	98.569
250.49	98.814	243.91	98.567
250.64	98.808	244.05	98.565
250.79	98.803	244.18	98.563
250.94	98.798	244.31	98.561